RHEINISCHE FRIEDRICH–WILHELMS–UNIVERSITÄT
BONN

Complex organic chemistry in high-mass star forming regions

Dissertation

zur

Erlangung des Doktorgrades (*Dr. rer. nat.*)

der

Mathematisch–Naturwissenschaftlichen Fakultät

der

Rheinischen Friedrich–Wilhelms–Universität, Bonn

vorgelegt von

Mélisse Bonfand-Caldeira

aus

Le Pont-de-Beauvoisin, Frankreich

Bonn 2019

Angefertigt mit Genehmigung der Mathematisch–Naturwissenschaftlichen Fakultät der Rheinischen Friedrich–Wilhelms–Universität Bonn

1. Referent: Prof. Dr. Karl M. Menten
2. Referent: Prof. Dr. Pavel Kroupa
Tag der Promotion: June 17$^{\text{th}}$, 2019
Erscheinungsjahr: 2019

Diese Dissertation ist auf dem Hochschulschriftenserver der ULB Bonn unter
http://nbn-resolving.de/urn:nbn:de:hbz:5n-55905 elektronisch publiziert

RHEINISCHE FRIEDRICH–WILHELMS–UNIVERSITÄT BONN

Abstract

by Mélisse Bonfand-Caldeira

for the degree of

Doctor rerum naturalium

The quest for interstellar complex organic molecules (COMs) lies at the heart of astrochemistry. One basic motivation is to figure out how the rich inventory of COMs found in meteorites and comets is connected to interstellar chemistry. While the number of COMs detected in the interstellar medium increases, we wish to understand whether chemical complexity is a natural outcome of interstellar chemistry, which degree of complexity can be reached, and when, where and under which conditions these molecules form and how their occurence evolves from interstellar clouds to planetary systems.

Most interstellar COMs were first detected toward the dense and warm parts of high-mass star-forming regions, called hot molecular cores. In particular, Sagittarius B2 (Sgr B2), one of the most active star-forming regions in our Galaxy, is an excellent target to study the production of COMs under extreme physical conditions (high densities, strong radiation field, high cosmic-ray flux).

In this thesis we take advantage of the high sensitivity of a new type of imaging spectral line survey made possible by the Atacama Large Millimeter/submillimeter Array (ALMA). It affords studies of the spatial structure and chemical content of active star-forming regions in Sgr B2 in unprecedented detail. We report the detection of three new hot cores in Sgr B2(N), one of Sgr B2's main star-forming sites. In a detailed comparative study, we determine their chemical composition, density, mass, temperature, and spatial structure. We check for association with maser sources and ultra-compact HII regions, signposts of recent high-mass star formation, as well as outflows, to evaluate the evolutionary stage of the hot cores. In the second part of the thesis we analyze their physical evolution from the cold pre-stellar phase to the present time. We use results of previous radiation-magnetohydrodynamical simulations of high-mass star formation and stellar structure calculations combined with a radiative transfer model to derive the thermal history of the sources. We compute time-dependent chemical abundances using the astrochemical code MAGICKAL, focusing especially on selected COMs to investigate in detail the chemical reactions and processes involved in their formation under the extreme conditions that characterize Sgr B2(N). We compare the chemical model results to the abundances derived from the observations toward the hot cores and find that a cosmic-ray ionization rate 50 times higher than the solar neighborhood value best characterizes Sgr B2(N)'s environmental conditions. We are also able to constrain the range of dust temperatures reached during the earlier pre-stellar phase at which COMs form on dust-grain surfaces. We show that COMs still form efficiently with minimum dust temperatures as high as 15 K, but the current chemical composition of the hot cores excludes minimum temperatures higher than 25 K.

Á ma grand-mère, Lucienne Côte.

List of publications related to this doctoral thesis

"Exploring molecular complexity with ALMA (EMoCA): Detection of three new hot cores in Sagittarius B2(N)"
M. Bonfand, A. Belloche, K. M. Menten, R. T. Garrod, H. S. P. Müller; 2017, A&A, 604, A60

"The complex chemistry of hot cores in Sgr B2(N): Influence of cosmic-ray ionization and thermal history"
M. Bonfand, A. Belloche, R. T. Garrod, K. M. Menten, E. Willis, G. Stéphan, H. S. P. Müller; 2019, A&A, 628, A27

List of softwares used in this doctoral thesis

GILDAS (CLASS, Weeds, GreG)
http://www.iram.fr/IRAMFR/GILDAS

RadMC–3D
http://www.ita.uni-heidelberg.de/ dullemond/software/radmc-3d/

Acknowledgements

I remember this day at school when we had to make a short presentation about a chosen job career in front of the other kids. I was ten years old and I knew I was going to be an astrophysicist ! Since then, every step I made in my life brought me closer to this goal and the dream finally became true when three and a half years ago I stepped for the first time in the entrance of the Max-Planck-Institute for Radioastronomy in Bonn. It was for me the beginning of an amazing experience of which this thesis is the accomplishment. Of course this would not have been possible without many people that I want to thank here.

First of all I would like to thank Prof. Dr. Karl M. Menten for giving me the opportunity to work in his group. It has been a privileged for me to work among experienced researchers, in a dynamic group doing great science, with endless sources of new ideas. I would like to thank especially my day to day advisor, Dr. Arnaud Belloche for teaching me with great care (almost) all what I know about astrophysics and preparing me to be (I hope !) a good researcher. Thank you for taking the time to explain things, share ideas, discuss problems, answer silly questions, and give valuable comments and advices which made me always try to give the best of myself for every task I did. You gave me strength and inspiration to continue working until the end and always with the smile even when I had to (re-)do (again) last-minute calculations/modifications just before submitting papers or proposals !

I would like to thank all the staff of the Max-Planck-Institute for Radioastronomy for creating such a good working atmosphere over the last three years. It will always feel a bit like home here ! I would like to address a special thank to Eva Schmelmer, Barbara Menten, and Le Tran who made my life here in Bonn so much easier helping me with (german) paper work.

I would like to thank the members of my thesis advisory committee, Dr. Silke Britzen and Prof. Dr. Pavel Kroupa, who followed my thesis work for the last three years, as well as Prof. Dr. Klaus Desch and Prof. Dr. Hubert Schorle who kindly accepted to join my thesis promotion committee.

I thank the International Max Planck Research School for Astronomy & Astrophysics for giving me access to various lectures and supporting me for conferences. In the same way I thank the Collaborative Research Centre 956 that funded my doctoral thesis and also gave me the opportunity to join an amazing exchange program in the USA.

I thank the University of Virginia for hosting me as a visiting student for a few months. In particular, I want to thank Prof. Dr. Rob Garrod for inviting me to work in his group. Thank you also to Eric, Gwendoline, Minwha, Christopher, Mattew, Aspen, and Ilsa for the great time we had in Charlottesville !

I would like to say a big thank you to all the staff of the APEX telescope for being always so kind every time I visited. Traveling to Chile during my doctoral studies was an amazing experience that I will never forget !

A very special thank you goes to Dr. Bérengère Parise and Dr. Pierre Hily-Blant who gave me the opportunity to make my very first research internships when I was still a young student in my early years at the university. Without you and your constant support I would probably not be sitting here finishing to write this thesis today.

A huge thank you to the best officemates ever Vivien Thiel, Arshia Jacob, Laura Busch, and Yuxin Lin who made my days at work so much nicer ! Thank you for all the fun we had together, all the cakes we shared, and for not letting me go completely crazy especially for these

last months.

A special thank you to my fellow radio-lab monkeys Hans Nguyen (aka Wei-Wei) and Eric Jimenez-Andrade for all the “amazing” hours we spent together in the radio lab. I will never forget the day Ka Tat tried to convince us that it would be fun to tutor this lab...

A big thank you to all students, post-doc and others I have met over the last three years and who made Germany feel like home ! I am thinking of Nina, Maitraiyee, Carsten, Christos, Dario, Enrico, Fateme, Mathilde, Marilyn, Alessandro, Ka Tat, Alvaro, Basilio, Behnam, Joey, Kevin, Henning, Jackie, Gisela, Pavol, Sac, Sergio, Alberto, Veselina, Victoria, Wonju...

Thank you Alban Ceau and Yann Cohen for traveling all the way to visit me here in Bonn.

Thank you Benjamin Adroit for the “frenchiness” you brought to my german life ! Bonn is not the same without you and your craziness.

Thank you Michael Mattern for your company during the long nights at work, for the chicken evenings, for solving all my python issues and keeping me from throwing the computer away when things are not working like I want. Thank you for your constant support and for always trying to make me smile even when I do not want to.

I want to thank also my three brothers, Teva, Yann, and Joss Bonfand who fill me with so much love and happiness every day, at any time and wherever I am in the world. Growing up with you always made me feel like part of a “clan” ! No one knows how to enjoy bad jokes as good as you do and to laugh about everything... even when it is actually not fun ! Thank you Yann for spending so much time telling me about the stars when I was a kid and feeding my interest for astronomy !

Finally, I would like to address my biggest thank you to the strongest woman I know, who taught me that everything in life is possible if you work hard for it, who always supported me, always believed in me, my mother, Manuella Caldeira. I hope today you can be proud of me. Thank you so much for making me the person I am and encouraging me to follow my dreams the get the life I always wanted to have.

Contents

Nomenclature

Frequently used acronyms

ALMA	Atacama Large Millimeter/submillimeter Array
APEX	Atacama Pathfinder Experiment
CMB	Cosmic microwave background
CMZ	Central molecular zone
CNM	Cold Neutral Medium
COM	Complex organic molecule
CR	Cosmic ray
CRIR	Cosmic-ray ionization rate
EMoCA	Exploring Molecular Complexity with ALMA
FIR	Far infrared
FWHM	Full width at half maximum
GC	Galactic center
GMC	Giant molecular cloud
HIM	Hot ionized medium
HMC	Hot molecular core
HPBW	Half power beam width
IRAM	Institut de Radioastronomie Millimétrique
ISM	Interstellar medium
ISRF	Interstellar radiation field
JVLA	Karl G. Jansky Very Large Array
LSB	Lower side band
MAGICKAL	Model for Astrophysical Gas and Ice Chemical Kinetics and Layering
MC	Molecular clouds
MDC	Massive dense core
MIR	Mid infrared
NIR	Near infrared
PA	Position angle
PWV	Precipitable water vapor
ReMoCA	Re-exploring Molecular Complexity with ALMA
SFR	Star formation rate
SPW	Spectral window
USB	Upper side band
UV	Ultra violet
WIM	Warm ionized medium
WNM	Warm neutral medium

Physical units

1 W	$= 1\ \mathrm{kg\ m^2\ s^{-3}}$
1 J	$= 1\ \mathrm{kg\ m^2\ s^{-2}}$
1 Jy	$= 10^{-26}\ \mathrm{W\ m^{-2}\ Hz^{-1}}$
1 eV	$= 1.602{\times}10^{-19}\ \mathrm{J}$

Physical constants

Speed of light (in vacuum)	$c = 2.998 \times 10^8\ \mathrm{m\ s^{-1}}$
Planck constant	$h = 6.626 \times 10^{-34}\ \mathrm{J\ s}$
Boltzmann constant	$k_\mathrm{b} = 1.381 \times 10^{-23}\ \mathrm{J\ K^{-1}}$
Stefan–Boltzmann constant	$\sigma = 5.670 \times 10^{-8}\ \mathrm{W\ m^{-2}\ K^{-4}}$
Gravitational constant	$G = 6.670 \times 10^{-11}\ \mathrm{m^3\ kg^{-1}\ s^{-2}}$
Mass H atom	$m_\mathrm{H} = 1.673 \times 10^{-27}\ \mathrm{kg}$
Mean molecular weight per free particle	$\mu = 2.37$
Molecular weight per hydrogen molecule	$\mu_{\mathrm{H}_2} = 2.8$

Astronomical constants

Astronomical unit	$1\ \mathrm{au} = 1.496 \times 10^{11}\ \mathrm{m}$
Parsec	$1\ \mathrm{pc} = 3.086 \times 10^{16}\ \mathrm{m}$
Year	$1\ \mathrm{yr} = 3.156 \times 10^7\ \mathrm{s}$
Solar mass	$M_\odot = 1.989 \times 10^{30}\ \mathrm{kg}$
Solar radius	$R_\odot = 6.957 \times 10^8\ \mathrm{m}$
Solar luminosity	$L_\odot = 3.828 \times 10^{26}\ \mathrm{W}$
Effective temperature of the Sun	$T_\mathrm{eff} = 5770\,\mathrm{K}$

Chapter 1

Introduction

Contents

In order to explain the origin of large interstellar organic molecules, building blocks of the ingredients of life as we know it on Earth, it is crucial to understand how, when, where,and under which conditions they form. This can be done by studying the close interplay between newly formed stars and the surrounding galactic interstellar medium. In this chapter I give a brief overview of the current theories on how high-mass stars form, and of the physical processes at work in the interstellar medium and their influence on the interstellar chemistry. Then I present the galactic center region, in particular the galactic center cloud Sagittarius B2 (Sgr B2), which is an excellent target to test our current understanding of high-mass star formation and interstellar chemistry under extreme physical conditions, not met in other regions forming high-mass stars. *This chapter is largely based on Lequeux (2005); Zinnecker & Yorke (2007); Krügel (2008); Herbst & van Dishoeck (2009); Draine (2011); Motte et al. (2018). Other references are mentioned explicitly in the text.*

1.1 The interstellar medium in the Milky Way

Our Galaxy, the Milky Way, is a complex system of stars, gas, and dust, bound by their own gravity and in constant interaction. The matter between the stars, or interstellar medium (ISM), is mostly composed of gas (∼99% of the ISM mass), mixed with interstellar dust particles, which represent only ∼1% of the ISM mass. Most of this interstellar matter is concentrated within a

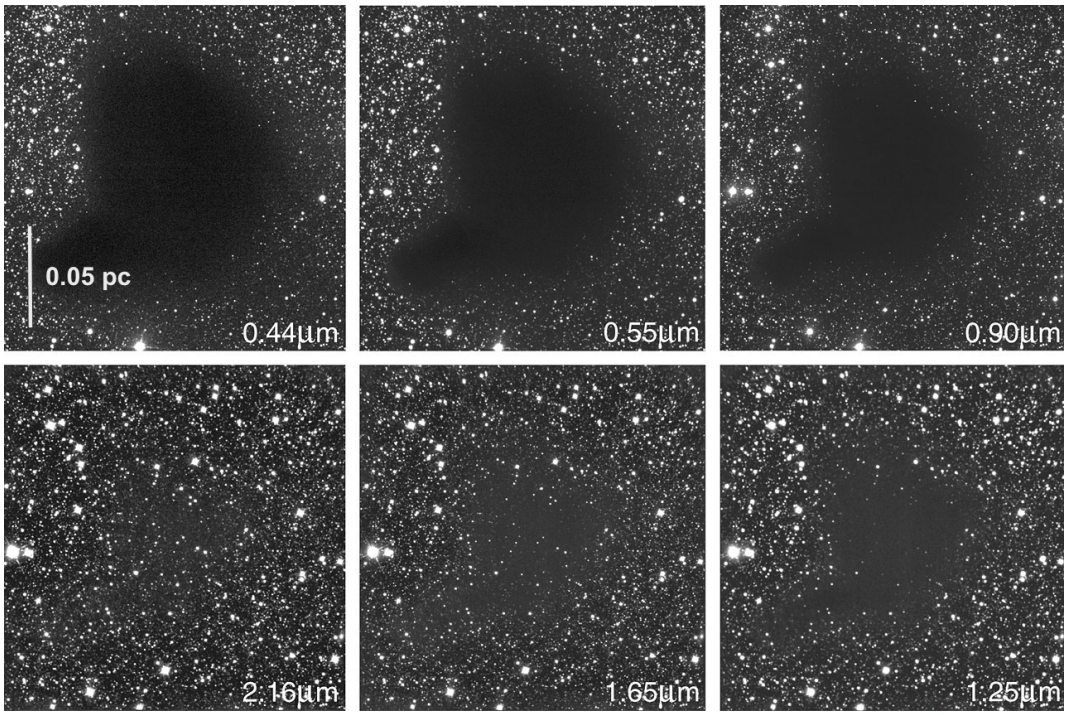

Figure 1.1: Dark molecular cloud Barnard 68 imaged in six different wavelengths, indicated in the lower right corner and increasing clockwise. The three top panels were obtained with the Very Large Telescope (VLT), while the three bottom panels were obtained with the New Technology Telescope (NTT). They show that the absorption of the light emitted by background stars diminishes with increasing wavelength. With the near infrared camera of the NTT (at 2.16 μm) one can see through the cloud. *Image credit: ESO.*

relatively thin disk, only 400–600 pc height, with a diameter of ∼20–30 kpc around the Galactic center (GC), often referred to as the Galactic disk.

The interstellar gas is mostly composed of hydrogen (∼70% of the total ISM gas), by far the most abundant element in the Universe. About 60% of the interstellar hydrogen is found in atomic form (H), ∼20% in the form of H_2 molecules, and finally ∼20% is ionized (H^+). The ISM gas also contains a small fraction of helium (∼28% by mass) and heavier elements (∼2%).

Interstellar dust grains are tiny solid particles composed of silicates and carbonaceous matter, with sizes ranging from ∼10 nm to 0.5 μm. Dust particles are ubiquitous in the ISM, as revealed by the presence of dark "patches" observed toward the Milky Way that obscure the stars located within and behind them (see Fig. 1.1). Interstellar dust grains account for most of the visual extinction, that is the difference between the visual magnitude of a star in the absence of absorbing material (mostly dust) and the actual observed magnitude. Dust particles absorb a large fraction of the photons emitted by stars in the ultra-violet (UV), visible, and near infrared (NIR) wavelength range. The absorbed energy is then re-emitted thermally at mid- and far-infrared wavelengths (MIR and FIR, respectively), depending on the temperature of the emitting dust grains (see Fig. 1.2). In fact, the spectral energy distribution (SED) of emission from a uniform population of dust grains depends on the frequency-dependent dust optical depth (see Sects. 2.2.1 and 2.2.2) which modifies the blackbody shape of the dust SED.

Although dust represents only a tiny fraction of the ISM's total mass, it is a crucial ingredient

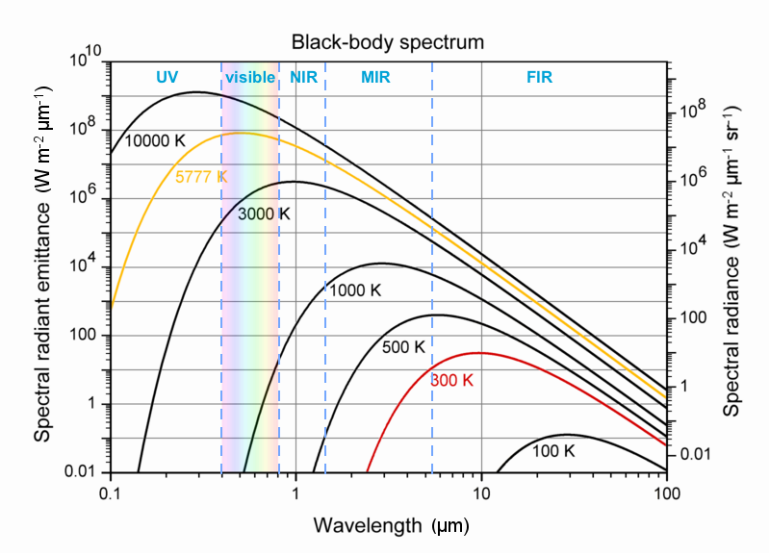

Figure 1.2: The thermal radiation spontaneously emitted by any heated matter can be approximated by a (modified) blackbody radiation. The spectral radiant emittance represents the radiant flux emitted by a given surface per unit area and per unit wavelength, while the spectral radiance gives the radiant flux per unit solid angle. The intensity of the emission and the peak wavelength depend on the body's effective temperature which is assumed to be uniform and constant. For instance, stars like our Sun (with an effective temperature of 5777 K, yellow line) mostly radiate in the visible part of the spectrum. For lower temperatures, the peak of the blackbody spectrum moves to longer wavelengths. Abbreviations stand for: ultra-violet (UV), near-infrared (NIR), mid-infrared (MIR), and far infrared (FIR). *Image credit.*

for many physical and chemical processes. As dust grains can absorb efficiently part of the radiation emitted by stars, they provide shielding for gas-phase molecules against external UV photons, which would otherwise dissociate or ionize (and thus destroy) these molecules. In cold, dense regions, shielded from UV radiation, the refractory core of the grains can be coated by volatile ice mantles which form when gas-phase material happens to stick onto dust grains upon collisions. Dust grains then act like catalysts for chemical reactions that may not occur in the gas phase otherwise. In particular dust grains are responsible for the production of the most abundant molecule in the Universe, H_2, when two H atoms meet and react on their surface. The ice mantles of interstellar dust grains represent a major reservoir of heavy elements in the ISM. This material will eventually return to the gas phase upon desorption of the grain ices, possibly triggering a rich subsequent high-temperature gas-phase chemistry. Dust also plays an important role by regulating the heating and cooling of the interstellar gas. At densities above a few 10^4 particles per cubic centimeter, collisions with dust grains dominate gas cooling, as long as the dust temperature is lower than the gas kinetic temperature (that is the Maxwellian speed distribution of the gas components which can be atoms, molecules, or electrons). For densities above $\sim 10^6$ cm^{-3}, collisions are frequent enough for gas and dust temperatures to be closely linked and the gas kinetic temperature is essentially equal to the dust temperature. Measurements carried out toward various regions of the ISM at infrared to submillimeter wavelengths with the *Herschel* Space Observatory and the *Planck* space mission have unveiled dust temperatures ranging between ~10 and 30 K (see, e.g., Planck Collaboration

et al. 2014a,b; Peretto et al. 2010), from diffuse to denser interstellar material.

The distribution of the interstellar material in the Galactic disk is not homogeneous. From place to place, the ISM can have very different physical and chemical properties depending on the external radiation field (ISRF), turbulence, magnetic fields, and high-energy cosmic rays. In the following sections we will see how the ambient interstellar radiation field (Sect. 1.1.1), cosmic rays (Sect. 1.1.2), and the star-formation process (Sect. 1.1.5) affect the interstellar matter and what characterizes the different regions of the ISM (Sects. 1.1.3 and 1.1.4).

1.1.1 The interstellar radiation field

The ISM is bathed in an electromagnetic radiation field coming from different sources, that represents a continuous spectrum covering the wavelength regime between microwave (150 mm) and far-UV (FUV, 0.1 μm). Following the description of Draine (1978), Mathis et al. (1983), and Black (1994), the spectrum of the standard ISRF in the solar neighborhood can be represented by the sum of several modified blackbodies (see, e.g., Zucconi et al. 2001). The three major contributions to the ISRF spectrum are: i) the starlight, which dominates the emission between FUV and NIR, ii) the interstellar dust particles which emit in NIR and FIR, and iii) the cosmic microwave background (CMB) emission (blackbody radiation at 2.726 K), which dominates at wavelengths beyond the FIR regime.

The ISRF is not uniform in the ISM, in fact, its strength strongly depends on the galactic location (see Sect. 1.4.1). Hereafter we designate the strength of the radiation field toward a given region of the ISM with respect to the local standard of 1 G_0, in units of the standard Draine field (Draine 1978).

For interstellar dust grains that are not directly exposed to thermal radiation from close stars, the ambient ISRF is the main source of grain heating. In the low density regions of the ISM (*i.e.* low visual extinction), dust-grain ice mantles are easily destroyed by external UV photons. In high visual extinction regions, where the UV radiation is much attenuated by outer layers of dust, radiation at longer wavelengths becomes more relevant.

1.1.2 Cosmic rays

Cosmic rays mainly consist of very high-energy (*i.e* relativistic) protons (MeV–TeV), which are primarily produced upon the death of high-mass stars (see Sect. 1.2), in shock waves in supernova remnants (Drury 1983) or accelerated up to relativistic energies by means of shock processes (Padovani et al. 2016) within protostellar sources (that is stars that have not started burning hydrogen yet, see Set. 1.2.2). In the dense parts of the ISM, shielded from external UV radiation, cosmic-ray particles are the primary source of ionization. They may in principle ionize any species but H, H_2, and He are mostly affected due to their high abundances in the ISM. Each direct cosmic-ray ionization event (*i.e.* primary ionization) of H_2, H, or He, results in the production of a secondary electron:

$$\mathrm{X} + \mathrm{CR} \rightarrow \mathrm{X}^+ + e^- + \mathrm{CR}' \,, \tag{1.1}$$

where X is either H_2, H, or He. CR′ is used to account for the energy lost by the incident cosmic-ray particle CR. The secondary electrons produced upon reaction 1.1) have enough energy to cause additional ionizations (Goldsmith & Langer 1978), leading to subsequent ion-molecule chemical reactions. Reaction 1.1 may also be followed by electronic recombination with H_2^+ leading to the production of H_2 in an excited state. When de-exciting back to the ground

state, H_2 molecules produce cosmic-ray-induced UV radiation (Prasad & Tarafdar 1983) that can ionize and dissociate both gas-phase and grain-surface species, even in high density gas at high visual extinction where external UV radiation cannot penetrate. For a detailed review on the CR-induced chemistry in the ISM see, e.g. Dalgarno (2006) and Snow & Bierbaum (2008). Upon collision, cosmic rays may deposit a fraction of their energy into the grains, and thereby heat the dust (Leger et al. 1985; Ivlev et al. 2015).

The cosmic-ray flux toward a given region of the ISM is usually parametrized by the so-called cosmic-ray ionization rate (CRIR), ζ^{H_2}, which describes the total rate of ionization per H_2 molecule per second, including secondary ionizations. The first theoretical determination of the CRIR was made by Hayakawa et al. (1961) who investigated the CR-induced radiations from hydrogen atoms in interstellar clouds of neutral hydrogen. Their estimate was revised later by Spitzer & Tomasko (1968), who derived a lower limit of $\zeta^H = 6.8{\times}10^{-18}$ s^{-1}, which corresponds to $\zeta^{H_2} \sim 1{\times}10^{-17}$ s^{-1}, according to the approximation $\zeta^{H_2} \sim 1.53\zeta^H$ (Glassgold & Langer 1974) used under typical diffuse gas conditions (see Sect. 1.1.3). This value of ζ^{H_2} is often referred to as the standard CRIR.

Ionization cross sections for cosmic rays impacting molecular hydrogen and helium are higher for low-energy particles (Padovani & Galli 2013), therefore, low-energy cosmic rays (<1 GeV) are particularly important for the ionization processes in the ISM. However, measurements of the CRIR in this energy range cannot be obtained through direct detection from Earth because the low-energy cosmic rays are prevented from entering the heliosphere by the solar wind (Parker 1958). Instead, the CRIR can be estimated by interpreting the observed molecular abundances of specific species whose formation and destruction are driven by cosmic rays. Because of its relatively simple chemistry, H_3^+ is often used as an indirect probe for constraining the CRIR. It is formed via the reaction:

$$H_2^+ + H_2 \rightarrow H_3^+ + H \tag{1.2}$$

where H_2^+ is a direct product of primary ionization (Reaction 1.1).

Previous studies of the CRIR in various regions of the ISM have shown that the cosmic-ray flux is not homogeneous. It depends on both the galactic location (whether it is in a region likely affected by nearby high-mass star formation, see Sect. 1.4.1), and the gas densities. Indeed, even though cosmic rays can penetrate in the dense interior of gas clouds, they still lose energy as they ionize and excite the matter they travel through (see, e.g., Umebayashi & Nakano 1981). Numerous studies have sought to quantify the energy losses along the path of cosmic rays (see, e.g., Padovani et al. 2009; Rimmer et al. 2012; Neufeld & Wolfire 2017). The ionization rate is found to decrease for increasing column densities (that is the number of molecules detected per unit area along the line of sight to the observed region), with ζ^{H_2} usually ranging between $\sim 10^{-14}$ s^{-1} and 10^{-17} s^{-1} from diffuse to denser regions and depending on the galactic location.

1.1.3 Phases of the interstellar medium

As noted already before (Sect. 1.1), the ISM is not homogeneous. From one region to the other, the physical conditions can vary by orders of magnitude, with gas kinetic temperatures ranging from 10 to 10^6 K and densities spanning a range from $\sim 10^{-3}$ to $\gtrsim 10^6$ cm^{-3}. Based on the physical properties of the interstellar gas and depending on the state of hydrogen, which can be ionized (HII), neutral (HI), or molecular, the ISM can be divided into several distinct phases. Following the classification of Draine (2011), these phases are, with decreasing temperature and increasing density, the hot ionized medium (HIM), the warm ionized medium (WIM), the warm

Table 1.1: Physical conditions characterizing the phases of the ISM.

Phase	State of hydrogen[a]	T_K[b] (K)	n_H[c] (cm^{-3})
Hot ionized medium (HIM)	HII	$\geq 10^6$	$\sim 4\times10^{-3}$
Warm ionized medium (WIM)	HII	$\sim 10^4$	0.3–10^4
Warm neutral medium (WNM)	HI	$\sim 5\times10^3$	$\sim$0.6
Cold neutral medium (CNM)	HI	$\sim$100	$\sim$30
Molecular cloud (MC)	H_2	10–100	100–10^6

Notes. Physical properties characterizing each phase of the ISM. Parameters taken from Draine (2011). [(a)] HII designates the regions where most hydrogen is ionized (H^+), HI the regions mainly composed of atomic hydrogen, and H_2 the molecular gas. [(b)] Kinetic temperature of the gas. [(c)] Number density of total hydrogen $n_H = 2n(H_2)+n(H)$.

Table 1.2: Properties of interstellar molecular clouds.

Cloud type	State of carbon	A_v (mag)	n_H (cm^{-3})	N_H (cm^{-2})	T_K (K)
Diffuse	CII	$\sim$0.2–1	100–500	$\sim 2\times10^{19}$–2×10^{21}	30–100
Translucent	CI	1–5	500–5000	$\sim 2\times10^{21}$–7×10^{21}	15–50
Dense	CO	$>$5	$>10^4$	$>7\times10^{21}$	10–50

Notes. Physical properties of molecular cloud types following the classification of Snow & McCall (2006).

neutral medium (WNM), the cold neutral medium (CNM), and the molecular clouds (MC) (see Table. 1.1). These phases coexist in the ISM in pressure equilibrium.

In the low-density regions, the strong UV field emitted by surrounding stars maintains both a high degree of ionization and high temperatures. At higher densities, the temperature decreases as the UV ionization flux becomes less important. When there is no more UV photons with high enough energy ($\geq$13.6 eV, that is the ionization potential of atomic hydrogen) to ionize all H atoms, hydrogen can survive in atomic or molecular form. In the densest and coldest regions of the ISM, called molecular clouds, hydrogen is mostly found in H_2 molecules.

1.1.4 Molecular cloud types

Because it has a lower ionization potential (11.3 eV) than atomic hydrogen, carbon is expected to exist in MCs in ionized (CII), atomic (CI), or molecular (CO) form. Depending on the dominant reservoir of carbon, MCs can be divided into three categories which are, with decreasing density and increasing radius, diffuse, translucent, and dense MCs, where each gas cloud structure is usually nested within the previous one. Table 1.2 and Fig. 1.3 give qualitative characteristics of the different cloud types.

In diffuse and translucent clouds carbon is predominantly found in ionized or atomic form because CO molecules are dissociated by external UV photons and cosmic rays which easily penetrate inside the clouds. In these regions the chemistry is predominantly dominated by gas-phase ion-molecule reactions. Star formation takes place in the densest parts of MCs (see

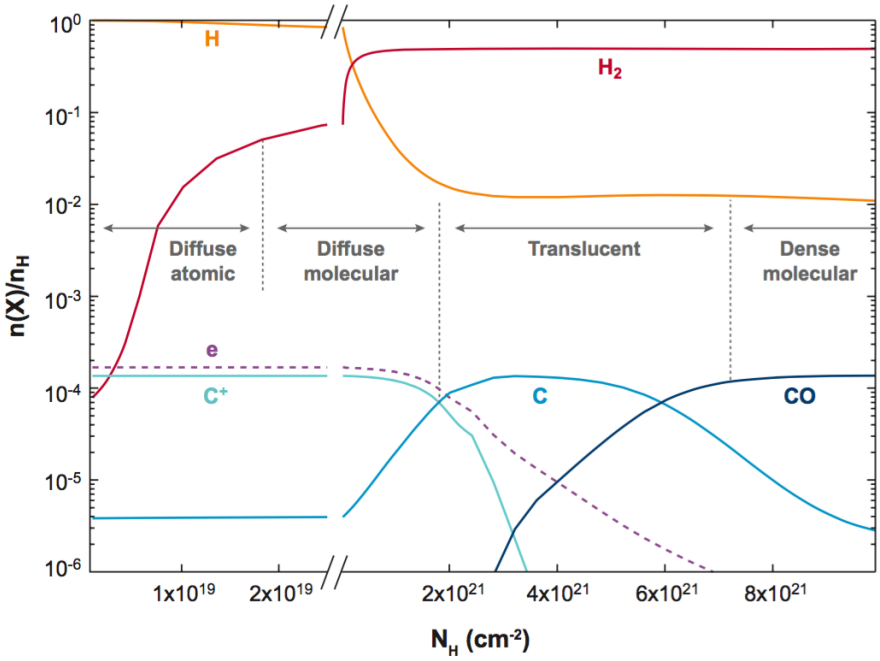

Figure 1.3: Abundances of the main reservoirs of carbon and hydrogen as a function of column density of total hydrogen predicted by the PDR meudon code (Snow & McCall 2006). It shows the three major transitions from diffuse atomic to dense molecular gas (see also Table 1.2). *Figure taken from Snow & Bierbaum (2008), adapted from Snow & McCall (2006).*

also Sect. 1.2), where the surrounding diffuse material provides shielding against the external ionizing UV flux. In dense MCs dust grains are often coated with thick ice mantles on which grain chemistry becomes important. In this region, ionization processes are governed by the CRIR.

1.1.5 The role of stars in the cycle of life of interstellar matter

The ISM is a dynamic, constantly-changing environment. Its physical and chemical evolution is driven by star formation, which continuously converts interstellar matter into stars (see also Sect. 1.2). During their lifetime, stars burn hydrogen and helium to produce heavier elements via nucleosynthesis. In particular, high-mass stars are the main reservoirs of elements heavier than carbon, such as iron, oxygen, silicon, and magnesium, which are the main constituents of Earth (Morgan & Anders 1980). This material enriched in heavy elements produced in the stars' interiors is distributed through the ISM via stellar winds and in planetary nebula or supernova explosions (see Fig. 1.4). New stars continuously form from the interstellar gas enriched by previous generations of stars, which maintains a continual mass exchange between stars and their surrounding media. In addition, high-mass stars dominate the energy input in galaxies via important feedback processes (UV radiation, strong stellar winds, outflows, supernova explosions), providing mixing and turbulence, playing an important role on the phase cycle and the structure of the ISM, triggering further turbulence and star-formation activity.

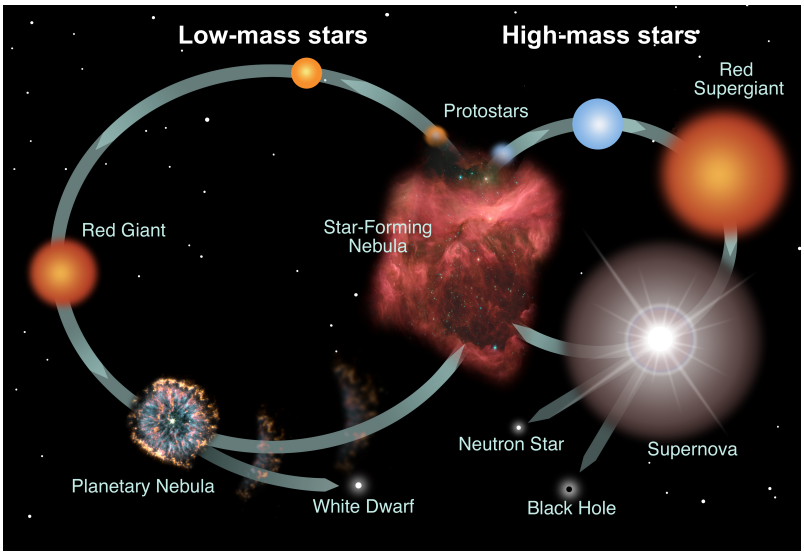

Figure 1.4: Schematic view of the close interplay between the ISM and the star-formation process. Stars formed from the interstellar material return matter back to the ISM during their life time via solar winds and at the end of their life through planetary nebula or supernova explosions, depending on their mass. *Image credit.*

1.2 High-mass star formation

Stars are commonly studied by analyzing the path described by their surface luminosity and the effective temperature (that is the temperature of a black body that would emit the same electromagnetic radiation) in the so-called *Hertzsprung-Russell* (HR) diagram (see Fig. 1.5). Based on their main-sequence mass, stars can be divided into three groups: i) low-mass (solar-type, with $M_* \leq 2\ M_\odot$), ii) intermediate-mass ($2\ M_\odot < M_* < 8\ M_\odot$), and iii) high-mass stars, also referred to as OB stars, which are usually defined as those with a mass $\geq$8 $M_\odot$ and luminosities $\geq 10^3\ L_\odot$. In the rest of this chapter I will focus on the formation and evolution of high-mass stars.

1.2.1 Theories and limitations

Although they are far less numerous than low-mass stars, high-mass stars play an important role in the physical, chemical, and morphological evolution of the Galaxy, as well as in the formation of planets and other stars as seen in Sect. 1.1.5. Despite the growing effort made to understand better high-mass star formation, from both an observational and a theoretical point of view, it is still an enigmatic process, of which the details are not well understood. Similarly to the widely recognized low-mass star-formation scenario, high-mass stars are thought to form from the global gravitational collapse of giant molecular clouds (GMCs) with accretion onto compact protostellar objects (Shu et al. 1987). However, Wolfire & Cassinelli (1987) showed that considering a spherically symmetric accretion structure, it is impossible for stars which have reached masses of about 10 $M_\odot$ to continue accreting material to grow further in mass. At this point the stellar wind and the strong radiation pressure working on the dust envelope must halt the accretion toward the central protostellar object. As stars of more than 10 $M_\odot$ exist, various scenarios have been proposed to circumvent this radiation pressure barrier, introducing

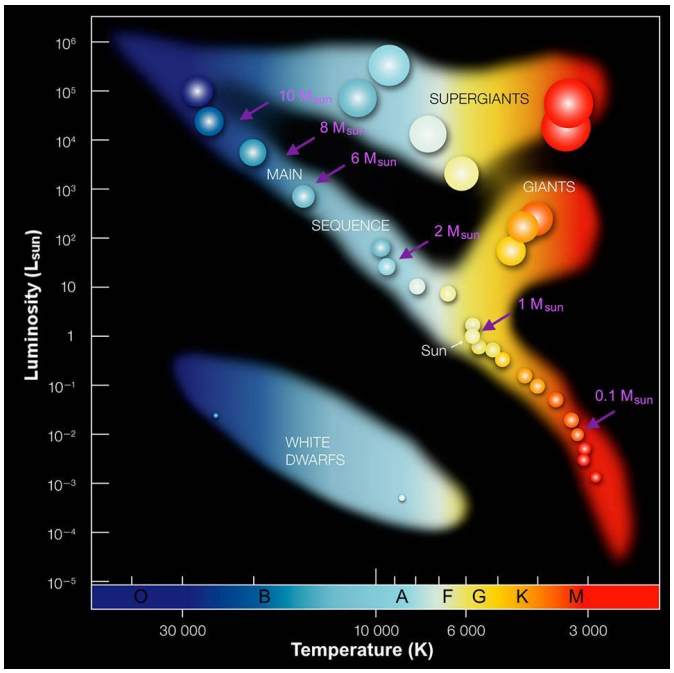

Figure 1.5: Hertzsprung-Russell diagram showing the stellar luminosity as a function of effective surface temperature. The surface temperature of a star determines its spectral type, indicated with black letters on the temperature axis. Most stars currently lie on the diagonal branch, called main sequence, at a position determined by their mass. A star reaches the main sequence when it starts hydrogen core fusion. After it has burnt a significant amount of its hydrogen, the star evolves away from the main sequence to become a red giant or a super giant, depending on its mass. For instance, a solar-like star will eventually evolve into a red giant, which will turn into a white dwarf after expelling its envelope (see also Fig. 1.4). *Image credit: ESO.*

high accretion rates ($\geq 10^{-4}$ $M_\odot$ Wolfire & Cassinelli 1987) and/or non-symmetric accretion geometry, such as disk accretion, which funnels the accretion in the equatorial plane with much higher rates per area (Yorke & Sonnhalter 2002). The two main theoretical models currently used to explain how high-mass stars form are shortly presented below. For more details, in particular on the theoretical aspects and the physical processes involved in high-mass star formation, see, e.g., Zinnecker & Yorke (2007) and Motte et al. (2018), and references below.

The monolithic collapse, or turbulent core model (e.g., McKee & Tan 2003; Krumholz et al. 2009), posits that high-mass stars form through the gravitational collapse of GMCs, supported by turbulence. The high accretion rates obtained in this model allows to overcome the radiative pressure barrier even in the spherical approximation. GMCs fragment into multiple smaller-size cores, that will collapse to form a single star or a binary system. The final stellar mass is already pre-assembled in the collapsing core which is isolated from the rest of the cloud. This is basically a scaled up version of the low-mass star-formation scenario, which supposes the existence of starless massive dense cores, objects that have pre-assembled masses sufficient to form high-mass stars but have not formed stars yet. There currently exist only a few candidates of starless massive dense cores (see, e.g., Louvet et al. 2018).

In the competitive accretion model, high-mass prestellar cores never develop. Stellar embryos form within stellar cluster where they have to compete for the same material (see, e.g.,

Bonnell et al. 2001; Bonnell & Bate 2006; Murray & Chang 2012). The most massive protostars are created at the center of stellar clusters, where more mass is available than in the outskirts of the clouds. The material can be drawn from the reservoir of the whole parent GMC, such that there is no connection between the mass of the birth core and the final stellar mass. This theory is supported by observations of high-mass stars usually born in clusters rather than isolated.

In fact, these two scenarios likely occur to some degree, depending on the initial environmental conditions within the GMC. Given the complexity of the high-mass star-formation process, it may also not proceed in the same way everywhere in the Galaxy. The two theories presented above mainly differ in the mass accretion processes and the choice of the initial conditions. While the turbulent core model assumes an initial cloud with a highly peaked density structure, the competitive accretion model uses uniform density and temperature. In order to build realistic models of high-mass star formation it is thus necessary to get the initial conditions right. This can be done by investigating observationally the early phases of star formation. However, it is still challenging to obtain reliable observational constraints on the earliest phases of star formation due to several technical limitations that hinder the study of early-type stars. Contrary to low-mass stars, high-mass stars continue accreting material after reaching the main sequence. Deeply embedded in a dense envelope with high levels of dust extinction, high-mass stars are invisible at optical and NIR wavelengths, limiting the observational means to FIR and longer wavelengths (mm/submm range). Once on the main sequence high-mass stars evolve quickly, with an optically-visible main-sequence lifetime considerably shorter than for low-mass stars, making them relatively short-lived and rare in comparison. Except for the Orion molecular cloud, located at about 400 pc from the Sun (Menten et al. 2007), most regions forming high-mass stars are far way, typically >1 kpc, compared to low-mass stars (120–140 pc for the nearest). Large distances make it difficult to reach high enough spatial resolution and sensitivity for detailed studies of their properties, in particular in the complex clustered structures where high-mass stars form. Observations require radio interferometers capable of reaching high spatial resolution to solve these problems (see Sect. 2.1.3). Another limitation in deriving accurate initial conditions is due to the strong feedback from other nearby high-mass stars (radiation, stellar winds, outflows), which disrupt these initial conditions.

1.2.2 Early phases of high-mass star formation

The optically-visible main-sequence life of high-mass stars is preceded by an embedded phase that lasts about 15% of their lifetime, which can be divided into several evolutionary stages. Following the evolutionary scenario for high-mass star formation presented by Motte et al. (2018), high-mass stars form in pre-existing GMCs where the gas is inhomogeneously distributed within an intricate network of elongated filamentary structures (see Fig. 1.6, stage 1). These filaments, which can have sizes ranging between ∼2 and 100 pc, with total masses from $\sim 10^2$ to $\sim 10^5$ $M_\odot$ (e.g, Arzoumanian et al. 2011; André et al. 2014; Mattern et al. 2018), build up bridges which connect the densest regions of the GMCs. Within GMCs, cold condensations of gas and dust are often referred to as infrared dark clouds (IRDCs) of which many show elongated filamentary structures. These IRDCs are thought to be the earliest stages of high-mass star formation. The most massive and densest IRDCs contain massive dense cores (MDCs), precursors of stellar embryos. From the relative number of starless IRDCs detected in the *Herschel* Infrared Galactic Plane (HI-GAL) survey compared to those with observable active star formation, Wilcock et al. (2012) estimated a statistical lifetime for the starless phase of IRDCs of $\sim 2.3{\times}10^5$ yr. In comparison, Jeffreson & Kruijssen (2018) performed theoretical calculations to estimate the

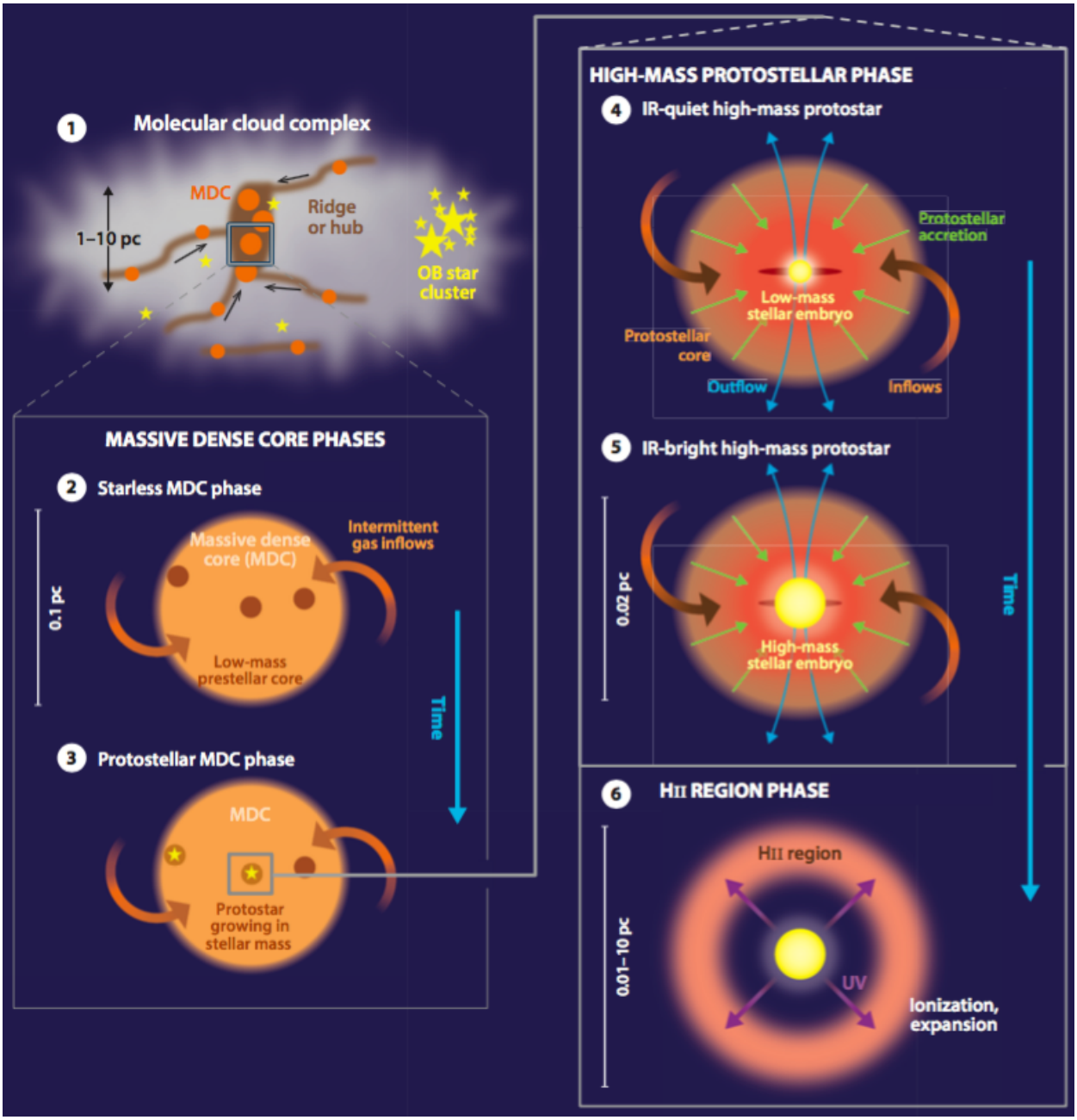

Figure 1.6: Schematic evolutionary diagram of the formation of high-mass stars proposed by Motte et al. (2018). *Figure taken from Motte et al. (2018), adapted from Tigé et al. (2017).*

lifetimes of GMCs based on the time-scales derived for the large-scale dynamical processes that affect the ISM. They found typical lifetimes of ∼20–60 Myr, with strong dependence upon galactocentric radius. For clouds located at galactocentric radii from ∼ 45 to 120 pc, Jeffreson et al. (2018) estimated lifetimes of 1.4–3.9 Myr, significantly shorter than in the rest of the galactic disk, but still a factor >6 longer than the IRDC starless phase estimated by Wilcock et al. (2012).

As the whole cloud complex undergoes global gravitational collapse, the material flows along

the filaments driving inflowing gas streams from the large scales of the entire cloud onto the MDCs (see Fig. 1.6, stage 2). MDCs are initially starless, dense ($n_{\rm H}$ = 10^4–10^5 cm^{-3}), with radius about 0.1 pc up to a few parsecs, and masses ranging from ∼10^2 to 10^3 $M_\odot$. At that stage they do not show evidence of internal heating yet. They are mostly heated via external radiation, such that they exhibit low temperatures, typically <25 K, decreasing from surface to center. It is during this early cold phase that gas-phase material starts to condense onto dust grains and grain-surface chemistry begins. MDCs may host low-mass prestellar cores, the gravitationally bound precursors to individual stars or binaries. They are compact (∼0.01–0.1 pc), dense, and with masses ranging between ∼1 and 10^2 $M_\odot$, but they do not yet show any evidence of star-formation activity or internal heating.

As the cloud contracts further, temperature and density gradually increase in the central prestellar core, until the outward thermal pressure is balanced by the inward pressure of gravitational collapse, leading to the formation of the first hydrostatic core. This core further contracts adiabatically, until its temperature reaches ∼2000 K, then hydrogen molecules are dissociated in its center and a second collapse forms a protostar (Fig. 1.6, stage 3). At that stage the protostar owes its brightness to its gravitational contraction. The kinetic energy from the infalling material impacting the surface of the protostar is converted to heat, which is radiated away, warming up the protostellar envelope. The ice mantles formed on dust grains during the earlier cold phase desorb into the gas phase, forming a compact cloud (∼0.1 pc in diameter) of dense molecular gas (10^5–10^8 cm^{-3}) and dust comprising a total mass of ∼10–10^3 $M_\odot$ (Fig. 1.6, stage 4). This is the hot molecular core (HMC) phase, characterized by a protostar surrounded by an envelope rich in chemical species, in particular complex organic molecules (COMs, see Sect. 1.3). This phase is thought to last about 10^5 yr (e.g., van Dishoeck & Blake 1998).

HMCs are signposted by maser emission, which results from the amplification by the surrounding medium of the radiation that travels through it. This amplified stimulated emission is caused by the inversion of energy level populations of some specific molecules which occurs either in the presence of an intense radiation field, such as that emitted from the central protostar, or via collisions. Water, methanol, and hydroxyl masers are usually observed close to newly formed protostars. Water masers have been found toward both low- and high-mass protostars and are thought to be associated with protostellar outflows (Elitzur et al. 1989; Codella et al. 2004). Menten (1991) classified methanol masers into two categories, class I and class II, depending on their excitation mechanism. Class I methanol masers are excited by collisionnal processes, such that they are often found in outflows, usually offset from the associated protostellar object. Class II methanol masers are radiatively excited and closely associated to high-mass protostars. The 6.7 GHz class II methanol transition in particular is the strongest and most widespread of the methanol masers. It is thought to be associated exclusively with regions forming high-mass stars (Minier et al. 2003; Xu et al. 2008) as for a methanol transition to exhibit maser emission, the pumping requires high dust temperature >150 K, high methanol column densities (>2×10^{15} cm^{-2}), and densities of $n_{\rm H}$ <10^8 cm^{-3} to excite the 6.7 GHz methanol maser transition (Sobolev et al. 1997). van der Walt (2005) estimated the lifetime of these class II methanol masers to be between 2.5 × 10^4 and 4.5 × 10^4 yr.

As the protostar continues to accrete material, growing further in mass, angular momentum is removed through powerful molecular outflows. When these outflows impact the surrounding gas, they produce shocks that may destroy dust grains. Silicon monoxide (SiO) is thought to be mainly produced in such shocks (Schilke et al. 1997), which makes it an excellent tracer of molecular outflows (see, e.g., Leurini et al. 2014).

The material collapsing onto the central protostar causes compression, raising the protostar temperature until thermonuclear fusion starts, converting hydrogen into helium (Fig. 1.6, stage 5). At this point where the high-mass stellar embryo reaches ignition temperatures for nuclear reactions, a true star is born and enters the main sequence, while it is still accreting material. The thermal energy generated through nuclear fusion produces a sharp increase of the protostar luminosity. This stage is characterized by high IR luminosity, strong dust continuum emission, but no detectable free-free emission yet, (that is the deceleration of charged particles, usually electrons, when deflected in the electric field of ions, without capture). As the stars grows in size it starts ionizing its surroundings, creating a hyper-compact HII (HCHII) region with a diameter $<$0.01 pc and densities $\geq 10^6$ cm^{-3} (Fig. 1.6, stage 6). As the HCHII region expands, it evolves into an ultra-compact HII (UCHII) region, which has a larger size (diameter $<$0.1 pc) and is less dense ($n_{\rm H} \sim 10^4$–10^6 cm^{-3}) than the preceding HCHII region. At this stage, the UCHII region has typically reached a size such that it is no longer gravitationally bound to the central protostar. As the UCHII region evolves it continues growing in size and decreasing in density for about 10^5 yr (Wood & Churchwell 1989; Peters et al. 2010) to become a compact HII and finally a classical HII region, with a diameter of typically $\sim$10 pc and a density $n_{\rm H} \sim 100$ cm^{-3}. This is the final stage in the high-mass star formation process. Accretion flows stop and the UV radiation and stellar winds arising from the central object begin to disrupt the parent gas cloud, dispersing away the rest of the gas and dust that were obscuring the central star which becomes visible at optical wavelengths.

1.3 Complex organic molecules in the interstellar medium

As noted already before (see Sect. 1.2.2), interstellar clouds, in particular dense HMCs are the sites where many molecular species are observed in the gas phase. Since the first detection of an interstellar molecule, methylidyne (CH), in 1937 (Swings & Rosenfeld 1937; Dunham 1937), more than 200 molecules[1] have been discovered in the ISM or in circumstellar envelopes of evolved stars (see McGuire 2018, and references therein). These molecules range in size from 2 to 70 atoms, comprising 16 different elements. Some of them are detected both in the gas phase and in the solid phase, *i.e.* on dust grains or within ice mantles. Some have also been found in comets as well as in external galaxies. Most of the detected interstellar molecules are organic in nature (*i.e.* they contain at least one atom of C), in particular all molecules with six or more atoms, which represent about one third of the $\sim$200 known species, are organic. These molecules are referred to as interstellar complex organic molecules (COMs, Herbst & van Dishoeck 2009).

Most COMs were detected for the first time at millimeter and submillimeter (mm-submm) wavelengths toward HMCs in Orion-KL and Sagittarius B2(N) (see Sect. 1.4.3), including the first interstellar sugar, glycolaldehyde (CH_2OHCHO Hollis et al. 2004). Over the past decades, observational studies have been extended to various environments such as hot corinos (that is the low-mass analogs of hot cores, see, e.g., Bottinelli et al. 2004; Sakai & Yamamoto 2011; Maury et al. 2014), diffuse and translucent clouds (e.g., Corby et al. 2015; Thiel et al. 2017; Liszt et al. 2018), cold quiescent regions (with $T_{\rm K} \sim 10$ K, see, e.g., Suzuki et al. 1986; Öberg et al. 2010; Bacmann et al. 2012; Vastel et al. 2014), circumstellar envelopes around evolved stars (Bujarrabal et al. 1988; Cernicharo 2000), shocked regions (Requena-Torres et al. 2006; Arce et al. 2008; Palau et al. 2017), photo-dissociation regions (Guzmán et al. 2014; Cuadrado

[1] see http://www.astro.uni-koeln.de/cdms/molecules

et al. 2017), protoplanetary disks (e.g., Öberg et al. 2015; Walsh et al. 2016; Bergner et al. 2018), and comets (e.g., Bockelée-Morvan et al. 2000, 2004; Altwegg et al. 2017). The presence of such large molecules in different regions of the ISM, suggests that the chemical processes responsible for their formation are local in nature, as these molecules may be destroyed at any time, in particular in low density regions, by direct UV radiation or CR-induced UV photons. Wherever COMs are detected, they are excellent diagnostic tools of the physical conditions of their environments and tell us about the temperature, ionization rate, radiation field, kinematic structure, and dynamics of the regions where they are observed (see Chaps. 3, 4, and 6). They allow us to study the build-up of molecular complexity in the ISM and can be used to investigate the chemical and physical processes at work in the regions forming high-mass stars, and their evolution from the early IRDC to the HMC phase. For instance, by comparing the composition of comets to that of the interstellar matter in regions forming stars, we gain insight into the origin of cometary material and its evolution from interstellar clouds to planetary systems. The strong correlation observed between the chemical composition of cometary ices and HMCs may suggest that the material found in comets, in particular the COMs, was formed through similar processes as those at work in regions forming high-mass stars (Bockelée-Morvan et al. 2000) and suffer little further processing in the Solar Nebula (*i.e.* the rotating disk of gas and dust from which the solar system was formed about 4.6 Gyr ago). More than 80 distinct amino acids, chemical building blocks of proteins that are ingredient of life as we know it on Earth, have been discovered in meteorites (see, e.g, Botta & Bada 2002). The simplest amino acid, glycine (NH_2CH_2COOH), has also recently been discovered in the coma of Comet 67P/Churyumov-Gerasimenko (Altwegg et al. 2016), suggesting that comets might have contributed to the emergence of life on Earth. To date, no amino acid has yet been detected in the ISM, but the quest continues, in particular since the detection of aminoacetonitrile (NH_2CH_2CN), a possible precursor of glycine (Belloche et al. 2008). The last considerations raise the questions of the degree of chemical complexity that can be reached in the ISM and the role of comets and meteorites in spreading molecular complexity. We want to know how, when, and where are COMs formed and how can they survive through the star-formation process, through the protoplanetary disk and beyond, to become part of new planetary systems.

Despite the plethora of COMs detected in various environments and the numerous studies focusing on the ISM complex chemistry, the precise origins of COMs and the mechanisms leading to their formation are still strongly debated. Astronomy is by nature an observational science for which direct laboratory experiments to test the validity of any theory or mechanism aiming to explain observations is always challenging. This is due to the limitations in reproducing in the laboratory the extreme physical conditions of the ISM. Numerical simulations, or models in which molecular abundances are calculated based on chemical networks comprising thousands of chemical reactions can be used to investigate numerically the complex set of chemical reactions and processes at work in the ISM (see Chap. 5). Such chemical models have yielded significant progress in our understanding of the complex ISM chemistry. In particular, it has been shown that grain-surface chemistry, followed by the subsequent sublimation of the ice mantles, plays an important role in the formation of COMs where pure gas-phase chemical processes fail in reproducing the observed abundances of some molecules (see, e.g., Garrod et al. 2007; Garrod 2008; Herbst & van Dishoeck 2009). A possible scenario for the formation of COMs involves surface chemical reactions between molecules accreted onto dust grains during the early cold stage of star formation. These reactions lead to the formation of larger species still frozen onto the grains but which eventually return to the gas phase, in particular during the

HMC stage, when the newly ignited protostar starts heating up its surroundings. For instance, using astrochemical models Garrod & Herbst (2006) showed that methyl formate (CH_3OCHO) detected in HMCs most likely has a grain-surface origin, while dimethyl ether (CH_3OCH_3) and formic acid (HCOOH) may originate from both gas-phase and grain-surface chemistry. This allows us to distinguish three types of COMs (Herbst & van Dishoeck 2009):

- Zeroth-generation species: formed in the gas and/or in the dust-grain ice mantles during the early cold stage of star formation and then return to the gas phase during the HMC phase.
- First-generation species: formed at least partially on dust grains during the warm-up phase of the star formation process, starting with the ignition of the central protostar.
- Second-generation species: formed exclusively in the hot gas phase during the HMC phase.

Further investigations of the physical and chemical processes responsible for the production of the numerous COMs observed in various environments are needed to understand better how the ISM can trigger chemical complexity. This is made thanks to a close interplay between observations, astrochemical modeling, and laboratory experiments.

1.4 The central molecular zone

Within the galactic disk, a large amount of molecular gas is found to be accumulated within a projected radius of about 200–500 pc around the GC, called the central molecular zone (CMZ). The total gas mass reservoir of the CMZ is estimated to be $\sim 5\times10^7$ $M_\odot$, with mean gas volume densities $\sim 10^4$ cm^{-3} (Morris & Serabyn 1996; Ferrière et al. 2007), with multiple density components ranging from 10^3 up to 10^7 cm^{-3}, at least a factor $\sim$100 higher than in the rest of the galactic disk ($\sim 10^2$ cm^{-3} Longmore et al. 2013). It contains several dense MCs with large velocity dispersion (15–50 km s^{-1}) toward which numerous COMs have been detected (see also Sect. 1.4.3).

1.4.1 Environmental conditions in the galactic center

The physical conditions within the CMZ are known to be extreme compared to the rest of the galactic disk, with in particular stronger radiation field ($\sim$ 500–1000 G_0, Lis et al. 2001; Clark et al. 2013), and higher CRIR (Oka et al. 2005; van der Tak et al. 2006; Yusef-Zadeh et al. 2007; Clark et al. 2013) than in solar neighborhood clouds (see, e.g., Morris & Serabyn 1996, for a detailed review on the structure and activity within the CMZ). Recently, Le Petit et al. (2016) used the Meudon photo-dissociation region (PDR) code to reproduce the large H_3^+ column densities observed in the diffuse gas component of the line of sight to the CMZ (n_H = 100 cm^{-2}, T_K = 200–500 K). They derived a CRIR of ζ^{H_2} $\sim$1–11$\times10^{-14}$ s^{-1}, that is a factor 8×10^2–8×10^3 higher than the standard value (1.3×10^{-17} s^{-1} for dense gas where all hydrogen is molecular, such that $\zeta^{H_2} \sim 2\zeta^H$, see Sect. 1.1.2), in agreement with the values obtained by Indriolo et al. (2015) from the analysis of OH^+, H_2O^+, and H_3O^+ observed by *Herschel* for various clouds in the CMZ. These extreme physical conditions could be the result of an enhanced star formation activity in the CMZ and/or higher stellar densities.

Due to the enhanced external radiation field, higher temperatures are observed towards the GC region than other regions forming high-mass stars in the galactic disk. Based on imaging

of formaldehyde transitions with the Atacama Pathfinder Experiment (APEX) 12 m telescope, gas kinetic temperatures in the CMZ are found to be ranging from 50 to more than 100 K (Ao et al. 2013; Ginsburg et al. 2016). Ott et al. (2014) showed that the kinetic temperature distribution of molecular clumps within the region between the supermassive black hole Sgr A* and Sgr B2 peaks at $\sim$ 38 K based on a survey of ammonia conducted with the Australia Telescope Compact Array (ATCA). From measurements carried out at infrared wavelengths with the *Herschel* space observatory, Longmore et al. (2012) derived dust temperatures ranging from 19 K to 27 K from the center to the edge of the GC cloud G0.253+0.016 (also known as "the Brick"). Guzmán et al. (2015) reported measurements of $T_{\rm d}$ = 20–28 K toward Sgr B2. In comparison, lower temperatures have been derived for clouds outside the GC region, with gas kinetic temperatures of $T_{\rm kin}$ = 10–30 K (Giannetti et al. 2013). Dust temperatures of 17 K have been measured toward dense cores embedded in the NGC 6334 MC (Tigé et al. 2017), which lies at a distance of 1.75 kpc from the Sun (*i.e.* far from the GC).

The extreme environment of the CMZ provides an excellent test of our current understanding of the star formation process, allowing us to investigate whether such extreme physical conditions enhance of suppress star formation activity.

1.4.2 Star formation efficiency in the galactic center

Despite its large reservoir of dense gas, the CMZ appears to be overall deficient in star formation, as most CMZ clouds currently do not show evidence of star-forming activity, except for a few well known star-forming regions (Sgr B2, Sgr A, and Sgr C). This apparent inactivity is in contrast with the dense-gas star-formation relation derived by Lada et al. (2010) for nearby clouds. This relation predicts a linear correlation between the star-formation rate (SFR, in $M_\odot$ yr^{-1}) and the amount of dense molecular gas ($n_{\rm H} \geq 10^4$ cm^{-3}) available. The overall SFR estimated for the CMZ (0.04–0.12 $M_\odot$ yr^{-1}, Longmore et al. 2013; Barnes et al. 2017; Kauffmann et al. 2017b; Lu et al. 2019) represents 3–10% of the global star formation rate of the Galaxy (1.2±0.2 $M_\odot$ yr^{-1} Lee et al. 2012), but is still about one order of magnitude lower than expected from Lada et al. (2010)'s relation, both on the scale of the entire CMZ (Longmore et al. 2013) and of individual clouds (Kauffmann et al. 2013, 2017a; Lu et al. 2019), except for Sgr B2 and Sgr C. The latter two stand out with larger fractions of mass in gravitationally bound regions and higher SFRs than the rest of the CMZ clouds which do not show evidence of star formation (Lu et al. 2019). Several recent studies (Kruijssen et al. 2014; Rathborne et al. 2014; Krumholz & Kruijssen 2015; Federrath et al. 2016; Krumholz 2017; Ginsburg et al. 2018) showed that the density threshold beyond which star formation occurs in the CMZ is about 10^5–10^7 cm^{-2}, much higher than in the rest of the galactic disk ($\sim 10^4$ cm^{-2}, Lada et al. 2010, 2012). A possible explanation for the overal low SFR in the CMZ may be that the investigated clouds are still at an early evolutionary stage and have not yet reached the conditions required to begin forming stars (Kruijssen et al. 2014; Krumholz & Kruijssen 2015; Krumholz 2017). A young generation of stars could also have been missed in the observations because still deeply embedded in dense gas envelopes. Besides, several theoretical studies on the evolution of the gas streams in the CMZ suggest that star formation in this region could be regulated by strong turbulence driven by the gas inflowing through the galactic bar (Kruijssen et al. 2014, 2015; Krumholz & Kruijssen 2015). This turbulence prevents the onset of star formation, resulting in episodes of low star formation activity during the cloud evolution.

Kruijssen et al. (2015) proposed an orbital model in which all the major CMZ clouds are subject to the gravitational potential around the GC, moving in several gas streams and follow-

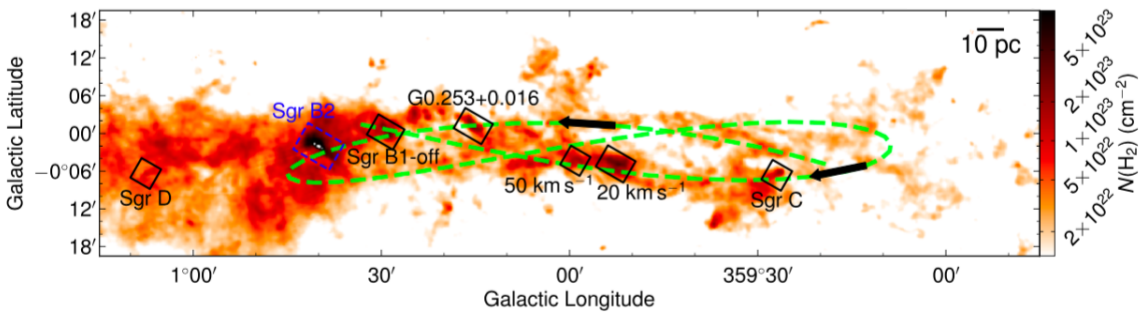

Figure 1.7: Column density map of the CMZ derived from *Herschel* data (Battersby et al. 2011). The major clouds of the CMZ are indicated at their current positions. The orbital model of Kruijssen et al. (2015) is shown with a green dashed line. The two black arrows indicate the direction of the gas streams in the model. *Figure taken from Lu et al. (2019).*

ing an absolute-time sequence of star formation (see green dotted line in Fig. 1.7). When a cloud passes close to the bottom of the gravitational potential, at the pericenter near Sgr A*, turbulence is dissipated and star formation begins. Figure 1.7 shows that the Brick (G0.253+0.016), Sgr B1-off, and Sgr B2 are moving along the same gas stream and have already passed the pericenter to Sgr A*. Lu et al. (2019) have recently confirmed the increase in SFR predicted by the orbital model of Kruijssen et al. (2015) from the quiescent G0.253+0.016 cloud, largely devoid of ongoing star formation, to the active star-forming region Sgr B2. They did not find a similar trend with increasing SFR for the clouds in the other gas stream (Sgr C, the 20 km s^{-1} cloud, and the 50 km s^{-1} cloud), which might suggest that star formation in these clouds is triggered by different mechanisms.

1.4.3 The galactic center cloud Sagittarius B2

As noted already before, the Sgr B2 molecular cloud is located in the CMZ, at a projected distance of 107 pc from the central supermassive black hole Sgr A* (see Fig. 1.8), and at a distance of 8.34 ± 0.16 kpc from the Sun (Reid et al. 2014). With a total luminosity of $\sim 2\times10^7$ $L_\odot$ and a total gas mass reservoir of $0.5–1\times10^7 M_\odot$ distributed within an envelope of ∼40 pc in diameter (Lis & Goldsmith 1990; Schmiedeke et al. 2016, see also Fig. 1.9), Sgr B2 is one of the most prominent regions forming high-mass stars in our Galaxy, containing about 15% of the gas mass present in the CMZ.

Previous studies have estimated the SFR of Sgr B2 to be 0.028–0.086 $M_\odot$ yr^{-1} (Belloche et al. 2013; Kauffmann et al. 2017b; Ginsburg et al. 2018; Lu et al. 2019), which represents 20–70% of the global SFR of the CMZ and 2–7% of the SFR of the Galaxy. These values strongly depend on the assumed stellar masses and timescales. For instance, Ginsburg et al. (2018) obtained SFR of 0.062 $M_\odot$ yr^{-1} from the masses computed from HII regions counts, including also dense cores not associated with HII regions. They used the orbital model of Kruijssen et al. (2015) to estimate the age of the Sgr B2 cloud, as the time since its passage to the pericenter (∼0.74 Myr). However, as these authors pointed out, a shorter timescale, given instead by the time since Sgr B2 was at the position of the Brick (∼0.43 Myr), which currently shows no strong evidence of star-forming activity, would lead to larger SFRs, meaning that Sgr B2 largely dominates the instantaneous SFR of the CMZ.

Due to its exceptional characteristics and its proximity to the GC, Sgr B2 provides us

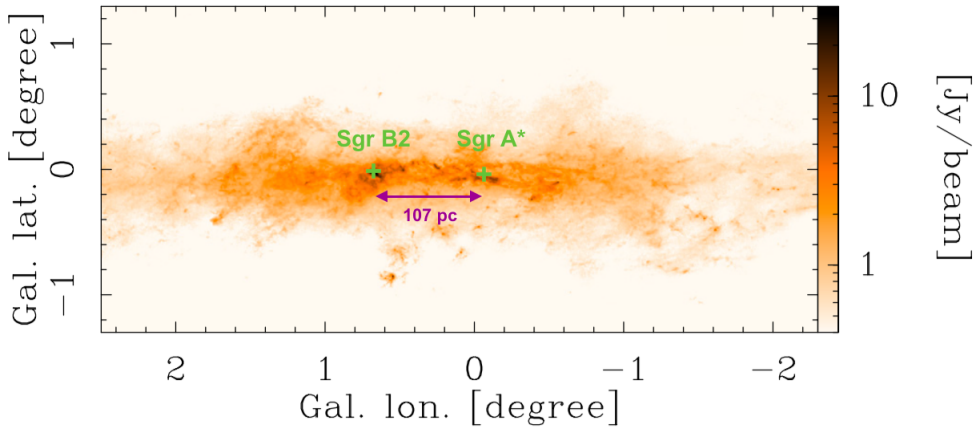

Figure 1.8: Dust emission *Planck*+APEX combined map at 870 μm showing the position of the Sgr B2 molecular cloud compared to Sgr A*. *Figure taken from Csengeri et al. (2016).*

with an interesting case study to investigate the influence of environmental factors on the high-mass star formation process and the associated complex chemistry, by comparing typical regions forming high-mass stars in the Galactic disk to the more extreme GC region. Over the last decades, Sgr B2 has been the target of extensive line and dust continuum studies at different scales (focusing on the compact high-mass protoclusters of the more extended envelope), over a broad range of frequencies, from submm to cm wavelengths (see, e.g., Benson & Johnston 1984; Carlstrom & Vogel 1989; Gaume & Claussen 1990; Martin-Pintado et al. 1990; Lis et al. 1991; Gordon et al. 1993; Hüttemeister et al. 1993, 1995; Gaume et al. 1995; Belloche et al. 2008; Qin et al. 2011; Belloche et al. 2013; Neill et al. 2014; Halfen et al. 2015; Corby et al. 2015; Belloche et al. 2016; Schmiedeke et al. 2016; Bonfand et al. 2017; Sánchez-Monge et al. 2017; Ginsburg et al. 2018). Recently, Ginsburg et al. (2018) imaged the continuum emission at 3 mm over an extended region spanning the whole Sgr B2 cloud along the dust ridge to Sgr Deep-South to explore the ongoing high-mass star formation at larger scales in the cloud. The continuum maps reveal the complex structure of the whole cloud which is fragmented into multiple dense and compact objects. In total, Ginsburg et al. (2018) reported the detection of 271 3 mm point sources, that they have identified as a mix of high-mass protostellar cores and (UC)HII regions. In particular, Sgr B2 contains two major sites of on-going high-mass star formation, Sgr B2(N)orth and Sgr B2(M)ain, separated by ∼2 pc, historically named based on their apparent north-south alignment in equatorial coordinates system (see Fig. 1.9). Strong evidence of on-going high-mass star formation has been found in the two clusters, with a particularly high concentration of HC- and UC-HII regions (Mehringer et al. 1993; Gaume et al. 1995; De Pree et al. 1998, 2015), as well as several 6.7 GHz class II methanol masers (Caswell 1996). Investigations focused on the two high-mass protoclusters revealed their different chemical composition. Due to its high densities (see, e.g, Bonfand et al. 2017), Sgr B2(N) in particular exhibits one of the richest molecular inventory observed in the Galaxy.

As noted already before, many of the first detections of interstellar molecules at radio and mm-submm wavelengths were made toward Sgr B2(N), in particular some of the most complex species ever detected in the ISM, such as acetic acid CH_3COOH (Mehringer et al.

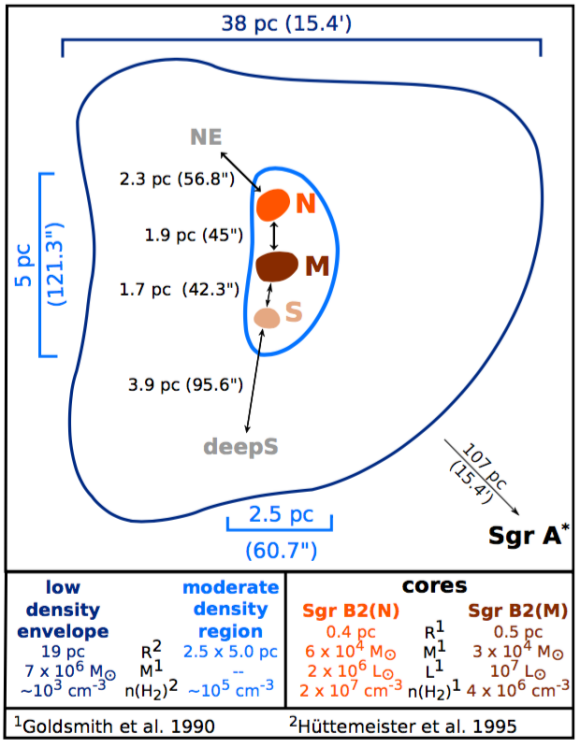

Figure 1.9: Sketch of the Sgr B2 region divided into a low-density envelope, an extended moderate density region, and compact massive dense cores following the structure proposed by Hüttemeister et al. (1993). The physical conditions within each region are indicated at the bottom. *Figure taken from Schmiedeke et al. (2016).*

1997), glycolaldehyde $CH_2(OH)CHO$ (Hollis et al. 2000), acetamide CH_3CONH_2 (Hollis et al. 2006), aminoacetonitrile NH_2CH_2CN (Belloche et al. 2008), N-methylformamide CH_3NHCHO (Belloche et al. 2017), and urea $NH_2C(O)NH_2$ (Belloche et al. 2019); see also the overview by Menten (2004). For this reason, Sgr B2(N) appears like one of the best targets for studying the complex interstellar chemistry and search for new species to expand our view of the chemical complexity of the ISM.

In this thesis work I will focus mainly on Sgr B2(N). The source is fragmented into multiple dense and compact HMCs (Bonfand et al. 2017; Sánchez-Monge et al. 2017; Ginsburg et al. 2018, see also Sect. 3.1.1), of which the two main cores, Sgr B2(N1) and Sgr B2(N2) (Belloche et al. 2016, see also Fig. 2.11), are separated by $\sim 5''$ in the North-South direction (corresponding to 0.2 pc in projection, Belloche et al. 2008; Qin et al. 2011). These HMCs have been the targets of several unbiased spectral line surveys (Belloche et al. 2013, 2016; Sánchez-Monge et al. 2017), which allowed to derive the detailed chemical composition of Sgr B2(N2).

1.5 Goals and outline of the thesis

As seen in the previous sections, high-mass stars are essential constituents of our Galaxy and there is currently still a need to improve our understanding of their formation. In particular, we wish to constrain better the physical processes and complex set of chemical reactions at play during the earliest stages of the high-mass star formation. To date the chemical composition of

several HMCs has been studied in detail, including Sgr B2(N1) and N2 (see, e.g., Belloche et al. 2008, 2009, 2013, 2014, 2017; Müller et al. 2016; Garrod et al. 2017), the Orion BN/LK HMC (see, e.g., Blake et al. 1987; Sutton et al. 1995; Beuther et al. 2009; Feng et al. 2015; Tercero et al. 2018), W3 (Helmich & van Dishoeck 1997; Qin et al. 2015), G29.96-0.02 (Beuther et al. 2009), G35.20-0.74N (Allen et al. 2017), and G35.03+0.35 (Allen et al. 2017). These investigations revealed a wide range of physical properties and chemical composition among these objects (see Sect. 3.6). In order to understand the cause for such a stricking diversity, further detailed studies are needed in particular at high angular resolution in the mm-submm range to overcome the observational difficulties that hinder the study of early-type stars (Sect. 1.2.1) and shed a new light on our view of high-mass star formation.

With a sensitivity and resolution significantly improved compared to what was previously achieved with single-dish telescopes, the Atacama Large Millimeter/submillimeter Array (ALMA, see Sect. 2.1.5) has opened completely new capacities for star formation studies, in particular increasing the number of known high-mass star forming regions and young stellar objects. Enlarging our inventory of high-mass stellar objects is crucial in order to build up a statistically relevant source sample to compare observations with numerical models in a robust way.

My thesis focuses on the star-forming region Sgr B2 which, due to its location in the CMZ, provides us with an excellent laboratory to study the influence of extreme physical conditions on the star-formation process as well as on the production of the numerous COMs detected toward this region. In this thesis I present the first comparative study of the detailed physical properties, chemical composition, and evolutionary stage of four HMCs embedded in Sgr B2(N), of which three are new detections. The thesis is structured as follows.

In Chapter 2 I present the data used in this thesis and the methods of analysis used to extract the properties of the investigated sources. In Chapter 3 I show how we take advantage of the high sensitivity provided by ALMA to search for faint hot cores/corinos in Sgr B2(N) and derive their chemical content from the analysis of their emission spectra. Chapter 4 presents the physical structure and history of the HMCs embedded in Sgr B2(N). I compare their current physical properties and characterize their evolution, with the aim to assess their evolutionary stage and to provide a physical model to trace their physical and chemical evolution from the early cold prestellar phase to the present time. This model is used as input for the chemical modeling of the sources in Chapter 5. The chemical kinetics code, MAGICKAL, is used to model the physico-chemical evolution of four HMCs, with the aim to explore the influence of physical properties, thermal history, and environmental conditions (cosmic-ray ionization rate, enhanced interstellar radiation field and high dust temperatures) on the building up of chemical complexity in Sgr B2(N). In Chapter 6 I test the results of the physico-chemical models by comparing the calculated abundances to the observed values. The fact that the sources originate from the same cloud material, with initially the same chemical composition, and are exposed to the same environmental conditions within Sgr B2(N) is used to constrain the cosmic-ray ionization rate, the minimum dust temperature and the interstellar radiation field that best reproduce the observations. Finally I give conclusions in Chapter 7 and Chapter 8 gives some prospects for improving our view of high-mass star formation.

Chapter 2

Data and methods of analysis

Contents

As seen in Chap. 1, the regions where stars form are characterized by high density and low temperature material, which emits at infrared and millimeter wavelengths. In the millimeter range, the radiation observed toward star-forming regions consists in a continuous component, which mainly arises from the dust thermal emission, and spectral lines emitted by the atoms and molecules contained in the gas. In this chapter I present the methods used in this thesis to interpret the electromagnetic signal measured toward our target source, Sgr B2(N). After a brief introduction to radio astronomy and interferometers, I describe in more detail the methods used to derive H_2 column densities, masses, molecular column densities, and rotational temperatures from the observational data used in this thesis.

2.1 Principles of radio astronomy

This section gives some basic principles of radio astronomy focusing on specific concepts needed to understand this thesis. For more details on telescope receivers, observational methods, and image reconstruction processes for interferometry, see, e.g., Klein (2006) and Wilson et al. (2009).

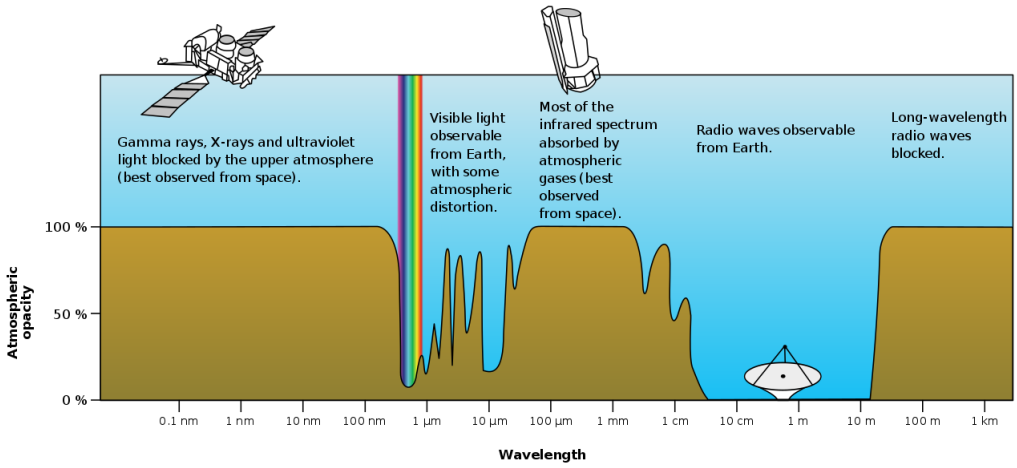

Figure 2.1: Sketch of the Earth atmospheric opacity as a function of wavelength. *Image credit: NASA*.

2.1.1 The radio atmospheric window

Radio astronomy covers the atmospheric window transparent (or partially) to radio waves, from ∼10 m down to ∼1 mm (*i.e.* frequencies from 30 MHz to 300 GHz, see Fig. 2.1). Shorter wavelengths are heavily absorbed by water and oxygen molecules contained in the atmosphere. In the millimeter range, there are narrow windows for which the radio waves are not strongly absorbed, where the atmospheric transmission depends on the weather conditions governed by the precipitable water vapor (pwv) content of the atmosphere. The limits of the atmospheric window observable from the ground can be extended by building telescopes in dry places and at very high altitude (e.g., the Atacama desert in Chile, see Sect. 2.1.5).

2.1.2 Measuring radio signals with a single-dish antenna

Single-dish antennas are used to collect weak radio waves from distant astronomical sources (Fig. 2.2). The incoming radiation is characterized by its specific intensity, I_ν, the electromagnetic power per unit area, unit frequency, and unit solid angle (W m^{-2} Hz^{-1} sr^{-1}). Assuming that the observed source emits as a blackbody at the temperature T, the source specific intensity I_ν is given by the Planck function:

$$B_\nu(T) = \frac{2h\nu^3}{c^2} \frac{1}{\mathrm{e}^{h\nu/k_\mathrm{b}T} - 1}\,, \tag{2.1}$$

where c is the speed of light, h the Planck constant, and k_b the Boltzmann constant. The brightness temperature of the source, T_B, is defined as the temperature of a blackbody that would have the same specific intensity (*i.e.* $B_\nu(T_\mathrm{B}) = I_\nu$). It is related to the specific intensity of the source via the effective brightness temperature, $J_\nu(T_\mathrm{B})$ as follows (see, e.g., Kutner & Ulich 1981):

$$J_\nu(T_\mathrm{B}) = \frac{c^2}{2\,k_\mathrm{b}\,\nu^2}\,B_\nu(T_\mathrm{B})\,. \tag{2.2}$$

In the case where the Rayleigh-Jeans approximation is valid ($h\nu << k_\mathrm{b}T$) thus $J_\nu(T_\mathrm{B}) = T_\mathrm{B}$.

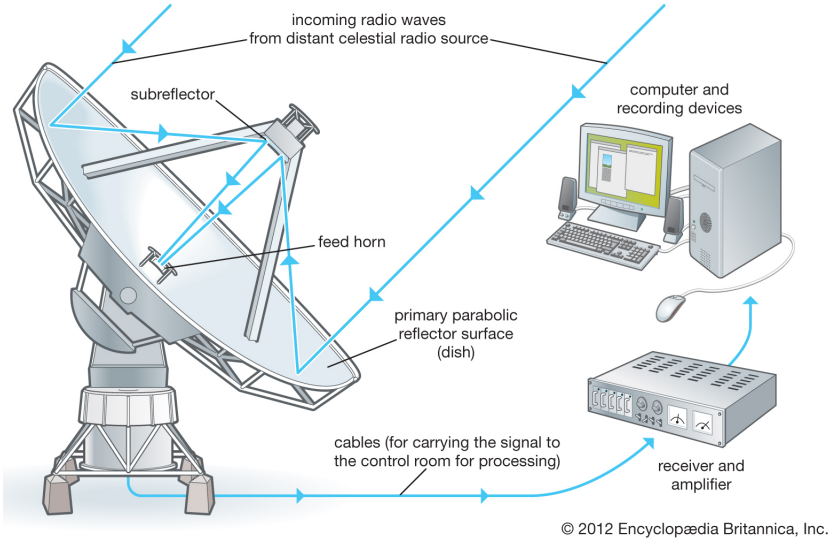

Figure 2.2: Functional scheme of a single-dish radio antenna. The pathway of the incoming radiation is shown in blue lines. *Image credit: Encyclopaedia Britannica, Inc.*

The amount of incident energy from the source received by the antenna is usually expressed as a flux density, F_ν, measured in unit of Jansky (1 Jy $= 10^{-26}$ W m^{-2} Hz^{-1}). The angular response (sensitivity) of a single-dish antenna is not uniform over its field of view. Diffraction creates a beam pattern composed of a main lobe (also called main beam or primary beam) plus multiple smaller sidelobes (Fig. 2.3). The main beam of a single-dish antenna can be approximated by a Gaussian function, *i.e.* a centrally peaked function with a smoothly decreasing response away from the center:

$$P(\theta) = \mathrm{e}^{-\theta^2/(2\theta_0^2)} \tag{2.3}$$

where θ is the angle to the main beam axis and θ_0 is given by:

$$\theta_0 = \frac{\theta_{\rm pb}}{\sqrt{8\ln(2)}} \tag{2.4}$$

with $\theta_{\rm pb}$ the half power beam width (HPBW) of the main beam, *i.e.* the angle between points of the main beam where the antenna power pattern falls to half of its maximum ($P\left(\frac{\theta_{\rm pb}}{2}\right) = 0.5$, see Fig. 2.3). The HPBW of the main beam, $\theta_{\rm pb}$, is usually used to describe the diameter of the field of view of the antenna and its angular resolution, *i.e.* its ability to separate two closely-spaced sources. $\theta_{\rm pb}$ depends on the wavelength (λ) of the incoming radiation and the diameter, D, of the dish:

$$\theta_{\rm pb} = k\frac{\lambda}{D}. \tag{2.5}$$

where k is a factor of order unity which depends on the antenna illumination.

The flux density measured per beam ($F_\nu^{\rm beam}$) is related to the specific intensity of the source (I_ν) via:

$$F_\nu^{\rm beam} = \int I_\nu \, P \, d\Omega \, . \tag{2.6}$$

For a source smaller than the telescope beam it leads to $F_\nu^{\rm beam} = I_\nu^{\rm beam}\,\Omega_{\rm beam}$, where $I_\nu^{\rm beam}$ is the beam-averaged intensity of the source and $\Omega_{\rm beam}$ the main beam solid angle, obtained by

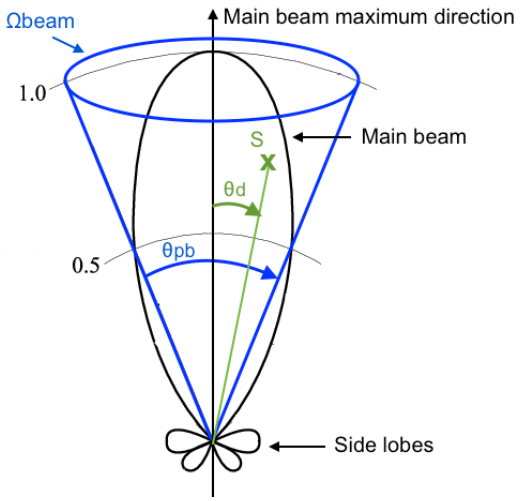

Figure 2.3: Sketch of the power pattern of a single-dish antenna. The HPBW of the main beam, $\theta_{\rm pb}$, is shown as the angle between the points where the power pattern falls to 0.5. The mean beam solid angle is marked with $\Omega_{\rm beam}$. For a source S, at a projected distance d from the beam center, the antenna sensitivity decreases with the angle $\theta_{\rm d}$ to the main beam axis (see Sect. 2.3.2).

integrating the telescope power pattern over the entire sphere (see Eqs. 2.3 and 2.4):

$$\begin{aligned}\Omega_{\rm beam} &= 2\pi \int P(\theta)\,\theta\,d\theta = 2\pi \int e^{-\frac{\theta^2}{2\theta_0^2}}\,\theta\,d\theta \\ &= 2\pi\,\theta_0^2 \\ &= \frac{\pi}{4\ln(2)} \times \theta_{\rm pb}^2\end{aligned} \tag{2.7}$$

From Eqs. 2.1 and 2.2 we can relate the flux density $F_\nu^{\rm beam}$ (in Jy beam^{-1}) to the effective brightness temperature of the source as follows:

$$F_\nu^{\rm beam} = \frac{2\,k_{\rm b}\,\nu^2}{c^2}\,\Omega_{\rm beam}\,J_\nu(T_{\rm B}) \tag{2.8}$$

If the emitting source can also be approximated by a Gaussian, then its full width at half-maximum (FWHM) is the result of the convolution of the observed sky signal by the telescope beam. In order to derive the actual source size, $\theta_{\rm s}$, one needs to deconvolve the observed source size, $\theta_{\rm obs}$, from the beam size, $\theta_{\rm pb}$ as follows:

$$\theta_{\rm s} = \sqrt{\theta_{\rm obs}^2 - \theta_{\rm pb}^2} \tag{2.9}$$

The fraction of the main beam filled by the source is given by the beam filling factor $b_{\rm ff}$:

$$b_{ff} = \frac{\theta_{\rm s}^2}{\theta_{\rm pb}^2 + \theta_{\rm s}^2} \tag{2.10}$$

In the case where the deconvolved source size $\theta_{\rm s}$ is much smaller than the beam size $\theta_{\rm pb}$, then $b_{ff} \sim \theta_{\rm s}^2/\theta_{\rm pb}^2 << 1$ and the measured brightness temperature is much smaller than the actual

source brightness temperature because of beam dilution. On the contrary, when $\theta_s >> \theta_{pb}$, then $b_{ff} \sim 1$, and the temperature measured in the beam is equal to the true effective brightness temperature of the source.

The sensitivity (or root-mean square deviation, rms) of the measured signal, σ (in K), is given by the so-called radiometer formula (see, e.g., Wilson et al. 2009):

$$\sigma = \frac{2\,T_{sys}}{\sqrt{\Delta\nu\,t}} \tag{2.11}$$

where $\Delta\nu$ is the frequency bandwidth and t the total integration time (*i.e.* on+off source). The system temperature, T_{sys}, corresponds to the sum of all noise contributors, which includes noise from the receiver, the atmosphere, the ground, and the source itself. It is commonly assumed that a line detection is secured above 3σ (*i.e.* $T_{peak} > 3\sigma$). Line surveys conducted with single-dish radio telescopes may easily reach the confusion limit (*i.e.* almost all channels contain spectral-line emission), leading to strong line blending. Because of their finite physical size, single-dish antennas are also limited in angular resolution, thus limiting their ability to separate the contribution of closely-spaced sources at different velocities, increasing even more the overlap between spectral lines in the observations. To reach higher angular resolution and thus diminish the line confusion in the observed spectra, several telescopes may be combined to interferometers.

2.1.3 Interferometers

The radio signal received from an astronomical source by the individual antennas forming an interferometer is correlated to simulate a larger telescope, with a diameter equivalent to the longest projected distance between two individual antennas. Each pointing made with the antenna array delivers an image of which the total field of view (*i.e.* the primary beam size) depends on the diameter, D, of the individual antennas (see Eq. 2.5 with $k = 1.13$ for instance for ALMA, Remijan 2015, see also Sect. 2.1.5). The angular resolution of the array can be estimated roughly from Eq. 2.5 using the maximum baseline B_{max} (instead of D), given by the maximum projected distance between a pair of antennas. For a given array configuration, different pairs of antennas provide different angular resolutions. The mean synthesized beam, θ_{beam} (HPBW) of the interferometer is given by the geometrical mean of the major and minor axes as follows:

$$\theta_{beam} = \sqrt{\theta_{min} \times \theta_{maj}} \tag{2.12}$$

The emission from the targeted source is resolved by the interferometer angular resolution when the source diameter (HPBW) $\theta_s \geq \frac{1}{3}\,\theta_{beam}$. The beam solid angle of the interferometer is given by (Eqs. 2.7 and 2.12):

$$\Omega_{beam} = \frac{\pi}{4\ln(2)} \times \theta_{min} \times \theta_{maj} \tag{2.13}$$

The raw data obtained with an interferometer are called visibilities. Each visibility consists of an amplitude and phase measured at a discrete point in the uv-plane where each uv coordinate corresponds to the vector between a given pair of individual antennas. The uv coverage of an interferometer depends on the number of antennas contained in the array, their spatial configuration and the integration time (earth rotation). As the number of antennas is finite and discrete, there are invariably gaps in the sampling of the uv plane. To reconstruct the true sky intensity distribution (*i.e.* to go from the uv plane to the image plane of the sky), the Fourier transform of the visibility function is calculated. The deconvolution and cleaning

processes interpolate the missing information in the uv plane to reconstruct an image as close as possible to the true brightness distribution.

Because the minimum baseline, $B_{\rm min}$, of an interferometer cannot be smaller than the diameter of the individual antennas, the short spacings in the uv plane, which correspond to large spatial scales in the plane of the sky, are not sampled. Therefore the final image is biased to the compact, small-scale emission of the true sky brightness distribution. The maximum scale that can be recovered in the final image, *i.e.* the largest angular structure to which the array is sensitive to, is given by (Remijan 2015):

$$\theta_{\rm max} \approx 0.6\,\frac{\lambda}{B_{\rm min}} \tag{2.14}$$

All extended emission with $\theta_{\rm s} > \theta_{\rm max}$ is thus filtered out by the interferometer.

The sensitivity in the final image (in Jy beam^{-1}) is given by (see, e.g., Wilson et al. 2009):

$$\Delta F_\nu = \frac{2k_{\rm b}\,T_{\rm sys}}{A_{\rm e}\,\sqrt{N(N-1)\Delta\nu\,t}} \tag{2.15}$$

where $T_{\rm sys}$ is the system temperature, $A_{\rm e}$ is the effective collecting area of the individual antennas, N is the number of antennas in the array, $\Delta\nu$ is the frequency bandwidth, and t the integration time. From Eq. 2.8 and 2.15 we derive the brightness temperature rms (in K):

$$\Delta T_{\rm B} = \frac{\lambda^2\,T_{\rm sys}}{\Omega_{\rm beam}\,A_{\rm e}\,\sqrt{N(N-1)\Delta\nu\,t}} \tag{2.16}$$

which depends on the angular resolution of the interferometer ($\Omega_{\rm beam}$, see Eq. 2.13). In the last decades many new radio astronomical instruments have been developed to achieve always higher angular resolution and sensitivity and to cover more parts of the electromagnetic spectrum. The following sections (Sect. 2.1.4 and 2.1.5) introduce two powerful interferometers which provided the data used for this thesis work, the Submillimeter Array (SMA) and the Atacama Large Millimeter/submillimeter Array (ALMA).

2.1.4 The Submillimeter Array

The Submillimeter Array (Ho et al. 2004) is an 8-antenna radio interferometer located in Hawaii (USA) (see Fig. 2.4). The SMA operates in the mm-submm range at frequencies from 180 GHz to 420 GHz. The 6 m diameter dishes can be arranged with baselines as long as 509 m, for a synthesized beam of a few 0.1″.

2.1.5 The Atacama Large Millimeter/submillimeter Array

The Atacama Large Millimeter/submillimeter Array is located at 5000 m altitude on the Chajnantor plateau in the Atacama desert in Chile (Fig. 2.5). The main array consists of 50 12m antennas which can be arranged in different configurations providing maximum baselines up to 16 km. The Atacama Compact Array (ACA) consists of four 12m plus 12 7m antennas, used to image large scale structures filtered out by the 12m array. The frequency range covered by ALMA is divided into several receiver bands, currently starting from 84 GHz (band 3), up to 950 GHz (band 10, see Fig. 2.6).

Figure 2.4: The eight 6 m antennas of the Submillimeter Array in Hawaii (USA). *Photo credit: N. Patel.*

Figure 2.5: Part of the radio antennas composing the Atacama Large Millimeter/submillimeter Array at the 5000m-altitude site on the Chajnator plateau (Chile). *Photo credit: M. Bonfand.*

2.2 Continuum emission and spectral line analysis

Dust and molecules found in regions forming high-mass stars are important tools to investigate their host environment as the properties of the observed continuum and spectral line emission are governed by the interaction between the (proto)star radiation and its surrounding envelope. In this section I describe the methods used in the thesis to analyze the observational data and characterize the dense gas found in HMCs (H_2 column density, mass, molecular column densities, systemic velocity, kinetic temperatures).

The following text is based on Goldsmith & Langer (1999), Lequeux (2005), Draine (2011), Mangum & Shirley (2015), and Krumholz (2017).

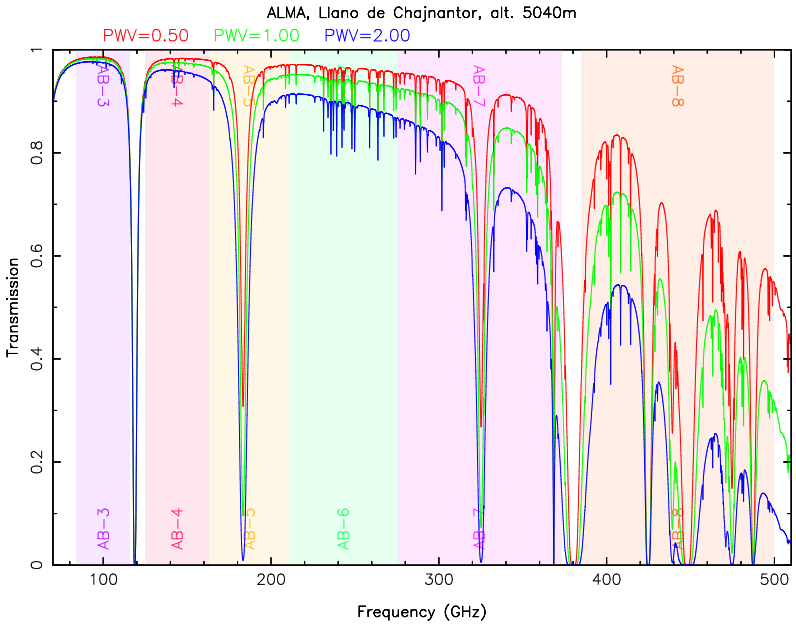

Figure 2.6: Atmospheric transmission in the ALMA frequency bands 3 to 8 (indicated with different background colors) as a function of the frequency and plotted in three different colors depending on the pwv. *This figrue was produced using the ALMA atmosphere-model tool.*

2.2.1 Radiative transfer

The radiative transfer equations describe how an electromagnetic radiation propagates through a given medium, which can be composed of atoms, molecules, ions, electrons, or also dust grains. We assume that the radiation emitted from a bright source with a specific intensity I_ν at the frequency ν, enter a slab of material (see Fig. 2.7). As it propagates through the traversed medium, if we neglect scattering events, the intensity of the incoming radiation varies on a small pathlength ds as follows:

$$dI_\nu = -I_\nu \, \alpha_\nu \, ds \, + \, j_\nu \, ds \tag{2.17}$$

where α_ν is the attenuation coefficient at the frequency ν (with dimension of 1/length) and j_ν the emissivity at the frequency ν (with dimension of power per unit volume per unit frequency per unit solid angle). The optical depth of the traversed matter, τ_ν (dimensionless), characterizes the attenuation of the incident radiation. The medium is optically thick to the incoming radiation if $\tau_\nu >> 1$, and optically thin if $\tau_\nu << 1$. The optical depth depends on the frequency such that a given medium can absorb all visible light although it is transparent at millimeter wavelengths.

The pathlength ds is linked to the optical depth of the traversed medium via:

$$d\tau_\nu = \alpha_\nu \, ds \tag{2.18}$$

where τ_ν increases as a function of the pathlength. Eq. 2.17 can be written as a function of τ_ν as follows:

$$dI_\nu = -I_\nu \, d\tau_\nu \, + \, S_\nu \, d\tau_\nu \tag{2.19}$$

where S_ν is the so-called source function $S_\nu = j_\nu / \alpha_\nu$.

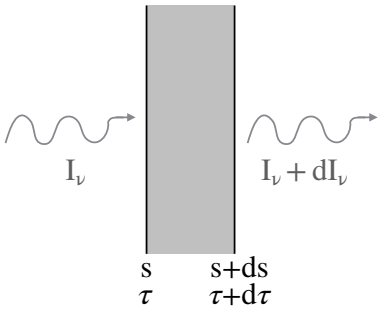

Figure 2.7: Sketch of the radiative transfer geometry. *Figure adapted from Draine (2011).*

In order to integrate Eq. 2.19, we multiply both sides of the equation by the integrating factor e^{τ_ν}:

$$\begin{aligned} e^{\tau_\nu}\,(dI_\nu + I_\nu\,d\tau_\nu) &= e^{\tau_\nu}\,S_\nu\,d\tau_\nu \\ d(e^{\tau_\nu}\,I_\nu) &= e^{\tau_\nu}\,S_\nu\,d\tau_\nu \end{aligned} \tag{2.20}$$

Now we can integrate Eq. 2.20, starting from $\tau_\nu = 0$ and $I_\nu = I_\nu(0)$, we obtain:

$$e^{\tau_\nu}\,I_\nu - I_\nu(0) = \int_0^{\tau_\nu} e^{\tau'}\,S_\nu d\tau' \tag{2.21}$$

A general solution to Eq. 2.21 is obtained by multiplying both sides of the equation by $e^{-\tau_\nu}$ as follows:

$$I_\nu(\tau_\nu) = I_\nu(0)\,e^{-\tau_\nu} + \int_0^{\tau_\nu} e^{-(\tau_\nu-\tau')}\,S_\nu\,d\tau' \tag{2.22}$$

which describes the intensity, $I_\nu(\tau_\nu)$, measured at the optical depth τ_ν, as the sum of the emission integrated over the path through the traversed material, attenuated by the effective absorption of the medium ($e^{-(\tau_\nu-\tau')}$), plus the background intensity $I_\nu(0)$ attenuated by the traversed medium ($e^{-\tau_\nu}$).

In local thermodynamic equilibrium (LTE), the energy levels of the molecules in the traversed medium are populated according to a single excitation temperature, $T_{\rm ex}$ (see Sect. 2.2.4). The intensity of the radiation traveling through the material is uniform (*i.e.* I_ν is conserved such that $\frac{dI_\nu}{d\tau_\nu} = 0$) and it can be described by a Planck function, such as $I_\nu = B_\nu(T_{\rm ex})$. From Eq. 2.19 we can write:

$$\frac{dI_\nu}{d\tau_\nu} = 0 = -B_\nu(T_{\rm ex}) + S_\nu \tag{2.23}$$

where S_ν must satisfy Kirchhoff's law:

$$S_\nu \equiv \frac{j_\nu}{\alpha_\nu} = B_\nu(T_{\rm ex}) \tag{2.24}$$

Thus Eq. 2.22 becomes:

$$I_\nu(\tau_\nu) = I_\nu(0)\,e^{-\tau_\nu} + \int_0^{\tau_\nu} e^{-(\tau_\nu-\tau')}\,B_\nu(T_{\rm ex})\,d\tau' \tag{2.25}$$

Furthermore, if $T_{\rm ex}$ is constant then:

$$I_\nu(\tau_\nu) = I_\nu(0)\,e^{-\tau_\nu} + B_\nu(T_{\rm ex})\,(1 - e^{-\tau_\nu}) \tag{2.26}$$

In order to get rid of the atmospheric contribution and to measure directly the true source intensity, without background contamination, a measurement is usually taken toward an "off-source" reference position containing only background emission (plus the atmospheric contribution), which is then subtracted to the intensity measured on-source:

$$\begin{aligned} I_{\nu,\mathrm{sou}} &= I_\nu - I_\nu(0) \\ &= I_\nu(0)\, e^{-\tau_\nu} + B_\nu(T_\mathrm{ex})\,(1 - e^{-\tau_\nu}) - I_\nu(0) \\ &= [-I_\nu(0) + B_\nu(T_\mathrm{ex})]\,(1 - e^{-\tau_\nu})\,. \end{aligned} \tag{2.27}$$

If we assumed that the background emission $I_\nu(0)$ can be approximated by a blackbody radiation at the temperature T_bg, then the specific intensity of the observed source is given by:

$$I_{\nu,\mathrm{sou}} = [B_\nu(T_\mathrm{ex}) - B_\nu(T_\mathrm{bg})](1 - e^{-\tau_\nu}) \tag{2.28}$$

2.2.2 Dust continuum properties

In the dense regions in which stars form, the dominant molecule, H_2, is difficult to observe directly because it has no permanent electric-dipole moment and therefore no allowed vibrational or rotational transitions in the (sub)mm range, but only many orders of magnitude weaker quadrupole transitions. In order to derive star-forming cloud properties (e.g., H_2 column density, mass, density), it is common to use dust-grain emission instead, which is an excellent tracer of column density and total cloud mass, provided the gas-to-dust mass ratio is known.

The thermal emission from interstellar dust grains depends on the dust column density, the strength of the external radiation field, the dust temperature, and other dust properties such as their chemical composition and size. As we have seen already before, dust grains are responsible for attenuation of radiation in the ISM. A grain bathed in the ISRF acquires an equilibrium temperature, T_d when it absorbs as much energy as it emits. The dust temperature is then given by the thermal balance for equilibrium (Krügel 2008), assuming that the rate of cooling of the dust is equal to the rate of radiative heating by the ISRF:

$$\int_0^\infty Q_\nu\, J_\nu D_\nu(A_\mathrm{v})\,\mathrm{d}\nu = \int_0^\infty Q_\nu\, B_\nu(T_\mathrm{d})\,\mathrm{d}\nu\,, \tag{2.29}$$

where the left-hand side describes the grain heating due to an incident radiation field with an averaged intensity J_ν, attenuated by dust grains ahead of the position considered in the cloud by the attenuation factor $D_\nu(A_\mathrm{v})$, and with Q_ν the frequency-dependent absorption and emission efficiency of the grains. The right-hand side of the equation corresponds to the primary cooling of dust grains, dominated by thermal emission of the grains in all directions. The energy balance equation can be expanded by adding any other relevant cooling or heating terms. For instance, we have seen that cosmic rays may be an important factor for the heating of dust grains (see discussion on the impact of the ISRF and cosmic rays on the dust temperature in Sects. 5.3.5 and 5.3.4, respectively). For a detailed derivation of the dust temperature solving the thermal balance for equilibrium see, e.g., Krügel (2008) and Hocuk et al. (2017) (see also Sect. 4.4.4).

For densities above a few 10^4 cm^{-3}, the dust-gas collisional coupling regulates the heat transfer between gas and dust, such that gas cooling is dominated by collisions as long as $T_\mathrm{d} < T_\mathrm{K}$. At higher densities (typically $\geq 10^6$ cm^{-3}) gas and dust are well coupled and T_d is equal to the kinetic temperature of the gas, which can be determined from molecular line observations.

The continuum emission measured at different frequencies can be used to investigate the cloud properties (density, mass, dust properties). For a source dominated by dust thermal emission, the flux density increases with frequency as $F_\nu \propto \nu^\alpha$, where the spectral index α is in the range from 2 (for optically thick dust) to 4 (optically thin dust), which leads to a dust emissivity index ($\beta = \alpha$ - 2) typically between 1 and 2 for clouds in the galactic disk (e.g. Schnee et al. 2010; Planck Collaboration et al. 2014a; Juvela et al. 2015; Reach et al. 2015). The variety of indices reflects the different properties of the emitting dust grains. For instance, values of α = 1–2 are usually found for HCHII regions, 0.6 for jets and winds, and -0.1 for optically thin HII regions.

For a gas cloud, with a mass density ρ, mixed with dust grains at the temperature $T_\mathrm{d} >> T_\mathrm{bg} = 2.736$ K, (*i.e.* we can neglect the cosmic microwave background temperature), we can express the flux density measured per telescope beam (in Jy beam^{-1}) as follows (Eqs. 2.28 and 2.6):

$$F_\nu^\mathrm{beam} = \Omega_\mathrm{beam}\, B_\nu(T_d)\,(1 - \mathrm{e}^{-\tau_\nu}), \tag{2.30}$$

which can be written as:

$$\tau_\nu = -\ln\left(1 - \frac{F_\nu^\mathrm{beam}}{\Omega_\mathrm{beam}\, B_\nu(T_d)}\right). \tag{2.31}$$

If we consider only absorption along the path, s, of the radiation traveling through the cloud, the optical depth is obtained by integrating the absorption coefficient α_ν (cm^{-1}) as follows $\tau_\nu = \int \alpha_\nu \,\mathrm{d}s = \int \kappa_\nu\, \rho \,\mathrm{d}s$, with κ_ν the dust absorption coefficient per unit of mass density of gas (in cm^2 g^{-1}). The dust absorption coefficient is given by the power law (Hildebrand 1983; Compiègne et al. 2011):

$$\kappa_\nu = \kappa_0 \left(\frac{\nu}{\nu_0}\right)^\beta, \tag{2.32}$$

with κ_0 the reference dust mass absorption coefficient at the frequency ν_0.

If we know the temperature and properties (τ_ν, α, β, κ_ν) of the dust grains, then we can compute the H_2 column density (*i.e.* the number of molecules per unit area along the line of sight) from the measured flux density as follows:

$$\begin{aligned} N_{\mathrm{H}_2} &= \int n_{\mathrm{H}_2}\, ds \\ &= \int \frac{\rho}{\mu_{\mathrm{H}_2}\, m_\mathrm{H}}\, ds \\ &= \frac{1}{\mu_{\mathrm{H}_2}\, m_\mathrm{H}\, \kappa_\nu} \int \kappa_\nu\, \rho\, ds \\ &= \frac{\tau_\nu}{\mu_{\mathrm{H}_2}\, m_\mathrm{H}\, \kappa_\nu} \end{aligned} \tag{2.33}$$

where $\mu_{\mathrm{H}_2} = 2.8$ is the mean molecular weight per hydrogen molecule (Kauffmann et al. 2008) and m_H the mass of atomic hydrogen. By replacing τ_ν by its expression (Eq. 2.31) in Eq. 2.33 we obtain:

$$N_{\mathrm{H}_2} = -\frac{1}{\mu_{\mathrm{H}_2} m_\mathrm{H} \kappa_\nu} \times \ln\left(1 - \frac{F_\nu^\mathrm{beam}}{\Omega_\mathrm{beam} B_\nu(T_d)}\right). \tag{2.34}$$

Uncertainties in the conversion between dust emission and gas column density mostly arise from the error on the dust opacity and temperature that are usually not well known.

The cloud mass is obtained by integrating the column density of gas across the source, assuming spherically symmetric emission (Hildebrand 1983) :

$$M_{\rm g} = N_{\rm H_2}\, \Omega_{\rm beam}\, \mu_{\rm H_2}\, m_{\rm H}\, D^2 \tag{2.35}$$

with D the distance to the cloud from the Sun.

2.2.3 Spectral line properties

Spectral lines are powerful tools to investigate the chemical composition and physical conditions of their emitting gas (see also Sects. 2.2.4 and 2.2.5). When the radiation emitted from a newly formed (proto)star passes through the line-of-sight gas, it is absorbed by interstellar atoms and molecules when $T_{\rm ex} < T_{\rm bg}$, resulting in dark absorption lines in the observed spectrum. For $T_{\rm ex} > T_{\rm bg}$ instead, excited atoms or molecules produce emission lines at the same frequencies. According to quantum chemistry, every transition of a given molecular species occurs at a specific frequency, given by the difference between two energy states. Each transition can be identified and assigned to a given species based on its frequency and can be investigated to derive the properties of the emitting gas. If we consider the case of a simple diatomic molecule, it can be observed through its electronic, vibrational or rotational transitions. Electronic transitions occur in the visible/UV range (*i.e.* at energies of the order of a few eV or 10^4 K) when one or more electrons jump to the next, higher, energy level (see Fig. 2.8). For every electronic state there are several possible vibrational states. Vibrational transitions are seen at lower energies, in the mid-infrared ($\sim$0.1 eV or 10^3 K), via vibrational motion of the nuclei (*i.e.* changes in the nuclei relative distance). Finally for every electronic and vibrational state there are rotational states. The rotational transitions occur at very low energies (10^{-3}–10^{-2} eV or 10–500 K) such that they can be detected in the mm-submm range with radio telescopes. Rotational levels are usually described by a single vibrational quantum number v = 0, 1, 2 etc., and the rotational quantum number J. For a given species X, a rotational transition between the upper and lower rotational states $J_{\rm u}$ and $J_{\rm l}$, respectively, within the vibrational state v will be referred to as $X_v(J_{\rm u-K_a,K_c}$–$J_{\rm l-K_a,K_c})$, with $K_{\rm a}$ and $K_{\rm c}$ the projections of the rotational angular momentum onto the symmetry axes of the molecule.

The analysis of spectral lines relies on the availability of accurate spectroscopic measurements made with laboratory experiments and through quantum chemical calculations. The characteristics of a given species (frequencies and intensities of the transitions, energy states, partition functions) are stored in spectroscopic databases such as the Cologne Database for Molecular Spectroscopy[1] (CDMS) and the Jet Propulsion Laboratory[2] database (JPL) catalog.

The shape of spectral lines give information on the velocity distribution and opacity structure of the gas. If the line-of-sight material is optically thick ($\tau_\nu >> 1$), only emission from the surface of the observed gas cloud reaches us. Spectral lines thus appear to be saturated, making the analysis more difficult. In the ideal case of optically thin emission, the material is transparent and the emission from every layer is visible. Optically thin spectral lines can be approximated with Gaussian profiles of which the linewidth (FWHM) is mainly due to the Doppler effect (*i.e.* the lines are broadened by the velocity distribution of the emitting species). Gas moving away from us emit at lower frequencies (*i.e.* it is red-shifted) than the rest frequency measured in the laboratory, while gas moving toward us emits at higher frequencies (*i.e.* it is blue-shifted).

[1] https://zeus.ph1.uni-koeln.de/cdms/molecules
[2] http://spec.jpl.nasa.gov/home.html

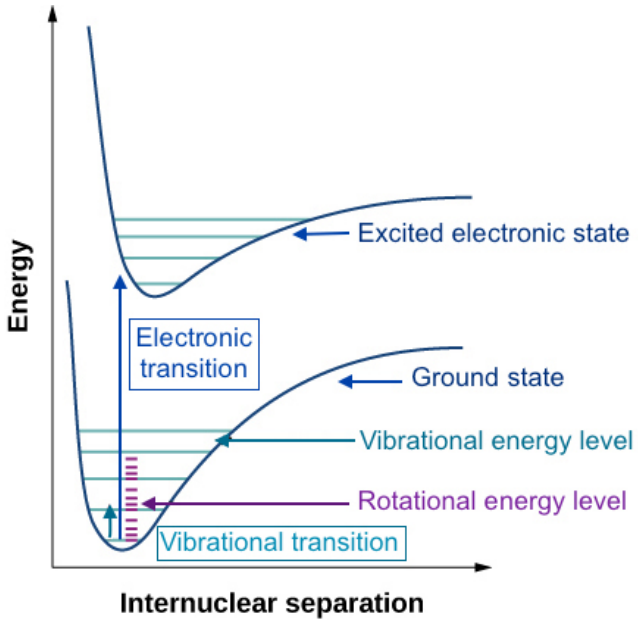

Figure 2.8: Sketch of the internal energy levels of a diatomic molecule. Vibrational energy levels are represented in light blue on the electronic potential energy curves (dark blue). For every electronic and vibrational state there are rotational states associated (purple). *Image credit.*

A gas cloud along our line of sight with a velocity distribution $\psi(v)$ emits at a frequency $\nu \sim \nu_0\,(1 - v/c)$, where ν_0 is the rest frequency of the observed transition and v the velocity of the cloud with respect to the Local standard of rest (LSR). By measuring the line profile of the observed transition, $\phi(\nu)$, we directly get the velocity distribution of the gas:

$$\phi(\nu) = \psi\left[c\left(1 - \frac{\nu}{\nu_0}\right)\right] \tag{2.36}$$

Asymmetrical line shapes can be caused by extra motions due to infall, rotation, or outflows, leading to additional line broadening. For instance, self-absorption (*i.e.* dip in the spectral line peak) with the blue peak stronger than the red peak is observed in case of infall motion, while molecular outflows give rise to high-velocity red- and blue-shifted emission wings.

2.2.4 Deriving molecular column densities

Molecular column densities can be derived based on the measurement of the line optical depth in the observed spectrum. For simplicity, suppose we have a gas composed of molecules whose energies are distributed in a simple two-level system (upper and lower) with energies E_u and E_l and statistical weights g_u and g_l, respectively. In the two-level system $E_\mathrm{u} > E_\mathrm{l}$ and the energy difference between the two levels is given by $h\nu$. The number of molecules in the upper energy state u is related to the line opacity as follows (Mangum & Shirley 2015):

$$N_\mathrm{u} = \frac{8\,\pi\,\nu^3}{c^3 A_\mathrm{ul}}\left[e^{\left(\frac{h\nu}{k_\mathrm{b} T_\mathrm{ex}}\right)} - 1\right]^{-1} \int \tau_\nu dv \tag{2.37}$$

where A_ul is the Einstein coefficient of spontaneous emission characterizing the probability of spontaneous radiative de-excitation. When the gas density is much higher than the critical

density, $n_{cr} = A_{\rm ul}/C_{\rm ul}$, where $C_{\rm ul}$ is the collisional rate coefficient, collisions (mainly with H_2) dominate the excitation over radiative processes. The two-level system is thus in thermal equilibrium (LTE) and the level populations follow the Boltzman distribution:

$$\frac{n_{\rm u}}{n_{\rm l}} = \frac{g_{\rm u}}{g_{\rm l}} e^{(-\frac{h\nu}{k_{\rm b}\,T_{\rm ex}})} \tag{2.38}$$

where the number density of molecules in the excited state, $n_{\rm u}$, relative to the lower state, $n_{\rm l}$, is described by a single excitation temperature, $T_{\rm ex}$, which equals the kinetic temperature of the gas, $T_{\rm K}$. When the gas density is smaller than the critical density, the energy levels are sub-thermally populated and $T_{\rm ex} < T_{\rm K}$.

At thermal equilibrium $N_{\rm u}$ (Eq. 2.37) is related to the total molecular column density (*i.e.* the total population of all energy levels in the molecule) with the rotational partition function $Q_{\rm rot}$ as follows:

$$\frac{N_{\rm tot}}{N_{\rm u}} = \frac{Q_{\rm rot}(T_{\rm ex})}{g_{\rm u}}\, e^{\frac{E_{\rm u}}{k_{\rm b}\,T_{\rm ex}}}\,. \tag{2.39}$$

Here $Q_{\rm rot}$ is the statistical sum over all rotation energy levels in the molecule, given by:

$$Q_{\rm rot} = \sum_i g_{\rm i}\, e^{-\frac{E_{\rm i}}{k_{\rm b}\,T_{\rm ex}}}\,. \tag{2.40}$$

From Eqs. 2.37 and 2.39 we express the total column density as a function of the opacity integrated over the velocity as:

$$N_{\rm tot} = \frac{8\,\pi\,\nu^3}{c^3}\,\frac{Q_{\rm rot}(T_{\rm ex})}{A_{\rm ul}\,g_{\rm u}}\, e^{\frac{E_{\rm u}}{k_{\rm b}\,T_{\rm ex}}}\,\left[e^{\left(\frac{h\nu}{k_{\rm b}\,T_{\rm ex}}\right)} - 1\right]^{-1} \int \tau_\nu {\rm d}v\,. \tag{2.41}$$

For emission lines the integral over optical depth may be converted to an integrated intensity in order to derive $N_{\rm tot}$ directly from the line intensity. To do so we express the radiative transfer equation (Eq. 2.28) in a form which involves the effective brightness temperature of the source (Eq. 2.2) as follows:

$$J_\nu(T_{\rm B}) = b_{\rm ff}\,[J_\nu(T_{\rm ex}) - J_\nu(T_{\rm bg})]\,(1 - e^{-\tau_\nu}) \tag{2.42}$$

with $b_{\rm ff}$ the beam filling factor of the source (Eq. 2.10). For simplicity we neglect the cosmic microwave background temperature as $J_\nu(T_{\rm ex}) >> J_\nu(T_{\rm bg})$. In the case of an optically thick line ($\tau_\nu >> 1$), Eq. 2.42 becomes $J_\nu(T_{\rm B}) \sim b_{\rm ff} J_\nu(T_{\rm ex})$ and the transition appears saturated. We cannot derive the total molecular column density as we see the intensity of the radiation emitted by the layer at $\tau_\nu \sim 1$, and not the deeper layers. In the case of optically thin emission ($\tau_\nu << 1$), Eq. 2.42 becomes:

$$J_\nu(T_{\rm B}) = b_{\rm ff}\, J_\nu(T_{\rm ex})\,\tau_\nu\,. \tag{2.43}$$

The optical depth integrated over velocity thus becomes:

$$\int \tau_\nu dv = \frac{1}{b_{\rm ff}}\,\frac{W}{J_\nu(T_{\rm ex})} \tag{2.44}$$

with $W = \int J_\nu(T_{\rm B}) dv$ the total integrated line intensity.

Finally from Eqs. 2.41 and 2.44 the total column density is given by:

$$N_{\rm tot} = \frac{8\,\pi\,k_{\rm b}\,\nu^2}{b_{\rm ff}\,h\,c^3}\,\frac{Q_{\rm rot}(T_{\rm ex})}{A_{\rm ul}\,g_{\rm u}}\, e^{\frac{E_{\rm u}}{k_{\rm b}\,T_{\rm ex}}}\,W \tag{2.45}$$

2.2.5 Population diagrams and rotational temperatures

In this section we show how to derive kinetic temperatures from molecules with multiple observed transitions spanning a large range of energies above the ground state, using the so-called population diagram analysis (Goldsmith & Langer 1999). A population diagram displays the column density divided by the statistical weight ($N_\mathrm{u}/g_\mathrm{u}$) of several molecular energy levels as a function of their energy above the ground state ($E_\mathrm{u}/k_\mathrm{b}$). Under LTE conditions, Eq. 2.39 shows that a plot of the natural logarithm of $N_\mathrm{u}/g_\mathrm{u}$ versus $E_\mathrm{u}/k_\mathrm{b}$ yields a straight line with a slope inversely proportional to the temperature:

$$\ln\left(\frac{N_u}{g_u}\right) = -\frac{E_u}{k_b T_\mathrm{rot}} + \ln\left(\frac{N_\mathrm{tot}}{Q_\mathrm{rot}}\right) \tag{2.46}$$

This relation assumes that the populations of all molecular energy levels are in equilibrium at the temperature often referred to as the rotational temperature, T_rot, which is equal to the kinetic temperature of the gas when all levels are thermalized.

As seen in Sect. 2.2.4, for optically thin lines ($\tau_\nu << 1$) the molecular column density may be expressed as a function of the integrated line intensity (Eqs. 2.37, and 2.44) as follows:

$$N_\mathrm{u} = \frac{8\,\pi\,k_\mathrm{b}\,\nu^2}{b_\mathrm{ff}\,h\,c^3\,A_\mathrm{ul}}\,W \tag{2.47}$$

which leads to:

$$\ln\left(\frac{8\,\pi\,k_\mathrm{b}\,\nu^2\,W}{b_\mathrm{ff}\,h\,c^3\,A_\mathrm{ul}\,g_\mathrm{u}}\right) = -\frac{E_u}{k_b T_\mathrm{rot}} + \ln\left(\frac{N_\mathrm{tot}}{Q_\mathrm{rot}}\right) \tag{2.48}$$

valid only if $T_\mathrm{ex} >> T_\mathrm{bg}$.

In the case of partially optically thick transitions, Eq. 2.42 becomes:

$$J_\nu(T_\mathrm{B}) = b_\mathrm{ff}\,J_\nu(T_\mathrm{ex})\left(\frac{1-e^{-\tau_\nu}}{\tau_\nu}\right)\tau_\nu \tag{2.49}$$

Following Goldsmith & Langer (1999), we define the opacity correction factor $C_{\tau_\nu} = \left(\frac{1-e^{-\tau_\nu}}{\tau_\nu}\right)$, by which the upper level column density, N_u, needs to be corrected to account for the finite optical depth of the observed transition. Combining Eqs. 2.46, 2.48, and 2.49 we can write:

$$\ln\left(\frac{N_u\,C_{\tau_\nu}}{g_u}\right) = \ln\left(\frac{8\,\pi\,k_\mathrm{b}\,\nu^2\,W}{b_\mathrm{ff}\,h\,c^3\,A_\mathrm{ul}\,g_\mathrm{u}}\right) + \ln C_{\tau_\nu} = -\frac{E_u}{k_b T_\mathrm{rot}} + \ln\left(\frac{N_\mathrm{tot}}{Q_\mathrm{rot}}\right). \tag{2.50}$$

2.3 The EMoCA imaging spectral line survey

Unbiased spectral line surveys covering a large range of frequencies are a prerequisite for a rigorous search for new species as it may be difficult, because of line confusion, to predict which transitions will be sufficiently free of contamination to be firmly identified. Combining high angular resolution and high sensitivity with a large instantaneous bandwidth, ALMA is a powerful asset in the search for new COMs. In this section we present a deep unbiased line survey of Sgr B2(N) conducted with ALMA in its Cycles 0 and 1, covering nearly the full 3 mm band (Fig. 2.6). The EMoCA survey (standing for Exploring molecular complexity with ALMA) aims at extending our view of the chemical complexity in the ISM. The phase center of the observations is located at $\alpha_\mathrm{J2000} = 17^h47^m19.87^s$, δ_J2000 = -28°22′16″, half way between the main HMCs N1 and N2. The survey is divided into five spectral setups, each one

Table 2.1: Information on the observational setups of the EMoCA survey.

Setup	Frequency range[a] LSB (GHz)	USB (GHz)	Date of observation (yyyy–mm–dd)	N_a[b]	Baseline range[c] (m)	t_{int}[d] (min)
S1	84.1–87.7	96.2–99.8	2012–08–27	26	17–400	54.7
S2	87.7–91.4	99.7–103.4	2012–09–28	25	20–387	44.1
S3	91.4–95.1	103.4–107.1	2012–06–06	18	15–395	40.2
			2012–06–18	22	15–395	40.4
S4	95.0–98.7	107.0–110.7	2012–07–04	21	17–398	8.1
			2012–08–01	24	19–442	34.9
			2012–08–10	26	21–400	35.0
S5	98.7–102.4	110.7–114.4	2014–04–05	38	15–413	24.4

Notes. [(a)] Frequency range covered by the lower side band (LSB) and upper side band (USB) of the setup. [(b)] Number of ALMA 12m antennas used simultaneously. [(c)] Minimum (B_{min}) and maximum (B_{max}) projected baseline separations. [(d)] On-source integration time.

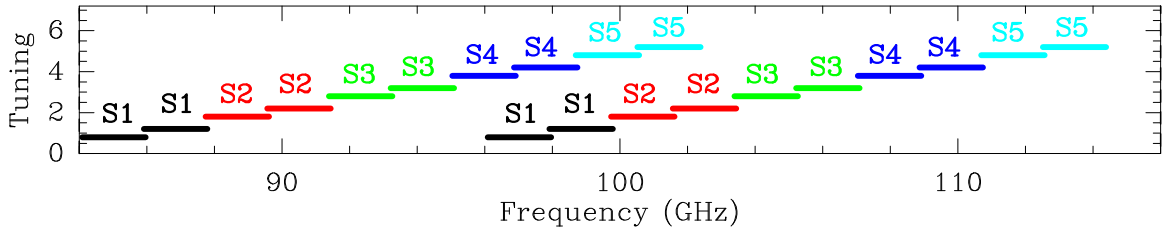

Figure 2.9: Frequency range covered by the EMoCA spectral setups (LSB and USB) in the ALMA band 3. Each setup is displayed with a different color (see also Table 2.1). The 20 horizontal lines correspond to the 20 spectral windows (see Table 2.2). *Image credit: A. Belloche.*

delivering four 1875 MHz wide spectral windows (two per sideband, see Fig. 2.9). Each pair of adjacent spectral windows has an overlap of about 50 MHz to compensate for possible edge effects. To cover a frequency range as large as possible, the four correlator bands were used simultaneously with a channel spacing of 244.141 kHz, in one polarization. The spectra were then smoothed to a spectral resolution of 488.3 kHz (1.7 to 1.3 km s^{-1}). In total the survey covers the frequency range 84.1–114.4 GHz with a high sensitivity of about ∼3 mJy/beam (∼0.16 K). Observations were performed at high angular resolution (with a mean synthesized beam ∼1.6″), to separate N1 and N2, allowing for a comparative study of the two cores. The size (HPBW) of the synthesized beam is given for each spectral window in Table 2.2. Table 2.1 gives further details about the frequency coverage, the range of baselines, and on-source integration time for each setup. Setups S1 and S5 were observed only once. Only the measurement sets for the last day of Setup S2 are used. For S3 and S4 measurement sets were merged into one single measurement set. A detailed description of the calibration, imaging, and deconvolution procedures is presented in Belloche et al. (2016).

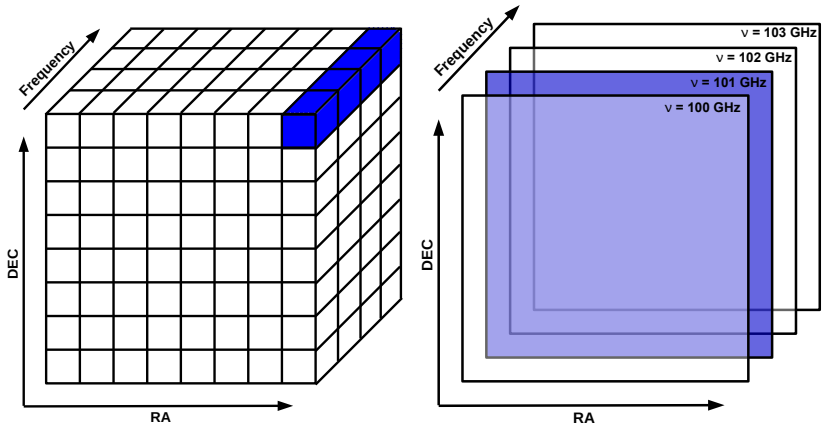

Figure 2.10: Three-dimensional datacube containing the flux density measured in the field of view of the interferometer. The cube is composed of several layers of position–position maps (RA and Dec) depending on the number of frequency (or velocity) channels (right panel). Each map is divided into a given number of pixels (left panel) with the pixel size which depends on the spatial resolution of the data. *Image credit: M. Mattern.*

2.3.1 Datacubes

The data from the EMoCA survey are stored in 20 three-dimensional (3D) cubes which consist of layers of position–position maps for a number of channels which depends on the bandwidth and frequency coverage of each spectral window (see Fig. 2.10). Each map contains the flux density distribution measured in the field of view per frequency (or velocity) interval. A map is divided into a number of pixels, depending on the chosen size of each individual pixel and the angular resolution of the observations. By extracting all the frequency channels for a given pixel, we obtain a single-position spectrum (blue-colored area, Fig. 2.10a). If we split up the data cube into frequency channels we create channel maps (blue-colored area, Fig. 2.10b). By adding up the maps along the frequency axis we create integrated intensity maps.

In order to produce separated datacubes containing either spectral lines or continuum emission, we use the spectra extracted toward the peak position of Sgr B2(N)'s HMCs. Due to the very high line density in the observed spectra, in particular toward the main HMCs N1 and N2 (see Sect. 3.1.1), it is difficult to determine the baseline level. In each spectral window of each setup, we select manually the channels that are free of strong line emission. A first order baseline is then subtracted to the selected channels using the CLASS software [3] to separate spectral lines from the continuum for the full datacubes. For each HMC different sets of channels are selected to account for their different systemic velocities. Table 2.2 gives the median noise level measured by Belloche et al. (2016) using the command GO NOISE in GREG in the channel maps of the full field of view of the continuum-subtracted datacubes. The noise level measured in each spectral window of the continuum-subtracted spectra (*i.e.* containing only the emission lines) obtained towards the sources N3, N4, and N5 (see Sect. 3.1.1) is also shown for comparison.

[3] See http://www.iram.fr/IRAMFR/GILDAS

Table 2.2: Noise level in the EMoCA spectral setups.

Setup	SPW[a]	Frequency range	Synthesized beam		Channel map rms[b]		Spectrum rms[c]					
			HPBW	P.A.			N3		N4		N5	
		(MHz)	($'' \times ''$)	(deg.)	(mJy beam^{-1})	(K)	(mJy beam^{-1})	(K)	(mJy beam^{-1})	(K)	(mJy beam^{-1})	(K)
S1	0	84091–85966	2.1×1.5	-85	3.0	0.16	2.6	0.14	2.9	0.15	4.1	0.22
	1	85904–87779	2.0×1.5	-83	2.7	0.14	2.7	0.14	2.6	0.14	3.9	0.21
	2	96154–98029	1.8×1.4	-85	3.0	0.16	2.9	0.15	3.1	0.16	4.5	0.23
	3	97904–99779	1.8×1.3	-85	3.1	0.16	3.4	0.18	2.9	0.15	3.8	0.20
S2	0	87729–89604	1.9×1.7	86	3.1	0.15	2.7	0.13	2.5	0.12	3.4	0.17
	1	89554–91429	1.8×1.6	52	2.8	0.15	2.5	0.13	2.5	0.14	3.9	0.21
	2	99728–101602	1.6×1.4	48	2.7	0.14	2.5	0.13	2.5	0.13	3.9	0.20
	3	101552–103427	1.6×1.4	49	2.7	0.14	2.5	0.13	2.8	0.15	3.8	0.20
S3	0	91368–93242	2.9×1.5	84	3.4	0.12	2.7	0.09	2.9	0.10	5.0	0.17
	1	93193–95067	2.8×1.5	83	3.1	0.10	3.3	0.11	2.4	0.08	4.7	0.16
	2	103365–105239	2.5×1.3	82	3.4	0.11	3.0	0.10	3.0	0.10	5.2	0.36
	3	105189–107064	2.5×1.3	82	3.6	0.12	3.1	0.11	3.4	0.12	5.7	0.19
S4	0	95021–96896	1.9×1.4	-82	1.9	0.10	1.9	0.10	2.1	0.11	2.7	0.14
	1	96846–98720	1.8×1.3	-82	1.9	0.10	2.1	0.11	2.0	0.10	2.8	0.15
	2	107019–108893	1.7×1.2	-83	2.2	0.11	3.0	0.16	2.1	0.11	3.2	0.17
	3	108843–110718	1.6×1.2	-82	2.3	0.12	2.2	0.12	2.2	0.12	3.6	0.19
S5	0	98672–100546	1.8×1.4	-76	2.8	0.14	2.9	0.14	2.5	0.12	3.8	0.19
	1	100496–102370	1.7×1.4	-76	2.7	0.13	2.5	0.13	2.3	0.12	3.9	0.19
	2	110669–112543	1.6×1.3	-72	3.5	0.17	3.2	0.15	3.7	0.18	4.9	0.23
	3	112494–114368	1.6×1.2	-77	4.9	0.24	4.0	0.20	4.0	0.20	5.8	0.29

Notes. [(a)] Spectral window (see also Fig. 2.9). [(b)] Median noise level measured in the channel maps with the command GO NOISE in GREG in the continuum-subtracted datacubes (Belloche et al. 2016). [(c)] Noise level measured in each spectral window of the continuum-subtracted spectra obtained toward N3–N5 (Sect. 2.3.1). The rms values are not corrected for the primary beam attenuation.

Table 2.3: Distance of N1–N5 to the phase center of the observations.

Source	$\theta_{\rm d}$[a]
N1	$2.4''$
N2	$2.6''$
N3	$8.3''$
N4	$17.0''$
N5	$25.4''$

Notes. [(a)] Distances computed based on the HMCs' absolute coordinates given in Table 3.1.

2.3.2 Extracting emission spectra

In order to study the hot core population in Sgr B2(N) we extract from the 20 continuum-subtracted datacubes, the spectra toward the peak position of each source (see Sect. 3.1.1). In Sect. 2.1.2 we saw that given the power pattern of the individual antennas, the sensitivity in the field of view varies as a function of the distance to the phase center (*i.e.* the angle to the main beam axis, see Fig. 2.3). The spectra observed toward each source are corrected for the primary beam attenuation, $P(\theta_{\rm d})$ (see Eq. 2.3), with $\theta_{\rm d}$ the distance of each HMC to the phase center (Table 2.3) and $\theta_{\rm pb}$ the HPBW of the ALMA antennas at the frequency of the EMoCA survey (Table 2.4). The correction factors ($1/P(\theta_{\rm d})$) applied to the spectra observed toward Sgr B2(N1–N5) are given in Table 2.4. Finally, for each spectrum the flux density measured per beam ($F_\nu^{\rm beam}$ in Jy beam^{-1}) is converted to effective brightness temperature (in K) using Eq. 2.8. At 100 GHz, the conversion factor from brightness temperature to flux density is $\sim$53 K Jy^{-1} beam.

Table 2.4: Primary beam correction factors.

Freq.	HPBW[a]	Correction factor[b]				
(GHz)	(″)	N1	N2	N3	N4	N5
84.1	69.2	1.00	1.00	1.04	1.18	1.45
114.4	50.9	1.01	1.01	1.08	1.36	1.99

Notes. [(a)] $\theta_{\rm pb}$ (HPBW) of the ALMA 12m single-dish antennas. [(b)] Frequency-dependent correction factors to account for the primary beam attenuation (see Sect. 2.3.2), computed based on the source distances to the phase center of observations (see Table 2.3).

2.3.3 Radiative transfer modeling of the line survey

In order derive the chemical content of the HMCs embedded in Sgr B2(N), we perform the radiative transfer modeling of the EMoCA spectral line survey using *Weeds* (Maret et al. 2011), which is part of the CLASS software. *Weeds* solves the radiative transfer equations under the LTE assumption, taking into account the finite angular resolution of the interferometer, the line opacity, line blending, and the continuum background. The spectroscopic predictions used in this thesis are taken from the CDMS and JPL catalogs. They are the same as in Belloche et al. (2016, 2017) and Müller et al. (2016), except for ethanol, methanol, and methyl cyanide, for which we use the new CDMS predictions. *Weeds* allows us to produce synthetic spectra that we compare directly to the observed continuum-subtracted spectra corrected for the primary beam attenuation. Each vibrationally or torsionally excited state of each molecule is modeled separately, based on the following parameters: rotational temperature (see Sect. 3.4), size (FWHM) of the emitting region (see Sect. 3.3), velocity offset with respect to the systemic velocity of the source (see Sect. 4.1.1), linewidth (see Sect. 3.2.1), and finally the column density is adjusted manually until a good fit to the data is obtained. In a spectrum with high spectral line density (see Sect. 3.1.1), the risks of mis-assigning lines are particularly high. Therefore, a line is assigned to a given molecule only if:

- ✓ a significant number of transitions are clearly detected,
- ✓ each line emitted in the frequency range of the survey is detected with the right intensity predicted by the LTE synthetic spectrum (unless it is blended with stronger lines from other species and thus cannot be clearly identified),
- ✓ no predicted line is missing in the observed spectrum.

The contribution from all firmly identified species is added linearly to build up a complete synthetic spectrum for each HMC. If for a given molecule the contribution of the vibrationally or torsionally excited states is not included in the partition function of the spectroscopic predictions used to produce the LTE synthetic spectrum, a vibrational correction factor $C_{\rm vib}$ is applied to the column density, given by (see, e.g., Endres et al. 2016):

$$C_{\rm vib} = \prod_{\rm i} \left(1 - e^{\frac{E_{\rm i}}{k_{\rm b} T_{\rm rot}}} \right)^{-1} , \tag{2.51}$$

where $T_{\rm rot}$ is the rotational temperature and $E_{\rm i}$ the energy of the known vibrational modes of the molecule.

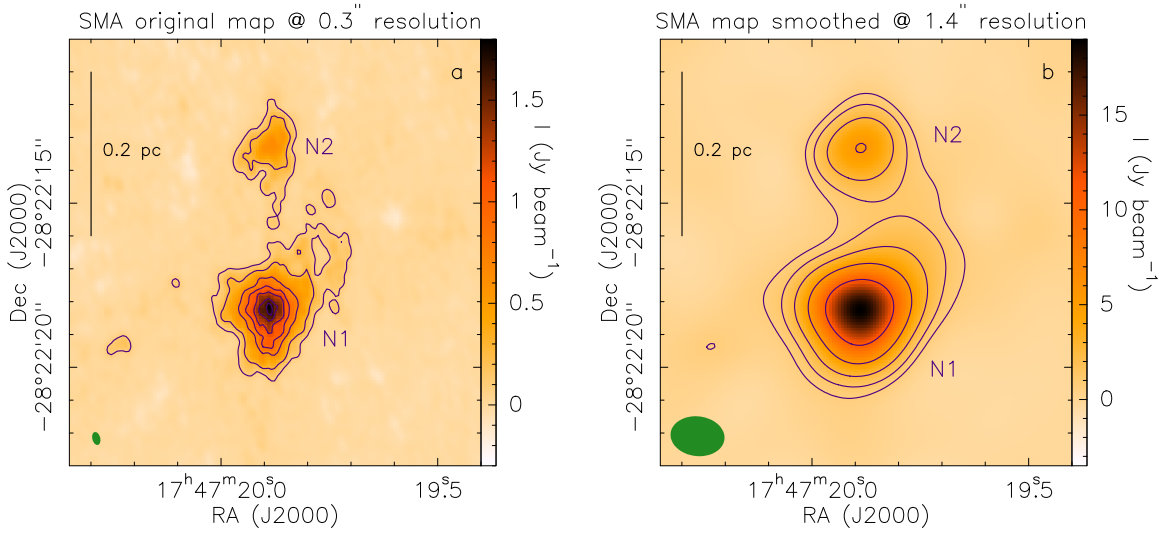

Figure 2.11: **a** Continuum emission map of the Sgr B2(N) region obtained with the SMA at 343 GHz (Qin et al. 2011). The synthesized beam ($0.4'' \times 0.24''$, PA = 14.4°) is shown as a green ellipse in the bottom left corner. The contour levels, shown as purple lines, are (1, 3, 7, 10, 13, 16, and 18)$\times 3\sigma$ with σ = 31 mJy beam^{-1}. **b** Same as **a** but smoothed to the ALMA resolution of the EMoCA survey ($1.7'' \times 1.2''$, PA = 83.4°). The contour levels start at 16σ and double up to 256σ, with σ = 42 mJy beam^{-1}. In both panels the continuum maps are corrected for the primary beam attenuation.

2.4 SMA continuum data

Qin et al. (2011) observed Sgr B2(N) using the SMA in its compact and very extended configurations, providing the high-angular-resolution continuum map used in this work (see Fig. 2.11**a**). The continuum map was obtained at 342.883 GHz, with a synthesized beam of $0.4'' \times 0.24''$ (PA = 14.4°). The map has been corrected for the primary beam attenuation and the 1σ rms noise level is 31 mJy beam^{-1} at the phase center.

2.4.1 Smoothing to the ALMA resolution

The SMA continuum map obtained at 342.883 GHz is be used in Sect. 4.2.3 to derive the dust properties in Sgr B2(N), in a joint analysis with our ALMA data. To this aim we first need to smooth the SMA map from its original resolution ($\sim 0.3''$ resolution, Fig. 2.11**a**) to the resolution of our ALMA data ($\sim 1.6''$, Table. 2.2). We convolve the SMA original map with a Gaussian kernel, depending on the required final angular resolution, using the task GAUSS SMOOTH of the GILDAS software. Figure 2.11**b** shows for instance the SMA map smoothed to $1.65'' \times 1.21''$ resolution.

Chapter 3

Star formation and chemical complexity in Sgr B2(N)

Contents

The high sensitivity of the EMoCA imaging spectral line survey allows us to extend our view of the distribution of active star-forming regions in the Sgr B2(N) molecular cloud, by searching for new star-forming cores. In this chapter I present the results of the analysis of the EMoCA data, focusing especially on the COMs detected toward three new HMCs discovered in Sgr B2(N).

This chapter is largely based on Bonfand et al. (2017) and Bonfand et al. (2019). Other references are mentioned explicitly in the text.

3.1 Spectral line density toward Sgr B2(N)

We take advantage of the high sensitivity of the EMoCA data to search for fainter sources in the vicinity of the two already known hot molecular cores N1 and N2. To this aim we count the number of channels with continuum-subtracted flux density above the 7σ threshold (1σ ~3 mJy/beam) over the whole frequency range of the EMoCA survey and for each pixel in the field of view. We exclude setup 3 which has the lowest angular resolution (HPBW $> 2''$, see Table 2.2). The channels located in frequency ranges overlapped by adjacent spectral windows were counted only once. The analyzed ranges thus cover 23.1 GHz with 47296 channels. The result of this channel count is shown in Fig. 3.1 as a spectral line density map of the Sgr B2(N) region. The contours represent the number of channels with flux density above the 7σ threshold, thus higher contours reflect the presence of more emission lines.

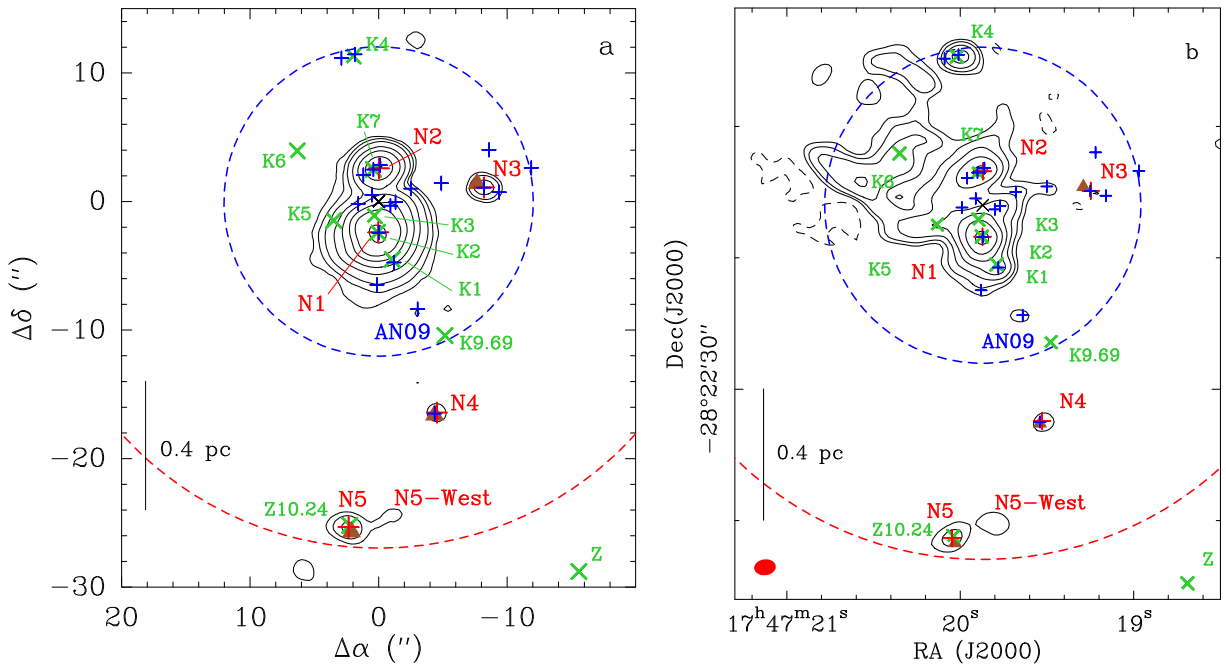

Figure 3.1: **a** Contour map of the number of channels with continuum-subtracted flux density above the 7σ level (1σ ∼3 mJy/beam). The contour levels are: 500, 1000, 2000, 5000, 10000, 20000, 30000, and 40000. The offsets are defined with respect to the phase center (see Sect. 2.3). **b** Continuum map of the Sgr B2(N) region obtained with ALMA at 108 GHz. Contour levels (positive in black solid line and negative in dashed line) start at five times the rms noise level, σ, of 3.0 mJy/beam and double in value up to 320σ. The red filled ellipse shows the synthesized beam ($1.65'' \times 1.21''$, PA=-83.4°). The map is not corrected for the primary beam attenuation. In both panels the red crosses mark peaks of spectral line density. The brown triangles represent the 6.7 GHz Class II methanol masers (Caswell 1996). The green crosses represent (UC)HII regions (Gaume et al. 1995; De Pree et al. 2015). The blue crosses represent the continuum sources identified by Sánchez-Monge et al. (2017) based on 1 mm ALMA data. The dotted red and blue circles represent the size (HPBW) of the primary beam of the 12 m antennas at 108 GHz and 242 GHz, respectively. The black cross represents the phase center. *Figure adapted from Bonfand et al. (2017).*

3.1.1 Detection of three new hot molecular cores

Figure 3.1 shows the peak positions of the known (UC)HII regions (Gaume et al. 1995; De Pree et al. 2015) and Class II methanol masers (Caswell 1996) in Sgr B2(N) as green crosses and brown triangles, respectively. The two main HMCs, N1 and N2, clearly appear as regions of high spectral line density, apparently associated with the UCHII regions K2 and K7, respectively. The map also reveals fainter peaks of spectral line density toward several other positions, of which three are associated with the three known Class II methanol masers, unveiling the presence of three new HMCs that we call N3, N4, and N5 (Bonfand et al. 2017). N5 is also associated with the UCHII region Z10.24.

We fit 2D Gaussians to the channel count map with the GILDAS procedure GAUSS-2D in order to derive the peak position of spectral line density toward the five HMCs, N1–N5. The results of the fits are listed in Table 3.1 and the position of the spectral line density

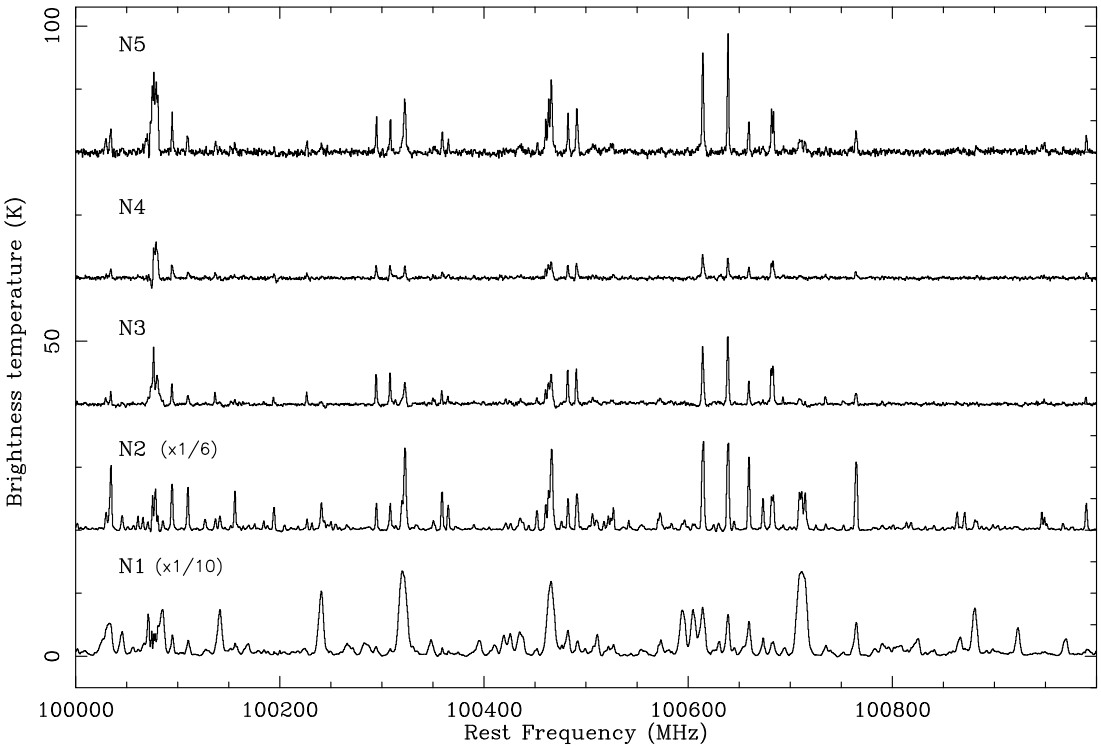

Figure 3.2: Part of the continuum-subtracted spectra observed with ALMA at 3 mm toward the five HMCs embedded in Sgr B2(N). The spectra have been corrected for the primary beam attenuation, and shifted along the y axis for display purposes. The spectra of N1 and N2 have been divided by 10 and 6, respectively, for display purposes. The frequency axis corresponds to the systemic velocities derived in Sect. 4.1.1. *Figure taken from Bonfand et al. (2017).*

peaks of each source is marked with a red cross in Fig. 3.1. These positions are adopted as reference positions of the HMCs, N1-N5. Table 3.1 also gives the distance of each HMC to the nearest UCHII region and/or the nearest Class II methanol maser. We note that there is a significant offset of 0.43″ (∼3600 au) between the position of peak line density of the HMC N2 and the position of the UCHII region K7 (see also Fig. 3.1). This offset between the two objects is confirmed by higher angular resolution observations (Sánchez-Monge et al. 2017, see also Sect. 8.1), suggesting that N2 and K7 are two distinct sources. A similar situation occurs for instance in the star-forming region W51e2, located at a distance of 5.4 kpc from the Sun. This source contains two objects separated by 0.8″, the HCHII region W51e2-W and the HMC W51e2-E (Shi et al. 2010; Ginsburg 2017). At the distance of Sgr B2(N), these two objects would have a separation of 0.5″, similar to the offset seen between K7 and N2.

A part of the continuum-subtracted spectra extracted toward the peak positions of the five HMCs, N1–N5, is shown in Fig. 3.2. It clearly shows that the spectral line density is much lower toward the new HMCs, N3–N5, than toward N1 and N2, considerably reducing the occurrence of line blending. Column 5 of Table 3.1 gives a rough estimate of the spectral line density per GHz obtained by dividing the number of channels with continuum-subtracted flux densities above 7σ derived toward each HMC by the number of channels across the typical FWHM of an emission line (see Sect. 3.2.1).

Table 3.1: Position and spectral line density of the five HMCs embedded in Sgr B2(N), along with the distance to nearest UCHII region and/or Class II methanol maser.

Source	$\Delta\alpha$; $\Delta\delta^a$ ($''$)	α_{J2000} ; $\delta_{J2000}{}^b$ 17^h47^m ; $-28^o22'$	$N_{channels}{}^c$	$n_l{}^d$ (GHz^{-1})	$d_{l-maser}{}^e$ ($''$)	$d_{l-UCHII}{}^e$ ($''$)	$FWHM_{UCHII}{}^f$ ($''$)
N1	+0.02(0.01) ; -2.40(0.01)	19.872(0.002)^s ; 18.40(0.01)$''$	40710	438	_	0.06(0.01)	0.12
N2	-0.02(0.01) ; +2.58(0.01)	19.868(0.001)^s ; 13.42(0.01)$''$	30546	460	_	0.42(0.01)	0.08
N3	-8.21(0.07) ; +1.09(0.06)	19.248(0.005)^s ; 14.91(0.06)$''$	3008	45	0.63(0.41)	_	_
N4	-4.52(0.11) ; -16.41(0.05)	19.528(0.008)^s ; 32.41(0.05)$''$	932	14	0.25(0.41)	_	_
N5	+2.34(0.01) ; -25.34(0.01)	20.047(0.007)^s ; 41.34(0.01)$''$	2369	35	0.43(0.40)	0.19(0.01)	<0.25

Notes. $^{(a)}$ Equatorial offsets of the spectral line density peak with respect to the phase center (see Sect. 2.3). The uncertainties in parentheses come from the 2D-Gaussian fit to the channel-count map. They are only statistical. $^{(b)}$ Same position given in J2000 Equatorial coordinates. $^{(c)}$ Number of channels with continuum-subtracted flux densities above 7σ. $^{(d)}$ Estimation of the spectral line density above 7σ (excluding setup 3) assuming mean linewidths of $\sim$7 km s^{-1} for Sgr B2(N1) and $\sim$5 km s^{-1} for the others HMCs (see Sect. 4.1.1 and Belloche et al. 2016). $^{(e)}$ Distance between the HMC and the closest Class II methanol maser or UCHII region. The uncertainties given in parentheses are calculated based on the errors given by the Gaussian fits. In the case of the methanol masers, they also take into account the uncertainty on the maser positions ($0.4''$) given by Caswell (1996). $^{(f)}$ Deconvolved angular size of the UCHII region (De Pree et al. 2015; Gaume et al. 1995).

3.1.2 Other positions

Recently, Sánchez-Monge et al. (2017) reported the detection of 20 continuum sources in Sgr B2(N) based on ALMA observations obtained at 1.3 mm (211–275 GHz) with a mean synthesized beam size (HPBW) that varies from $0.39''$ to $0.65''$ and a rms noise level in the range 10 to 20 mJy beam^{-1}. These sources are marked as blue crosses in Fig. 3.1a. Sánchez-Monge et al. (2017) investigated the nature of the continuum emission toward the 20 detected sources by fitting their fluxes over the whole frequency range of their ALMA observations to derive spectral indices. They found that the brightest sources show positive spectral indices, suggesting that they trace dust thermal emission, while fainter sources may have a free-free origin, tracing ionized gas from HII regions still bright at 1.3 mm. Figure 3.1 shows that two sources identified by Sánchez-Monge et al. (2017) are associated to the UCHII region K4 to the North of N2, which does not show high spectral line density (Fig. 3.1a) and thus does not harbor a HMC. Sánchez-Monge et al. (2017) identified three distinct sources toward N2 which could not be separated with the angular resolution of our 3 mm survey. One of these sources corresponds to N2, and another to the UCHII region K7. Sánchez-Monge et al. (2017) have also detected a continuum source toward N3, plus three more sources around it, which are not seen in our continuum data (Fig. 3.1b). Figure 3.1b shows extended emission North-West of N1 where several sources identified by Sánchez-Monge et al. (2017) lie along an elongated filamentary structure pointing toward the center of N1. South-West of N1, Sánchez-Monge et al. (2017) detected a continuum source, that they called AN09, that corresponds to a region of moderately high spectral line density in Fig. 3.1a, as well as continuum emission in Fig. 3.1b. It may be another faint hot core/corino. Figure 3.1b shows extended continuum emission to the West of N5, matching a position of high spectral line density in Fig. 3.1a and thus may unveil the presence of another HMC, hereafter N5-West. This position is outside the field of view of the 1.3 mm ALMA data of Sánchez-Monge et al. (2017), but emission toward this position is detected also in the new ReMoCa survey (see Sect. 8.1, and Belloche et al. 2019). Figure 3.3 shows a part of the continuum-subtracted spectrum extracted toward N5-West, overlaid in red

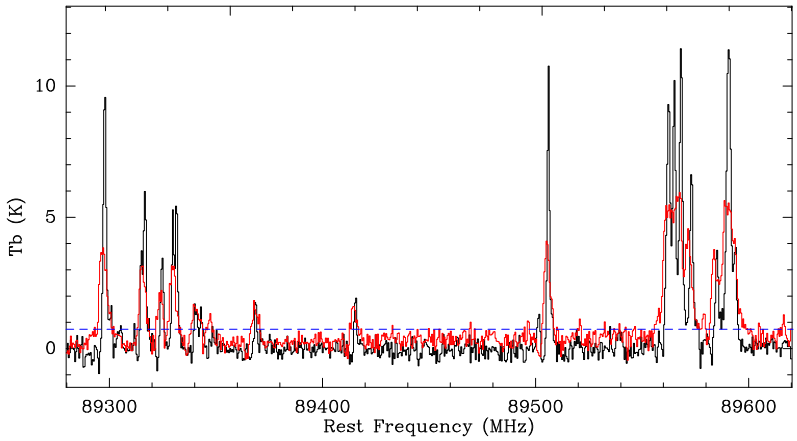

Figure 3.3: Part of the continuum-subtracted spectrum observed with ALMA at 3 mm toward N5-West (red), overlaid on top of the spectrum observed toward N5 (black). The spectra are corrected for the primary beam attenuation. The frequency axis corresponds to the systemic velocity of N5 (Sect. 4.1.1). The blue dotted line shows the 3 σ noise level.

on the spectrum observed toward N5 for comparison.

Other positions in the spectral line density map, such as the region inside the contour located South-East of N5, the one to the North of the UCHII region K9.69, and the one to the West of K4 show very low spectral line density with emission lines only in setups 2 and 5 (four spectral windows) with line intensities lower than toward the identified HMCs but a line content that is very similar. We note that some features also appear to be inconsistent while comparing the frequency ranges overlapped by adjacent spectral windows, therefore we believe these structures are not real emission and must be deconvolution artifacts. This is confirmed by the ReMoCa data (A. Belloche, priv. comm.).

In the rest of the thesis we focus our analysis especially on the three new HMCs, N3–N5, leaving aside the other positions not associated with tracers of high-mass star formation as well as the main hot core N1 because the high spectral line density observed toward its peak position makes the analysis of its 3 mm spectrum more difficult. Our results are compared to that obtained from the analysis of the secondary hot core N2, based on the same ALMA dataset (Müller et al. 2016; Belloche et al. 2016, 2017).

3.2 Radiative transfer modeling of the observed spectra

We use *Weeds* as described in Sect. 2.3.3 to perform the line identification and model the spectra observed toward the three new HMCs, N3–N5, in order to derive their chemical composition and characterize emission size and spatial distribution of the identified species.

3.2.1 Spectral line identification

The total number of emission lines (excluding setup 3) detected above the 7σ level toward the peak position of the four HMCs, N2–N5, is counted manually and given in Table 3.2. The HMCs have spectral line densities of 208, 31, 11, and 22 lines per GHz above 7σ, respectively. The line density derived here is lower than reported previously in Table 3.1. This is because in

Table 3.2: Statistics of the lines detected toward the three new HMCs, N3–N5, compared to N2.

Source	$N_{\rm l}$ [a]	$n_{\rm l}$ [b] ($\rm GHz^{-1}$)	$N_{\rm species}$ [c]	$N_{\rm iso}$ [c]	$N_{\rm exc}$ [c]	U-lines [d] (%)
N2 [*]	4801	208	52	79	83	44
N3	714	31	23	20	16	9
N4	249	11	20	10	5	11
N5	508	22	23	13	7	7

Notes. [(a)] Total number of emission lines detected above the 7σ level (see rms noise level in Table 2.2) excluding setup 3. [(b)] Line density above 7σ, excluding setup 3. [(c)] Number of identified molecules ($N_{\rm species}$), less abundant isotopologs ($N_{\rm iso}$), and vibrationally excited states ($N_{\rm exc}$). [(d)] Fraction of remaining unidentified lines above 7σ (Sect. 3.2.2). [(*)] A. Belloche, priv. comm.

Table 3.1 we made a rough estimate using the number of channels derived from Fig. 3.1, divided by the number of channels across the typical FWHM of an emission line. The typical linewidth (FWHM) of the emission lines observed toward each HMC is derived by fitting Gaussians to their observed spectra. From the Gaussian fits we derive median linewidths of approximately 5.0 km $\rm s^{-1}$ for the three new HMCs, ranging from 3.6 to 7.7 km $\rm s^{-1}$ for N3, from 3.5 to 7.0 km $\rm s^{-1}$ for N4, and from 3.5 to 7.5 km $\rm s^{-1}$ for N5 (see Table A.1). These values are similar to that derived by Belloche et al. (2016) for N2, ranging from 4.7 to 6.5 km $\rm s^{-1}$. When we use these values to estimate the total number of observed emission lines it does not give us an accurate estimate as a faint emission line may actually have only a single channel emitting above the 7σ threshold while a strong line will have more channels above the threshold than the number of channels covered by its FWHM.

Using *Weeds* as described in Sect. 2.3.3 we have identified so far about 90% of the emission lines detected above 7σ, that have been assigned to 23 and 20 main species toward N3/N5, and N4, respectively. This is much less than the 52 species identified so far toward N2 based on the same ALMA data (Belloche, priv. comm.). Among the new HMCs (N3–N5), N3 has the highest spectral line density although the same number of species has been identified toward N5, but fewer isotopologs and vibrationally excited states of these molecules are detected toward N5 than toward N3. The spectrum observed toward N4 shows a low spectral line density compared to the other HMCs and less species have been identified toward this source. The list of all species identified so far toward the three new HMCs, N3–N5 is given in Table 3.3. The full tables listing all-best fit parameters ($N_{\rm tot}$, $T_{\rm rot}$, θ_s, $v_{\rm off}$, and Δv) for each species identified toward the three HMCs, N3–N5, can be found in Table A.1. The full synthetic spectra derived for N3–N5 are show in Fig. A.1 overlaid on the observed spectra. In our modeling procedure, we try not to overestimate the observed peak flux density of any spectral line which may lead to a synthetic spectrum underestimating some emission lines. In general the LTE is a good approximation and the synthetic spectra reproduce relatively well the observed ones for the three HMCs, N3–N5. Strong disagreement between the synthetic and observed spectra can be seen for lines at frequencies contaminated by absorption, or in the case of methanol maser lines. For instance the 84521.169 MHz Class I methanol maser transition is detected with a peak intensity of ∼17 K toward N4, a factor ∼5 higher that the intensity predicted by the LTE model for this transition. In the spectrum observed toward N3, the Class II methanol maser lines at 107013.803 MHz and 108893.963 MHz are very narrow with a width of ∼1.4 km $\rm s^{-1}$ and

Table 3.3: List of species identified toward Sgr B2(N3–N5).

Species		N3	N4	N5
Ethyl cyanide	**C_2H_5CN** *	x	x	x
Vinyl cyanide	**C_2H_3CN** *	x	x	x
Methyl cyanide	**CH_3CN** *	x	x	x
Methanol	**CH_3OH** *	x	x	x
Ethanol	**C_2H_5OH** *	x	x	x
Methyl formate	**CH_3OCHO** *	x	x	x
Dimethyl ether	**CH_3OCH_3** *	x	x	x
Acetone	**CH_3COCH_3**	x	x	x
Acetaldehyde	**CH_3CHO** *	x	x	x
Formaldehyde	H_2CO	x	x	x
Ketene	H_2CCO	x	x	x
Formamide	**NH_2CHO** *	x		x
Methyl isocyanate	**CH_3NCO** *	x	x	x
Isocyanic acid	HNCO	x	x	x
Cyanoacetylene	HC_3N	x	x	x
Methylenimine	CH_2NH	x	x	x
Propyne	**CH_3CCH**	x	x	x
Methyl mercaptan	**CH_3SH** *	x	x	x
Thioformaldehyde	H_2CS	x	x	x
Carbonyl sulfide	OCS	x	x	x
Sulfur dioxide	SO_2	x		x
Sulfur monoxide	SO	x	x	x
Deuterated ammonia	NH_2D	x		x

Notes. A cross means that molecular transitions of the species have been detected above the 3σ threshold in the spectra observed toward the source (N3, N4, or N5). COMs are highlighted in bold face. (*) COMs that are studied in detail in this thesis work (chemical abundances, formation pathways).

the spectral resolution of the EMoCA data does not allow us to separate the thermal component from the very narrow maser component.

3.2.2 Unidentified lines

Last column of Table 3.2 gives the fraction of remaining unidentified lines (U-lines) in the spectrum observed toward the peak position of Sgr B2(N2–N5). In the case of N2, a line is considered to be unidentified when more than ∼25% of its peak intensity is not reproduced by the LTE best-fit synthetic spectrum. This is a conservative estimate, but necessary to account for possible contamination from other species not included in the synthetic spectrum, as the spectrum observed toward N2 is close to the confusion limit (*i.e* high occurrence of line blending). For the fainter HMCs, N3–N5, we count as a U-line, lines for which at least ∼50% of the emission peak is not reproduced by our LTE best-fit spectra. A list of selected U-lines in the spectra observed toward N3–N5 is given in Table A.2 along with their peak brightness temperatures. Several of the U-lines listed for N3 in this table are below 7σ toward N4 and N5.

Some of the remaining U-lines in the spectra observed toward N3–N5 are thought to be high velocity wings of absorption lines (see for instance SO and CS transitions in Fig. 4.1). U-lines in the spectra observed toward N3, N4, and/or N5 but that have been identified toward N2 suggest that our best-fit LTE model for N3–N5 may still need to be optimized. Finally the rest of the U-lines are thought to belong to vibrationally excited states of already identified molecules but for which the spectroscopic predictions are still missing (Belloche et al. 2013). Still, the presence of new molecules in the ALMA spectra is not excluded.

3.3 Emission size and spatial distribution of the detected molecules

In order to get information about the spatial structure of the three new HMCs we investigate for each identified molecule the rotational transitions within the vibrational ground state that are well reproduced by the LTE synthetic spectra, are not severely contaminated by other species, and have a high signal-to-noise ratio (typically ≥ 8 up to $\sim$99). We fit 2D Gaussians to the integrated intensity maps of these transitions, using the GAUSS-2D task of the GILDAS software, and derive the size of the emitting region as well as its peak position. It is difficult to constrain the size of the three new HMCs because the emission is resolved only for a few spectral lines, mainly from COMs. A list of all transitions that show resolved emission is given in Table A.3 for each of the three HMCs, N3–N5, along with the results of the Gaussian fits to their integrated intensity maps which are also plotted in Figs 3.4, 3.5, and 3.6 for N3, N4, and N5, respectively. For each transition listed in Table A.3, the deconvolved major and minor diameters (FWHM) of the emission ($\theta_{\rm maj}$ and $\theta_{\rm min}$) are used to calculate the average deconvolved size of the emitting region ($\sqrt{\theta_{maj} \times \theta_{min}}$ (see Table A.3). For N3, only four transitions, of OCS and C_2H_5CN, show spatially resolved emission. The first row of Fig. 3.7 shows their integrated intensity maps. The result of the Gaussian fit is displayed in blue and the red ellipse shows the deconvolved emission size. The middle row of Fig. 3.7 shows the maps of four transitions for which the emission of Sgr B2(N4) is resolved. In total for this source, 12 transitions from seven distinct species show resolved emission with a higher signal-to-noise ratio ($\geq$8 up to $\sim$16, see Table A.3). Finally, the bottom row of Fig. 3.7 shows four maps produced for N5. In total for this HMC, 22 transitions from six distinct species show resolved emission with a signal-to-noise ratio from $\sim$10 to 99 (see Table A.3).

Because only few transitions show resolved emission toward the three new HMCs, we decided to adopt for each source a single source size as the mean deconvolved size derived from the results of the 2D-Gaussian fits (see Table A.3). We obtain source diameters (FWHM) of 1.0$\pm$0.3″ for N4, and 1.0$\pm$0.4″ for N5, which is slightly smaller than the size of N2 ($\sim$1.2″, with values ranging between 0.8″ and 1.5″; Belloche et al. 2016, 2017). The emission toward N3 is more compact, with a molecular emission size of 0.4$\pm$0.1″. These source sizes are used in *Weeds* to produce the LTE synthetic spectra containing all identified molecules (see Sect. 3.2.1, Table A.1).

For each spectral line that is well reproduced by the LTE synthetic spectra, is not severely contaminated by other species, and has a high signal-to-noise ratio, the 2D Gaussian fitted to its integrated intensity map also gives us the information on its emission peak position. Figure 3.8 shows the spatial distribution of all the species identified so far toward the three new HMC N3–N5 where each cross represents the mean peak position of a given species, also listed in Table A.4. It shows that, within the uncertainties, the emission peak of most species is consistent with the reference position of the HMCs.

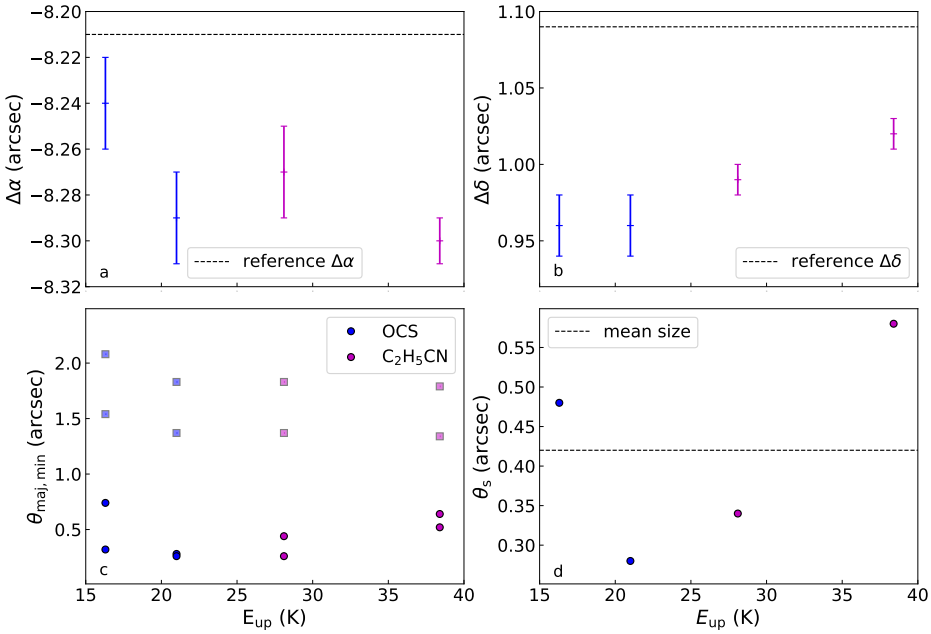

Figure 3.4: Results of the 2D-Gaussian fits to the integrated intensity maps showing resolved emission toward N3. **a, b** Fitted position. The error bars are the uncertainties given by the Gaussian fits. **c, d** Fitted size. The dots represent the deconvolved major and minor diameters (FWHM) of the emission (**c**) and the resulting average source size (**d**). The squares represent the major and minor axes of the synthesized beam (**c**). The dashed lines represent the reference position of the HMC (**a, b**), and the mean deconvolved angular size (**d**). *Figure taken from Bonfand et al. (2017).*

Table 3.4: Rms noise levels and contour levels used in Fig. 3.7.

Source	Transition	σ^a	Levels^b
N3	OCS(7-6)	49.8	4, 8, 16, 22
	OCS(8-7)	50.8	
	$C_2H_5CN(10_{0,11}\text{-}10_{0,10})$	37.2	
	$C_2H_5CN(11_{2,8}\text{-}11_{3,7})$	37.5	
N4	$CH_3OH(13_2\text{-}12_3)$	23.5	4, 6, 8, 10, 12
	$CH_3CN(6_3\text{-}5_3)$	30.2	
	$H_2CCO(5_{1,5}\text{-}4_{1,4})$	17.1	
	$CH_3CCH(6_2\text{-}5_2)$	20.8	
N5	$C_2H_5CN(11_{2,8}\text{-}11_{3,7})$	36.0	4, 8, 16, 32, 64
	$CH_3CN(6_3\text{-}5_3)$	47.4	
	OCS(9-8)	20.0	
	$CH_3OH(6_2\text{-}7_1)$	28.0	

Notes. $^{(a)}$ Rms noise level measured in the integrated intensity map in mJy beam^{-1} km s^{-1}. $^{(b)}$ Contour levels in unit of σ.

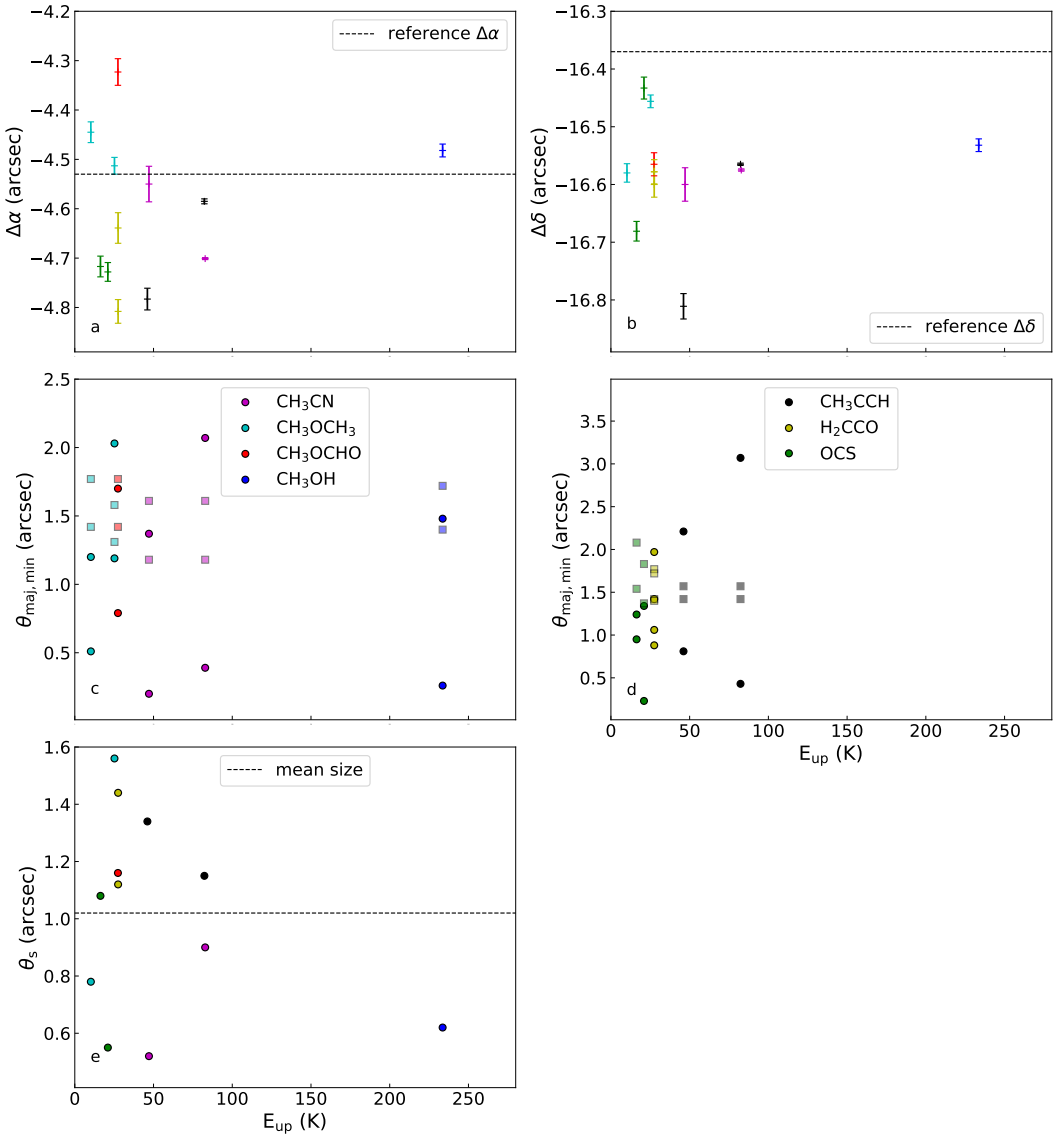

Figure 3.5: Results of the 2D-Gaussian fits to the integrated intensity maps showing resolved emission toward N4. **a, b** Fitted position. The error bars are the uncertainties given by the Gaussian fits. **c, d, e** Fitted size. The dots represent the deconvolved major and minor diameters (FWHM) of the emission (**c, d**) and the resulting average source size (**e**). The squares represent the major and minor axes of the synthesized beam (**c, d**). The dashed lines represent the reference position of the HMC (**a, b**), and the mean deconvolved angular size (**e**). *Figure taken from Bonfand et al. (2017).*

Only three molecules detected toward N3 show significant offsets between their emission peaks and the reference position of the HMC. The SO emission detected toward N3 peaks on average ∼0.5″ South-West of the HMC (see Fig. 3.9d). Figures 3.9a and b present the integrated intensity maps of vibrational ground state transitions of CH_3CCH and HC_3N, respectively. Both maps show the same extended emission shape as SO, with the peak positions shifted beyond 0.5″ from the HMC reference position. These NE-SW elongated emission features coincide spatially

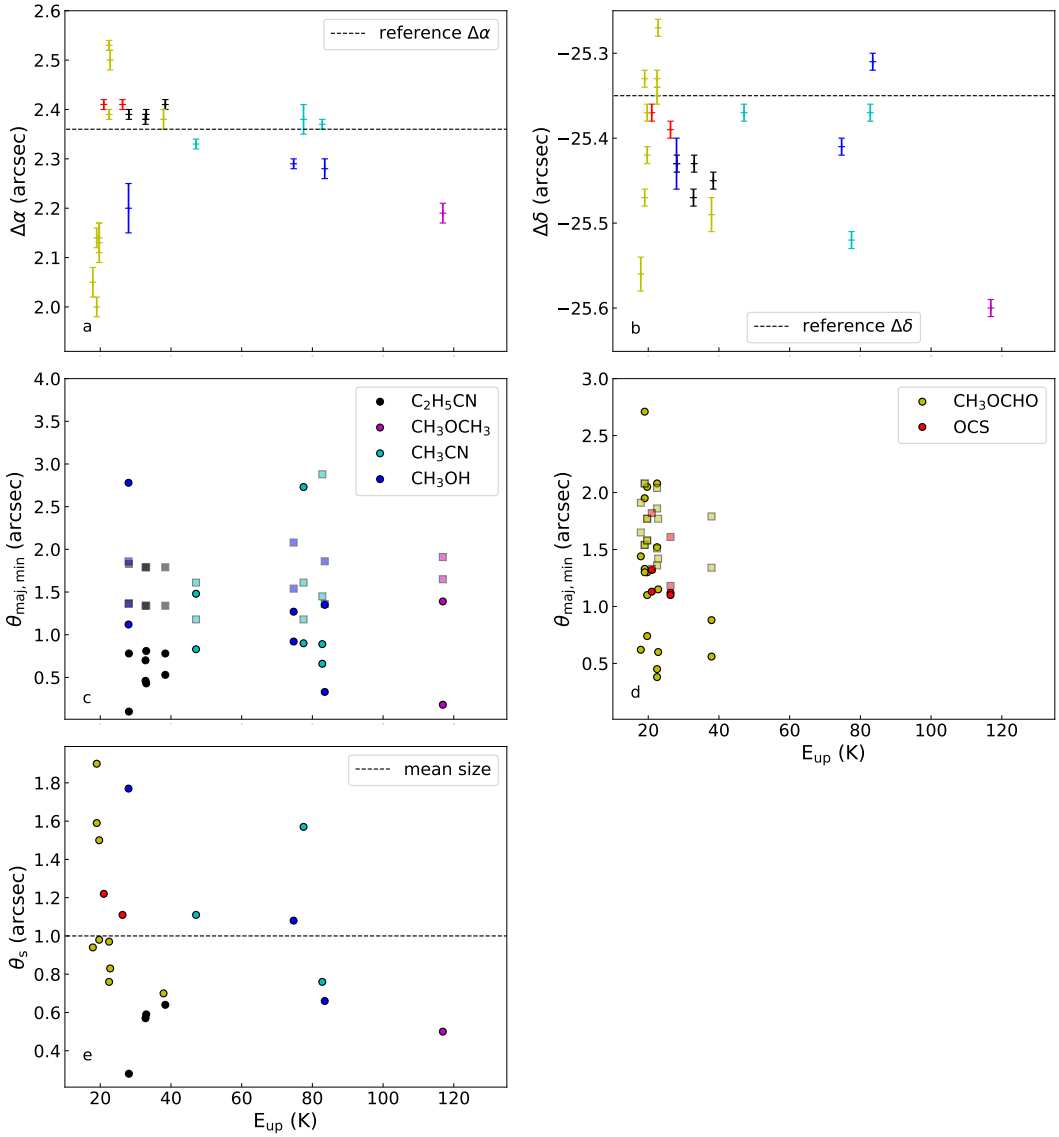

Figure 3.6: Same as in Fig. 3.5 but for N5. *Figure taken from Bonfand et al. (2017).*

with the axis of the molecular outflow detected in N3 (see Sect. 4.1.2). The molecules could thus be present in the outflow. The vibrationally excited transitions of HC_3N show a more compact morphology (see Fig. 3.9b), tracing the regions closer to the protostar, with a peak position that is consistent with the reference position of N3. The v_7=1 transitions of HC_3N thus trace the HMC better than the $v = 0$ transitions. Similar results have recently been obtained toward the high-mass star-forming region G328.2551–0.5321 by Csengeri et al. (2018), who suggested that the vibrationally excited $HC_3N v_7$=1 transitions are good candidates for tracing emission from compact accretion discs around high-mass protostars. All other species detected toward N3 peak within a distance of ∼0.3″ from the reference position of the HMC. In the case of N4 (Fig. 3.8b) and N5 (Fig. 3.8c), all molecules peak within distances of approximately 0.6″ and 0.4″ from the HMC position, respectively. For both N4 and N5, HC_3N in its vibrational ground state shows broad lines contaminated by other species therefore we used transitions in its first

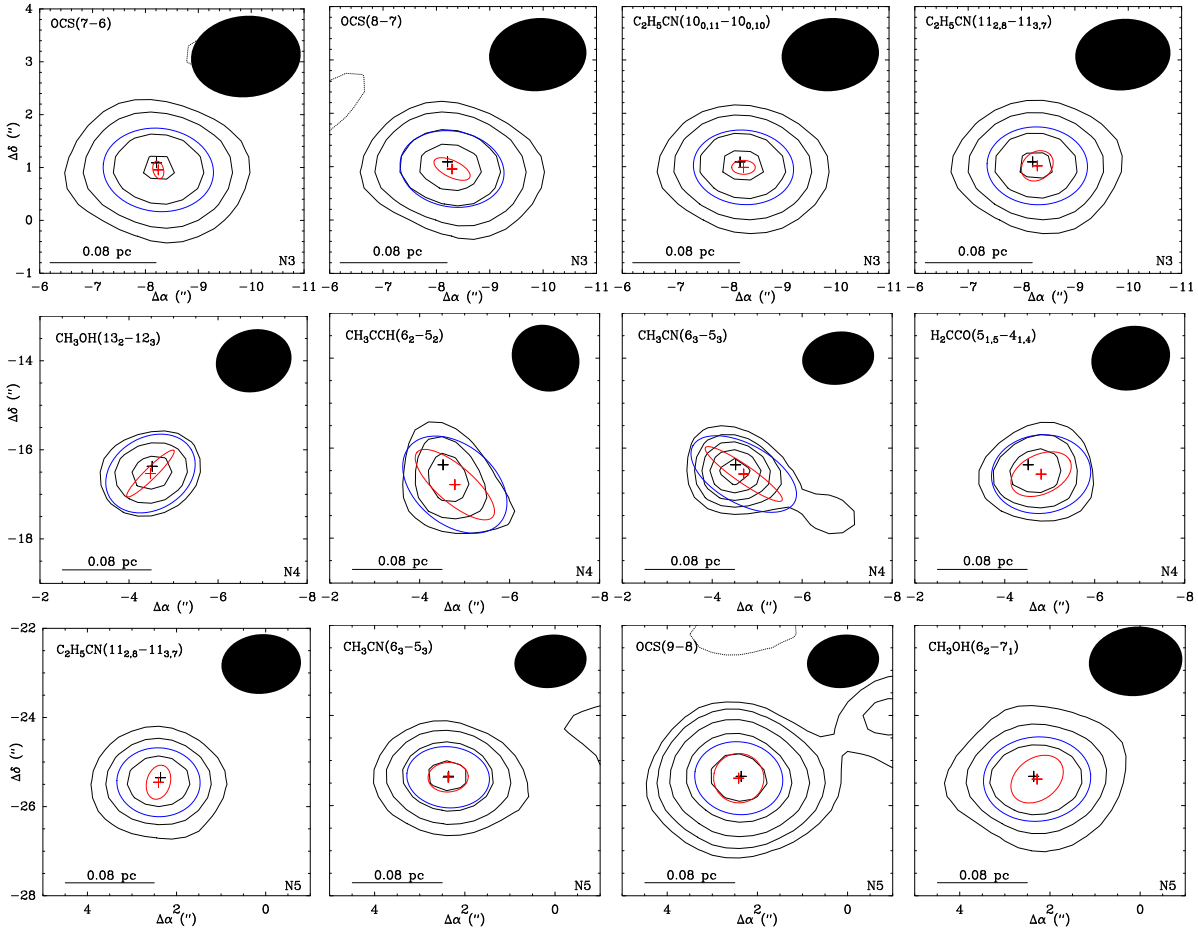

Figure 3.7: Integrated intensity maps of selected transitions toward N3 (top row), N4 (middle row), and N5 (bottom row). For each map, the red cross shows the peak position of the emission and the black cross is the reference position of the HMC. The blue ellipse represents the result of the Gaussian fit (FWHM) to the map while the red ellipse is the deconvolved emission size (FWHM). The black filled ellipse represents the synthesized beam. The rms and contour levels used in each panel are indicated in Table 3.4. *Figure taken from Bonfand et al. (2017).*

vibrationally excited state, $v_7 = 1$.

3.4 Rotational temperature

In order to derive rotational temperatures for the species identified toward the three new HMCs, N3–N5, population diagrams are plotted as described in Sect. 2.2.5, based on the molecular transitions that are well reproduced by the LTE synthetic spectra and not severely contaminated by lines from other species. We present here the results obtained for CH_3OCHO and C_2H_5OH which have many well detected lines spread over a large energy range. To derive the rotational temperature of CH_3OCHO, we use both its ground and first vibrationally excited states, modeled with the same parameters ($N_{\rm mol}$, $T_{\rm rot}$, source size, $v_{\rm off}$, Δv). Only the ground state transitions are used for ethanol. Figure 3.10 shows the resulting population diagrams plotted using Eq. 2.50. We applied to both the observed and synthetic populations the opacity correction factor (see Sect. 2.2.5) using the opacities of our LTE radiative transfer model (see

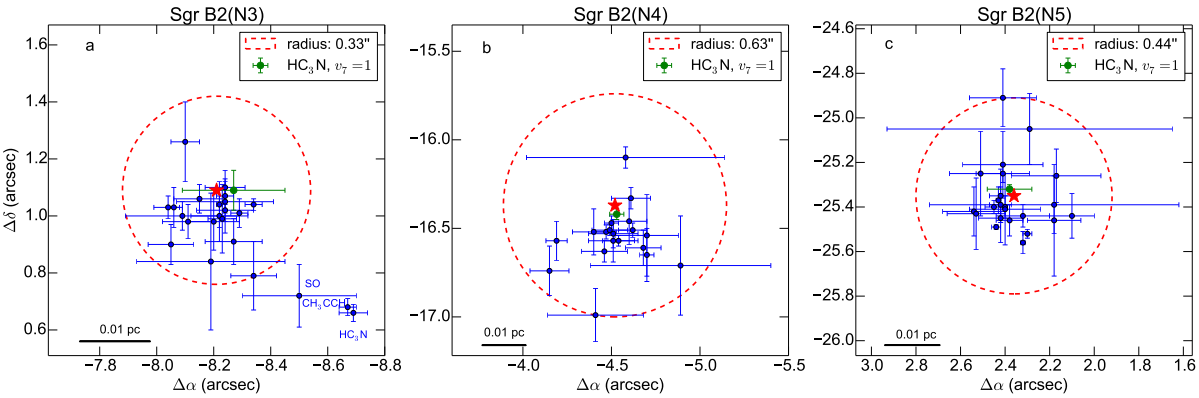

Figure 3.8: Spatial distribution of the molecules identified toward N3, N4, and N5. In each panel, the red star represents the position of the HMC derived from Fig. 3.1. Blue crosses represent the mean peak position of each species. Error bars correspond to the standard deviation weighted by the uncertainties given by the GAUSS-2D routine. The radius of the dashed circle is given in the top right corner. The average peak position of HC_3N, $v_7 = 1$ is shown in green. *Figure adapted from Bonfand et al. (2017).*

values of τ_{max} in Table 3.5). Since a transition can be partially contaminated by other species, we also subtracted from the measured integrated intensities the contribution of contaminating molecules using our LTE synthetic spectra that include all species identified so far. The synthetic and observed points are closer to one another after this correction, however the synthetic data points are globally below the observed ones. This can be explained by our modeling procedure in which we try not to overestimate the observed peak flux density of any spectral line. The modeled spectrum can then well reproduce the observed spectrum in terms of peak flux density, but it will not necessarily exactly fit the whole line profile because we use a single linewidth to model all detected lines. In addition, even after removing the contamination from other species, the measured integrated intensities can still be affected by residual contamination from U-lines.

The synthetic data points are not affected by contamination from other species and should be strictly aligned. The residual dispersion of the synthetic data points seen in the population diagrams can be explained by the frequency boundaries set to integrate the intensity which are a compromise between covering the line as much as possible and limiting the contamination from other species emitting at nearby frequencies in the observed spectrum.

After correction for the opacity and contamination from other species, the observed data points are roughly aligned and can be fitted by a single straight line, meaning one single temperature component. The blue line in Fig. 3.10 shows the weighted linear fit to the observed data points. From Eq. 2.50 we derive the excitation temperatures for C_2H_5OH and CH_3OCHO toward N3–N5 (see Table 3.5). We proceed in the same way for all species identified so far toward the three HMCs. For all detected molecules not showing numerous emission lines spread over a broad energy range in the HMCs' spectra, we set the temperature to 145 K in our LTE model, which allows in most cases to reproduce well the observed spectra of the three new HMCs.

We assume that the derived excitation temperatures are equal to the kinetic temperature of the gas. Table A.1 shows that the gas kinetic temperatures derived toward N3–N5 vary from

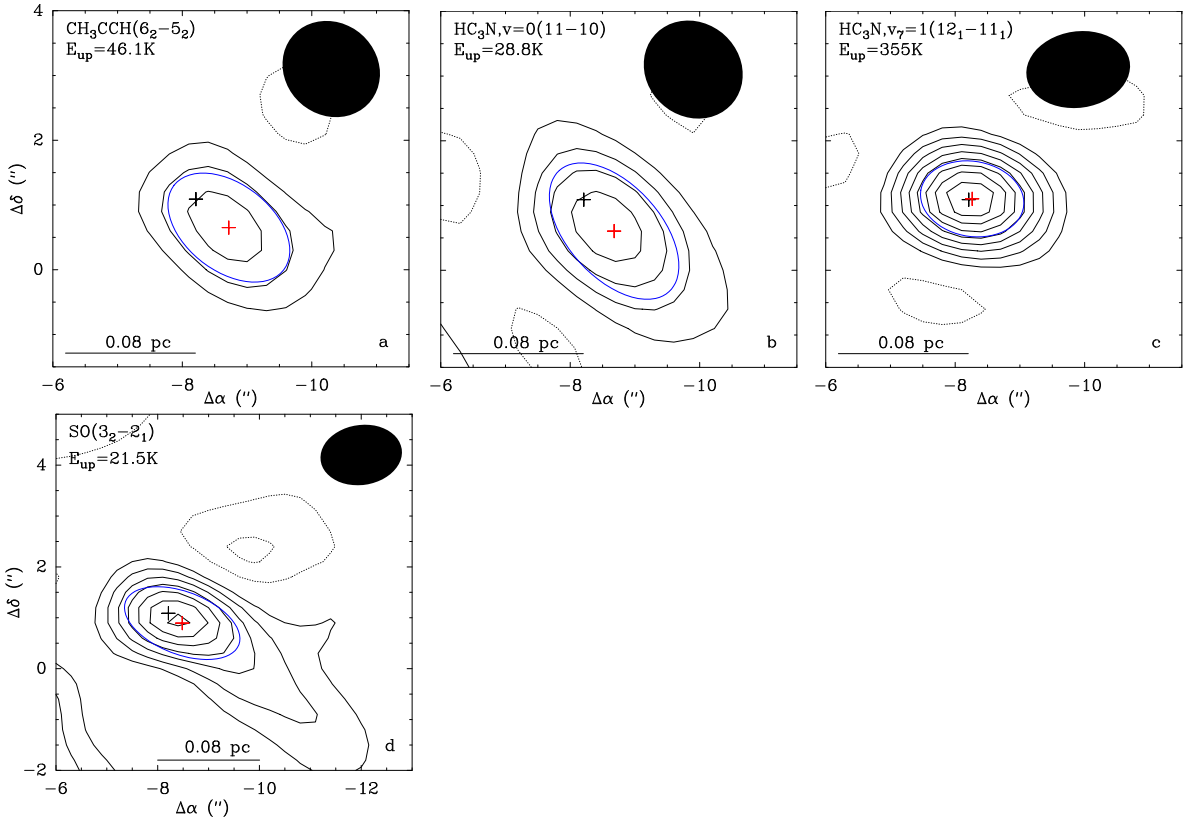

Figure 3.9: Integrated intensity maps of selected transitions detected toward N3. The contour levels start at 3σ (rms $\sim$3 mJy beam^{-1}) and increase with a step of 3σ. In each map the blue ellipse shows the result of the 2D-Gaussian fit (FWHM). The black cross represents the position of the HMC derived from Fig. 3.1 and the red cross marks the peak position derived from the fit. The black filled ellipse represents the synthesized beam. The upper level energy of each transition is indicated in temperature unit in each panel. *Figure taken from Bonfand et al. (2017).*

$\sim$145 K to 190 K, which is comparable to the temperatures derived for N2. Hereafter we use the average temperature T_0 = 150 K as the observational constraint to characterize the gas kinetic temperature at the radius r_0 corresponding to the COM emission region (see Sect. 3.3).

3.5 Chemical composition of the new hot molecular cores

In Sect. 3.2.1 we gave the list of all species identified so far in the 3 mm emission spectra observed toward the three new HMCs, N3–N5. In this section we focus on the 11 COMs highlighted in Table 3.3, which include N-,O-, and S-bearing species, in order to provide a broad census of the chemical composition of the sources. Figure 3.11a compares the molecular column densities derived for each of these 11 COMs for the three new HMCs as well as N2 for comparison. In the case of methyl cyanide (CH_3CN), we investigate its isotopologs $^{13}CH_3CN$ and $CH_3^{13}CN$ because the vibrational ground state transitions of CH_3CN are optically thick. We assume the isotopic ratio $[CH_3CN]/[^{13}CH_3CN] = [CH_3CN]/[CH_3^{13}CN] = 21$ derived by Belloche et al. (2016) to obtain the column density of CH_3CN.

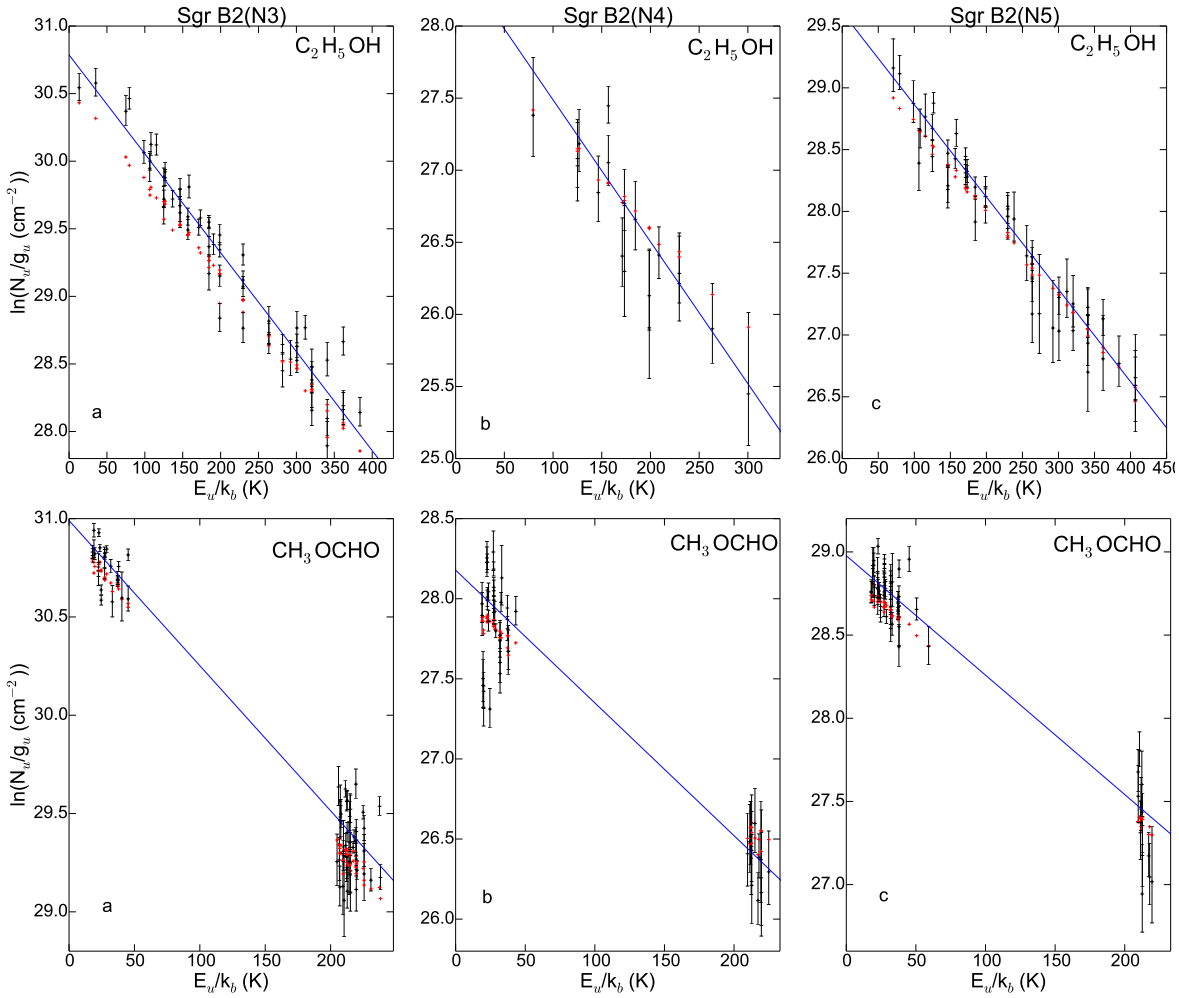

Figure 3.10: Population diagrams of C_2H_5OH (top row) and CH_3OCHO (bottom row) for **a** N3, **b** N4, **c** N5. The black points are computed using the integrated intensities of the observed spectrum while the red points are computed using the integrated intensities of our synthetic model. The error bars on the observed data points are 1σ uncertainties on N_u/g_u. Both the observed and synthetic populations are corrected for the optical depth (see Eq. 2.50). The contamination from all other species included in the full LTE synthetic spectrum has been removed from the observed data points. The blue line is the weighted linear fit to the observed populations. *Figure adapted from Bonfand et al. (2017).*

The column densities plotted here have been estimated from the radiative transfer modeling of the observed spectra based on simple assumptions, such as a single excitation temperature to characterize all transitions from a given molecule under the LTE approximation, as well as a single source size. Because the HMC emission toward N3–N5 appears to be resolved in our data for only a few species (see Sect. 3.3), we made the assumption for each of these three sources that all molecules are emitted from the same region characterized by a single size. This may not be true if some molecules trace more extended regions (see Sect. 3.3). Therefore, while comparing the chemical composition of the HMCs, it is important to keep in mind that the column density derived for each molecule strongly depends on the adopted source size. For instance we have used a source size of $1.0''$ to fit the spectrum observed toward N5, although the

Table 3.5: Rotational temperatures derived from population diagrams.

Source	Species	States[a]	N_l[b]	τ_{max}[c]	T_{rot}[d] (K)
N3	C_2H_5OH	$v = 0$	57	0.24	140.9(4.6)
	CH_3OCHO	$v = 0$, $v_t = 1$	70	0.80	140.8(2.6)
N4	C_2H_5OH	$v = 0$	18	0.01	131.1(21.5)
	CH_3OCHO	$v = 0$, $v_t = 1$	47	0.04	134.6(10.5)
N5	C_2H_5OH	$v = 0$	50	0.07	138.1(5.6)
	CH_3OCHO	$v = 0$, $v_t = 1$	58	0.15	148.6(8.0)
N2	C_2H_5OH	$v = 0$	156*	0.87*	139.6(1.6)
	CH_3OCHO	$v = 0$, $v_t = 1$	106*	0.70*	142.4(4.4)

Notes. [(a)] Vibrational or torsional states taken into account to fit the population diagrams. [(b)] Number of lines plotted in the population diagram. [(c)] Maximum opacity. [(d)] Rotational temperature derived from the fit. The standard deviation is indicated in parentheses. Values for N2 are taken from Belloche et al. (2016) and Müller et al. (2016). [(*)] Belloche et al. priv. comm.

results of the 2D-Gaussian fit to the integrated intensity maps of C_2H_5CN transitions suggest a smaller mean emission size of $\sim$0.5″ for this molecule (see Table A.3). The column density of C_2H_5CN presented here for N5 might thus be underestimated. In order to estimate the uncertainties on the estimated molecular column densities, we varied for each species detected toward Sgr B2(N3–N5) the emission size and rotational temperature within the uncertainties given by the 2D Gaussian fits and population diagrams, respectively. Comparing the column densities derived with our best-fit models (Table A.1) with the models obtained while varying temperature and source size, we find that for all investigated species, the column densities vary at most by a factor four. In the case of N2 we simply assume uncertainties of 30% on the molecular column densities of all investigated species. The resulting uncertainties on the molecular column densities are plotted as errorbars on the histograms (Fig. 3.11).

Figure 3.11b shows chemical abundances (molecular column densities relative to H_2) for the same 11 COMs, computed using the H_2 column densities derived in Sect. 4.2.4 (see Table 4.6). Given the large uncertainties on the calculated H_2 column densities it may be more robust instead to compare the abundance ratios relative to a given species. In Fig. 3.11c we plot the abundances relative to methanol measured toward each HMC. It shows that the overall chemical composition of N3 is very similar to that of N5, with at most a factor two of difference between the abundances (relative to methanol) of all detected COMs. N4 shows higher abundances of O- and S-bearing species (relative to methanol) than N3 and N5, except for formamide, but lower abundances relative to H_2. The chemical composition of N2 differs significantly from that of the other HMCs. For instance, C_2H_5CN is about four times more abundant (with respect to methanol) in N2 than toward the other HMCs, in addition, the ratio $[C_2H_5CN]/[C_2H_3CN]$ is three times higher. The abundances (relative to methanol) of the O-bearing species CH_3OCHO and CH_3OCH_3 are significantly lower toward N2 compared to the other sources. Finally, NH_2CHO shows an astonishing ratio relative to methanol about 15 times higher toward N2 than toward N3–N5.

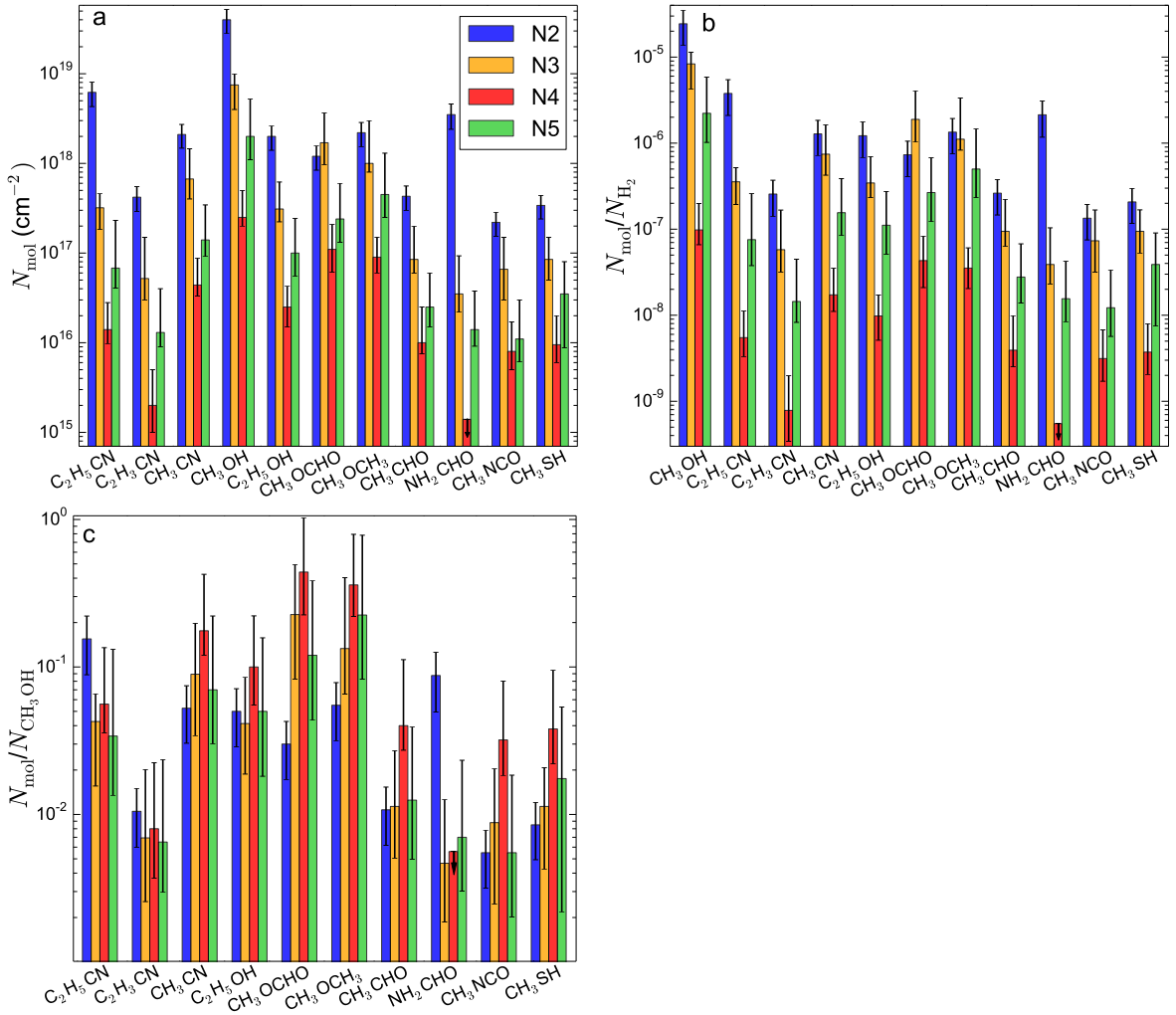

Figure 3.11: **a** Column densities of 11 COMs detected toward Sgr B2(N2–N5). The errorbars show uncertainties on the derived column densities. **b** Chemical abundances with respect to H_2. The errorbars are calculated from the uncertainties on the molecular column densities and the H_2 column densities (Table 4.6). **c** Abundances relative to methanol. The errorbars are calculated from the uncertainties on the molecular column densities. In all panels, the arrow indicates an upper limit. *Figure taken from Bonfand et al. (2019).*

3.6 Comparison with other hot molecular cores

In order to extend our view of the chemical complexity in typical regions forming high-mass stars, Fig. 3.12 compares the chemical content of N2–N5 to that of the Orion BN/KL (Becklin-Neugebauer/Kleinmann-Low) nebula, located in the Orion Molecular Cloud 1 (OMC 1) at a distance of 388 pc ± 5 pc from the Sun (Kounkel et al. 2017), as well as the larger-distance HMCs G35.20-0.74N (2.2 kpc Zhang et al. 2009), G35.03+0.35 (2.32 kpc Wu et al. 2014), and G29.96-0.02 (6 kpc Pratap et al. 1999). The figure shows some similarities between the 12 represented sources/positions. For instance, the abundance ratios [C_2H_5OH]/[CH_3OH], [CH_3OCHO]/[CH_3OH], and [CH3OCH3]/[CH_3OH] are relatively uniform for all sources, except for G35.03-0.35. On the other hand significant differences can be seen in the abundance

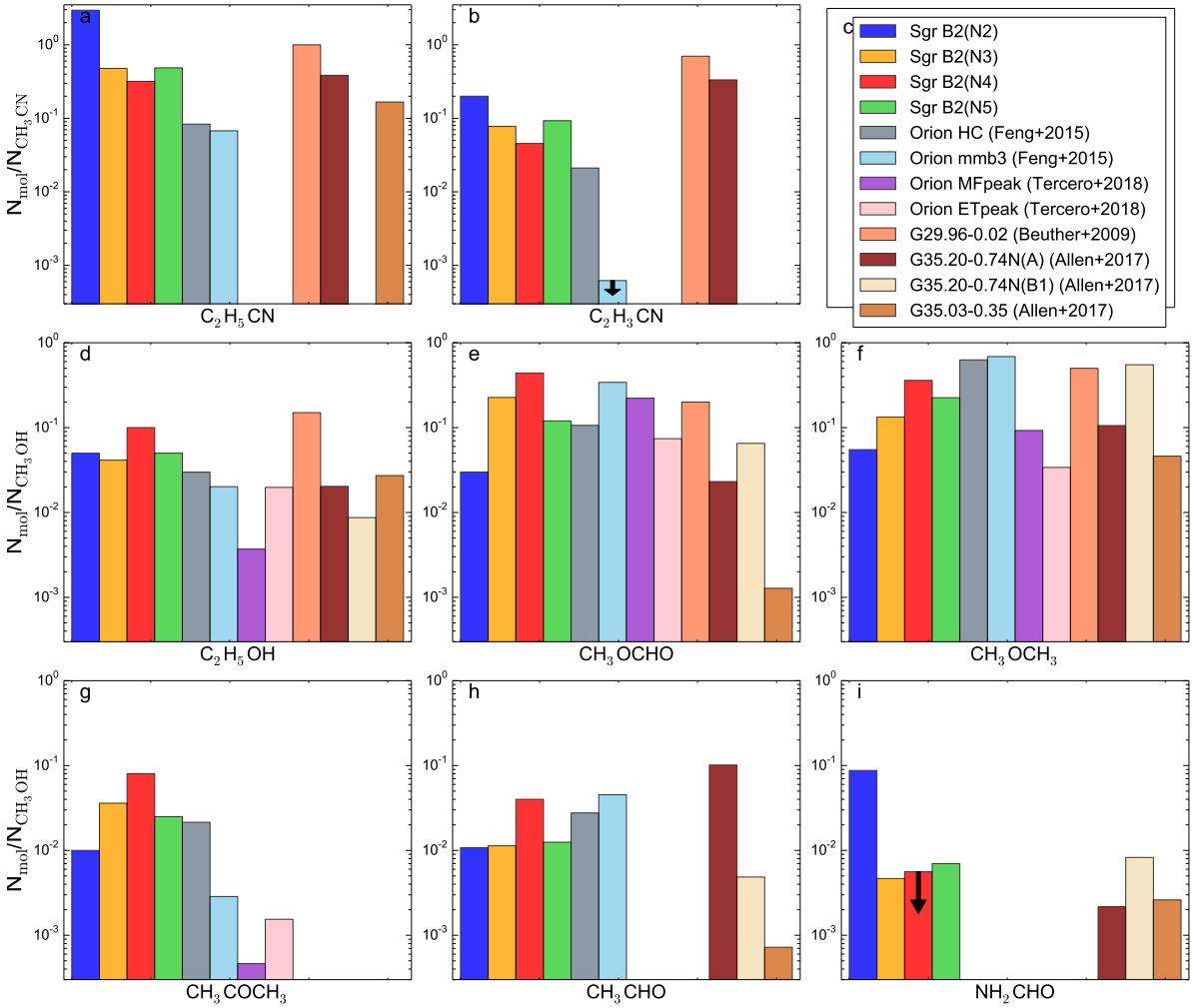

Figure 3.12: Abundance of selected COMs relative to methyl cyanide (panels **a** and **b**), or methanol (panels **d**–**i**), measured toward the sources/positions listed in panel **c**. The column densities toward Orion HMC and mmb3 (that corresponds to the compact ridge) are taken from Feng et al. (2015), based on combined SMA observations at 1.3 mm (230 GHz) and IRAM-30m single-dish observations (with a combined synthesized beam $\sim 3.6'' \times 2.6''$). CH_3CHO is a tentative detection (Feng et al. 2015). The abundances of C_2H_5OH, CH_3OCHO, CH_3OCH_3, and CH_3COCH_3 relative to methanol toward the methyl formate (MF) and ethanol (ET) emission peaks are taken from Tercero et al. (2018), obtained from ALMA data at $\sim 1.5''$ resolution. The column densities toward G29.96-0.02 are taken from Beuther et al. (2009), obtained from SMA data at $\sim$ 0.9 mm ($\sim$ 338 GHz), with an angular resolution of $0.6'' \times 0.5''$. The column densities toward G35.03-0.35 and two compact objects in G35.20-0.74N are taken from Allen et al. (2017) (after fixing an error related to the column density of methanol), based on ALMA observations obtained at $\sim$0.9 mm with an angular resolution of $\sim 0.4''$. The species for which no column densities are available at a given position are not displayed in the figure. The arrows show upper limits.

ratios $[C_2H_3CN]/[CH_3CN]$, $[CH_3COCH_3]/[CH_3OH]$, and $[NH_2CHO]/[CH_3OH]$.

As Sgr B2, Orion BN/KL is widely recognized as one of the richest molecular reservoirs in our Galaxy. Due to its proximity compared to other typical region forming high-mass stars, it has

been extensively studied over a large range of frequencies, from far-IR to (sub)mm wavelengths (see *e.g.* Sutton et al. 1986; Blake et al. 1986; Bergin et al. 2010; Tercero et al. 2010, 2011; Crockett et al. 2014; Cernicharo et al. 2016). Orion BN/KL contains several protostellar objects, moving away from a common region where an explosive event occured 550±25 yr ago (Gómez et al. 2005; Rodriguez et al. 2005, 2017; Luhman et al. 2017). As a result Orion BN/KL shows a complex structure, disrupted by this explosion (see, e.g, Fig. 2 of Feng et al. 2015). Several remarkable sources, with distinct spectral signatures, physical conditions, and spatial scales have been identified (see, e.g., Blake et al. 1987; Schilke et al. 2001; Tercero et al. 2010), of which two in particular are known to be rich in COMs: the so-called Orion HMC, dense clump with high kinetic temperatures ($\sim$ 200–300 K), rich in N-bearing species; and the compact ridge, at the interface between a molecular outflow and the ambient gas, with lower temperatures (T $\sim$ 150 K) and mostly dominated by O-bearing species (Blake et al. 1987; Wright et al. 1996; Liu et al. 2002). Recently interferometric data obtained at high angular resolution have allowed to separate the emission regions of various COMs and showed a clear spatial differentiation even among the complex O-bearing species (see, e.g, Tercero et al. 2018). Figure 3.12 shows that abundances (relative to methanol or methyl cyanide) can vary by orders of magnitude from one position to the other in Orion. Species such as the cyanide C_2H_3CN as well as CH_3COCH_3 clearly peak toward the HMC, the latter with abundances relative to methanol similar to that measured toward N3 and N5, while the O-bearing species CH_3OCHO peaks toward the compact ridge, with abundances relative to methanol similar to that of N3 and N4, significantly higher than toward N2. Some COMs peak in between the Orion HMC and the compact ridge, like ethanol (Tercero et al. 2018), with an abundance relative to methanol similar to that measured toward N3 and N5. These spatial differences may reflect different formation pathways for the different COMs and/or different gas kinetic temperatures. Recent studies based on ALMA observations at high angular resolution suggested that the Orion HMC region could be externally heated by outflow shocks rather that by a central protostellar object (Wright & Plambeck 2017; Orozco-Aguilera et al. 2017). In addition, the chemical content of this region has likely been affected by the explosion of Orion-KL as suggested by Favre et al. (2017). Recently, Pagani et al. (2019) suggested that some species have been pushed away due to the explosion, such that the spatial differentiation of chemical species in Orion-KL region corresponds to the time dependence of the chemistry in the cloud complex. This last consideration makes Orion-KL particularly interesting to test the predictions of chemical models on the time-dependent variations of COM abundances compared to other sources where the spatial distribution of molecules can not be discerned and thus does not deliver information on the temporal evolution on the abundances of these molecules.

Chemical differentiation in particular between O- and N-bearing species has been observed also in other star forming regions, at smaller scale (<1000 au). It is the case for G35.20-0.74N (Allen et al. 2017), where, as mentioned already earlier, the cyanides as well as CH_3CHO clearly peak on the core A, while the O-bearing species CH_3OCHO, CH_3OCH_3, and NH_2CHO peak toward B1 (see Fig. 3.12). Allen et al. (2018) suggested that the cyanides can be used as a chemical clocks in HMCs, indicating that the core in which ethyl and vinyl cyanide are not detected (G35.20-0.74N(B1)) is presumably younger than the other sources they investigated.

Such a clear spatial differentiation is not observed toward Sgr B2(N) on the scale of its individual HMCs (see Sect. 3.3), however, investigating observations at higher angular resolution would be needed to confirm this statement and to determine whether a chemical differentiation between N- and O-bearing species occurs in Sgr B2(N)'s HMCs (see Sect. 8.1). Recently,

Csengeri et al. (2018) investigated the young high-mass star-forming region G328.2551-0.5321 where methanol and other O-bearing species show two distinct bright emission peaks spatially offset from the peak of the cyanides (see also Csengeri et al. subm.). They suggested that in this source, methanol traces the accretion shocks resulting from the interaction between the collapsing envelope and the accretion disk, while the cyanide emission may trace the more compact hot region radiatively heated by the protostar. In this scenario, the O-bearing COM emission detected in the envelope of G328.2551-0.5321 arises from accretion shocks rather than from the region radiatively heated by the protostar itself. Observations at higher angular resolution will also tell us if a similar mechanism could be at play in Sgr B2(N) at scales smaller than the beam of the EMoCA survey.

Chapter 4

Physical structure and evolution of Sgr B2(N)'s hot cores

Contents

In order to enable further investigations of the chemical evolution of Sgr B2(N)'s hot cores, we need to know their physical properties and evolution. In this chapter I present the analysis of the kinematic structure of Sgr B2(N)'s hot cores as well as the results of the analysis of the ALMA continuum data from which we derive H_2 column densities, densities and masses. I present the physical model used in this thesis to characterize the evolution of Sgr B2(N)'s sources and their properties from the earlier pre-stellar phase to the present time. Finally I propose a star formation evolutionary sequence for the HMCs embedded in Sgr B2(N) and discuss the limitations of our physical model.

This chapter is largely based on Bonfand et al. (2017) and Bonfand et al. (2019). Other references are mentioned explicitly throughout the text.

4.1 Kinematic structure of Sgr B2(N)'s hot cores

4.1.1 Systemic velocity

We derive the systemic velocity of the three HMCs, N3–N5, by fitting 1D Gaussians to the observed emission lines which are well reproduced by the LTE synthetic spectra and are not severely contaminated by other species. We obtain a velocity of 74 km s^{-1} for N3, 64 km s^{-1} for N4, and 60 km s^{-1} for N5. We note that N3 and N4 have the same velocity as N2 and N1, respectively.

4.1.2 Molecular outflows

Based on the analysis of the EMoCA dataset, Higuchi et al. (2015) reported the detection of a bipolar molecular outflow in the integrated intensity maps of the SiO(2-1) and $SO_2(12_{4,8}–13_{3,11})$ transitions toward the main hot core N1. The maps show that both species share the same kinematics, with bipolar outflow lobes symmetrically displaced about N1's peak position in the East–West direction (Higuchi et al. 2015, see their Figs. 4 and 5). They estimated an average dynamical time of $\sim 5\times10^3$ years.

In the same way we investigate the spectra observed toward the four other HMCs embedded in Sgr B2(N), N2–N5. In order to assess the presence of outflows toward these sources, we analyze spectral lines from typical outflow tracers. We cannot use the same transitions as Higuchi et al. (2015) to probe molecular outflows as these lines are too weak toward N3–N5. Figure 4.1 shows two other transitions of SO (2_2–1_1 and 3_2–2_1) observed toward N3 (top row) and N5 (bottom row). In both cases the spectral lines show broad wing emission at blue- and red-shifted velocities compared to the systemic velocity of the source. The bottom row of Fig. 4.1 presents another transition of SO with a lower upper energy level, as well as the CS(2-1) transition observed toward N5. Both transitions show a deep absorption profile and strong, broad wings in emission. We plot in Fig. 4.2 the integrated intensity maps of blue- and red-shifted emission for each line along with the map of the line core. The wing boundaries to integrate the blue- and red-shifted emission were chosen to avoid contamination from the line core emission predicted by the LTE model (magenta spectrum in Fig. 4.1) and contamination from other species (green spectrum in Fig. 4.1). All maps clearly show a bipolar morphology for both N3 and N5, with distinct blue and red lobes shifted compared to the line core emission, which suggests the presence of outflows. The integrated intensity maps of the SO lines observed toward N3 (Fig. 4.2, top row) show a similar kinematic structure with the peak position of the blue wing clearly shifted North-East of the line core, while the red one is slightly shifted to the South. The maps of the SO(2_3-1_2) and CS(2-1) transitions observed toward N5 show a clear bipolar structure oriented NE-SW (Fig. 4.2, bottom row). The other two transitions of SO exhibit a different morphology, with the red lobe shifted East of the continuum emission. The reason for this behavior is unclear but we note that the velocities over which the red-shifted wing emission is integrated are lower than the ones used for SO(2_3-1_2) and CS(2-1) (see Table 4.2). Our interpretation that N3 and N5 drive outflows is reinforced by the fact that H_2O maser emission is found in the close vicinity of both sources (see Fig.4.3).

For all transitions shown in Fig. 4.1, the distance r between the peak positions of the blue- and red-shifted outflow lobes and the HMC reference positions are given in Table 4.2. We calculate the maximum outflow velocities, $V_{\rm max}$, for the blue and red lobes as the difference between the high end of the velocity range set to integrate the wing emission and the systemic

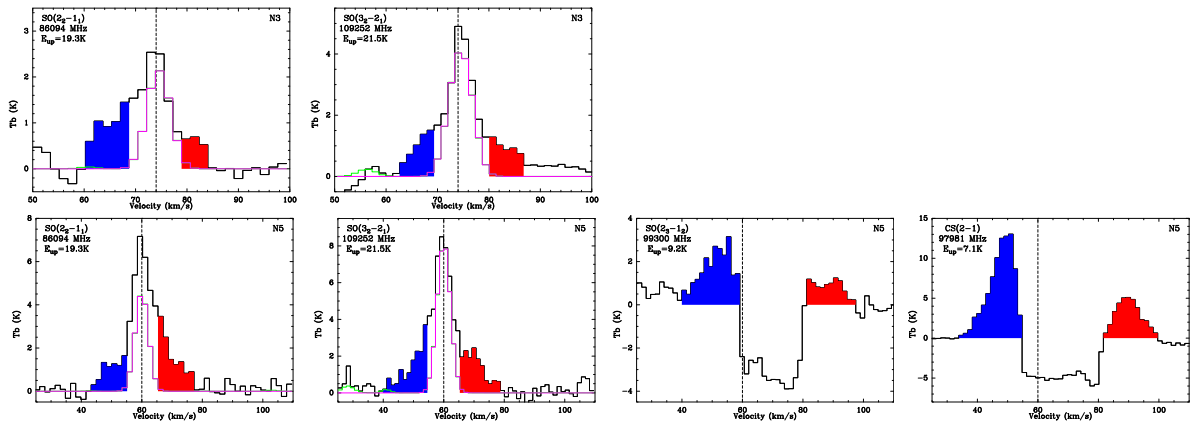

Figure 4.1: Spectra of the lines investigated to search for outflows toward N3 (top row) and N5 (bottom row). The dashed vertical line marks the systemic velocity of the source and the high velocity wings are highlighted in blue and red. The magenta spectrum represents our best-fit LTE model while the green spectrum shows the model that contains all the species identified so far. The rest frequency and upper level energy (in temperature unit) of each transition are indicated in each panel. *Figure taken from Bonfand et al. (2017).*

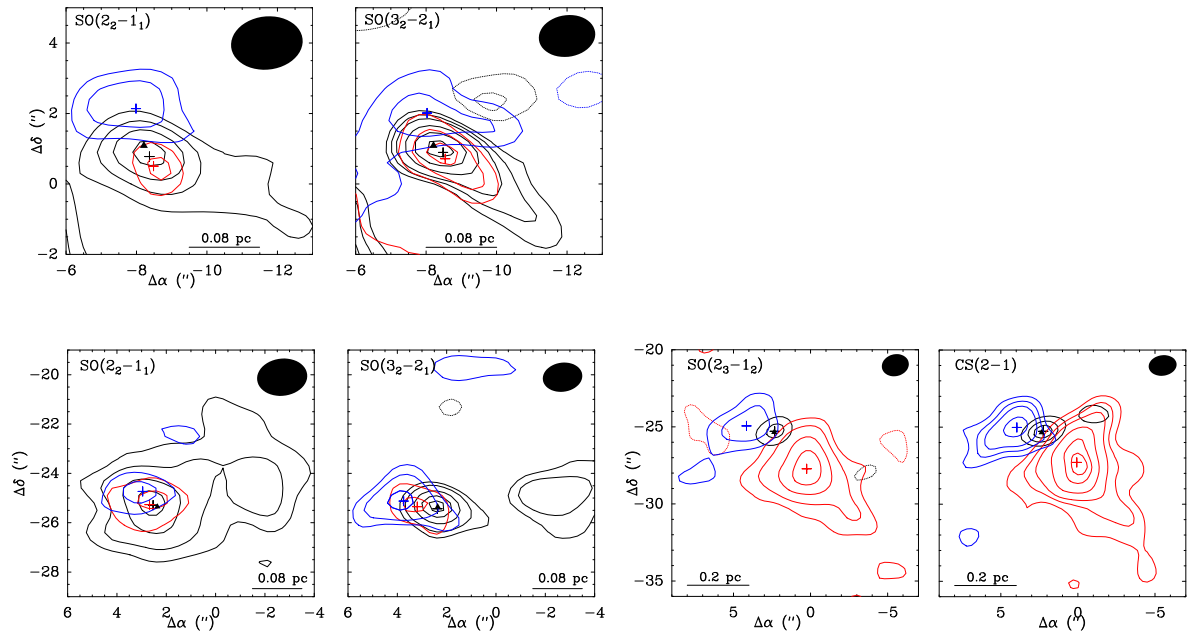

Figure 4.2: Integrated intensity maps of the lines shown in Fig. 4.1 toward N3 (top row) and N5 (bottom row). In each panel, maps of the blue- and red-shifted wing emission are presented as blue and red contours, respectively, overlaid on the integrated emission of the line core (black contours). For the line cores affected by absorption, the black contours represent the continuum emission. Rms noise levels and contour levels used for each map are listed in Table 4.1. Each cross corresponds to the peak position of the emission. The black triangle marks the reference position of the HMC (N3 or N5) derived from Fig. 3.1. *Figure taken from Bonfand et al. (2017).*

velocity of the source. From these values we then calculate the dynamical timescale of each outflow lobe as $t_{\rm dyn} = \frac{r}{V_{\rm max}}$, assuming that the inclination of the outflow axis with respect to the

Table 4.1: Rms noise levels and contour levels used in Fig. 4.2.

	N3			N5		
Transition	Range[a]	rms[b]	Contours[c]	Range[a]	rms[b]	Contours[c]
	blue	41		blue	45	
$SO(2_2\text{-}1_1)$	core	37	3,5,7,9	core	45	4,6,10,14
	red	16		red	45	
	blue	24		blue	28	
$SO(3_2\text{-}2_1)$	core	23	4,6,8,12,16,20	core	88	4,8,15,23
	red	15		red	34	
	_	_		blue	84	
$SO(2_3\text{-}1_2)$	_	_	_	core	88	4,8,15,23
	_	_		red	56	
	_	_		blue	98	
CS(2-1)	_	_	_	core	64	8,13,18,28,38,43
	_	_		red	102	

Notes. [a] The velocity ranges are shown in Fig. 4.1. [b] Rms noise level, σ, in mJy beam^{-1} km s^{-1} measured in the integrated intensity map. [c] Contour levels in units of σ.

Table 4.2: Properties of the molecular outflows toward N3 and N5.

Source	Transition	$V_{\rm LSR}$[a] (km s^{-1})	$r_{\rm blue}$[b] ($''$)	$r_{\rm red}$[b] ($''$)	$\Delta V_{\rm blue}$[c] (km s^{-1})	$\Delta V_{\rm red}$[c] (km s^{-1})	$V_{\rm blue}^{\rm max}$[d] (km s^{-1})	$V_{\rm red}^{\rm max}$[d] (km s^{-1})	$t_{\rm dyn}$[e] (10^3yr)
N3	$SO(2_2\text{-}1_1)$	74.0	1.07 (NE)	0.64 (SW)	[61.1 ; 67.9]	[79.8 ; 83.2]	12.9	9.2	3.0
	$SO(3_2\text{-}2_1)$	74.0	1.04 (NE)	0.53 (SW)	[63.2 ; 68.5]	[80.7 ; 86.1]	10.8	12.1	2.8
N5	$SO(2_2\text{-}1_1)$	60.0	0.87 (NE)	0.35 (E)	[44.0 ; 54.3]	[66.1 ; 76.4]	16.0	16.4	1.5
	$SO(3_2\text{-}2_1)$	60.0	1.37 (E)	0.83 (E)	[40.4 ; 53.9]	[65.9 ; 78.0]	19.6	18.0	2.3
	$SO(2_3\text{-}1_2)$	60.0	1.86 (E)	3.17 (SW)	[40.6 ; 58.4]	[81.9 ; 96.7]	19.4	36.7	3.6
	CS(2-1)	60.0	1.86 (E)	3.00 (SW)	[34.6 ; 53.9]	[82.4 ; 98.8]	25.4	38.8	3.0

Notes. [a] Systemic velocity of the source. [b] Distance of the emission peak of the blue/red-shifted lobe compared to the reference position of the HMC. The direction is indicated in parentheses. [c] Velocity range adopted to integrate the emission from the blue/red-shifted wing. [d] Maximum outflow velocity of the blue/red-shifted wing calculated as the difference between the high end of the velocity range and $V_{\rm LSR}$. [e] Average dynamical time of the outflow, assuming an inclination of 45° ($r/V_{\rm max}$) .

line of sight is approximately 45° as the maps show two distinct blue and red lobes. We obtain average dynamical timescales of ∼2–4 $\times 10^3$ yr, similar to the dynamical timescale derived by Higuchi et al. (2015) for N1 (∼5$\times 10^3$ years).

Figure 4.3 shows that several H_2O masers are also found in the close vicinity of N2. However, the transitions of typical outflow tracers investigated in the spectra observed toward N2 do not have high velocity wings that would suggest the presence of an outflow (see Fig. 4.4, top row). The main hot core N1 coincides with the centroid position of a powerful H_2O maser compact ($4'' \times 2''$ sized) outflow (Fig. 4.3). For their (collisional) pumping, H_2O masers require much higher temperatures (∼400 K) and densities (∼ 10^9 cm^{-3}) than the values we derived for N1 (see Sect. 3.4 and 4.2.4). These conditions are met for instance in the post shock regions of fast shocks (Elitzur et al. 1989; Hollenbach et al. 2013).

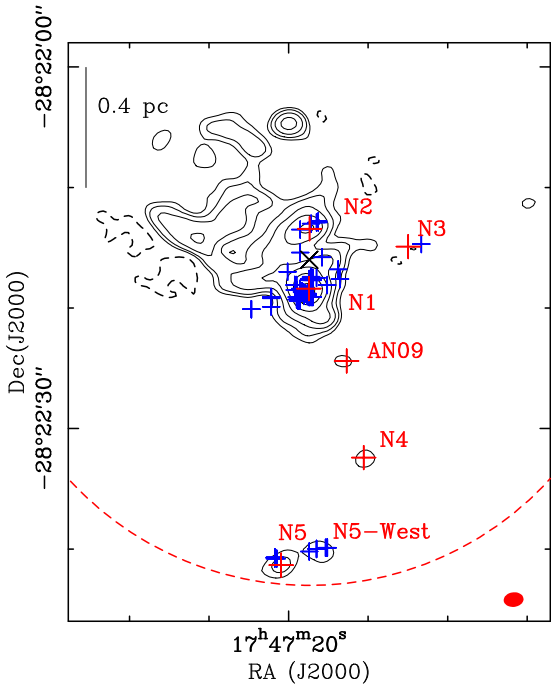

Figure 4.3: Continuum map of the Sgr B2(N) region obtained with ALMA at 108 GHz. Contour levels (positive in black solid line and negative in dashed line) start at five times the rms noise level, σ, of 3.0 mJy beam^{-1} and double in value up to 320σ. The filled ellipse shows the synthesized beam (1.65″ × 1.21″, PA=-83.4°). The black cross represents the phase center. The red crosses mark the positions of the cores embedded in Sgr B2(N). The blue crosses represent the known H_2O masers (McGrath et al. 2004). The dashed red circle represents the size (HPBW) of the primary beam of the ALMA 12m antennas at 108 GHz. *Figure taken from Bonfand et al. (2017).*

No water maser emission is detected toward N4 (Fig. 4.3) and we do not see evidence for a bipolar structure in this source either. The same transitions as those investigated for the other HMCs are too weak to show wing emission (see for instance SO lines in Fig. 4.4, bottom row). It is thus difficult to conclude on the presence of a bipolar structure in N4. The lack of molecular outflow might reflect the youth of the source compared to the others, the outflow structure in this case might be too small to be detected at the resolution of the EMoCA data. Further investigations of higher angular resolution observations will be needed to assess this question (see also Sect. 8.1).

4.2 Continuum properties of Sgr B2(N)'s hot cores

In order to calculate H_2 column densities from the dust thermal emission arising from the HMCs embedded in Sgr B2(N) we need to know the dust properties, in particular the dust mass opacity coefficient κ_ν, which depends on the dust emissivity exponent β. To derive these parameters we use our 3 mm ALMA data, after correction for the contribution of the free-free emission, and the SMA continuum map of Qin et al. (2011) obtained at ∼0.9 mm (343 GHz) and smoothed to the EMoCA resolution.

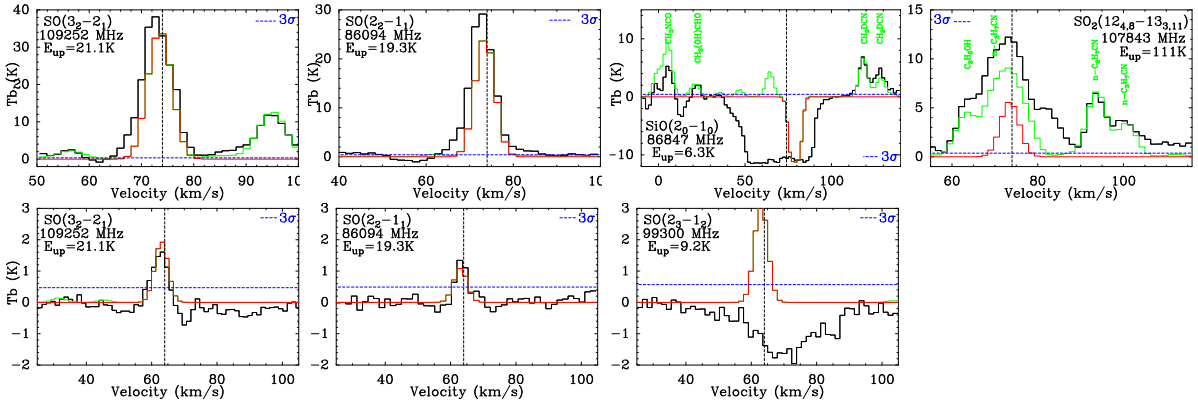

Figure 4.4: Lines of typical outflow tracers detected toward N2 (top row) and N4 (bottom row). In each panel the red spectrum represents our best-fit LTE synthetic spectrum obtained for the investigated species. The green spectrum shows the model that includes all the molecules identified so far toward the HMCs (N2 or N4). The dashed horizontal line shows the 3σ level. The systemic velocity of the source is marked with the dashed vertical line. The rest frequency and upper level energy (in temperature unit) of each transition are indicated in each panel. *Figure adapted from Bonfand et al. (2017).*

4.2.1 Dust continuum emission

Figure 4.5a shows the continuum map obtained at 108 GHz with ALMA. At this frequency only four of the five HMCs embedded in Sgr B2(N) are clearly detected. Strong continuum emission is detected toward the main HMCs, N1 and N2, while N4 and N5 appear much weaker. N3 is not detected at all. In order to investigate the dust continuum properties of each object, we extract 20 continuum maps, one from each spectral window of the EMoCA survey, at different frequencies covering the whole frequency range of the survey (see Fig. B.1). We measure for each source the peak flux density $F_\nu^{\rm beam}$ (in Jy beam^{-1}) by fitting 2D Gaussians to the 20 continuum maps using the GAUSS-2D task of the GILDAS software. The flux is then corrected for the primary beam attenuation in the continuum maps.

In the case of N3 which is not detected above the 5σ threshold in the 3 mm continuum maps (see Fig. B.1), we measure the rms noise level in the maps using the command GO NOISE of the GILDAS software in order to compute upper limits. The average peak positions of the continuum emission associated to the HMCs derived from the 2D-Gaussian fits are marked with blue crosses in Fig. 4.5a. The offset between these positions and the reference positions of the HMCs is at most one fourth of the beam (see Table 4.3). Table 4.3 also gives the size (FWHM) of the continuum sources derived from the 2D-Gaussian fits as well as the distance of each HMC to the closest (UC)HII region.

4.2.2 Free-free contamination

The submillimeter continuum emission observed toward Sgr B2(N) is commonly attributed to thermal emission from interstellar dust (Kuan & Snyder 1996). However, the free-free emission arising from (UC)HII regions may contribute significantly to the flux density measured in the continuum maps. In order to evaluate the contamination from the free-free emission in the ALMA continuum maps at 3 mm, we compared our data to the SMA continuum map of Qin et al. (2011) obtained at 343 GHz (see Fig. 2.11). At this frequency the contribution of the

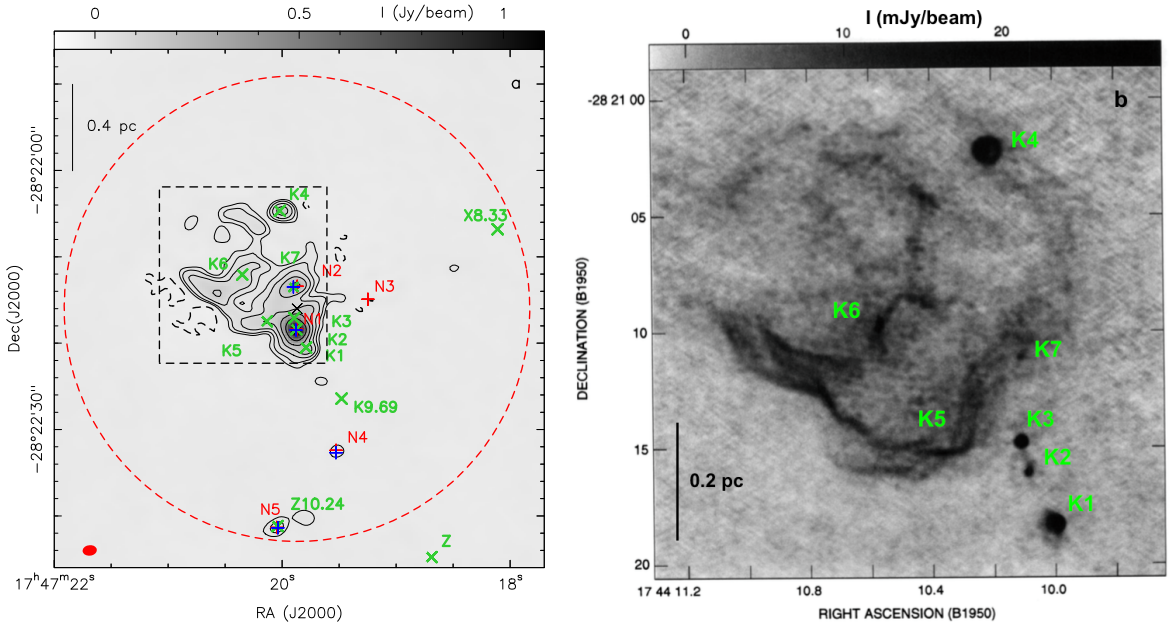

Figure 4.5: **a** Continuum map of the Sgr B2(N) region obtained with ALMA at 108 GHz. Contour levels (positive in black solid line and negative in dashed line) start at five times the rms noise level, σ, of 3.0 mJy beam^{-1} and double in value up to 320σ. The black cross represents the phase center. The red crosses mark the reference position of each HMC derived from Fig. 3.1. The green crosses mark the position of the known (UC)HII regions. The red crosses mark the average peak positions of the continuum emission derived from 2D-Gaussian fits to the 20 ALMA continuum maps. The dashed red circle represents the size (HPBW) of the primary beam of the 12 m antennas at 108 GHz. The filled red ellipse shows the mean synthesized beam. The map is not corrected for the primary beam attenuation. **b** Continuum map obtained within the region marked by a dashed line square in panel **a**, with the Very Large Array (VLA) at 22 GHz by Gaume et al. (1995). (UC)HII regions are labeled in green.

free-free emission to the flux density is lower than 0.1% and can safely be ignored. The extended continuum emission seen in our ALMA data toward N1 and N2 (see Fig. 4.5a) has no counterpart in the SMA map, suggesting that it is free-free emission arising from the numerous (UC)HII regions surrounding the HMCs. We note that the overall shape of the extended continuum emission seen in the ALMA data is similar to the shape of the 1.3 cm free-free emission reported by Gaume et al. (1995) (see Fig. 4.5b). This confirms that the extended emission detected with ALMA is most probably dominated by free-free emission. Therefore, the flux densities measured in the ALMA continuum maps toward the HMCs associated with (UC)HII regions (that is N1, N2, and N5), need to be corrected for the free-free contamination. In addition, N2 is located in the direction of extended 1.3 cm free-free emission seen in Fig. 4.5b. Figure 4.6b shows the profile of the continuum emission along the direction going through N2 indicated with the red line in Fig. 4.6a. In order to estimate the contribution of free-free emission expected toward N2 in the ALMA continuum maps, we decompose the profile shown in Fig. 4.6b into a peak, which we attribute to dust emission associated with the HMC, and a pedestal, which we attribute to the extended free-free emission. We proceed in the same way for the 20 ALMA continuum maps. The weighted linear fit to the results shown in Fig. 4.6c (excluding setup 3) gives us the correction to subtract from the measured peak flux density $F_\nu^{\rm beam}$ as a function of frequency.

Table 4.3: Position and size of the ALMA continuum sources at 3 mm, and distances to HMCs and UCHII regions.

Source	$\Delta\alpha$; $\Delta\delta^a$ ($''$)	$\alpha_{\rm J2000}$; $\delta_{\rm J2000}{}^b$ 17^h47^m ; -28°22′	FWHM$_c{}^c$ ($''$)	$d_{\rm c-l}{}^d$ ($''$)	$d_{\rm c-UCHII}{}^e$ ($''$)
N1	+0.12(0.03) ; -2.48(0.05)	19.879(0.002)^s ; 18.48(0.05)$''$	2.1(0.2)	0.13(0.04)	0.10(0.05)
N2	+0.42(0.11) ; +2.50(0.15)	19.902(0.008)^s ; 13.50(0.15)$''$	2.6(0.3)	0.45(0.11)	0.02(0.11)
N4	–4.50(0.31) ; -16.69(0.65)	19.529(0.050)^s ; 32.69(0.65)$''$	0.7(0.1)	0.28(0.65)	_
N5	+2.21(0.15) ; -25.38(0.18)	20.037(0.002)^s ; 41.38(0.18)$''$	2.0(0.4)	0.14(0.15)	0.20(0.18)

Notes. $^{(a)}$ Equatorial offsets of the continuum peak with respect to the phase center (see Sect. 2.3). The uncertainties in parentheses represent the standard deviation weighted by the errors given by the 2D-Gaussian fit. $^{(b)}$ Same position given in J2000 Equatorial coordinates. $^{(c)}$ Average deconvolved angular size of the continuum source derived from 2D-Gaussian fits to the ALMA continuum maps. The uncertainty given in parentheses corresponds to the standard deviation. $^{(d)}$ Distance between the continuum peak position and the position of the closest HMC derived from Fig. 3.1. The uncertainty given in parentheses is calculated based on the errors given by the 2D-Gaussian fits. $^{(e)}$ Distance between the continuum peak position and the peak position of the closest UCHII region (Gaume et al. 1995; De Pree et al. 2015). The uncertainty given in parentheses is calculated based on the errors given by the 2D-Gaussian fit.

For the continuum maps extracted from the frequency range covered by setup 3 (with the lowest angular resolution), we directly apply the corrections estimated from the plots of the continuum profile. The corrections estimated from Fig. 4.6c represent the contamination from the extended free-free emission detected in the ALMA continuum maps but a correction for the free-free emission arising directly from the UCHII region K7 in the vicinity of N2 still has to be applied. We estimate the flux expected from K7 based on the flux reported by De Pree et al. (2015). They measured an integrated flux of 30 mJy at 44.2 GHz for a source size of 0.08$''$. We assume that the free-free emission of K7 is optically thin and thus that the measured flux is proportional to ν^α, with $\alpha = -0.1$. From this relation we extrapolate a flux of ∼28 mJy for the frequency range of the ALMA survey. This value is also subtracted from the peak flux density of N2. We proceed in the same way for N5 based on the flux reported by Gaume et al. (1995) toward Z10.24. They measured an integrated flux of 36 mJy at 22.4 GHz for a source size <0.25$''$. We extrapolate this value to the ALMA frequency range assuming optically thin emission, and we obtain ∼31 mJy. This value is directly subtracted from the values of the peak flux density measured in the ALMA continuum maps toward N5. In the case of N1 we use the flux measured by De Pree et al. (2015) toward K2 and K3 at 44.2 GHz. They measured integrated flux densities of 80 mJy toward K2 for a source size of 0.12$''$ and 242 mJy toward K3 for a source size of 0.27$''$. K3 being located 1.3$''$ North-East of K2, we estimate that only∼15% of the free-free emission arising from this UCHII region contributes to the total flux density measured in the ALMA synthesized beam of ∼1.6$''$ centered on K2. We thus obtain a total free-free contribution of ∼116 mJy that we subtract from the flux densities measured toward N1 in the ALMA continuum maps.

The fraction of free-free emission estimated toward N1 varies between ∼17% at 85 GHz and ∼9% at 114 GHz. The free-free contribution is higher toward N2, from ∼75% at 85 GHz, down to ∼32% at 113.5 GHz, and it varies between 40% and 60% toward N5. We do not apply a correction factor for N3 and N4 because they are not associated with any known (UC)HII region. The flux densities measured toward Sgr B2(N)'s HMCs in the ALMA continuum maps

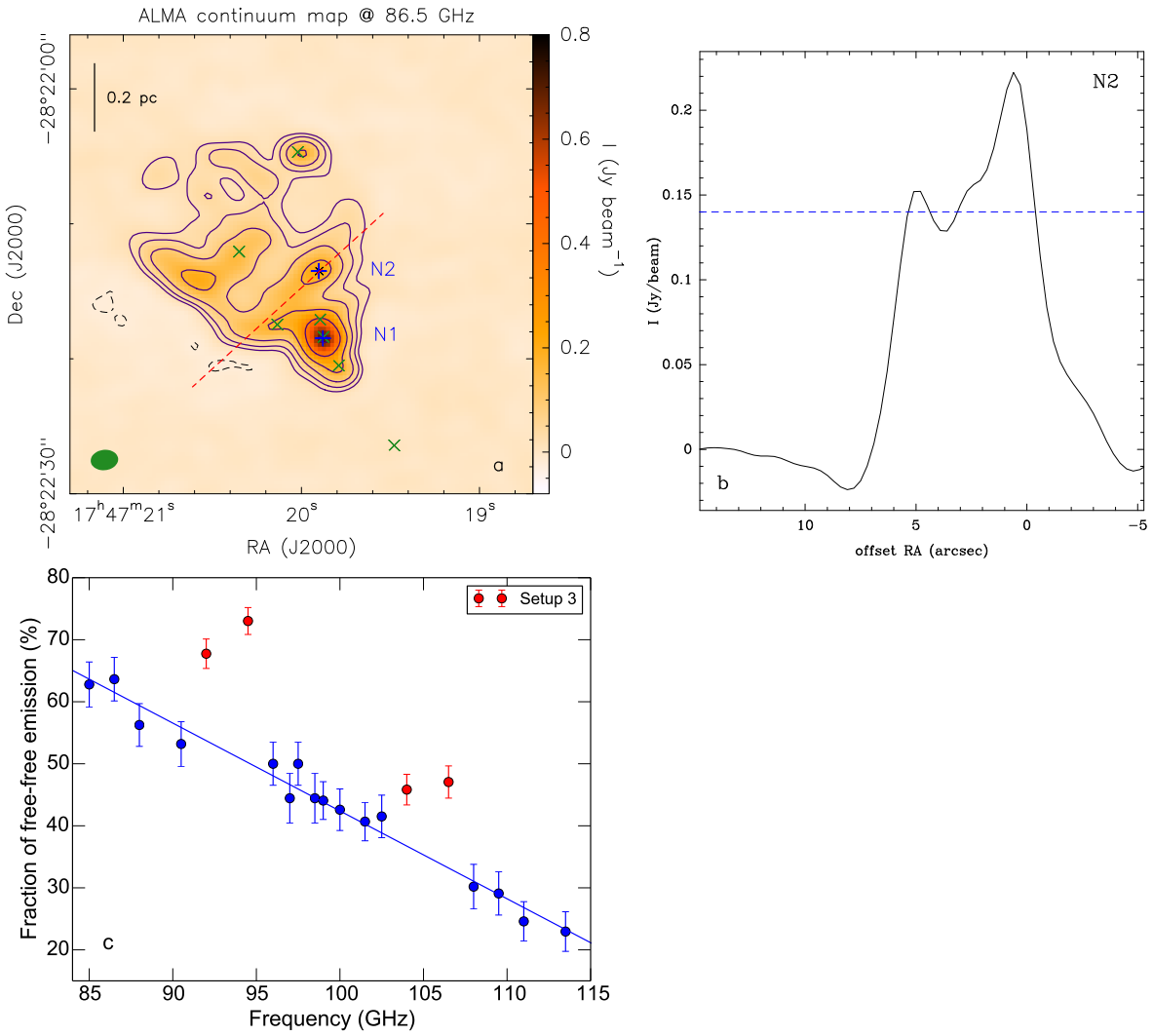

Figure 4.6: **a** Continuum map obtained at 86.5 GHz with ALMA. Contour levels (positive in solid line and negative in dashed line) start at 5σ (σ ~3.0 mJy beam^{-1}) and double in value up to 320σ. The green filled ellipse shows the synthesized beam (Table 2.2). The blue crosses mark the positions of peak continuum emission (see Table 4.3). The green crosses represent (UC)HII regions. The map is not corrected for the primary beam attenuation. **b** Profile of the continuum emission along the direction plotted in red in panel **a**. The blue line marks the estimated level of extended free-free emission. **c** Fraction of free-free emission relative to the total flux density measured toward N2. This does not include the contribution of K7. The blue line is the weighted linear fit to the results excluding setup 3 that has a worse angular resolution and is shown in red. *Figure adapted from Bonfand et al. (2017).*

after correction for the free-free contribution are given in Table B.1, along with the values obtained for the SMA map smoothed to the EMoCA resolution for comparison.

4.2.3 Dust properties

In order to compute H_2 column densities from the dust thermal emission measured in the continuum maps in Sect. 4.2.1 we need to know the dust properties. Assuming that the dust

Table 4.4: Dust opacity of Sgr B2(N)'s HMCs calculated for a dust temperature of 150 K.

Source	$\tau_{\rm ALMA}{}^{a}$	$\tau_{\rm SMA(1.6'')}{}^{b}$	$\tau_{\rm SMA(0.3'')}{}^{c}$
N1	0.36	0.95	$-^{*}$
N2	0.05	0.19	0.61
N3	<0.009		
N4	0.008		
N5	0.03		

Notes. $^{(a)}$ Dust opacity calculated based on the ALMA data. $F_\nu^{\rm beam}$ has been corrected for the primary beam attenuation and the free-free contamination. $^{(b)}$ Dust opacity calculated based on the SMA map smoothed to the EMoCA resolution (∼1.6″). $^{(c)}$ Dust opacity calculated based on the SMA map at its original resolution (∼0.3″). $^{(*)}$ Optically thick and inconsistent with a temperature of 150 K.

temperature is given by the gas kinetic temperature derived in Sect. 3.4 ($T_{\rm dust} \sim T_{\rm K}$ ∼150 K >> $T_{\rm bg}$), we compute the dust opacity toward each HMC using Eq. 2.31, with $F_\nu^{\rm beam}$ the peak flux density measured in the continuum maps (in Jy beam^{-1}) after correction for the primary beam attenuation and, in the case of the ALMA data, for the free-free contribution (see Sect. 4.2.2). The resulting opacities are given in Table 4.4 for both the ALMA and SMA data. It shows that the thermal emission from the dust is optically thin for all cores except N1 at the SMA frequency. In the SMA map at its original resolution (∼0.3″), the dust emission of N1 is optically thick and inconsistent with a temperature of 150 K. From Eq. 2.30 and assuming optically thick emission, we derive a lower limit to the dust temperature of 200 K at a scale of 0.3″.

From Eqs. 2.31, 2.32, and 2.33 we can derive the dust emissivity index β, using the flux densities measured in the ALMA continuum maps at 100 GHz and in the SMA data at 343 GHz:

$$F_\nu^{\rm ALMA} = \Omega_{\rm ALMA} B_\nu^{\rm ALMA}(T_d) \left[1 - \exp\left(-\mu_{\rm H_2} m_{\rm H} \kappa_0 \left(\frac{\nu_{\rm ALMA}}{\nu_0}\right)^{\beta} N_{\rm H_2}\right)\right]$$

and

$$F_\nu^{\rm SMA} = \Omega_{\rm SMA} B_\nu^{\rm SMA}(T_d) \left[1 - \exp\left(-\mu_{\rm H_2} m_{\rm H} \kappa_0 \left(\frac{\nu_{\rm SMA}}{\nu_0}\right)^{\beta} N_{\rm H_2}\right)\right],$$

which can also be written as:

$$N_{\rm H_2} \left(\frac{\nu_{\rm ALMA}}{\nu_0}\right)^{\beta} = -\frac{1}{\mu_{\rm H_2} m_{\rm H} \kappa_0} \times \ln\left(1 - \frac{F_\nu^{\rm ALMA}}{\Omega_{\rm ALMA} B_\nu^{\rm ALMA}}\right)$$

and

$$N_{\rm H_2} \left(\frac{\nu_{\rm SMA}}{\nu_0}\right)^{\beta} = -\frac{1}{\mu_{\rm H_2} m_{\rm H} \kappa_0} \times \ln\left(1 - \frac{F_\nu^{\rm SMA}}{\Omega_{\rm SMA} B_\nu^{\rm SMA}}\right).$$

Then β is given by:

$$\beta = \ln\left[\frac{\ln\left(1 - \frac{F_\nu^{\rm ALMA}}{\Omega_{\rm ALMA} B_\nu^{\rm ALMA}}\right)}{\ln\left(1 - \frac{F_\nu^{\rm SMA}}{\Omega_{\rm SMA} B_\nu^{\rm SMA}}\right)}\right] \times \frac{1}{\ln\left(\frac{\nu_{\rm ALMA}}{\nu_{\rm SMA}}\right)}, \tag{4.1}$$

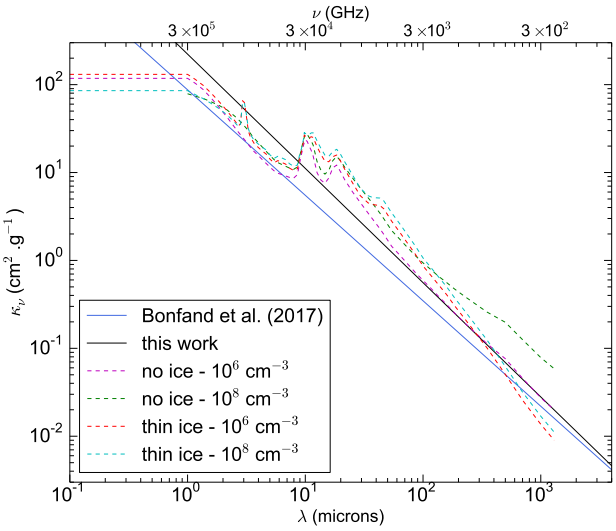

Figure 4.7: Dust mass opacity spectra for a standard gas-to-dust mass ratio of 100. The dashed lines show the results of Ossenkopf & Henning (1994)'s simulations after 10^5 yr of dust coagulation with gas densities of 10^6 cm^{-3} and 10^8 cm^{-3} and for dust grains without ice mantle and with thin ice mantle. The blue solid line shows the κ_ν used to compute H_2 column densities in Bonfand et al. (2017). The black solid line shows the κ_ν used in this thesis computed with Eq. 2.32, and based on Ossenkopf & Henning (1994)'s model for grains without ice mantle and for gas densities of 10^6 cm^{-3} (magenta dashed line). *Figure taken from Bonfand et al. (2019).*

which only depends on the peak flux density measured on the continuum maps, the beam solid angle, the Planck function, and the frequency. We perform the calculations using the flux densities measured toward N1 and N2 in the 20 ALMA continuum maps selected over the whole frequency range of the EMoCA survey and the SMA map smoothed to the corresponding ALMA resolution. We excluded setup 3 in the calculations because of its low angular resolution. We obtain $\beta = 0.8\pm0.1$ and $\beta = 1.2\pm0.1$ for N1 and N2, respectively. As mentioned above, the continuum emission detected with SMA toward N1 is very optically thick. Even if the emission in the SMA map smoothed to the EMoCA resolution should be less optically thick and our analysis does not assume optically thin emission, it is likely that the value derived for β toward N1 is underestimated due to these high opacities. It could also be that we have underestimated the contribution of free-free emission toward N1 at the ALMA frequencies. Therefore, we consider the value obtained toward N2, $\beta = 1.2$, as more reliable for all sources. According to Ossenkopf & Henning (1994)'s simulations of dust coagulation in cold dense cores, a dust emissivity exponent of $\beta = 1.2$ suggests an intermediate dust opacity spectrum between the models of dust grains without ice mantles and those with thin ice mantles (see Fig. 4.7). Here we adopt a dust emissivity exponent of $\beta = 1.3$, with $\kappa_0 = 0.0199$ cm^2 g^{-1} (of gas) at $\nu_0 = 230$ GHz (*i.e.* $\lambda_0 = 1.3$ mm), which corresponds to the model with grains without ice mantle and for gas densities of 10^6 cm^{-3} (see magenta dashed line in Fig. 4.7). The resulting dust mass opacity coefficient, κ_ν, is plotted with black solid line in Fig. 4.7.

4.2.4 H_2 column densities

From the dust thermal emission measured toward the HMCs and the dust properties derived in the previous sections we can now compute H_2 column densities using Eq. 2.34. Figure 4.8 shows the resulting H_2 column densities computed from the dust thermal emission measured toward each HMC in the ALMA continuum maps as a function of frequency, before and after correction for the free-free contribution. The results obtained based on the SMA data smoothed to the EMoCA resolution are also shown for comparison. The calculated H_2 column densities are also given in Table B.1. When a source is not detected in the ALMA continuum maps, upper limits corresponding to five times the noise level are plotted in Fig. 4.8. Here it is important to keep in mind that the beam is slightly different as a function of frequency, especially in the frequency range covered by setup 3 which has the lowest angular resolution (HPBW $>$ $2''$). Therefore we calculate the average H_2 column density of each HMC excluding setup 3. Table 4.5 summarizes the results obtained from the ALMA data before and after the correction for the free-free contribution and for the SMA map smoothed to the EMoCA resolution and at its original resolution for comparison. The resulting H_2 column densities slightly differ from our previous analysis of the same ALMA data presented in Bonfand et al. (2017), where we assumed a dust mass opacity coefficient ($\kappa_{100GHz} = 5.9{\times}10^{-3}$ cm^2 g^{-1}) $\sim$ 1.1 times smaller than the value we derived at the same frequency here (see Fig. 4.7).

In the case of N3 which is not detected in the ALMA continuum maps at 3 mm (Bonfand et al. 2017), we use the peak flux density measured by Sánchez-Monge et al. (2017) ($0.094{\pm}0.016$ Jy beam^{-1}, see their Table 1, source AN08) in the continuum map obtained with ALMA at 242 GHz and with an angular resolution of $0.4''$ (see also Sect.3.1). To compare the resulting H_2 column density with the upper limit derived from our ALMA dataset at 3 mm we need to extrapolate the upper limit on the H_2 column density obtained at the ALMA angular resolution of $\sim 1.6''$ to the resolution of the 1 mm ALMA data ($0.4''$). Assuming a spherical symmetry and a density profile proportional to $r^{-1.5}$ *i.e.* a column density scaling with $r^{-0.5}$, we obtain an upper limit of $6.2{\pm}2.8{\times}10^{23}$ cm^{-2} at a resolution of $0.4''$, which is consistent within the uncertainties with the H_2 column density we derived from the ALMA data at 1 mm. Sánchez-Monge et al. (2017) derived a H_2 column density of $4.5{\times}10^{24}$ cm^{-2} (see their Table 3) from the integrated flux measured over a source size of $0.59''$ (see Table 1 of Sánchez-Monge et al. 2017). We note that they used a mean molecular weight of $\mu = 2.33$, which corresponds to that of the mean free particle, so that their calculated value has to be divided by $\sim$1.2 to obtain the H_2 column density. This gives $N_{H_2} = 3.7{\times}10^{24}$ cm^{-2}, a factor $\sim$ 4 higher than the value we derived in this paper. This difference is due to the different assumptions made to compute the H_2 column density. They assumed a lower dust temperature of 100 K and used a dust mass opacity coefficient ($\kappa_{230\,\mathrm{GHz}} = 0.011$ cm^2 g^{-1}) $\sim$ 1.8 times smaller than our value at the same frequency.

In a previous analysis of Sgr B2(N) based on the same ALMA survey, Belloche et al. (2014) calculated a peak H_2 column density at 98.8 GHz of $4.2{\times}10^{24}$ cm^{-2} for N2, for a beam size of $1.8'' \times 1.3''$, which is approximately three times higher than our result. This difference results in part from the dust mass opacity coefficient they assumed ($\kappa_{98.8\mathrm{GHz}} = 4.3{\times}10^{-3}$ cm^2 g^{-1}), $\sim$1.5 times smaller than the value we derive for this frequency based on our combined analysis of the ALMA and SMA data sets. In addition, they assumed that all the continuum emission is due to dust while we took into account the contribution of the free-free emission. This results in an additional factor $\sim$2 on the H_2 column density. From the flux density measured toward N2 in the SMA map at its original resolution we derived a H_2 column density of $\sim 4.0(\pm 0.3){\times}10^{24}$ cm^{-2}.

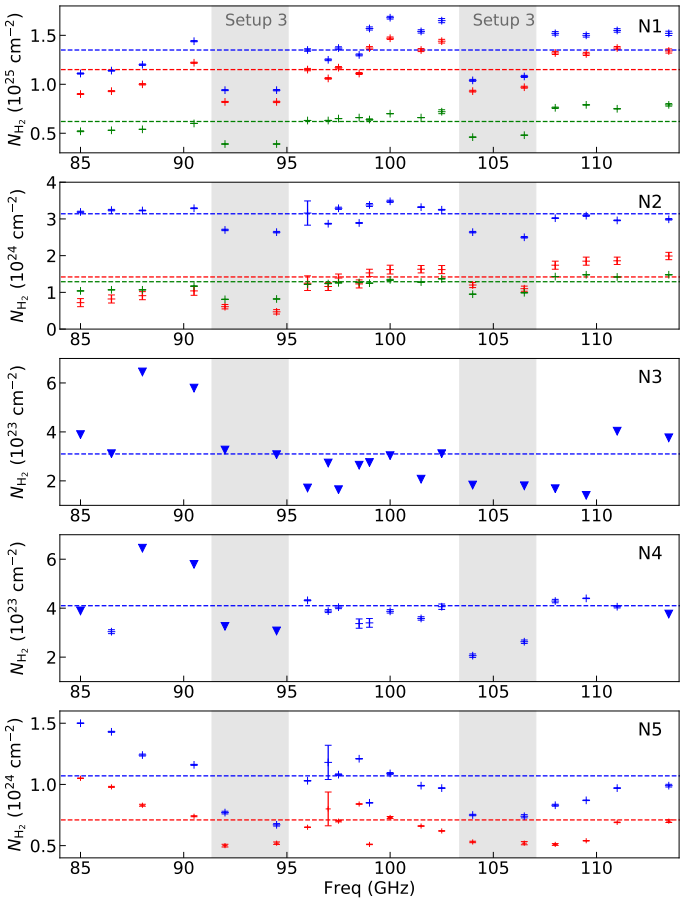

Figure 4.8: H_2 column densities as a function of frequency for the five HMCs embedded in Sgr B2(N). The values obtained based on the ALMA data before and after correction for the free-free contribution are shown as blue and red crosses, respectively. The green crosses represent the results obtained based on the SMA map at 343 GHz smoothed to the angular resolution of the ALMA maps. Error bars are calculated from the error on $F_\nu^{\rm beam}$ given by the GAUSS-2D routine and take into account the uncertainty on the correction for the free-free emission. The triangles represent 5σ upper limits. The dashed line in each panel is the average H_2 column density (or upper limit for N3) excluding setup 3. *Figure taken from Bonfand et al. (2017).*

Based on the same map, Qin et al. (2011) calculated an H_2 column density of 1.5×10^{25} cm^{-2} toward N2. They used the same dust temperature, but they assumed optically thin emission and a dust mass opacity coefficient $\kappa_{343\rm GHz} = 6.8\times10^{-3}$ cm^2 g^{-1} that is 4.9 times smaller than the value we obtain at this frequency from our combined ALMA/SMA analysis. In addition, we derived a dust opacity of 0.61 for N2 in the original SMA map (see Table 4.4), which implies that they underestimated the column density by a factor ∼1.3. The two effects explain the factor ∼3.8 of difference between the two studies.

The results given in Table 4.5 show that N2, N4, and N5 have H_2 column densities about 8, 28 and 16 times lower than that of the main hot core N1, respectively. The H_2 column densities derived at a resolution of ∼1.6″ do not necessarily reflect the density of the compact region with warm dense gas from which the COM emission arises (see Sect. 3.3). Therefore, in

Table 4.5: H_2 column densities of Sgr B2(N)'s HMCs for a dust temperature of 150 K.

Source	N_{H_2} (10^{24} cm^{-2})				
	ALMA$_{\rm dust+freefree}$ [a]	ALMA$_{\rm dust}$ [b]	ALMA$_{(0.4'')}$ [c]	SMA$_{(1.6'')}$ [d]	SMA$_{(0.3'')}$ [e]
N1	13.5(1.8)	11.5(1.8)		6.24(0.68)	_ [*]
N2	3.14(0.17)	1.42(0.39)		1.29(0.15)	3.95(0.27)
N3	<0.31(0.14)	<0.31(0.14)	0.90(0.17)		
N4	0.41(0.04)	0.41(0.04)			
N5	1.07(0.19)	0.71(0.16)			

Notes. The uncertainties are given in parentheses and correspond to the standard deviations weighted by the error on $F_\nu^{\rm beam}$ and on the correction factor for the free-free emission. [(a)] H_2 column densities calculated based on the ALMA data after correction for the primary beam attenuation, for a mean synthesized beam size of ∼1.6″. [(b)] ALMA$_{\rm dust}$ is in addition corrected for the free-free contribution. [(c)] In the case of N3 we used the peak flux density measured by Sánchez-Monge et al. (2017) at 242 GHz in ALMA data obtained at 0.4″ resolution (see Sect. 4.2.4). [(d)] H_2 column densities calculated based on the SMA map smoothed to the EMoCA resolution (∼1.6″). [(e)] H_2 column densities calculated based on the SMA map at its original resolution (∼0.3″) . [(*)] The dust emission toward N1 being optically thick we cannot derive its H_2 column density.

order to derive chemical abundances (molecular column densities relative to H_2), we need to extrapolate the H_2 column densities obtained at the ALMA angular resolution of ∼ 1.6″ to the more compact region where the COM emission comes from (Sect. 3.3).

From the emission lines detected toward N3, we derived an average deconvolved source size of 0.4″ (see Sect. 3.3), therefore we can directly use the H_2 column density computed from the peak flux density measured in the 1 mm ALMA continuum map at 0.4″ resolution (see column 4 of Table 4.5). In the case of N2 and N5 we derived deconvolved source sizes >2.0″ from the 3 mm ALMA continuum maps (see Table 4.3), larger than the ALMA angular resolution of 1.6″. For both HMCs, we thus extrapolate the H_2 column density obtained at the ALMA angular resolution of ∼ 1.6″ (see column 3 of Table 4.5) to the more compact region where the molecular emission comes from (∼1.2″ and 1.0″ for N2 and N5, respectively, see Sect. 3.3), assuming the column density scales with $r^{-0.5}$. Finally, the ALMA continuum maps yield an average deconvolved source size of 0.7″ for N4, smaller than the ALMA resolution. Therefore, we correct the H_2 column density obtained for N4 for the beam dilution with the factor $\frac{HPBW^2+\theta_s^2}{\theta_s^2} = \frac{1.6^2+0.7^2}{0.7^2}$. The resulting H_2 column densities used to compute chemical abundances in Sect. 3.5 are listed in Table 4.6.

4.3 Current physical properties of Sgr B2(N)'s hot cores

The H_2 column densities computed from the dust thermal emission measured in the ALMA continuum maps (Sect. 4.2.4) allow us to determine densities and masses. Rotational temperatures and emission source sizes are used to estimate the current luminosities of the sources.

Table 4.6: H_2 column densities of Sgr B2(N)'s HMCs used to derive chemical abundances.

Source	θ_s [a] ($''$)	N_{H_2} [b] (10^{24} cm^{-2})
N2	1.2(0.4)	1.64(0.53)
N3	0.4(0.1)	0.90(0.17)
N4	0.7(0.1)	2.55(0.66)
N5	1.0(0.4)	0.90(0.27)

Notes. Uncertainties are given in parentheses. [(a)] Size for which the H_2 column density is calculated as described in Sect. 4.2.4. [(b)] H_2 column density calculated for the size indicated in the previous column. This value is used in Fig. 3.11b to plot chemical abundances relative to H_2. The uncertainties are calculated based on the uncertainties on the average H_2 column densities given in Table 4.5 and on the source sizes.

Table 4.7: Physical properties of four HMCs embedded in Sgr B2(N).

Source	R [a] (10^3 au)	N_{H_2} [b] (10^{24}cm^{-2})	M_g (R) [c] ($M_\odot$)	r_0 [d] (10^3 au)	T_0 [e] (K)	ρ_0 [f] (10^{-19}g cm^{-3})	n_0 [g] (10^7 cm^{-3})	L_{tot} [h] (10^5 $L_\odot$)	t_{source} [i] (10^5 yr)	M_* [j] ($M_\odot$)	r_{init} [k] (10^6 au)
N2	8.01(0.50)	1.42(0.39)	151(42)	6.01(1.50)	150 $(^{+90}_{-20})$	3.20(1.53)	1.37(0.65)	2.63$(^{+3.13}_{-1.58})$	2.10$(^{+2.10}_{-1.60})$	42$(^{+20}_{-15})$	1.65(0.67)
N3*	2.00(1.25)	0.90(0.17)	6(1)	2.00(0.50)	150$(^{+20}_{-5})$	5.27(2.96)	2.25(1.26)	0.45$(^{+0.16}_{-0.20})$	0.20$(^{+0.05}_{-0.06})$	18$(^{+3}_{-6})$	0.77(0.55)
N4	8.01(0.50)	0.41(0.04)	43(4)	5.01(1.50)	150$(^{+40}_{-5})$	1.21(0.57)	0.52(0.24)	3.92$(^{+4.17}_{-2.62})$	3.06$(^{+2.34}_{-2.26})$	51$(^{+25}_{-22})$	0.72(0.52)
N5	8.01(0.50)	0.71(0.16)	72(17)	5.01(2.00)	150$(^{+30}_{-5})$	2.09(1.31)	0.89(0.56)	2.82$(^{+1.77}_{-1.52})$	2.25$(^{+1.25}_{-1.45})$	44$(^{+12}_{-14})$	1.04(0.78)

Notes. The uncertainties are given in parentheses. [(a)] Radius of the mean synthesized beam of the ALMA data (Eq. 4.2) [(b)] Average peak H_2 column density for a mean synthesized beam radius R (Eq. 2.34). The uncertainty corresponds to the standard deviation weighted by the error on the ALMA peak flux density, $F_\nu^{\rm beam}$, and on the correction factor for the free-free emission (see Sect. 4.2.2). [(c)] Gas mass of the envelope contained in R (Eq. 2.35). [(d)] Radius of the COM emission (Sect. 3.3). [(e)] Excitation temperature derived from population diagrams (Sect. 3.4). [(f)] Dust mass density at the radius r_0 assuming a standard gas-to-dust mass ratio of 100. [(g)] Density of total hydrogen ($n_{\rm H}$+$2n_{\rm H_2}$) at $r = r_0$ (Eq. 4.6). [(h)] Estimated current luminosity of the source (Sect. 4.3.2). [(i)] Age of the source estimated from its current luminosity (Sect. 4.3.2). [(j)] Mass of the protostar derived from its current luminosity (Sect. 4.4.1, Fig. 4.13c) [(k)] Initial radius of the envelope of the source (Sect. 4.4.3) [(*)] For N3 which is not detected in the ALMA continuum maps at 3 mm, we used the peak flux density measured at 1.3 mm (Sánchez-Monge et al. 2017) with 0.4$''$ resolution (that is R = 2003 au) to derive the H_2 column density and gas mass.

4.3.1 Masses and densities

The masses derived using Eq. 2.35 from the H_2 column densities computed from the dust emission are listed in Table 4.7 for N2–N5, assuming a spherically symmetric envelope with a radius R:

$$R = D\sqrt{\frac{\Omega_{\rm beam}}{\pi}} = \frac{D\,\theta_b}{2\sqrt{\ln 2}} \tag{4.2}$$

with $\theta_{\rm b}$ = 1.6$''$ the mean synthesized beam of the ALMA observations (or 0.4$''$ in the case of N3, Sánchez-Monge et al. 2017).

The gas density in the envelope of each source is assumed to follow a power-law distribution:

$$n_{\rm H}(r) = n_0 \left(\frac{r}{r_0}\right)^{\alpha} , \tag{4.3}$$

where n_0 is the total hydrogen density at r_0, the radius given by Eq. 4.2 with $\theta_{\rm s}$ the source diameter derived from the COM emission (Sect. 3.3). We assume α = -1.5, holding for a free-falling envelope (Shu 1977). As in dense clouds most of the hydrogen is in molecular form here $n_{\rm H_2}(r) = \frac{n_{\rm H}(r)}{2}$. From the masses calculated above, we can compute n_0 as follows:

$$M_{\rm g}(R) = \int_0^{\rm R} \frac{{\rm d}M_{\rm g}(r)}{{\rm d}r}\,{\rm d}r = 4\pi \int_0^{\rm R} \rho_{\rm g}(r)\, r^2\,{\rm d}r = 4\pi \int_0^{\rm R} r^2 \mu_{\rm H_2}\, m_{\rm H}\, n_{\rm H_2}(r)\,{\rm d}r\,. \tag{4.4}$$

By replacing $n_{\rm H}$(r) by its expression (Eq. 4.3) we obtain:

$$M_{\rm g}(R) = 2\pi \int_0^{R} \mu_{\rm H_2}\, m_{\rm H}\, n_0\, r_0^{1.5}\, r^{0.5}\,{\rm d}r\,, \tag{4.5}$$

which finally gives us:

$$n_0 = \frac{M_{\rm g}(R)}{\frac{4}{3}\,\pi\,\mu_{\rm H_2}\, m_{\rm H}\, r_0^{1.5}\, R^{1.5}} \tag{4.6}$$

The resulting densities are given for each HMC in Table 4.7.

4.3.2 Luminosities

We use the radiative transfer code RADMC-3D (version 0.41, Dullemond et al. 2012) to compute temperature profiles in the envelope of N2–N5. RADMC-3D performs radiative transfer calculations using the Monte-Carlo method for a given dust distribution and computes the associated dust temperatures. Each source is modeled as a single protostar surrounded by a 1D spherically symmetric envelope with a radius of 10^6 au (*i.e.* 4.8 pc), which is divided into $5{\times}10^4$ cells. The protostar is defined as a point-source and we assume simple black body radiation by specifying the effective temperature of the protostar, $T_{\rm eff}$. The total luminosity of the protostar is given by the Stefan-Boltzmann law:

$$L_{\rm tot} = 4\,\pi\,\sigma\,R_*^2\,T_{\rm eff}^4 \tag{4.7}$$

where σ is the Stefan-Boltzmann constant and R_* the radius of the protostar.

For simplicity we adopt a single type of interstellar grains and do not include scattering. We use the dust opacities from Ossenkopf & Henning (1994) for dust without ice mantle and coagulated with gas densities of 10^6 cm^{-3} (see Sect. 4.2.3). For each source $5{\times}10^5$ photon packages are emitted one after the other from its central protostar. As they move through the envelope of the source, the photon packages interact with the dust, being absorbed and immediately re-emitted in a different direction and at a different frequency. Every time a photon package penetrates a cell of the envelope, it increases the energy of that cell and thus the dust temperature. The final dust temperature is obtained after all photons have escaped through the outer cell of the model grid (that is the outer edge of the protostellar envelope).

The dust mass density in the envelope of each source is assumed to follow the same power-law distribution as the gas density (Eq. 4.6), with $\rho_0 = \frac{n_0}{2} \times \mu_{\rm H_2} \times \frac{m_{\rm H}}{\chi_{\rm d}}$, assuming a standard gas-to-dust mass ratio of $\chi_{\rm d} = 100$. The dust mass densities are given for each HMC in Table 4.7. Figure 4.9 shows the calculated dust mass density profiles in the envelope of N2–N5. Because

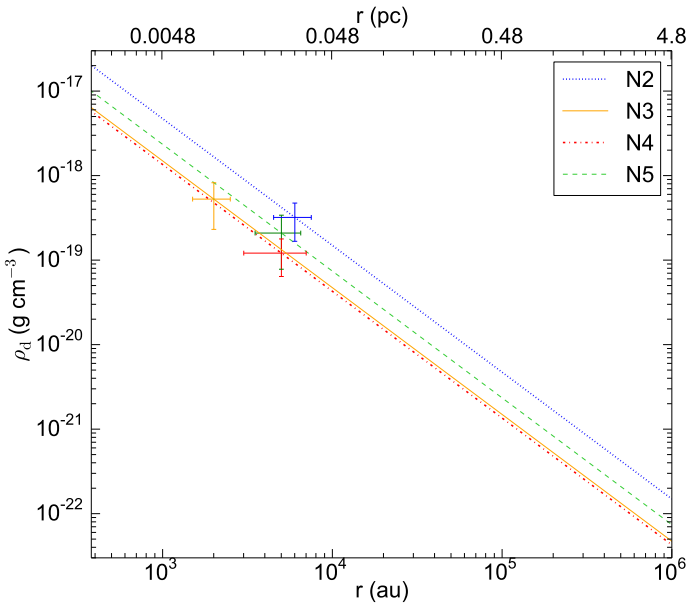

Figure 4.9: Dust mass density profiles derived for Sgr B2(N)'s sources assuming $\rho_d \propto r^{-1.5}$ (Shu 1977). For each source the observational constraint, $\rho(r_0) = \rho_0$ is plotted with errorbars. *Figure taken from Bonfand et al. (2019).*

of the high densities reached in the inner envelopes of the sources, photon packages may get trapped inside optically thick regions in the radiative transfer model, considerably slowing down the simulations. To prevent this effect, we use the so-called Modified Random Walk Method (MRW, Fleck & Canfield 1983) that allows RADMC-3D to predict where the photon package will go next and save computation time.

For each source the total luminosity of the central protostar is adjusted manually until the calculated dust temperature matches the gas kinetic temperature T_0 (see Sect. 3.4) derived from the COM emission at r_0 (see Sect. 3.3). It gives us an estimate of the current luminosity of the sources. We plot in Fig. 4.10 the dust temperature profiles computed by RADMC-3D in the envelope of the four investigated sources along with the luminosity of their central protostars, which are also listed in Table 4.7.

4.4 A physical model for high-mass star formation in Sgr B2(N)

In order to perform the time-dependent chemical modeling of Sgr B2(N)'s hot cores, we need to know their physical history starting from the earlier pre-stellar phase where cold grain-surface chemistry takes place. However, the early stages of high-mass star formation, prior to core formation, are still poorly known. Based on the fraction of star-forming versus quiescent clumps detected in the APEX Telescope Large Area Survey of the Galaxy (ATLASGAL), Csengeri et al. (2014) estimated an upper limit of $\sim 7.5\pm2.5\times10^4$ yr for the quiescent deeply embedded phase ($\bar{n} \sim 4\times10^5$ cm^{-3}) prior to the onset of free-fall collapse, for objects with densities ranging from $\sim 10^4$ to 10^5 cm^{-3} (Csengeri et al. 2017). As seen in Sect. 1.2.2, Wilcock et al. (2012) estimated a lifetime for the starless phase of IRDCs of $\sim2.3\times10^5$ yr, which is a factor $\sim$3 longer than the pre-stellar phase estimated by Csengeri et al. (2014). We decide to use an intermediate time

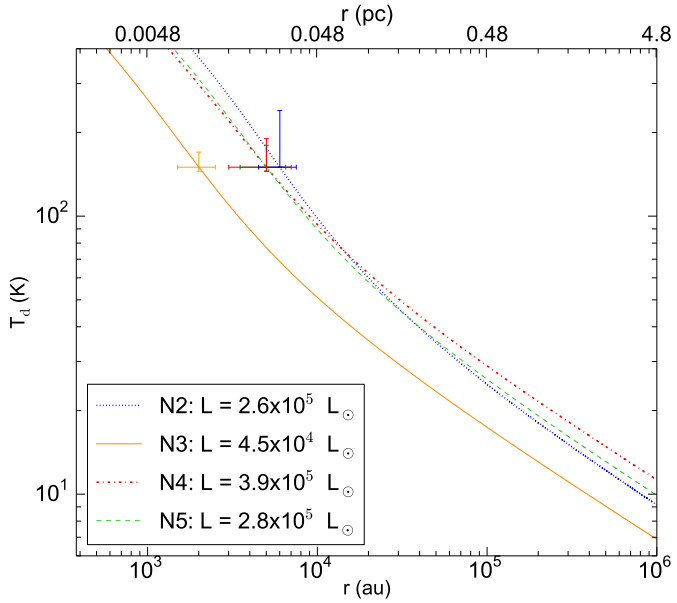

Figure 4.10: Dust temperature profiles computed for Sgr B2(N)'s sources using RADMC-3D, assuming a dust mass density distribution proportional to $r^{-1,5}$ (Fig. 4.9). The observational constraint $T(r_0) = T_0$ used to estimate the current luminosity of each source is plotted with errorbars. *Figure taken from Bonfand et al. (2019).*

of 1 Myr, which is between the IRDC starless phase derived by Wilcock et al. (2012) and the molecular cloud lifetime determined by Jeffreson et al. (2018) (see Sect. 1.2.2), to characterize the low density, cold pre-stellar phase prior to the ignition of the central protostar. During this phase, the envelope of the source undergoes quasi-static contraction, leading to the formation a centrally peaked pre-stellar core. It is followed by a second stage starting with the ignition of the central protostar which rapidly wamrs up its surrounding envelope. In this stage the envelope undergoes a free-fall collapse characterized by the free-fall speed, $v_{\rm ff}$:

$$v_{\rm ff} = \frac{dr}{dt} = \sqrt{2GM_{\rm g}(r)\left(\frac{1}{r} - \frac{1}{r_{\rm start}}\right)} \tag{4.8}$$

with $\mathrm{M_g(r)}$ the mass of gas internal to r. The free-fall collapse starts from the conditions reached at the end of the first stage. In order to characterize the evolution of the physical conditions in the envelopes of N2–N5 during the collapse phase, we trace the trajectory of a parcel of gas gradually infalling toward the central protostar (see Fig. 4.11). The starting radius, $r_{\rm start}$, in Eq. 4.8 is chosen such that the parcel of gas reaches r_0 at $t = t_{\rm source}$ (that is the current age of the source, see Table. 4.7 and Sect. 4.4.1), according to the free-fall governed by its enclosed mass.

The two stages of our physical model along with the associated timescales are schematized in Fig. 4.12. The physical properties (density, visual extinction, dust and gas temperature, and luminosity) achieved at different stages of the high-mass star formation process in our physical model for N2–N5 are given in Table 4.8. The derivation of these parameters is detailed in the following sections.

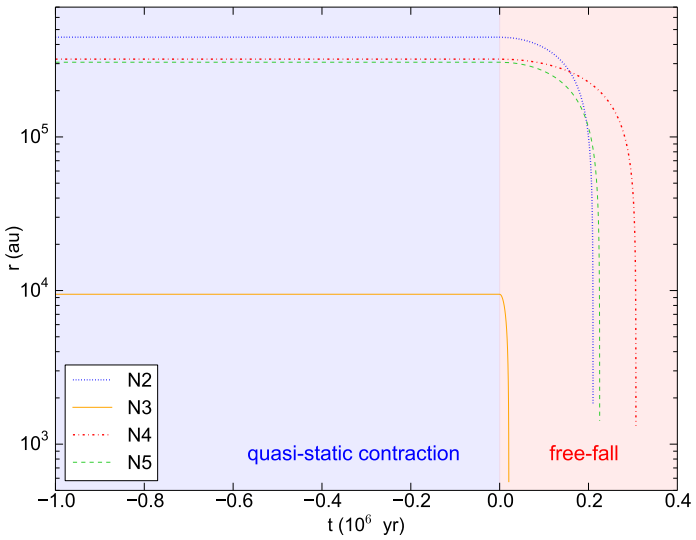

Figure 4.11: Trajectory of a parcel of gas in the envelope of Sgr B2(N2–N5) as function of time. For each source the quasi-static contraction phase is characterized by a single constant radius, $r_{\rm start}$ (see Table 4.8). During the free-fall collapse phase, the parcel of gas gradually falls toward the central protostar with the free-fall speed $v_{\rm ff}$ (Eq. 4.8). *Figure taken from Bonfand et al. (2019).*

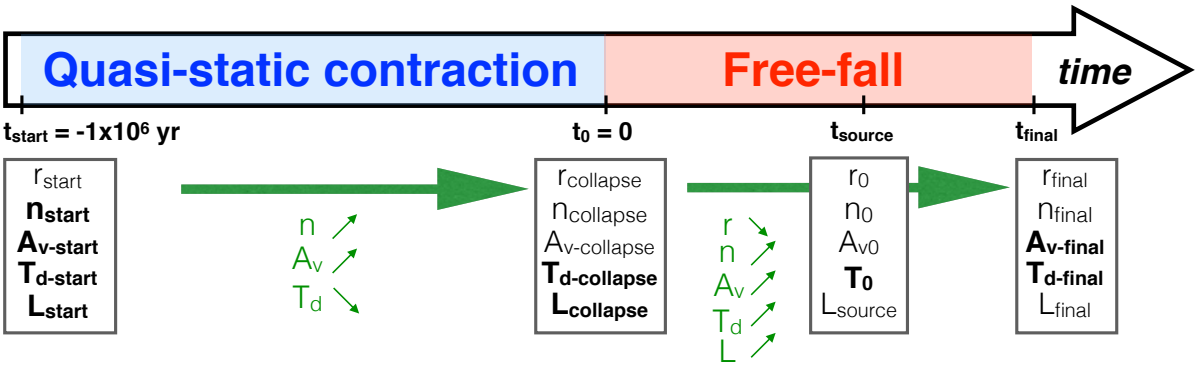

Figure 4.12: Two-stage physical model assumed for the time evolution of Sgr B2(N)'s sources. The physical properties derived at the boundaries of each stage are shown in boxes (see also Table 4.8). The parameters that are common to all sources are highlighted in boldface. The evolution of the physical parameters during each stage is indicated with green arrows. The evolution of $T_{\rm d}$ during the first stage depends on the adopted minimum temperature. *Figure taken from Bonfand et al. (2019).*

4.4.1 Protostellar evolution

As it accretes its surrounding material, a newly formed protostar grows in mass, thus increasing its total luminosity (see Sect. 1.2.2). In order to determine the time evolution of stellar properties (accretion rate, mass, and luminosity) in the early phases of star formation, we use the published results of theoretical calculations for high-mass star formation.

Table 4.8: Parameters of the physical models for Sgr B2(N2–N5).

Parameters	N2	N3	N4	N5
		$\mathbf{t_{start} = -1.0 \times 10^6}$ **yr**		
$r_{\rm start}$ (au)	4.46(5)	9.46(3)	3.21(5)	3.06(5)
$n_{\rm start}$ (cm^{-3})	3.00(3)	3.00(3)	3.00(3)	3.00(3)
$A_{\rm v-start}$ (mag)	2.0	2.0	2.0	2.0
$T_{\rm d-start}$ * (K)	16.0	16.0	16.0	16.0
$T_{\rm K-start}$ (K)	$T_{\rm min}$	$T_{\rm min}$	$T_{\rm min}$	$T_{\rm min}$
$L_{\rm start}$ ($L_\odot$)	0	0	0	0
		$\mathbf{t_0 = 0}$		
$r_{\rm collapse}$ (au)	$r_{\rm start}$	$r_{\rm start}$	$r_{\rm start}$	$r_{\rm start}$
$n_{\rm collapse}$ (cm^{-3})	2.14(4)	2.19(6)	1.00(4)	1.86(4)
$A_{\rm v-collapse}$ (mag)	75.3	297	19.1	43.7
$T_{\rm d-collapse}$ (K)	$T_{\rm min}$	$T_{\rm min}$	$T_{\rm min}$	$T_{\rm min}$
$T_{\rm K-collapse}$ (K)	$T_{\rm min}$	$T_{\rm min}$	$T_{\rm min}$	$T_{\rm min}$
$L_{\rm collapse}$ ($L_\odot$)	0	0	0	0
		$\mathbf{t_{final}}$		
$t_{\rm final}$ (yr)	2.10(5)	2.06(4)	3.07 (5)	2.25(5)
$r_{\rm final}$ (au)	1.38(3)	5.70(2)	1.32(3)	1.42(3)
$n_{\rm final}$ (cm^{-3})	8.27(7)	1.48(8)	3.81(7)	5.91(7)
$A_{\rm v-final}$ (mag)	500	500	500	500
$T_{\rm d-final}$ (K)	400	400	400	400
$T_{\rm K-final}$ (K)	400	400	400	400
$L_{\rm final}$ ($L_\odot$)	2.63(5)	4.71(4)	3.92(5)	2.82(5)

Notes. Physical properties derived for each source at three different stages of the high-mass star formation process (see also Fig. 4.12). The cloud free-fall collapse is halted at a $T_{\rm d}$ = 400 K. $X(Y)$ means $X \times 10^Y$. $^{(*)}$ $T_{\rm d-start}$ = 16 K is valid for our models with $T_{\rm min}$ = 10 K and 15 K. For $T_{\rm min}$ = 20 K, $T_{\rm d-start}$ = 20 K.

Peters et al. (2011) report the results from the first 3D radiation-magnetohydrodynamical (RMHD) simulations of high-mass star formation including ionization feedback. They model the free-fall collapse of a magnetized rotating molecular cloud containing 1000 $M_\odot$. The central core, with a gas density of $\rho = 1.27 \times 10^{-20}$ g cm^{-3} within a radius of 0.5 pc, is surrounded by an envelope characterized by a density distribution $\propto r^{-1.5}$. They assume an initial temperature of 30 K. After the first 20 kyr of simulation, many sink particles are formed, simulating a group of young stars all contributing to the radiative feedback (see their Fig. 1a, run E). In the initial accretion phase the first sink particle reaches a high accretion rate $> 10^{-3} M_\odot$ yr^{-1}, which falls down to $\sim 10^{-4} M_\odot$ yr^{-1} after 0.7 Myr (see their Fig. 1b, run E). At the end of the simulation, the first sink particle is by far the most massive one. Although its accretion rate drops significantly when secondary sink particles form, it continues accreting material until the end of the simulation. Based on the accretion rate evolution of the most massive sink particle, without taking into account the influence of the formation of secondary particles, we approximate the relation $\dot{M}(t)$, characterizing the time-dependent evolution of the accretion rate for a young high-mass protostar. Figure 4.13a (dashed line) shows the accretion rate as a function of time for a protostar that starts accreting material from its surrounding envelope

Table 4.9: Indices of the power-law functions for density and visual extinction.

	Index	
Source	$n_{\rm H}(t)$	$A_{\rm v}(t)$
N2	-0.17	-0.32
N3	-0.57	-0.43
N4	-0.10	-0.20
N5	-0.16	-0.27

Notes. Indices of the power-law functions $n_{\rm H}(t)$ (Fig. 4.14)a and $A_{\rm v}(t)$ (Fig. 4.14)b.

at $t_0 = 0$. By integrating the relation $\dot{M}(t)$ we obtain the protostellar mass as a function of time, $M(t)$. Figure 4.13b (dashed line) shows that after 10^6 yr the protostar reaches a final mass of about 30 $M_\odot$. In order to derive the time-dependent evolution of the protostellar luminosity from the relation $M(t)$ (Fig. 4.13b), we use the mass-luminosity relation derived by Hosokawa & Omukai (2009) for spherically accreting protostars with a constant accretion rate of $\dot{M} = 10^{-4} M_\odot$ yr^{-1} (see Fig. 4.13c). The resulting luminosity is plotted as a function of time in Fig. 4.13c (dashed line). It shows that after 10^6 yr the protostar reaches a final luminosity of $\sim 10^5$ $L_\odot$, which is not high enough to reproduce the luminosities estimated for Sgr B2(N2-N5) (up to $3.9{\times}10^5$ $L_\odot$, Sect. 4.3.2). In order to form more massive and thus more luminous protostars, we simply assume that the accretion rate does not drop below $10^{-4} M_\odot$ yr^{-1} (Fig. 4.13a, solid line). Using this simple assumption, protostars with masses $> 10^2$ $M_\odot$ and luminosities up to $\sim 2{\times}10^6$ $L_\odot$ are formed after 10^6 yr (Figs. 4.13b and d, solid lines). We use the relation $L(t)$ (Fig. 4.13d) to estimate the age, $t_{\rm source}$, of Sgr B2(N2-N5) based on their current luminosity derived in Sect. 4.3.2 (see also Table 4.7).

4.4.2 Density evolution

At the beginning of the quasi-static contraction phase we assume the same initial conditions as in Garrod (2013) and subsequent papers, with low density of $n_{\rm start} = 3{\times}10^3$ cm^{-3}, typical for translucent clouds (Snow & McCall 2006). We make the simple assumption that the density at a given radius increases linearly as a function of time in log-log space, from $n_{\rm start}$ to $n_{\rm collapse}$, which is the density reached at the end of the pre-stellar phase according to Eq. 4.3 (within the radius $r_{\rm start}$, see also Table 4.8). For each source $n_{\rm H}(t)$ is thus described by a power-law function (in semi-log space), plotted in Fig. 4.14a.

After the onset of the free-fall collapse, the density along the trajectory of the free-falling parcel of gas follows the power-law profile given by Eq. 4.3. For simplicity we neglect the time variation of $n_{\rm H}(r)$. The gas densities computed along the trajectory of the parcel of gas infalling through the envelopes of N2–N5 are plotted in Figs. 4.15a and 4.16a.

4.4.3 Visual-extinction evolution

The quasi-static contraction phase starts at visual extinction, $A_{\rm v-start} = 2$ mag, typical for translucent clouds (Snow & McCall 2006). For simplicity we assume that the visual extinction at a given radius increases linearly as a function of time in log-log space from $A_{\rm v-start}$ to $A_{\rm v-collapse}$, which is the visual extinction reached at the end of the pre-stellar phase according

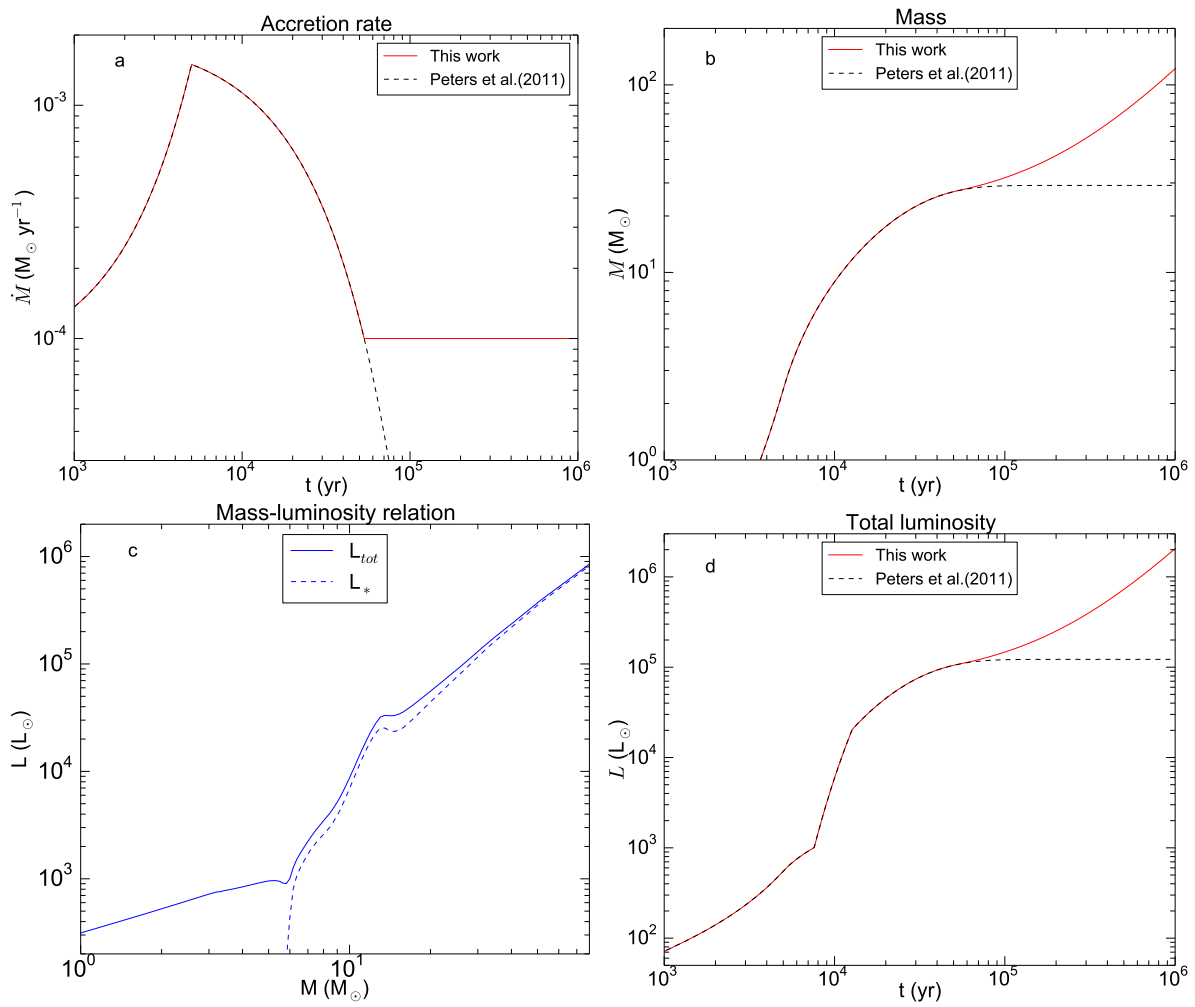

Figure 4.13: **a** Accretion rate as a function of time approximated from the results of RMHD simulations of high-mass star formation presented by Peters et al. (2011) (dashed line). **b** Protostellar mass evolution as a function of time derived from the accretion rate relation, $\dot{M}(t)$ (panel a, dashed line). **c** Total luminosity (solid line) and protostar luminosity (dashed line) as a function of the protostellar mass given by the mass-luminosity relation of Hosokawa & Omukai (2009). **d** Total luminosity of the protostar as a function of time derived from the relation $M(t)$ (panel b, dashed line) and using the mass-luminosity relation of Hosokawa & Omukai (2009) (panel c, solid line). In panels **a**, **b**, and **d** the solid red line shows the result obtained if we keep the accretion rate constant at 10^{-4} $M_\odot$ yr^{-1} after $\sim 6{\times}10^4$ yr in panel **a**. *Figure taken from Bonfand et al. (2019).*

to Eq. 4.9 (within the radius $r_{\rm start}$, see also Table 4.8). $A_{\rm v}(t)$ is plotted for the four source, N2–N5, in Fig. 4.14b.

After the onset of the free-fall collapse, the visual extinction along the trajectory of the free-falling parcel of gas is computed from the gas density as follows (Bohlin et al. 1978):

$$A_{\rm v}(r) = A_{\rm v-start} + \frac{3.1}{5.8 \times 10^{21}} \int_{r_{\rm init}}^{r} n_{\rm H}(r)\, {\rm d}r \tag{4.9}$$

with $r_{\rm init}$ the initial radius of the source envelope computed such that $n_{\rm H}(r_{\rm init}) = n_{\rm start}$, thus

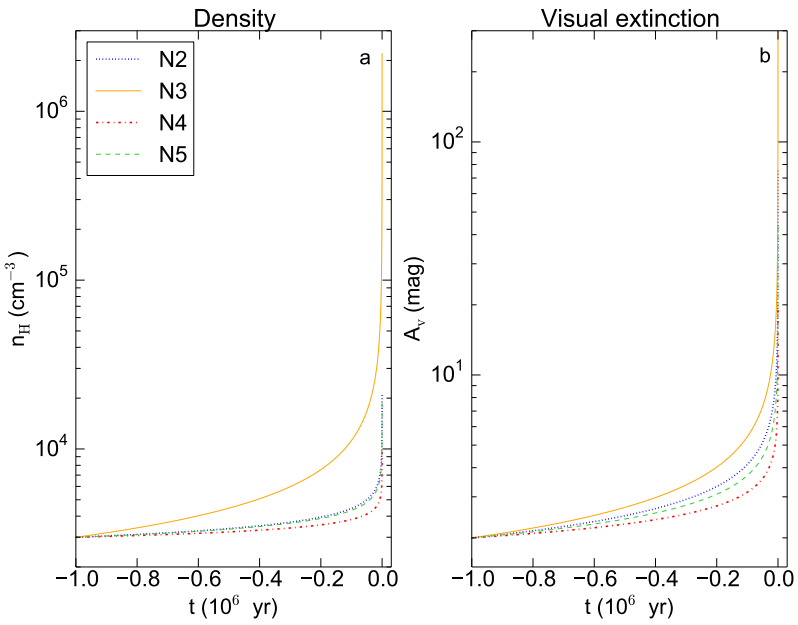

Figure 4.14: **a** Time evolution of the total hydrogen density during the quasi-static contraction phase for Sgr B2(N)'s sources. Densities are derived for a constant radius, $r = r_{\rm start}$. **b** Same as a but for the evolution of the visual extinction. The indices of the power-law functions plotted in both panels are given in Table. 4.9. *Figure taken from Bonfand et al. (2019).*

$r_{\rm init} = r_0 \left(\frac{n_{\rm start}}{n_0}\right)^{-\frac{1}{1.5}}$ (see Table 4.7). During the free-fall collapse phase the visual extinction increases with density, until $A_{\rm v-max} = 500$ mag. For simplicity we neglect the time variation of $A_{\rm v}(r)$. The visual extinction computed along the trajectory of the parcel of gas infalling through the envelopes of N2–N5 are plotted in Figs. 4.15b and 4.16b.

4.4.4 Thermal history

During the quasi-static contraction phase preceding the free-fall collapse, as density and visual extinction increase we expect a gradient of temperature in the outer part of the envelopes of N2–N5 where dust grains are initially exposed to external UV photons. In order to characterize the behavior of the dust temperature during the cold phase preceding the warming up of the envelope, we adopt the visual-extinction-dependent parametric equation of the dust temperature derived by Garrod & Pauly (2011) and Zucconi et al. (2001) (see Fig. 4.17). Assuming exposure to a standard ISRF (1 G_0), the dust temperature is given by (Garrod & Pauly 2011):

$$T_{\rm d} = 18.67 - 1.637\,A_{\rm v} + 0.07518\,A_{\rm v}^2 - 0.001495\,A_{\rm v}^3 + 0.316\ {\rm K} \tag{4.10}$$

which is valid in the range $0 \leq A_{\rm v} \leq 10$ mag. For the range $10 \leq A_{\rm v} \leq 400$ mag we use the equation given by Zucconi et al. (2001):

$$T_{\rm d}^{Zuc} = [T_{\rm d}({\rm VNIR})^{5.6} + T_{\rm d}({\rm MIR})^{5.6} + T_{\rm d}({\rm FIR})^{5.6}))]^{1/5.6} \tag{4.11}$$

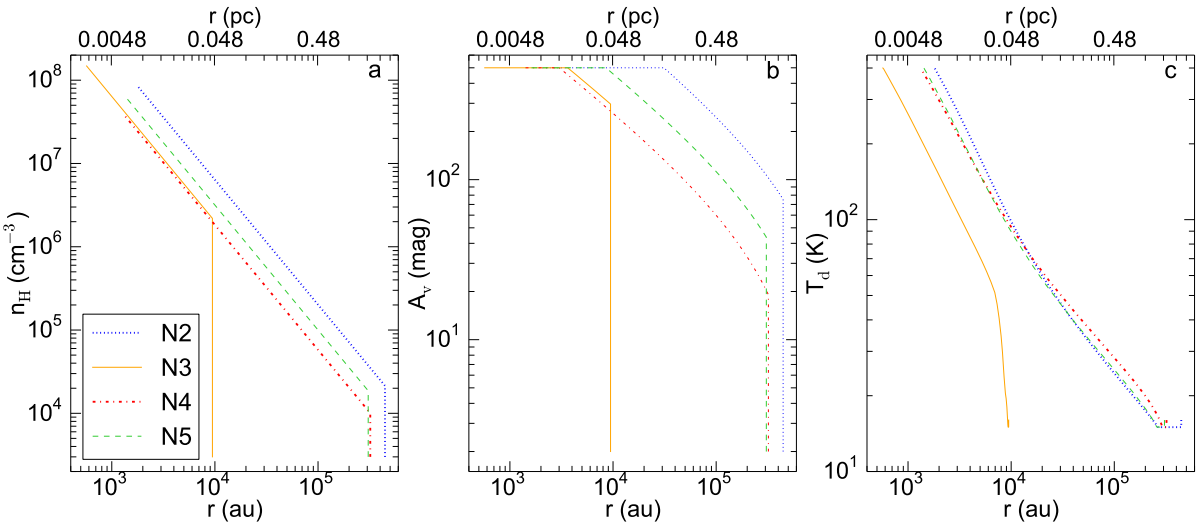

Figure 4.15: **a** Gas density along the trajectory of a parcel of gas gradually infalling through the envelope. The quasi-static contraction phase is characterized by the density increasing over time at a constant radius (Fig. 4.14a). The subsequent free-fall collapse phase assumes a density distribution proportional to $r^{-1.5}$. **b** Visual extinction calculated as a function of the density along the trajectory of a parcel of gas gradually infalling through the envelope. The quasi-static contraction phase is characterized by the extinction increasing over time at a constant radius (Fig. 4.14b). During the free-fall collapse phase the extinction increases with density (Eq. 4.9) until $A_{v-max} = 500$ mag. **c** Temperature evolution along the trajectory of a parcel of gas gradually infalling through the envelope (see also Fig. 4.19). The evolution of the temperature during the quasi-static contraction phase is shown for a minimum temperature $T_{min} = 15$ K. *Figure taken from Bonfand et al. (2019).*

where VNIR, MIR, and FIR stand for the contributions from the visual plus near-infrared, mid-infrared, and far-infrared, respectively, given by:

$$T_d(\text{VNIR}) = 43A_v^{-0.56} - 77A_v^{-1.28} \tag{4.12}$$

$$T_d(\text{MIR}) = 7.9A_v^{-0.089}(1.8 - 0.098A_v^{0.5} + 7.9 \times 10^{-5}A_v^{1.5})^{1/5.6} \tag{4.13}$$

$$T_d(\text{FIR}) = 6.2 - 0.0031A_v\,. \tag{4.14}$$

For an initial visual extinction of $A_{v-start} = 2$ mag, Eq. 4.10 leads to $T_{d-start} = 16$ K. Then, as the outer layers of the cloud progressively become optically thicker, it also gets colder (T_d <10 K for A_v >8 mag, see Fig. 4.17). However, as seen previously in Sect. 1.4.1, dust temperature measurements toward the GC region report higher dust temperatures (20–28 K, see Sect. 5.3.4). In order to keep our physical model physically meaningful and account for the higher temperatures expected toward the GC region for dust grains likely exposed to a stronger ISRF than the standard value, we define an arbitrary minimum dust temperature, T_{min}, which represents the lowest temperature that is allowed in the models for N2–N5. Figure. 4.18 shows the dust temperature as a function of time obtained from Eqs. 4.10 and 4.11, assuming different T_{min}. For simplicity, the gas kinetic temperature, T_K, is held constant throughout the whole quasi-static contraction phase, with $T_K = T_{min}$.

The cold 1 Myr pre-stellar phase, is followed by the ignition of the central protostellar

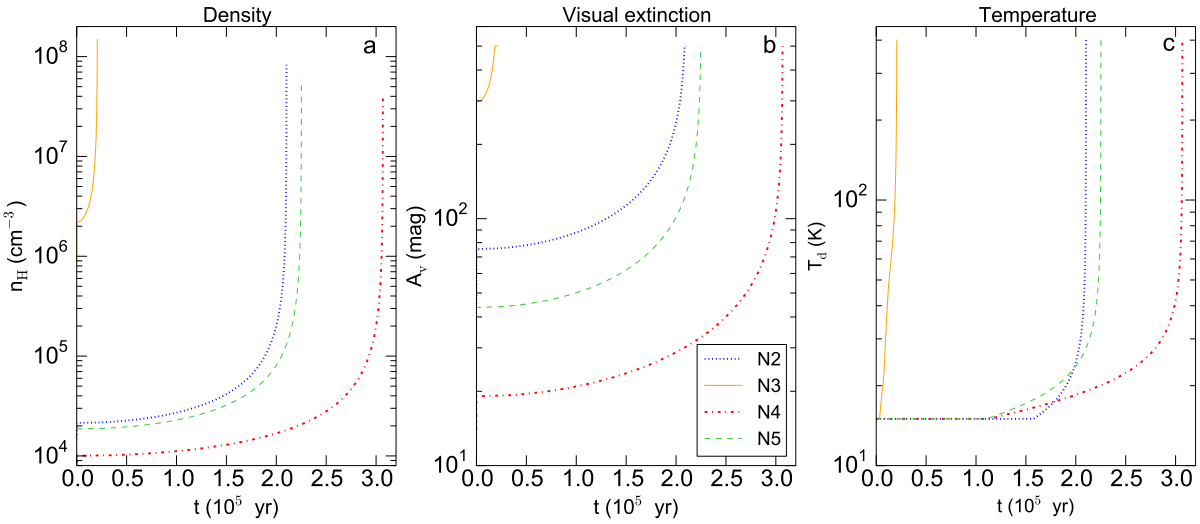

Figure 4.16: **a** Gas density as a function of time along the trajectory of a parcel of gas gradually infalling through the envelope of Sgr B2(N)'s sources (see also Fig. 4.15). **b** Visual extinction evolution as a function of time along the trajectory of a parcel of gas gradually infalling through the envelope of the sources, until $A_{\mathrm{v-max}} = 500$ mag. **c** Dust temperature evolution as a function of time along the trajectory of a parcel of gas gradually infalling through the envelope of the sources, until $T_{\mathrm{max}} = 400$ K and for $T_{\mathrm{min}} = 15$ K. Gas and dust temperatures are assumed to be well coupled. *Figure taken from Bonfand et al. (2019).*

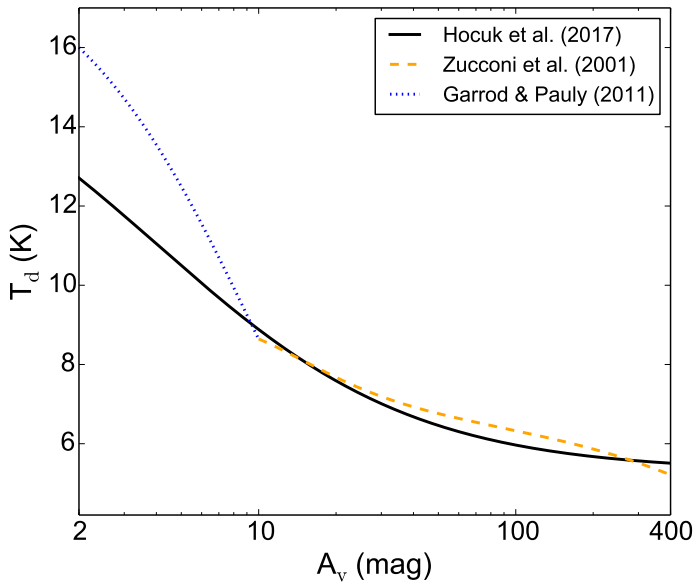

Figure 4.17: Parametric expressions for the dust temperature as a function of visual extinction.

object. As its total luminosity increases, the temperatures in the envelope increase and thermal heating from the central protostar progressively dominating the dust heating over the external radiation field. Based on the evolution of the luminosity over time, $L(t)$ (Sect. 4.3.1), we compute for each source dust temperature profiles for different luminosities, that is at different

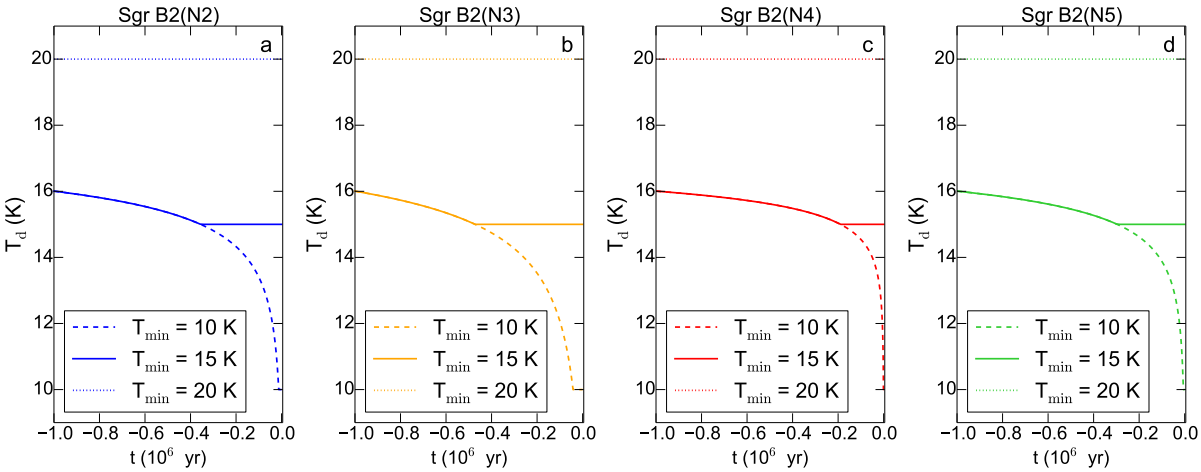

Figure 4.18: Time evolution of the dust temperature during the quasi-static contraction phase (Eqs. 4.10 and 4.11). Temperatures are computed for a constant radius, $r = r_{\rm start}$, and assuming three different $T_{\rm min}$. *Figure taken from Bonfand et al. (2019).*

stages of star formation (see Fig. 4.19). Based on the relation $r(t)$ (Fig. 4.11) we derive the temperature evolution along the trajectory of a parcel of gas free-falling through the envelopes of Sgr B2(N2-N5) during the collapse phase (see Fig. 4.19, solid red line). The free-fall collapse phase stops when the temperature reaches $T_{\rm max} = 400$ K. Given the high densities and high visual extinctions reached in the envelope of Sgr B2(N2-N5), gas and dust temperatures are assumed to be well coupled during the free-fall collapse phase such that $T_{\rm K} = T_{\rm d}$.

4.5 Star formation evolutionary sequence in Sgr B2(N)

In order to assess the evolutionary stage of the HMCs embedded in Sgr B2(N) we compare their association with Class II methanol masers, (UC)HII regions, and molecular outflows, which are thought to trace different phases of star formation, from the IRDC to the UCHII phase. As seen previously in Sect. 1.2.2, Class II methanol masers are expected to trace the early stages of high-mass star formation, when protostellar objects are formed, but not yet evolved enough to ionize the surrounding gas and produce a detectable (UC)HII region. The maser emission then remains active after first, a hyper-, and then an ultra compact-HII region has formed around the (proto)star and finally stops as the UCHII region expands. van der Walt (2005) estimated the lifetime of Class II methanol masers between 2.5×10^4 and 4.5×10^4 yr. After this period, the HII region then exists without the maser emission. This suggests that the main HMCs, N1 and N2, are already more evolved than the fainter sources, N3–N5, for which the maser emission is still detectable. N5 is associated with both a UCHII region and a Class II methanol maser, which might suggest that it is in an evolutionary phase between N3/N4 and N1/N2, when a UCHII region has formed and coexists with maser emission. Class II methanol masers are also thought to appear before an outflow is detectable (Codella et al. 2004), then both coexist in the same phase before the maser switches off. Because no outflow has been clearly detected toward N2, it might suggest that the source is more evolved than the other cores because a UCHII region is already detected in the source and no Class II methanol maser has been reported. However, Belloche et al. (2017) mentioned that chemical models

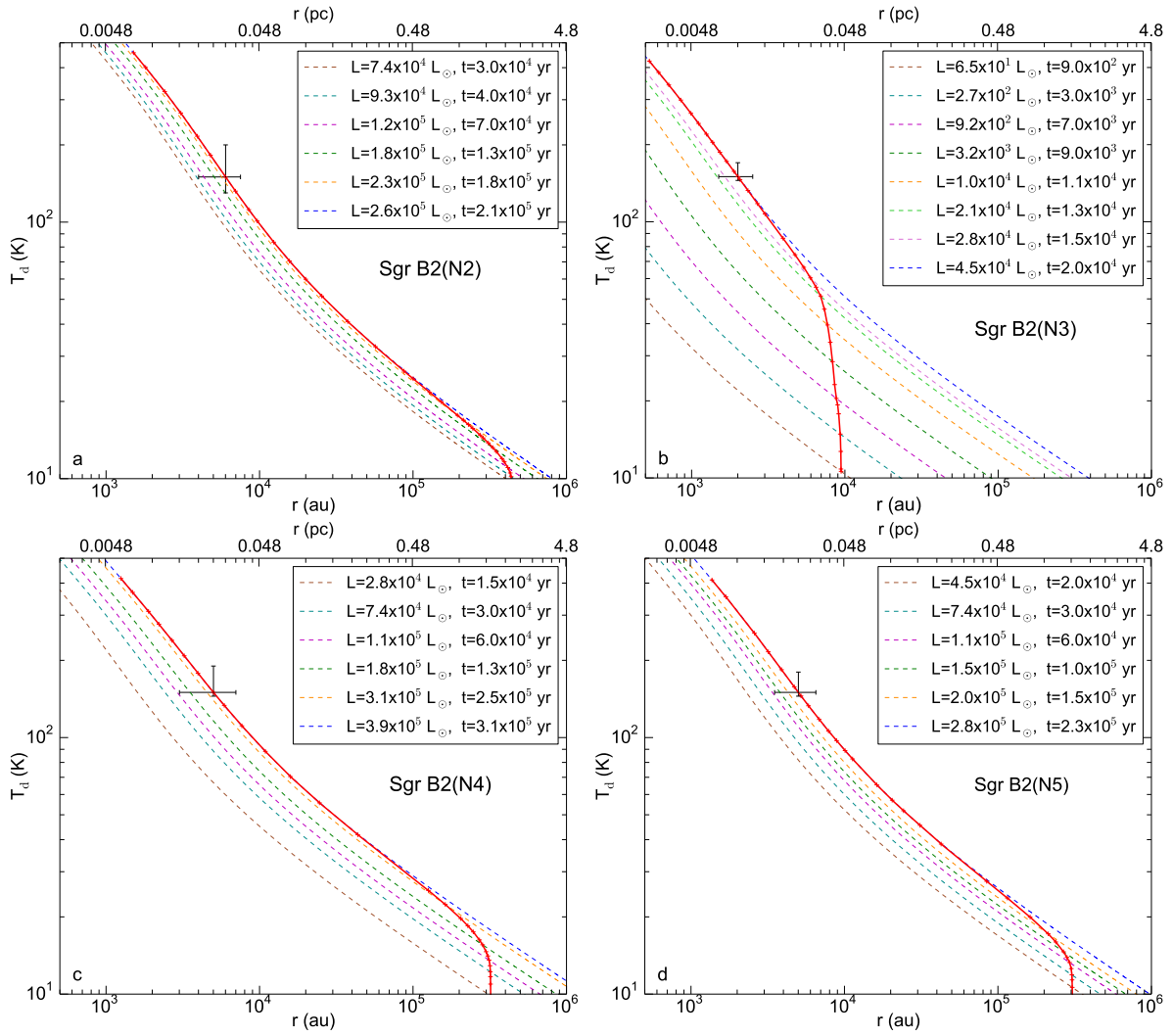

Figure 4.19: In each panel the dashed lines show the dust temperature profiles in the envelope during the free-fall collapse phase, computed using RADMC-3D with different luminosities (*i.e.* at different evolutionary stages). The observational constraint, $T(r_0) = T_0$, used to derive the current luminosity of the source is plotted with errorbars. In each panel the solid red line shows the evolution of the dust temperature along the trajectory of a parcel of gas infalling toward the central protostar. *Figure taken from Bonfand et al. (2019).*

predict a decrease in the gas phase fractional abundance of C_2H_5CN after sublimation of the ice mantles of interstellar dust grains while the abundance of C_2H_3CN increases (see their Fig. 3). An abundance ratio of $[C_2H_5CN]/[C_2H_3CN] = 14.8$ is measured toward N2, about 2–3 times higher than that of N3–N5 (6.2, 7.0, and 5.2, respectively, see Table A.1 and Fig. 3.11), which might suggest that it is younger than the other sources. This last consideration is in contradiction with the conclusion derived from the association of N2 with an already detectable UCHII region. One explanation could be that the COM emission observed toward N2 in our 3 mm data comes from a source associated neither with the UCHII region K7 nor the water masers detected in this region, and too young to show outflow emission on the scales probed with the EMoCA survey. Indeed, as noted already before, we measured a significant offset of

0.42″ (see Table 3.1) between the position of peak line density and the position of the UCHII region, K7. This hypothesis seems to be confirmed with ALMA datasets obtained at higher angular resolution (∼0.4″), with the detection of several distinct continuum sources around N2/K7 (Belloche et al. 2019; Sánchez-Monge et al. 2017). The case of N1 is also puzzling because as discussed in Sect. 4.1.2, its position coincides with a powerful water maser outflow which may actually originate from a different source than that which drives the UCHII region K2, a situation reminiscent of the archetypical UCHII region W3(OH), which has powerful OH and methanol masers in its expanding envelope (Menten et al. 1992) and is separated by 5″ from the multiple HMC W3(OH)-H_2O (Wyrowski et al. 1999). Like Sgr B2(N1), the latter drives a powerful bipolar H_2O maser outflow (Hachisuka et al. 2006), but shows no methanol maser emission.

Figure 4.20 shows an attempt to classify Sgr B2(N)'s HMCs according to their estimated evolutionary stage. Among the three new HMCs, N5 would be the most evolved source because it is associated with both an outflow and a Class II methanol maser, and has already entered the UCHII phase. N4 appears to be the youngest core because it is only associated with Class II methanol maser emission. With an associated methanol maser and a detected outflow but no associated UCHII region, N3 would be in-between. As mentioned above, the status of N2 is unclear. In Sect. 3.1.2 we have also identified two more objects in the map of spectral line density (Fig. 3.1), AN09 and N5-West which both lack association with any known class II methanol masers or (UC)HII region. This could suggest that these protostellar objects are even younger than N4. However N5-West coincides with the positions of several water masers (see Fig. 4.3). Another explanation could be that it is an intermediate- or low-mass object which does neither trigger class II methanol maser emission nor produce a HII region during its lifetime.

In Fig. 4.20 we also give estimates of the class II methanol maser, UCHII, and HMC lifetimes in Sgr B2(N). In a previous analysis of Sgr B2(N), Belloche et al. (2013) used the UCHII regions reported by Gaume et al. (1995) to estimate a star formation rate of 0.028–0.039 $M_\odot$ yr^{-1} averaged over 10^5 yr for the whole Sgr B2 complex. We assume a constant star formation rate to estimate the lifetime of Sgr B2(N)'s HMCs. Combining the results of Gaume et al. (1995) and De Pree et al. (2015), we count ten HII regions within the ALMA primary beam centered between N1 and N2 (see Fig. 4.5b). Eight of these sources are UCHII regions. Only five HMCs are detected in the same area. Considering a lifetime of $\sim 10^5$ yr for the UCHII regions (Peters et al. 2010), we estimate a lifetime of $10^5 \times \frac{5}{8} \sim 6\times10^4$ yr for Sgr B2(N)'s HMCs. In the same way we derive a statistical lifetime of approximately 4×10^4 yr for the Class II 6.7 GHz methanol masers detected in this area, which is, given the low number statistics of the Sgr B2(N) region, surprisingly consistent with the lifetime derived by van der Walt (2005) for Class II methanol masers (2.5×10^4 to 4.5×10^4 yr).

Our classification of the HMCs embedded in Sgr B2(N) in a single evolutionary sequence has to be seen as tentative only. We note some contradictions between the evolutionary sequence for the HMCs embedded in Sgr B2(N) estimated based on their association with Class II methanol masers, UCHII regions, and/or outflows, and the ages of the sources derived from their current luminosities (see Sect. 4.4.1). For instance, in our simple treatment, given its lower luminosity, N3 is apparently younger than the other sources (see Table 4.7), which is not consistent with the evolutionary sequence suggested above. This may show some limitations on our physical model for high-mass star formation in Sgr B2(N) (see discussion in Sect. 4.6).

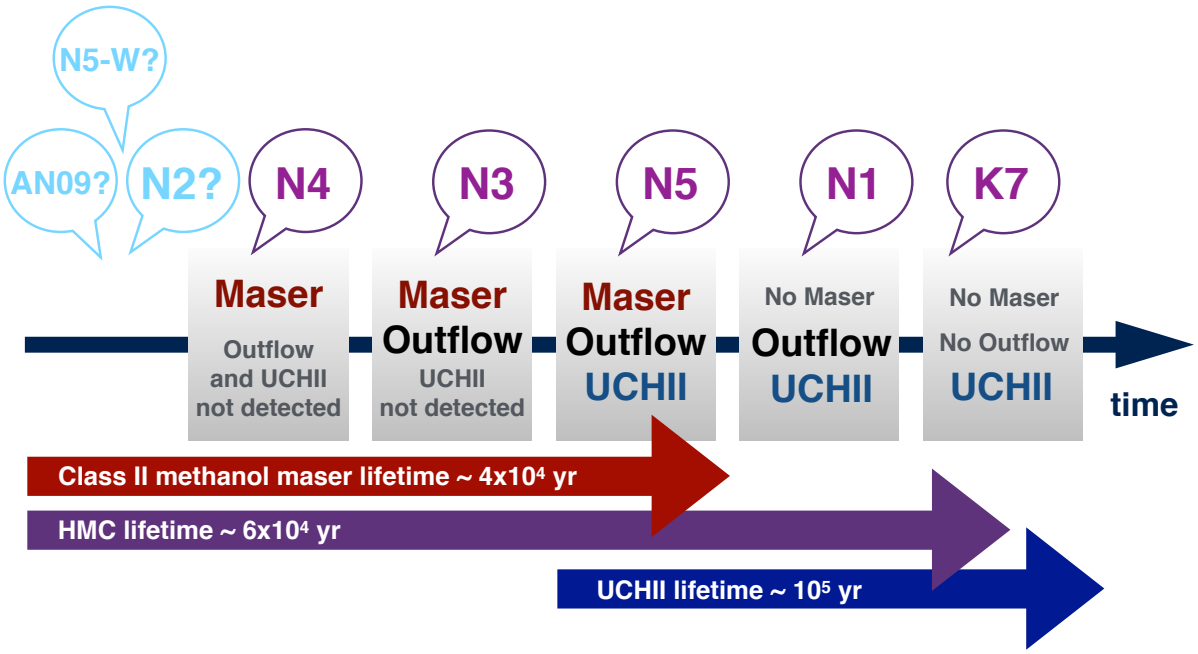

Figure 4.20: Proposed evolutionary sequence for all the HMCs embedded in Sgr B2(N) based on their associations with UCHII regions, Class II methanol masers, and outflows. The status of the sources indicated in light blue is unclear. The UCHII region K7 and the HMC N2 may not be associated but instead two different sources. *Figure adapted from Bonfand et al. (2017).*

4.6 Limitations on our physical model for Sgr B2(N)'s hot cores

The contradictions presented in the previous section between the evolutionary sequence for the HMCs embedded in Sgr B2(N) estimated based on their association with class II methanol masers, UCHII regions, and/or outflows, and the ages derived from their current luminosities point out some caveats in the physical models derived for N2–N5. First the ages of the HMCs, $t_{\rm source}$, estimated using the relation $L(t)$ derived in Sect. 4.4.1 are unlikely to be accurate because our analysis assumes that the evolution of the accretion rate, $\dot{M}(t)$, is the same for all sources, although the density measured at a given radius toward N2 is a factor 3.2, 3.5, and 2.0 higher than that of N3, N4, and N5, respectively (Fig. 4.15b). In addition, the simulations of Peters et al. (2011) were set up for a molecular cloud with a central core gas mass density of $\rho_{\rm g} = 1.27 \times 10^{-20}$ g cm^{-3} (that is a dust mass density $\rho_{\rm d} = 1.27 \times 10^{-22}$ g cm^{-3} assuming a standard gas-to-dust mass ratio of 100) within a radius of 0.5 pc, which is about 10–40 times lower than the values we derive for Sgr B2(N2-N5) at the same radius (Fig. 4.9). Using the mass-luminosity relation provided by Hosokawa & Omukai (2009) for a constant accretion rate of 10^{-4} $M_\odot$ yr^{-1}, the final mass of $\sim$ 30 $M_\odot$ obtained using the model from Peters et al. (2011) leads to a final luminosity of $\sim 10^5 L_\odot$, significantly lower than the values we derive for Sgr B2(N2-N5) (see Table. 4.7). Our simplified treatment, in which we assumed that the accretion rate does not drop below $10^{-4} M_\odot$ yr^{-1} to form more massive and more luminous objects, results in significant differences in the time evolution of N3's physical parameters ($n_{\rm H}$, $A_{\rm v}$, and T) compared to the other three sources. Given its lower luminosity, N3 is apparently younger than the other sources (see Table 4.7). In the framework of our model, this results in a faster increase of the density and temperature along the trajectory of the modeled parcel

of gas during the free-fall collapse phase of N3. This might suggest that the relations $\dot{M}(t)$, $M(t)$, and $L(t)$ we derived in Sect. 4.4.1 do not represent accurately the physical evolution of N2-N5. Furthermore, in the evolutionary sequence shown in Fig. 4.20, N4 appears younger than N3, based on the molecular outflow signature detected toward N3, while N4 does not show any evidence of outflow yet. This is in contradiction with the analysis in which we find that N3 is the youngest of the four investigated hot cores. This is another indication that the short evolution timescale we obtain here for N3 may not represent well the physical evolution of the source. We also point out that the ages estimated for N2, N4, and N5 are about four times longer than the hot core lifetime we estimated in the previous section on the basis of a very simple statistical argument involving the number of detected hot cores and UCHII regions. This might suggest that the accretion rate, $\dot{M}(t)$, of these sources is/was actually higher than what we have assumed here.

Finally, as noted already in Sect. 3.6, Csengeri et al. (2018) found that methanol traces the accretion shocks resulting from the interaction between the collapsing envelope and a potential accretion disk toward G328.2551-0.5321, such that the O-bearing COM emission detected in the envelope of G328.2551-0.5321 arises from accretion shocks rather than from the region radiatively heated by the protostar itself. If such a mechanism is at play in Sgr B2(N) at scales smaller than the beam of the EMoCA survey, then inferring the luminosity of the protostars from the rotational temperature measured at the radius of the COM emission as we did in Sect.3.2 would be wrong. The thermal history derived for Sgr B2(N2–N5) (see Sect. 4.4.4) would then be incorrect.

In order to better represent the extreme physical conditions (densities/masses, luminosities) of Sgr B2(N)'s hot cores and give an accurate estimate of their age, RMHD simulations treating specifically their different physical properties will be needed. In addition a more self-consistent treatment of the accretion rate, mass, and luminosity evolution (that is, taking into account the time-dependent evolution of the accretion rate to derive the mass-luminosity relation) is also required. However, our treatment here is not intended to represent the complexity of cloud-collapse dynamics but rather to provide a simple way to model the behavior of the cloud chemistry under such conditions. Applied to Sgr B2(N)'s sources our simplified approach will enable us to investigate the evolution of their chemical composition using chemical models (see Chaps. 5 and 6).

Chapter 5

Chemical modeling of Sgr B2(N)'s hot cores

Contents

In the previous chapters (Chap. 3 and 4) I showed how we used observational data to derive the physical properties and current molecular inventory of Sgr B2(N)'s hot cores. In this chapter I show the results of the time-dependent chemical simulations based on the physical history of Sgr B2(N)'s hot cores. We use the astrochemical code MAGICKAL (Garrod 2013) to compute time-dependent chemical abundances and study the mechanisms that are responsible for the production of specific COMs. In particular, we investigate the influence of different environmental factors (CRIR, minimum dust temperature and ISRF) on the formation of COMs.

This chapter is largely based on Bonfand et al. (2017) and Bonfand et al. (2019). Other references are mentioned explicitly in the text.

5.1 Astrochemical models

Astrochemical models are widely used over a broad range of physical conditions to investigate in detail the mechanisms that are responsible for the production of the numerous (complex) species detected in the ISM. Based on chemical networks containing thousands of chemical reactions and processes (see Sect. 5.1.1), chemical models allow us to study the coupled gas-grain chemistry evolution over time (see Sect. 5.1.2) in various regions of the ISM. The accuracy of such models is limited by the availability and robustness of laboratory measurements of the rates of the chemical reactions and processes included in the chemical network used by the model. There are still many processes, in particular grain-surface processes, suffering from the lack of theoretical and experimental data, which has an impact on the accuracy of chemical model results (see

Sect. 6.2). That is why a constant effort is needed from theoreticians, experimentalists, and observers to improve the state-of-the-art chemical models and our understanding of the ISM chemistry. An excellent way to test the predictions of chemical models is to compare the numerical results directly to the observations (see Chap. 6).

Several databases gathering information on known interstellar chemical reactions and processes and the reaction rates associated are available online such as the UMIST database for astrochemistry[1], the Ohio State University (OSU) network[2], and the Kinetic Database for Astrochemistry[3] (KIDA).

In order to constrain the evolutionary stage of Sgr B2(N)'s hot cores, we compared in Sect. 4.5 the observed $[C_2H_5CN]/[C_2H_3CN]$ ratio to published results of time-dependent chemical simulations for dense core evolution with a cold collapse phase up to a maximum density $n_H = 2{\times}10^8$ cm^{-2}, followed by a warm-up phase from 8 to 400 K. In order to give a more accurate explanation for the chemical differences observed between the hot cores, a more explicit and individualized modeling treatment of the time- and space-dependent chemistry in each source is required. Assuming that Sgr B2(N)'s hot cores presumably originate from the same cloud material (*i.e.* with similar elemental abundances), we can assess, by comparing the results of the chemical simulations against each other, the impact of the different physical properties of the sources on the chemistry, independently from other influencing factors. By varying a set of control parameters, we can investigate the impact on the calculated chemical abundances of different environmental factors (CRIR, external UV field, minimum dust temperature, see Sect. 5.2). If we assume that Sgr B2(N)'s hot cores are exposed to the same environmental conditions, varying the input parameters will help us to determine the values that best reproduce the observations and thus characterize the GC region (see Sect. 6.3).

5.1.1 The chemical network

The chemical network used in this thesis work is originally based on the *osu2005.chem* network and has been expanded to include all reactions and processes related to specific species such as the alkanethiols CH_3SH and C_2H_5SH (Müller et al. 2016), N-methylformamide (CH_3NHCHO) (Belloche et al. 2017), methyl isocyanate (CH_3NCO) (Belloche et al. 2017), and n-butyl cyanide (n-C_4H_9CN) and its three branched isomers ($s-$, $i-$, and $t-C_4H_9CN$, Garrod et al. 2017). The chemical network contains 1333 distinct chemical species (not including deuterated species) of which neutrals can exist either as gas-phase, grain-surface, or ice-mantle species, while charged species are found only in the gas phase. The network comprises 13374 chemical reactions and processes coupling the following three phases: gas, grain-surface, and ice-mantle as described in Sects. 5.1.1.1, 5.1.1.2, and 5.1.1.3, respectively. These sections are largely based on Garrod (2013). More information on interstellar chemical processes and the associated reaction rates can be found in Duley & Williams (1984), Hasegawa et al. (1992), Millar & Williams (1993), and Krügel (2007).

5.1.1.1 Gas-phase chemistry

The chemical network includes bimolecular gas-phase chemical reactions, that is reactions between two reactant partners which can be neutral species, ions (anions or cations), or free

[1] http://www.udfa.net/
[2] http://faculty.virginia.edu/ericherb/research.html
[3] http://kida.obs.u-bordeaux1.fr/

electrons. In addition, gas-phase species are affected by direct UV photo-dissociation and photo-ionization by the ambient interstellar radiation field, as well as by the secondary UV photons emitted following H_2 excitation by cosmic rays. Table 5.1 gives the list of all gas-phase reaction types included in the chemical network, along with the associated rate coefficient, k, which characterizes the reaction efficiency. Most gas-phase reactions can be described by a rate coefficient (in $cm^3\ s^{-1}$) given by the the Arrhenius law:

$$k(T) = \alpha \left(\frac{T_K}{300}\right)^{\beta} e^{\left(-\frac{E_a}{T_K}\right)} \tag{5.1}$$

where the rate coefficient parameters α (in $cm^{-3}\ s^{-1}$) and β are read from the chemical network for each chemical reaction. The activation energy of the reaction, E_a (in K), represents the potential barrier between reactants and products. In the case where there is more than one production channel (*i.e.* one reaction leading to different sets of products), the rate coefficient has to be multiplied by the branching ratio given in the chemical network.

At low temperatures, only chemical reactions with low to no activation-energy barriers may occur. Neutral-neutral reactions (Table 5.1, reactions 1–3) can have significant activation energies ($E_a >> T_K$) implying small rate coefficients and thus slow reactions. Ion-molecule reactions (Table 5.1, reactions 4–7) are usually faster in the gas phase (because they have no barrier). The resulting protonated species may recombine with free electrons (Table 5.1, reactions 10–11), acting as an efficient destruction mechanism for molecules with high proton affinities. Recombination reactions may also serve as the final step in the production of COMs by transforming protonated species into stable neutral molecules.

Interaction of gas-phase species with the ambient interstellar radiation field results either in the dissociation of those species into several new products (Table 5.1, reaction 13) or ionization (Table 5.1, reaction 14). The rate coefficient, k_{uv}, associated to both types of reactions corresponds to the lifetime of a given species AB againt photolysis (in s^{-1}) and depends on the interstellar radiation field strength as follows:

$$k_{uv} = \alpha_{uv}\, e^{-\gamma_{uv} A_v}\, \chi_{uv} \tag{5.2}$$

where χ_{uv} represents the scaling factor with respect to the standard external radiation field (1 G_0), in units of the standard Draine radiation field (Draine 1978). The rate coefficient parameters α_{uv} (in s^{-1}), and γ_{uv} are read from the chemical network. At high visual extinction k_{uv} becomes very small and direct UV photo-dissociation and photo-ionization of gas-phase species become inefficient. Both processes may still be significant when governed by CR-induced UV photons (regardless of the visual extinction). The rate coefficients only depend on the CRIR as follows:

$$k_{CR} = \alpha_{CR}\, \zeta_{H_2} \tag{5.3}$$

such that k_{CR} increases with CRIR.

The fraction of chemical reactions and processes included in the chemical network for which rate coefficients have been measured experimentally at the low temperatures that prevail in the ISM is extremely small. For the cases where room temperature measurements are available, rate coefficient can be extrapolated at higher/lower temperatures, but in the complete absence of experimental data, rate coefficients have to be estimated, usually based on the information on chemically related reactions. In addition, branching ratios are also often not measured.

Table 5.1: Gas-phase chemical reactions and processes included in the chemical network.

Reaction type	Reaction ID	Chemical reaction		Rate coefficient[a]
Neutral-neutral	1	Associative ionization	$A + B \rightarrow AB^+ + e^-$	k
	2	Exchange	$A + BC \rightarrow AB + C$	k
	3	Radiative association	$A + B \rightarrow AB + h\nu$	k
Ion-molecule	4	Cation/anion-neutral	$A^{+(-)} + B \rightarrow C^{+(-)} + D$	k
	5	Charge exchange	$A^+ + B \rightarrow A + B^+$	k
	6	Radiative association	$A^+ + B \rightarrow AB^+ + h\nu$	k
	7	Anion-neutral	$A^- + B \rightarrow AB + e^-$	k
Ion-ion	8	Anion-cation	$A^+ + B^- \rightarrow C + D$	k
	9	Mutual neutralization	$A^+ + B^- \rightarrow A + B$	k
Reaction with free e^-	10	Radiative recombination	$A^+ + e^- \rightarrow A + h\nu$	k
	11	Dissociative recombination	$AB^+ + e^- \rightarrow A + B$	k
	12	Raditiave attachment	$A + e^- \rightarrow A^- + h\nu$	k
Photo-dissociation	13	UV photons[*]	$AB + h\nu \rightarrow A + B$	$k_{\rm uv}$ / $k_{\rm CR}$
Photo-ionization	14	UV photons[*]	$AB + h\nu \rightarrow AB^+ + e^-$	$k_{\rm uv}$ / $k_{\rm CR}$

Notes. [(a)] k is expressed in $\mathrm{cm^3\ s^{-1}}$ (Eq. 5.1), while $k_{\rm uv}$ and $k_{\rm CR}$ are given in $\mathrm{s^{-1}}$ (Eqs. 5.2 and 5.3). [(*)] Here UV photons originate from either the ambient interstellar radiation field or the CR-induced UV field.

5.1.1.2 Grain-surface chemistry

Dust grains play an important role in the interstellar chemistry as gas-phase species can use grain surfaces as a third reaction partner to form more complex molecules. Dust grains act like catalysts as they allow two possible reactants to encounter more frequently on their two-dimensional surface than in the gas phase, where some reactions would be otherwise too slow. The grains may also carry away the excess energy when two species react on their surface and stabilize the product, and lower the activation energy for reactions with a barrier. At low temperature, gas-phase species (atoms and molecules) may be depleted from the gas phase as they freeze out onto dust grains, building up ice mantles. Those species will eventually return to the gas phase via non-thermal desorption mechanisms or when ices sublimate upon dust grains heating. All grain-surface species are assigned energy barriers against diffusion on the grain surface, $E_{\rm b}$, and binding energies, $E_{\rm d}$ (also called desorption energy), which correspond to the energy needed to release surface species back into the gas phase. Both energy barriers are poorly constrained, suffering from the lack of experimental and theoretical data. The binding energies derived experimentally for some surface species may be extrapolated to produce values for other species. Energy barriers against diffusion are set to a fixed fraction of the associated binding energy: $E_{\rm b}/E_{\rm d} = 0.35$. Table 5.2 gives a list of the binding energies used in the chemical network for a selection of molecules investigated in this thesis work.

By collision, gas-phase species may stick to grain surfaces. The accretion efficiency is given by the rate coefficient $k_{\rm acc}$ (in $\mathrm{s^{-1}}$) which depends on the dust grain density as follows:

$$k_{\rm acc} = v_{\rm th}\, n_{\rm d}\, \sigma_{\rm d}\, S \tag{5.4}$$

where $\sigma_{\rm d}$ is the cross section of accretion onto the grain surface, $n_{\rm d}$ the gas-phase number density of dust grains, S the sticking efficiency, and $v_{\rm th} = \sqrt{\frac{8\,k_{\rm b}\,T_{\rm K}}{\pi\,m}}$ is the thermal velocity of the gas at the temperature $T_{\rm K}$. On the grain surfaces, reactions occur via the Langmuir-Hinshelwood mechanism (see Fig. 5.1). While heavy species are usually held stationary in

Table 5.2: Binding energies.

Species	E_d (K)
H	450
H_2	430
H_2CO	2050
H_2CS	2800
C_2H_5CN	5537
C_2H_3CN	4637
CH_3CN	6150
CH_3OH	5534
C_2H_5OH	6259
CH_3OCHO	5200
CH_3OCH_3	3675
CH_3CHO	2775
NH_2CHO	5556
CH_3NCO	3575
CH_3SH	5534

Notes. Binding energies used in the chemical network for selected species (see Garrod 2013, and references therein).

binding sites (*i.e.* potential minima), lighter species, in particular hydrogen atoms, may leave their site via desorption, thermal hopping over the energy barrier to the next binding site, or quantum tunneling under the barrier. When two species meet in the same binding site they may react and the product of this reaction may remain on the grains to form progressively larger molecules, or be ejected into the gas phase via chemical desorption when the energy released by the reaction can break the surface-molecule bond (Garrod et al. 2007). For chemical reactions with activation-energy barriers, competition occurs between the reaction and the diffusion of one of the reactants to the next binding site. The same energy barriers as for gas-phase reactions are adopted for surface reactions which have not been studied experimentally. The rate of reaction between two species A and B is given by:

$$k_\mathrm{AB} = \frac{\nu\,\kappa(AB)}{\nu\,\kappa(AB) + k_\mathrm{hop}(A) + k_\mathrm{hop}(B)} \left[\frac{k_\mathrm{hop}(A) + k_\mathrm{hop}(B)}{f_\mathrm{back}\,N_\mathrm{s}}\right] \tag{5.5}$$

where $\kappa(AB) = \exp(-E_\mathrm{a}/T_\mathrm{d})$ represents the probability of reaction upon a single collision between the reactants, ν is the frequency of collision of the reactants typically of the order of 10^{12} Hz (Hasegawa et al. 1992), N_s is the total number of binding sites on the grain surface, and the back-diffusion factor f_back accounts for the probability that the particles may return to a previously visited binding site while they are migrating over the surface (Willis & Garrod 2017). The coefficient k_hop describes the diffusion rate of species on the grain surface from one binding site to another. It depends on the barrier against diffusion of the surface species:

$$k_\mathrm{hop} = \nu_0\, e^{-\left(\frac{E_\mathrm{b}}{T_\mathrm{d}}\right)} \tag{5.6}$$

where $\nu_0 = \sqrt{\frac{2\,n_\mathrm{s}\,E_\mathrm{d}}{\pi^2\,m_\mathrm{A}}}$ is the characteristic vibrational frequency of the particle in its binding site, with n_s the number of binding sites per unit surface and m_A the mass of the surface

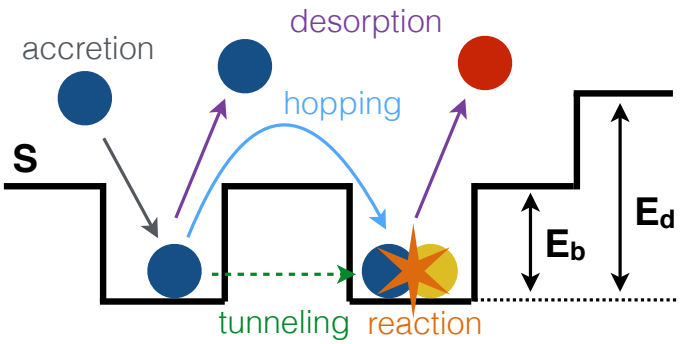

Figure 5.1: Sketch of the Langmuir-Hinshelwood surface mechanism, adapted from Herbst & van Dishoeck (2009). The dust-grain surface is represented as a periodic potential where gas-phase species are accreted onto potential minima with a sticking efficiency S. Accreted particles can migrate on the grain surface by either thermal hopping over the potential barrier separating two binding sites, given by $E_{\rm d}$, or quantum tunneling under the barrier. When two species lie in the same minimum, they may react and the product of the reaction is either ejected into the gas phase or stays on the grain surface leading to further chemical reactions. $E_{\rm d}$ represents the energy needed to release species from the grain surface back into the gas phase.

species A. When thermal hopping over the grain surface is much faster than the reaction ($k_{\rm hop} >> \nu\kappa(AB)$), then the overall rate of reaction (Eq. 5.5) depends only on the reaction probability $\kappa(AB)$. On the contrary, when $k_{\rm hop} << \nu\kappa(AB)$, then $k_{\rm AB}$ is limited only by the thermal hopping of the two reactants. However, at low temperatures (around 10 K), reactions probabilities are so small that quantum tunneling may become the dominant process for grain surface reactions, in particular those involving atomic hydrogen. In this case, a simple rectangular barrier treatment is used to determine the rates of tunneling reactions

Like in the gas phase, grain surface species may be dissociated via either direct UV photo-dissociation or CR-induced UV photons. Both processes are applied to grain-surface species with the same rates as in the gas phase. Photo-dissociation of surface material leads to the production of highly reactive species with unpaired electrons, called radicals, such as OH, HCO, NH, NH_2, CH_3, CH_2OH, and CH_3O, which are essential to the production of more complex species.

As mentioned earlier, species accreted onto the grain surface may eventually go back into the gas phase. At low temperature ($T_{\rm d} << E_{\rm d}$) desorption of grain-surface material is dominated by non-thermal processes including reactive desorption (also referred to as chemical desorption), which occurs when the energy released in the formation of the new product breaks the surface-molecule bond (Garrod et al. 2007), and UV-induced photo-desorption from either the ambient radiation field or the CR-induced UV field. Direct UV photo-desorption dominates at low visual extinction, quickly outstripped by CR-induced photo-desorption when the visual extinction increases. When the dust temperature is high enough to overcome the binding energies of surface species, then thermal desorption dominates all other desorption mechanisms. Thermal desorption is characterized by the rate coefficient $k_{\rm evap}$:

$$k_{\rm desor} = \nu_0 \, e^{-\frac{E_{\rm d}}{T_{\rm d}}} \tag{5.7}$$

5.1.1.3 Ice-mantle chemistry

Ice mantles are formed by the accretion and accumulation of gas-phase species onto the dust grains. The rate of growth of the ice mantles is determined by the net rate of deposition of material onto the grain surface and by the degree of surface coverage of bare grains. When full coverage is achieved, the grain-surface material is incorporated into the mantle, which is covered up by new material accreted from the gas. A similar process occurs in the opposite direction, following desorption of surface material, when the ice mantle beneath becomes the new surface layer. These processes do not represent a physical transport of material but rather the covering and uncovering of the bulk ice material as the first layer of ice is constantly renewed from the interaction with the gas phase. True exchanges of material between the surface and the mantle are possible via swapping mechanisms. Every swap from the mantle to the surface is matched by a corresponding swap of material in the other direction. Mantle species can also migrate within the bulk ice via swapping with an adjacent molecule (mainly water molecules). The mobility of ice-mantle species depends on their swapping energy barrier, defined as $E_{\rm swap}/E_{\rm d}$=0.7, based on the simple assumption that mantle species are bound to twice as many partners as surface species. The surface reactions included in the network are applied to the ice-mantle chemistry with the same activation-energy barriers (when present). Photo-dissociation of ice mantle species via both the external UV photons and the CR-induced UV field is included in the network without attenuation. No desorption process is allowed from the mantle directly into the gas phase. Desorption of ice mantle material must be preceded first by a transfer of material to the surface.

5.1.2 Solving the time-dependent rate equations

The formation (or destruction) rate of each species present in the chemical network is obtained by multiplying the average population of the reactants by the rate coefficient associated to each reaction. This gives the net gain (or loss) of each species as a function of time. For instance in the case of the two-body gas-phase reaction between species A and B, the net loss of species A in the absence of other formation or destruction channels is given by the differential equation:

$$-\frac{{\rm d}\langle A\rangle_{\rm g}}{{\rm d}t} = k\,\langle A\rangle_{\rm g}\,\langle B\rangle_{\rm g} \tag{5.8}$$

where $\langle X\rangle_{\rm g}$ (in cm^{-3}) represents the average number density of gas-phase species X (*i.e.* number of particles per unit volume of an arbitrary large cell of gas). Direct UV photo-dissociation or ionization are characterized by the differential equation:

$$-\frac{{\rm d}\langle AB\rangle_{\rm g}}{{\rm d}t} = k_{\rm uv}\,\langle AB\rangle_{\rm g} \tag{5.9}$$

In order to compute chemical abundances as a function of time, the chemical code builds up a set of $N_{\rm spec}$ ordinary differential equations (ODEs), also called rate equations (REs), with $N_{\rm spec}$ the total number of species in the chemical network. The whole set of rate equations is integrated numerically over time starting from pre-defined initial conditions (elemental abundances, density, visual extinction, and temperature, see Sect. 5.1.3).

While the rate equations method is very accurate when applied to pure gas-phase chemistry, the treatment of grain-surface reactions is more complicated because average populations do not represent accurately single grains. On the grain surface, the absolute reaction rate between

two species A and B in the same binding site is given by:

$$R_{\mathrm{AB}} = k_{\mathrm{AB}} \langle A \rangle_{\mathrm{d}} \langle B \rangle_{\mathrm{d}} \tag{5.10}$$

where $\langle X \rangle_{\mathrm{d}}$ (in cm^{-3}) is the average population of species X on the grain surface over a large number of dust grains (*i.e.* the average number of particles of species X present on the surface layer multiplied by the gas-phase number density of dust grains). When surface reactions proceed faster than accretion, the average population of reactive species on the grain surface ($\langle A \rangle_{\mathrm{d}}$, $\langle B \rangle_{\mathrm{d}}$) may fall below unity and stochastic effects become important. In this regime, commonly referred to as accretion-limited regime, the rate-equation treatment yields incorrect reaction rates since the overall reaction efficiency is governed by the accretion of the gas-phase species A and B onto the dust grains rather than their diffusion over the grain surface. Several approaches can be used to treat the stochastic behaviors of grain-surface chemistry, such as Monte Carlo simulations (see, e.g., Vasyunin et al. 2009). However such methods are difficult to integrate with the deterministic treatment of the rate-equation-based gas-phase chemistry and computationally time consuming. A faster and efficient way to solve the coupled gas-phase and grain-surface chemistry, approaching the results of stochastic methods, can be obtained using the modified rate equation (MRE) approach presented by Garrod (2008). This method consists in replacing the surface reaction rate R_{AB} (Eq. 5.10) by the rate of accretion of one species times the probability that the other species is present on the grain surface, and vice versa, whenever $\langle A \rangle_{\mathrm{d}}$ and $\langle B \rangle_{\mathrm{d}}$ are lower than unity. Garrod et al. (2009) showed that the MRE approach described above produces excellent agreement with exact Monte Carlo methods over a broad range of physical parameters and using a large chemical network.

5.1.3 MAGICKAL

MAGICKAL (Model for Astrophysical Gas and Ice Chemical Kinetics and Layering, Garrod 2013) is a single-point model which computes chemical abundances for a single representative point in the envelope of the modeled source at each time step. It allows us to simulate the chemical evolution along the trajectory of a parcel of gas through the free-falling envelope. Therefore the resulting chemical abundances characterize a range of distances from the cold outer edge to the warm innermost part of the protostellar envelope. The time-dependent chemical abundances are computed based on the gas-grain chemical network (Sect. 5.1.1) using the MRE method (Sect. 5.1.2). The gas-phase material is assumed to be initially in atomic or ionized form, except for H_2 (see Table 5.3). We assume that most hydrogen is initially in molecular form because converting hydrogen from atomic to molecular form on grains would otherwise take too long at low density, delaying significantly the formation of other interstellar molecules. The initial abundances are based on the so-called low-metal abundances of Graedel et al. (1982) except for He, C, N, and O, for which abundances are taken from the diffuse cloud values given by Wakelam & Herbst (2008). The electron abundance is set equal to the sum of the positive ion abundances. The initial abundances of species that are not listed in Table 5.3 are assumed to be zero. Assuming that Sgr B2(N)'s hot cores originate from the same cloud material, the same set of initial abundances is used to model all four hot cores.

MAGICKAL is a full time-dependent model where both chemistry and physical properties evolve as a function of time. The physico-chemical evolution of the sources is modeled in one stage, from the early cold phase of the star-formation process to the warm up of the dense cores, starting from a set of initial conditions (n_{start}, $A_{\mathrm{v-start}}$, and T_{min}, Sects. 4.4.2, 4.4.3, and 4.4.4, respectively). A set of physical parameters (r, n_{H}, A_{v}, T_{g}, and T_{d}) is associated to each time

Table 5.3: Gas-phase initial abundances used in the chemical models.

Species	n_i/n_H
H_2	0.5
H	2.0(-3)
He	9.0(-2)
C	1.4(-4)
N	7.5(-5)
O	3.2(-4)
S^+	8.0(-8)
Na^+	2.0(-8)
Mg^+	7.0(-9)
Si^+	8.0(-9)
P^+	3.0(-9)
Cl^+	4.0(-9)
Fe^+	3.0(-9)

Notes. Initial gas-phase abundances taken from Garrod (2013) expressed with respect to the total density of hydrogen ($n_H = n(H) + 2n(H_2)$). $X(Y)$ means $X \times 10^Y$.

step according to the physical profiles derived for each source in Sects. 4.4.2–4.4.4. At each time step, the associated physical parameters are fed into the chemical model from an external file, reducing the computational time as no additional physical equation has to be solved during the chemical simulation. Therefore the same chemical code can be used to model different sources with different physical conditions by changing only the input file with the physical parameters.

In addition to the shielding against external UV photons provided by dust grains, MAGICKAL includes H_2 and CO self-shielding (Lee et al. 1996). A shielding factor that controls the photo-destruction of H_2 and CO is calculated based on the visual extinction and the fractional abundances of the two species at each time step.

The same grain properties are adopted for all chemical simulations. The dust grain population is composed of silicate spherical grains with a single fixed radius of 0.1 micron and a mass density of 3 g cm^{-3}. The density of dust grains, n_d, follows that of hydrogen, assuming a standard gas-to-dust mass ratio of 100. Each individual grain has 10^6 binding sites on the surface. A sticking coefficient of $S = 1$ is adopted for all neutral species, meaning that every gas-phase species that collides with dust grains sticks to it.

The external radiation field strength (χ_{uv}), the minimum dust temperature threshold (T_{min}), and the cosmic-ray ionization rate (ζ_{H_2}) are left as free parameters. In the following sections we explore the influence of these three parameters on the calculated chemical abundances.

For more details on the MAGICKAL chemical code, see Garrod (2013).

5.2 Chemical simulations

In order to model the time-dependent physico-chemical evolution of Sgr B2(N2–N5) and explain the formation of specific COMs detected toward the hot cores, we use the astrochemical code MAGICKAL as described in Sect. 5.1.3. To investigate the impact of environmental conditions on the production of COMs and constrain the physical parameters that best reproduce the

Table 5.4: Main grid of chemical models.

ζ^{H_2} (s^{-1})	T_{min} (K)				
	10	15	20	25	28
1.3×10^{-17}	T10-CR1	**T15-CR1**	T20-CR1	_	_
1.3×10^{-16}	T10-CR10	T15-CR10	T20-CR10	_	_
6.5×10^{-16}	T10-CR50	T15-CR50	T20-CR50	T25-CR50*	T28-CR50*
1.3×10^{-15}	T10-CR100	T15-CR100	T20-CR100	_	_
6.5×10^{-15}	T10-CR500	T15-CR500	T20-CR500	_	_
1.3×10^{-14}	T10-CR1000	T15-CR1000	T20-CR1000	_	_

Notes. Our standard model, with T_{min} = 15 K and $\zeta^{H_2} = 1.3\times10^{-17}$ s^{-1}, is highlighted in boldface. It is referred to as N2-T15-CR1, N3-T15-CR1, N4-T15-CR1, and N5-T15-CR1 for N2, N3, N4, and N5, respectively. (*) Chemical model run only for N2.

observations we run a grid of chemical models varying the following input parameters: T_{min}, χ_{uv}, and ζ_{H_2}, to account for cold/warm dust grains in the outer envelope of the sources and different exposures to cosmic rays and external UV photons.

As mentioned already in Sect. 1.4.1 the CRIR in the GC region is expected to be higher than in the solar neighborhood. Higher dust temperatures are also expected than in the rest of the galactic disk. In order to explore the impact of cosmic rays on the production of COMs and constrain the CRIR that best reproduces the observations toward Sgr B2(N), we run chemical simulations using CRIR values ranging from the standard value $\zeta_0^{H_2} = 1.3\times10^{-17}$ s^{-1} up to $1000\times{\zeta^{H_2}}_0 = 1.3\times10^{-14}$ s^{-1} (see Sect. 5.3.3). For simplicity we assume that cosmic rays are not attenuated in the envelope of the source. We explore the impact of the minimum dust temperature reached in the chemical simulations with T_{min} ranging from 10 K up to 28 K (see Sect. 5.3.4). We have seen that in the outer layers of the source's envelope which are exposed to external UV photons, the ISRF is the main responsible for heating up the dust material. In order to explore the impact of the ISRF strength on the dust temperature and the chemistry, we run chemical models accounting for a strength of the ISRF higher than the standard value, by scaling the parametric equation for dust temperature with factor χ_{uv} ranging from 100 G_0 up to 1000 G_0 (see Sect. 5.3.5).

In summary, we run for each hot core a main grid of 18 chemical models, one for each set of physical parameters ($\zeta^{H_2} = 1.3\times10^{-17}$ s^{-1} – 1.3×10^{-14} s^{-1} and T_{min}= 10 K, 15 K, and 20 K, see Table 5.4). In addition two additional chemical models are run with T_{min}=25 K and 28 K for N2. All these models assume a standard ISRF (1 G_0). Finally seven more chemical models are run only for N2, to test the impact of the ISRF (see Table 5.5).

All simulations run from t_{start} to t_{final}. Because of the general uncertainties on chemical reactions and processes above 400 K (see, e.g., Harada et al. 2010), all simulations stop when the temperature in the envelope of the sources reaches 400 K (*i.e.* $T(t_{final})$ = 400 K).

5.3 Results of the chemical simulations

From the cold, low density pre-stellar phase to the warm and dense hot core phase, the chemistry of the collapsing cloud can be divided into two phases:

Table 5.5: Additional chemical models for Sgr B2(N2).

ζ^{H_2} (s^{-1})	$T_d(A_v)$ (K)	
	$T_d^{uv\,a}$	$T_d^{hoc\,b}$
1.3×10^{-17}	N2-CR1-UV100	–
	N2-CR1-UV500	–
	N2-CR1-UV1000	–
6.5×10^{-16}	N2-CR50-UV100	N2-CR50-Thoc-UV100
	N2-CR50-UV500	–
	N2-CR50-UV1000	–

Notes. $^{(a)}$ Dust temperature computed using Eq. 5.25. $^{(b)}$ Dust temperature computed with Eq. 5.24.

(i) The freeze-out phase. It covers the whole pre-stellar phase, as well as the early cold phase of the free-fall collapse. The chemistry is dominated by surface reactions. In the outermost layers of the envelope of the source, as the visual extinction increases, the dust temperature falls, and gas-phase material freezes out onto interstellar dust grains forming ice mantles. These ice mantles are essential for the conversion of atomic hydrogen into H_2. Ice mantles also provide the surface on which more complex species can form via the addition of reactive radicals following photo-dissociation processes on the grain surfaces.

(ii) The warm-up phase. It occurs during the free-fall collapse of the source envelope. As the central protostar heats up its surrounding envelope, the temperature rises and surface species with low binding energies start desorbing from the grain surfaces, until the entire grain mantle evaporates. Surface products are released into a very dense and warm environment, leading to a rapid change in the chemistry as a wide variety of species may interact in the gas phase.

Sections 5.3.1 and 5.3.2 present the results of the standard chemical models N(2-5)-T15-CR1 during the freeze-out and the warm-up phases, respectively. All abundances refer to fractional abundances with respect to the total hydrogen density ($n_H = 2n(H_2) + n(H)$) unless specified otherwise. The influence of varying the CRIR, the minimum dust temperature, and the UV field strength on the production of COMs are discussed in Sects. 5.3.3, 5.3.4, and 5.3.5, respectively.

5.3.1 The freeze out: building up ice mantles

Figure 5.2 shows that the growth of the ice mantle during the cold phase prior to the free-fall collapse is not linear as a function of time. For the four standard chemical models, N(2-5)-T15-CR1, an ice thickness of one layer is achieved after 6.4×10^3 yr of simulation (*i.e.* t = -0.9936×10^6 yr). After 1 Myr (*i.e.* $t_0 = 0$), about 110 ice layers have formed for N2, N4, and N5, while 161 layers did for N3. This is due to the large densities computed at r_{start} in the envelope of N3 during the contraction phase (up to 2×10^6 cm^{-3}, see Fig. 4.15a). The accretion of material onto the dust grains is thus more efficient in model N3-T15-CR1, leading to rapid deposition of new ice layers. For all models, the net deposition rate continues to increase until the end of the quasi-static contraction phase, indicating that the depletion of gas-phase material has not reached completion yet.

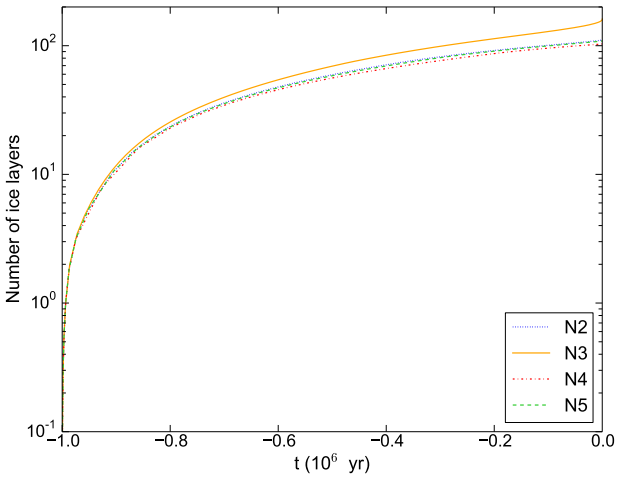

Figure 5.2: Growth of the dust-grain ice mantles over time during the quasi-static contraction phase prior to the free-fall collapse for the standard models N(2-5)-T15-CR1. *Figure taken from Bonfand et al. (2019).*

Figure 5.3a shows for the four standard models, the chemical composition of the dust grain mantles at each ice layer, based on the surface ice that gets incorporated into the mantle. A timescale is indicated at the top of each panel indicating the time at which each ice layer was deposited onto the dust grains (see also Fig. 5.2). The chemical composition within the first 50 ice layers of the grain mantles is similar for the four models. Water is clearly the dominant ice constituent, while CO and CO_2 are also present in significant quantities (see also Fig. 5.3b). Because of the somewhat high dust temperature ($T_{\rm min}$ = 15 K) during the whole quasi-static contraction phase, the conversion from atomic to molecular hydrogen on the grain surface is slow, leading to high H abundances in the gas phase (a few 10^{-3}, see Fig. 5.3c). The surface reaction OH + CH_4 → H_2O + CH_3 is found to be the main mechanism responsible for the formation of water ice, rather than the reaction of OH with atomic or molecular hydrogen expected at lower dust temperatures ($T_{\rm d}$ = 10 K, see, e.g., Garrod & Pauly 2011). The rapid conversion of gas-phase atomic carbon to CO at the beginning of the simulations (Fig. 5.3c) causes a sharp decline in the abundance of CH_4 ices, which in turn affects the abundance of water ice (Fig. 5.3a and c). Once on the grains, CO is mobile enough at $T_{\rm d}$ = 15 K to react with OH radicals to form CO_2, limiting the fraction of OH going toward H_2O. The abundance of solid-phase CO_2 reaches a peak within the first 10^5 yr of the simulation, representing 60–65% of the water abundance (Fig. 5.3b). Then, a rapid switch-over occurs and CO dominates over CO_2 due to the high accretion rate of gas-phase CO onto dust grains.

Table 5.6 gives the chemical composition of the ice mantles obtained at the end of the 1 Myr contraction phase for the four standard models. It shows that models N2-T15-CR1, N4-T15-CR1, and N5-T15-CR1 build up ices with similar chemical composition, that differs from that of model N3-T15-CR1. In particular, the high accretion rate of gas-phase species in model N3-T15-CR1 leads to the production of much more H_2CO and CH_3OH. These species form on the grain surface, by the successive hydrogenation of CO accreted from the gas phase. They are essential for the production of more complex molecules. These differences are due to the higher densities computed during the contraction phase at $r_{\rm start}$ in the more compact inner region of N3 compared to the other sources. High densities have an impact on the accretion

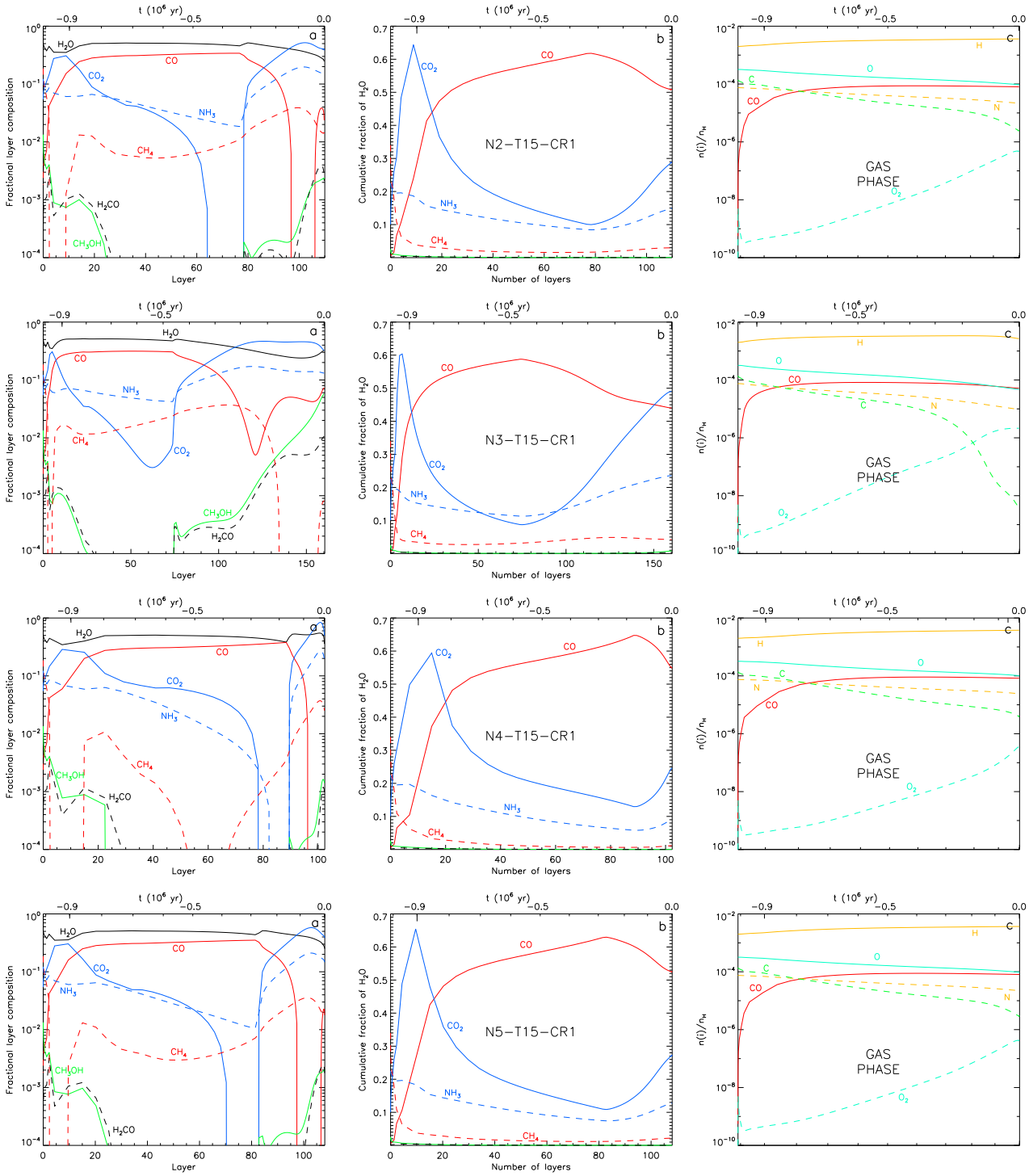

Figure 5.3: Calculated evolution of the ice-mantle and gas-phase chemistry during the cold quasi-static contraction phase prior to the free-fall collapse. The results from the standard models N(2-5)-T15-CR1 are displayed from top to bottom. **a** Calculated fractional ice-mantle composition by ice layer. **b** Cumulative fractional composition of the ices with respect to water, summed over the grain mantle up to an ice thickness given on the abscissa. **c** Gas-phase fractional abundances (with respect to total hydrogen) of atomic and simple diatomic species as a function of time with the same time axis as panels (a) and (b) to facilitate the comparison. *Figure taken from Bonfand et al. (2019).*

Table 5.6: Ice mantle composition.

	Standard models				Observations	
Species	N2	N3	N4	N5	Elias 16 [*]	W33A [*]
H_2O	100	100	100	100	100	100
CO	51	44	55	52	25	8
CO_2	29	49	25	27	18	13
NH_3	15	24	9	13	≤9	15
CH_4	3	4	1	2	_	1.5
H_2CO	0.07	0.3	0.02	0.05	_	6
CH_3OH	0.07	0.8	0.03	0.05	<3	18

Notes. Abundances of the main ice constituents, summed over all the ice layers formed at the end of the quasi-static contraction phase. These results are for the standard models and are given in percentage of the water ice value. [(*)] Observational values from Gibb et al. (2000) and references therein.

rate of gas-phase species onto the dust grains, such that after 1 Myr simple species such as gas-phase CO, atomic hydrogen, carbon and nitrogen are more depleted in model N3-T15-CR1 than in models N4/N5-T15-CR1 (see Fig. 5.3c).

Observations of ice-mantle chemical content are done in absorption, which requires a strong background illuminating source, limiting the number of sightlines that can be studied. For the comparison to our chemical model results we show in Table 5.6 the composition of ices observed in the line of sight of the background field star Elias 16 (Whittet et al. 1998) and toward the high-mass protostar W33A (Gibb et al. 2000). The chemical composition of the ice mantles in models N2-T15-CR1, N4-T15-CR1, and N5-T15-CR1 are comparable (within a factor ~ 2) to that of the material along the line of sight to Elias 16 but significantly differ from that of W33A. This could be due to the different dust temperatures during the pre-stellar phases of the different sources.

5.3.2 The warm-up phase: COMs in the gas phase

The freeze-out phase is followed by the warm-up of the source's envelope, when the central protostar progressively heats up its surroundings. At early times and low temperatures in the free-fall collapse phase, ice mantles continue to grow by accreting gas-phase species until the temperature is sufficiently high to induce a release of surface species into the gas phase. As the gas and dust temperatures progressively rise both surface and gas-phase chemistry are affected. H atoms do not reside long enough on the grain surfaces to be the dominant reaction partners anymore, while heavier species begin to diffuse more quickly. Reactions with significant activation-energy barriers can occur efficiently both in the gas and on the grains, until the temperature is high enough to fully sublimate the ice mantles. In this section we focus on the behavior of 11 COMs during the warm up of the source to investigate the complex set of chemical reactions that drive their production and determine whether the chemical simulations favor the cold chemistry at the surface of dust grains, warm gas-phase processes, or a mixture of both as main formation pathways. The activation energies (when present) of the reactions investigated in this section are listed in Table C.1.

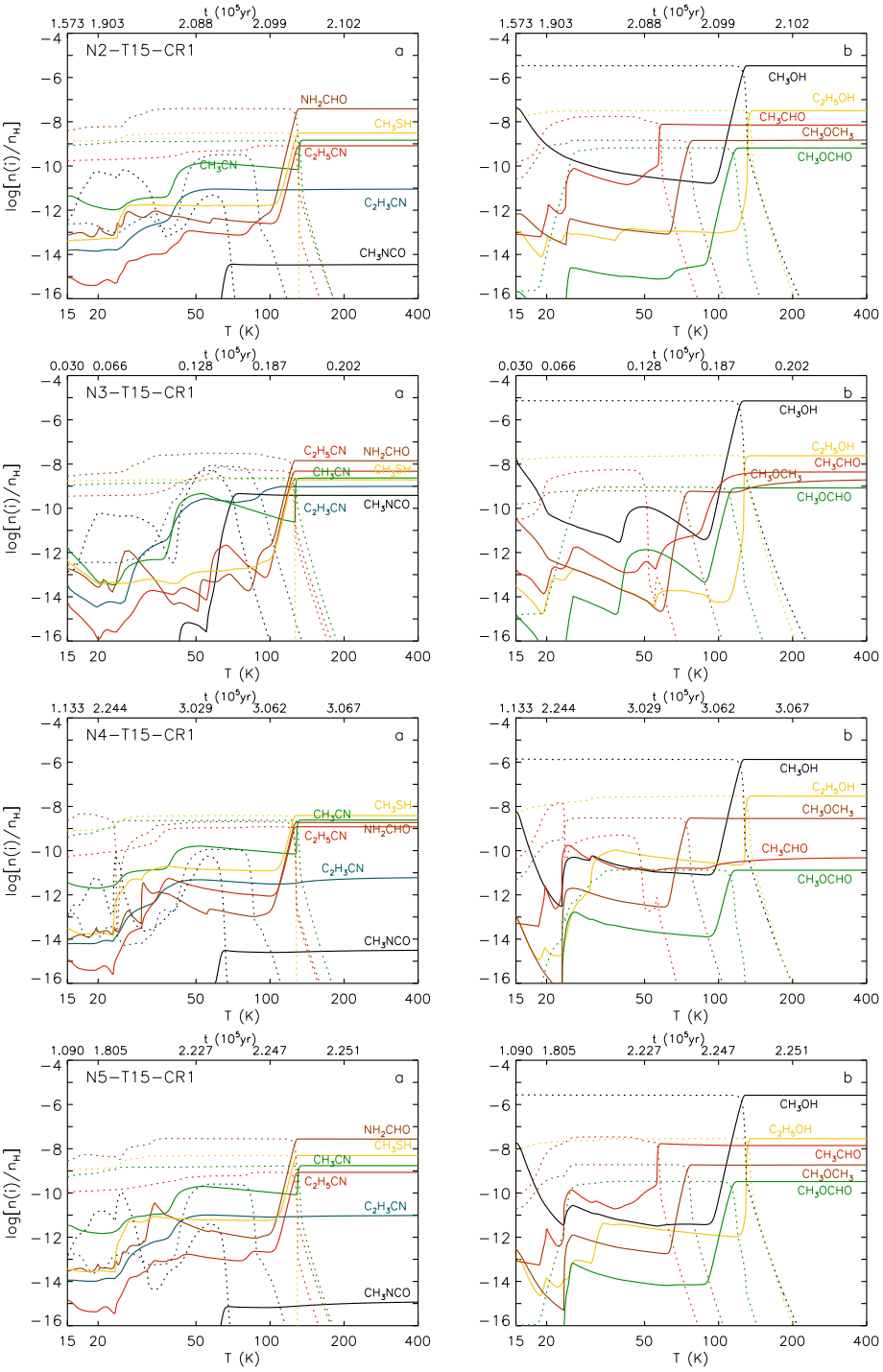

Figure 5.4: Calculated fractional abundances of 11 COMs detected toward N2–N5. The results for the standard models, N(2-5)-T15-CR1, are shown from top to bottom, as a function of the temperature in the envelope of the sources during the free-fall collapse phase (gas and dust temperature are assumed to be well coupled). The timescale shown at the top of each panel is derived from the time-dependent evolution of the temperature in the envelopes of the sources (see Sect. 4.4.4). In each panel, solid lines show the fractional abundances (with respect to total hydrogen) in the gas phase while dotted lines show the abundances of the same species on the grains (ice-surface+mantle). *Figure taken from Bonfand et al. (2019).*

Table 5.7: Peak gas-phase abundances and associated temperatures for the standard models.

Species	N2-T15-CR1			N3-T15-CR1			N4-T15-CR1			N5-T15-CR1		
	final[a]	peak[b]	T^c	final[a]	peak[b]	T^c	final[a]	peak[b]	T^c	final[a]	peak[b]	T^c
	$(n[i]/n_{\rm H})$		(K)	$(n[i]/n_{\rm H})$		(K)	$(n[i]/n_{\rm H})$		(K)	$(n[i]/n_{\rm H})$		(K)
C_2H_5CN	8.2(-10)	8.2(-10)	131.4	4.7(-9)	4.8(-9)	127.1	1.2(-9)	1.2(-9)	128.5	8.5(-10)	8.6(-10)	129.7
C_2H_3CN	9.0(-12)	9.1(-12)	61.4	9.8(-10)	9.8(-10)	400.0	6.0(-12)	6.0(-12)	400.0	9.6(-12)	1.0(-11)	56.2
CH_3CN	1.5(-9)	1.5(-9)	145.6	2.4(-9)	2.4(-9)	134.4	2.4(-9)	2.4(-09)	138.9	1.7(-9)	1.7(-9)	145.3
CH_3OH	3.4(-6)	3.4(-6)	131.4	7.1(-6)	7.2(-6)	127.1	1.3(-6)	1.3(-6)	127.9	2.6(-6)	2.6(-6)	129.7
C_2H_5OH	3.2(-8)	3.2(-8)	147.3	2.4(-8)	2.4(-8)	143.8	2.9(-8)	2.9(-08)	140.0	2.9(-8)	2.9(-8)	143.4
CH_3OCHO	6.5(-10)	6.5(-10)	129.6	8.3(-10)	8.4(-10)	126.3	1.3(-11)	1.3(-11)	120.6	3.3(-10)	3.3(-10)	126.5
CH_3OCH_3	1.4(-9)	1.4(-9)	80.1	1.9(-9)	1.9(-9)	400.0	2.8(-9)	3.0(-9)	77.6	1.9(-9)	1.9(-9)	78.9
CH_3CHO	7.1(-9)	7.7(-9)	59.4	4.4(-9)	4.4(-9)	182.8	4.8(-11)	1.7(-10)	24.4	1.4(-8)	1.7(-8)	58.4
NH_2CHO	3.8(-8)	3.8(-8)	131.4	1.4(-8)	1.5(-8)	127.1	1.9(-9)	1.9(-9)	127.9	2.7(-8)	2.8(-8)	129.7
CH_3NCO	3.5(-15)	3.6(-15)	70.6	3.8(-10)	4.6(-10)	75.1	3.1(-15)	3.1(-15)	67.0	1.2(-15)	1.2(-15)	400.0
CH_3SH	3.1(-9)	3.1(-9)	131.4	1.9(-9)	2.0(-9)	126.3	3.9(-9)	3.9(-9)	127.9	4.9(-9)	4.9e(-9)	129.7

Notes. $X(Y)$ means $X\times10^Y$. [(a)] Gas-phase fractional abundances (with respect to total hydrogen) calculated by the standard models at the end of the simulations. [(b)] Gas-phase peak fractional abundances (with respect to total hydrogen) reached during the free-fall collapse phase. [(c)] Temperature at which the peak fractional abundance is achieved.

Figure 5.4 shows the results obtained for the standard chemical models N(2-5)-T15-CR1 during the free-fall collapse phase. Each panel (a and b) shows the evolution of the fractional abundances (with respect to total hydrogen) of a subset of COMs. Panel (a) shows the N-bearing species C_2H_5CN, C_2H_3CN, CH_3CN, NH_2CHO, and CH_3NCO, as well as CH_3SH. Panel (b) shows the O-bearing species CH_3OH, C_2H_5OH, CH_3OCHO, CH_3OCH_3, and CH_3CHO. The calculated fractional abundances are plotted as a function of temperature in the envelope of the source (in log scale) for easy comparison between all models. A timescale is also indicated at the top of each plot. The figure shows that in most cases, the solid-phase abundances directly determine the final gas-phase abundances. This suggests that the gas-phase abundances observed in the warm inner part of the envelope of the sources are dominated by the sublimation of the dust-grain ice mantles. The peak gas-phase fractional abundances of the 11 COMs are given in Table 5.7 along with the temperatures at which they are achieved in each chemical model. For comparison we also list the fractional abundances reached at the end of the simulations (*i.e.* $T = 400$ K). Most species reach their peak abundance right after desorption into the gas phase (except for C_2H_3CN and CH_3NCO). Once in the gas, most species quickly reach steady fractional abundances, since any gas-phase species that sticks to the grains is rapidly desorbed because of the high temperature. The O-bearing species CH_3OH, C_2H_5OH, NH_2CHO, CH_3OCHO, as well as CH_3CN, C_2H_5CN, and CH_3SH desorb from the grains at high temperatures, around 120–147 K. The other species which desorb at lower temperatures (via thermal or chemical desorption), or which are formed directly in the gas phase via ion-molecule reactions, are particularly exposed to gas-phase destruction through photo-dissociation by CR-induced UV photons or reactions with gas-phase ions.

In Figure 5.4 we can also distinguish two apparently distinct groups of COMs with different origins. The cyanides C_2H_5CN and CH_3CN, as well as C_2H_5OH, CH_3OH, and CH_3SH are already present on the grains with significant abundances before the warm-up phase (*i.e.* $T = 15$ K), suggesting that their formation mostly relies on the earlier, cold chemistry. In contrast, other species form on the grains up to ~ 50 K, in particular the O-bearing species

CH_3CHO, CH_3OCHO, CH_3OCH_3, and CH_3NCO, suggesting that their production relies on warmer chemistry. The mechanisms responsible for the formation of these species are investigated in detail below.

There is little gas-phase production of methanol, it is mostly formed on the grains via successive hydrogenation of the CO accreted from the gas phase:

$$CO \xrightarrow{H} HCO \xrightarrow{H} H_2CO \xrightarrow{H} CH_3O \xrightarrow{H} CH_3OH. \tag{5.11}$$

The high gas-phase fractional abundance of CH_3OH at the beginning of the free-fall collapse phase is mostly due to chemical desorption from the dust grains. Model N3-T15-CR1 shows a modest increase in gas-phase methanol abundance around T $\sim$ 40 K, caused by the electronic recombination of $HC(OH)OCH_3^+$, product of the reaction between protonated methanol (formed from reaction of H_2CO with gas-phase ions) and formaldehyde when the latter is released abundantly into the gas phase.

Ethanol is predominantly produced on the grains, mostly via the sequence:

$$CH_3 \xrightarrow{C} C_2H_3 \xrightarrow{H} C_2H_4 \xrightarrow{H} C_2H_5 \xrightarrow{O} C_2H_5O \xrightarrow{H} C_2H_5OH, \tag{5.12}$$

followed by later desorption into the gas phase.

Formamide is mainly produced on the grains via the successive hydrogenation of OCN that is accreted from the gas phase:

$$OCN \xrightarrow{H} HNCO \xrightarrow{H} NH_2CO \xrightarrow{H} NH_2CHO. \tag{5.13}$$

The abundance of methyl cyanide mostly derives from the grain-surface hydrogenation reaction:

$$CH_2CN + H \rightarrow CH_3CN, \tag{5.14}$$

where CH_2CN is formed via the grain-surface atomic-addition sequence: $CN \xrightarrow{C} C_2N \xrightarrow{H} HC_2N \xrightarrow{H} CH_2CN$. At low temperatures ($T < 50$ K), CH_3CN is also produced in the gas phase via the electronic recombination of protonated methyl cyanide (CH_3CNH^+), product of the ion-molecule reaction between CH_3^+ and HCN.

Methyl formate begins the free-fall collapse phase with modest abundances on the grains. It is formed more efficiently at later times ($T \sim$ 20–30 K), mainly via the grain-surface radical-radical addition reaction:

$$HCO + CH_3O \rightarrow CH_3OCHO, \tag{5.15}$$

followed by later desorption into the gas phase. Model N3-T15-CR1 shows a modest increase in the gas-phase abundance of CH_3OCHO around $\sim$ 40 K, when formaldehyde is abundantly released into the gas phase and reacts with protonated methanol to form protonated methyl formate, $HC(OH)OCH_3^+$. Gas-phase CH_3OCHO is then produced via the electronic recombination of $HC(OH)OCH_3^+$.

Methyl mercaptan is predominantly formed on the grains via the successive hydrogenation reactions:

$$H_2CS \xrightarrow{H} CH_2SH/CH_3S \xrightarrow{H} CH_3SH, \tag{5.16}$$

where H_2CS is formed during the cold quasi-static contraction phase via the successive hydrogenation of surface CS accreted from the gas phase. Above $\sim$ 20 K, H_2CS is accreted onto the grains directly from the gas phase, where it is formed via the electronic recombination of H_3CS^+, deriving from the ion-molecule reaction $S^+ + CH_4$.

The production of vinyl cyanide involves a mixture of ice-surface and gas-phase processes. C_2H_3CN is formed on dust grains mainly through the hydrogenation reaction:

$$C_2H_2CN + H \rightarrow C_2H_3CN. \tag{5.17}$$

Here C_2H_2CN is formed via the successive hydrogenation of HC_3N that is accreted from the gas phase: $HC_3N \xrightarrow{H} C_2H_2CN \xrightarrow{H} C_2H_3CN$. As hydrogenation continues on the grain surfaces, C_2H_3CN is quickly converted to C_2H_5CN as follows:

$$C_2H_3CN \xrightarrow{H} C_2H_4CN \xrightarrow{H} C_2H_5CN. \tag{5.18}$$

Ethyl cyanide can thus maintain a steady abundance on the grains, dominating vinyl cyanide at all times. Only a small fraction of solid-phase C_2H_3CN contributes to the gas-phase abundance as it is quickly destroyed via ion-molecule reaction right after desorption. C_2H_3CN may then be formed in the gas phase via the reaction:

$$C_2H_4 + CN \rightarrow C_2H_3CN + H. \tag{5.19}$$

Due to their low binding energies to water ices, CH_3NCO, CH_3OCH_3, and CH_3CHO desorb at low temperatures (60–80 K). Methyl isocyanate starts the free-fall collapse phase with modest abundances on the grains. It is more efficiently produced around 20 K through the radical-addition reaction:

$$CH_3 + OCN \rightarrow CH_3NCO. \tag{5.20}$$

At low temperatures ($T < 50$ K), methyl isocyanate may be destroyed on the grains via hydrogenation reactions to form CH_3NHCO. In addition, CH_3NCO is quickly destroyed via gas-phase ion-molecule reactions right after desorption, leading to very low gas-phase fractional abundances at the end of the simulations ($< 10^{-14}$ with respect to total hydrogen, for all standard models but N3-T15-CR1). In model N3-T15-CR1, methyl isocyanate is formed much more abundantly on the grains, mainly because of the high abundance of surface CH_3 accreted from the gas phase. Therefore it cannot be destroyed completely once it is released into the gas phase, explaining the higher fractional abundances of gas-phase CH_3NCO observed in this model.

Dimethyl ether is mostly formed on the surface of dust grains up to $T \sim 20$–30 K, through the radical-addition reaction:

$$CH_3 + CH_3O \rightarrow CH_3OCH_3. \tag{5.21}$$

In model N3-T15-CR1, the gas-phase fractional abundance of dimethyl ether increases when methanol desorbs from the dust grains around 130 K. Here gas-phase CH_3OCH_3 is formed via the electronic recombination reaction $CH_3OCH_4^+ + e^- \rightarrow CH_3OCH_3 + H$, where $CH_3OCH_4^+$ is a product of the reaction between methanol and protonated methanol.

Finally, acetaldehyde is formed on the grains up to $T \sim 30$ K, via the surface reactions:

$$CH_2 + HCO \rightarrow CH_2CHO \xrightarrow{H} CH_3CHO, \tag{5.22}$$

$$CH_3 + HCO \rightarrow CH_3CHO. \tag{5.23}$$

Surface acetaldehyde may be destroyed either by reacting with CH_3 to form $CH_4 + CH_3CO$, or with NH_2 to form $NH_3 + CH_3CO$. In particular in models N3-T15-CR1 and N4-T15-CR1, only

a small fraction of solid-phase CH_3CHO contributes to the gas-phase fractional abundance. At lower temperature ($T \sim 24$ K), surface CH_3CHO is released into the gas phase via chemical desorption from the reaction CH_2CHO + H. Once in the gas phase, CH_3CHO becomes the dominant reaction partner for gas-phase ions, damping ionic abundances and thus limiting the destruction of other gas-phase species. In models N3-T15-CR1 and N4-T15-CR1 acetaldehyde is formed directly in the gas phase via the reaction $C_2H_5 + O \rightarrow CH_3CHO + H$, when C_2H_5 desorbs from dust grains around ~ 90 K.

The gas-phase fractional abundances (with respect to total hydrogen) obtained at the end of the simulations (*i.e.* at $T = 400$ K), are given in Table. C.2. Figure 5.5 shows the final gas-phase fractional abundances obtained by the standard chemical models N(2-5)-T15-CR1. Similar results are obtained for models N2-T15-CR1 and N5-T15-CR1. The model N4-T15-CR1 shows low fractional abundances of CH_3CHO, CH_3OCHO, and NH_2CHO, in average 90, 25, and 10 times lower than the other models, respectively. Model N3-T15-CR1 significantly differs from the other models, with higher abundances of cyanides, an astonishing $[C_2H_5CN]/[C_2H_3CN]$ ratio more than 18 times lower than the other models, and an extremely high abundance of CH_3NCO, more than five orders of magnitude higher than for the other models.

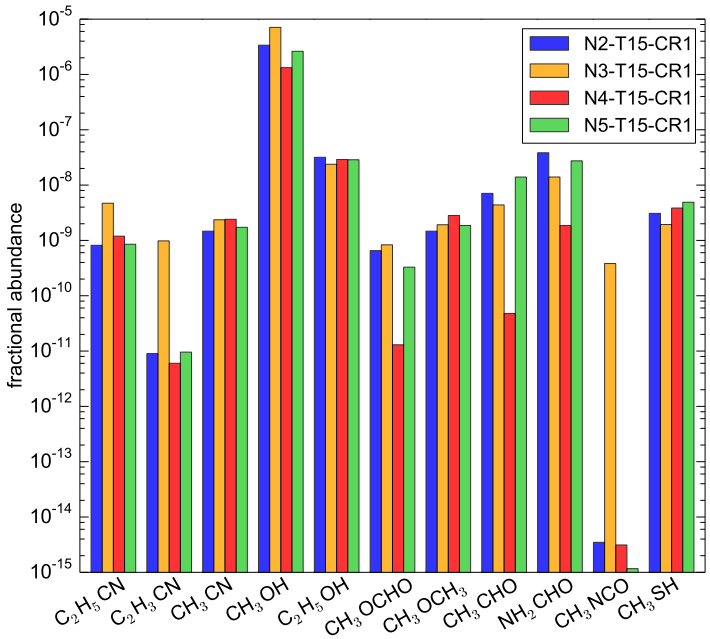

Figure 5.5: Fractional abundances (with respect to total hydrogen) calculated for the standard models at the end of the simulations (that is at $T = 400$ K). *Figure taken from Bonfand et al. (2019).*

5.3.3 Influence of cosmic rays on the chemistry

In this section we explore the influence of ζ^{H_2} on the chemistry and in particular its impact on the production of COMs. Cosmic rays play a role both in the cold grain-surface chemistry and during the later warm-up stage. The CRIR adopted in the chemical simulation directly impacts the dissociation rate of surface molecules (see Eq. 5.3), influencing the amount of reactive radicals that can react on the grain surface to form more complex species. In the gas

phase, the CRIR controls the density of ions and thus the frequency of ion-molecule reactions, which mainly act to destroy COMs.

Figure 5.6 shows the composition of the ice mantles built up during the cold phase prior to the free-fall collapse for Sgr B2(N2), with $\zeta^{H_2} = 10\times\zeta_0^{H_2}$ (N2-T15-CR10), $100\times\zeta_0^{H_2}$ (N2-T15-CR100) and $1000\times\zeta_0^{H_2}$ (N2-T15-CR1000), compared to the standard model (N2-T15-CR1). Panels a and b show that the chemical composition of the ices exposed to a CRIR enhanced by a factor of 10 are relatively similar to that obtained for the standard model N2-T15-CR1. Bigger differences can be seen in the composition of the ice mantles for higher ionization rates (panels c and d). Models N2-T15-CR100 and N2-T15-CR1000, produce thicker ice mantles on the grains (up to 153 ice layers for N2-T15-CR100 after 1 Myr, Fig. 5.6b), compared to the low-CRIR models ($\zeta^{H_2} \leq 10\times\zeta_0^{H_2}$). At higher CRIR, water is still the main ice constituent, but the grain mantles are strongly depleted in CO_2 and CO compared to the low-CRIR models, because most surface CO_2 is photo-dissociated via CR-induced UV photons, and most gas-phase CO quickly reacts with He^+ before it can be accreted onto dust grains. We also note that gas-phase molecular hydrogen is rapidly destroyed via CR-induced UV photons, leading to enhanced abundances of atomic hydrogen. This can be seen in models N2-T15-CR100 and N2-T15-CR1000 where CH_4 and NH_3 are produced more efficiently on the grains than in the low CRIR models. Ammonia maintains a fairly stable abundance on the surface at all time since surface NH_2, the product of NH_3 photo-dissociation, is quickly hydrogenated to form NH_3 again. Finally in the high CRIR models ($\zeta^{H_2} \geq 100\times\zeta_0^{H_2}$), the ice mantles are significantly depleted in H_2CO and CH_3OH which are efficiently destroyed via surface reactions with atomic hydrogen.

All results for models N2/N5-T15 with different CRIR values can be found in Appendix. C.2.2. Here we discuss in detail the evolution of the fractional abundances obtained for models N2-T15 with a CRIR value enhanced by a factor 10, 100, and 1000 compared to the standard value. Figure 5.7 shows that all the investigated COMs are sensitive to the value of the CRIR. The results obtained for model N2-T15-CR10 are similar to that of the standard model, except for the O-bearing species CH_3NCO, C_2H_5OH, and CH_3CHO. Higher gas-phase fractional abundances of ethanol and methyl isocyanate are obtained at the end of the simulation for N2-T15-CR10. However, the final gas-phase fractional abundance of CH_3CHO obtained for N2-T15-CR10 is one order of magnitude lower than that of N2-T15-CR1. This is because of the reactions with atomic hydrogen destroying acetaldehyde at the surface of dust grains. Only a small fraction of the CH_3CHO formed on the grains thus desorbs around $\sim$ 60 K and contributes to its final gas-phase abundance. The CH_3CHO present in the gas phase at lower temperatures (*i.e.* before thermal desorption) mainly derives from chemical desorption, but then it is quickly destroyed as it reacts with ions.

At higher CRIR, in the model N2-T15-CR100, ethanol reaches a final gas-phase fractional abundance about two orders of magnitude higher than in the standard model. Methyl isocyanate is formed approximately three orders of magnitude more abundantly than in the standard model, although it is strongly destroyed on the grain surface by reactions with atomic hydrogen. In fact the final gas-phase fractional abundance of CH_3NCO derives from the CR-induced photo-dissociation of CH_3NHCO which desorbs from the grains around $T \sim 90$ K.

Finally in the model with the highest ionization rate, N2-T15-CR1000, all COMs are strongly affected by cosmic rays (Fig. 5.7, bottom panel). Most species are destroyed right after desorption into the gas phase, where they react with one of the most abundant ions, H_3O^+, product of the reaction between H_3^+ and water, after the latter desorbs from the grain surface. For

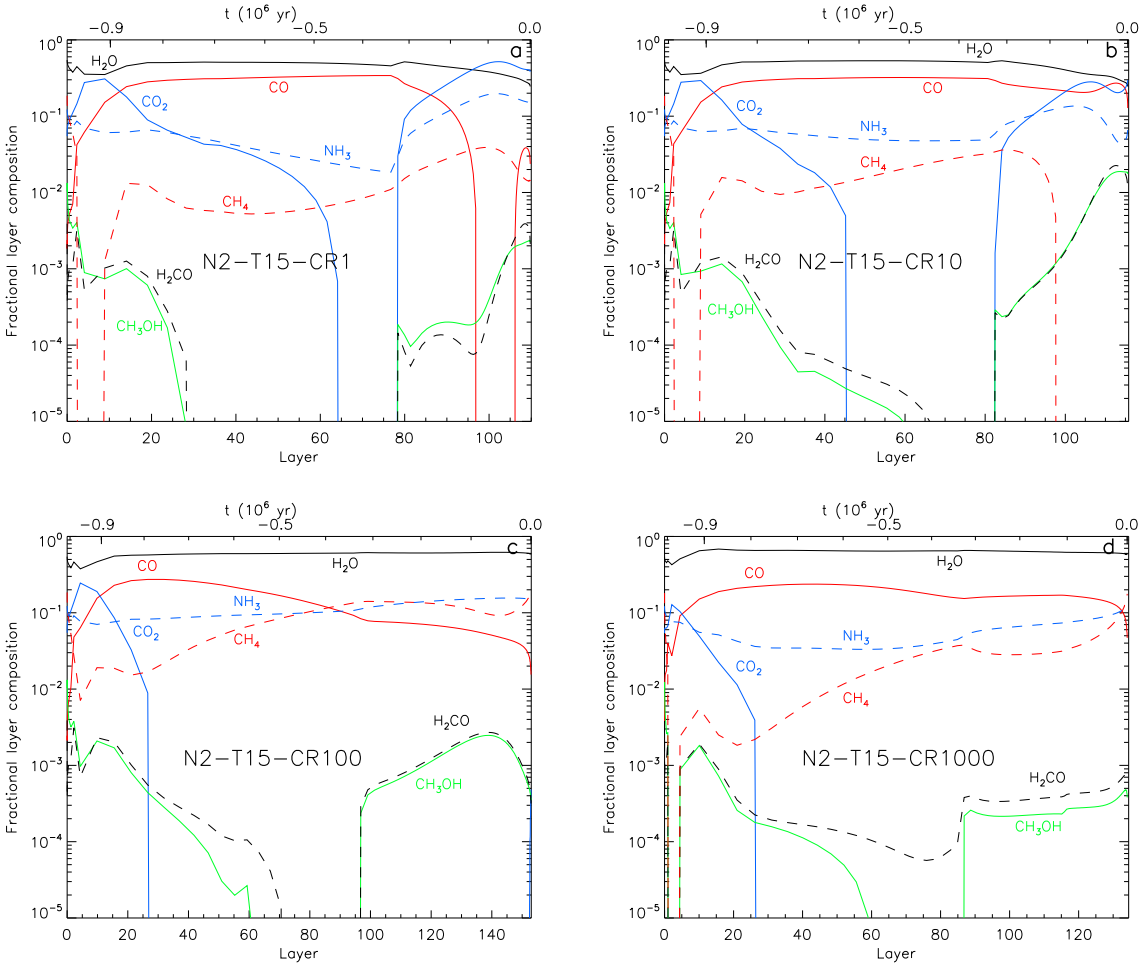

Figure 5.6: Composition of the ice mantles built up during the cold quasi-static contraction phase for models **a** N2-T15-CR1, **b** N2-T15-CR10, **c** N2-T15-CR100, and **d** N2-T15-CR1000. *Figure taken from Bonfand et al. (2019).*

the COMs with little to no gas-phase formation routes, this leads to low final fractional abundances. This is the case for C_2H_5OH, CH_3OH, CH_3OCHO, NH_2CHO, C_2H_5CN, and CH_3SH. The gas-phase abundance of dimethyl ether decreases by more than three orders of magnitude right after it desorbs from the dust grains. At later times, CH_3OCH_3 is formed in the gas phase via dissociative recombination of $CH_3OCH_4^+$, product of the ion-molecule reaction $CH_3OH_2^+$ + CH_3OH, when methanol desorbs from dust grains, around ∼130 K. The main contribution to the final gas-phase abundance of C_2H_3CN and CH_3CN also comes from gas-phase reactions. Vinyl cyanide is mostly formed via the gas-phase reaction CN + C_2H_4 → C_2H_3CN + H, when C_2H_4 desorbs from the dust grains around 70 K, and the dissociative recombination of $C_2H_6CN^+$. The later reaction is particularly efficient since $C_2H_6CN^+$ is produced from the ion-molecule reaction H_3O^+ + C_2H_5CN. The gas-phase abundance of vinyl cyanide thus increases as ethyl cyanide is destroyed. Methyl cyanide reaches its peak gas-phase abundance at early times, around 57 K, after which it is strongly destroyed by ion-molecule reactions. The main contribution to CH_3CN's final gas-phase abundance comes from gas-phase recombination of CH_3CNH^+, product of the ion-molecule reaction CH_3^+ + HCN.

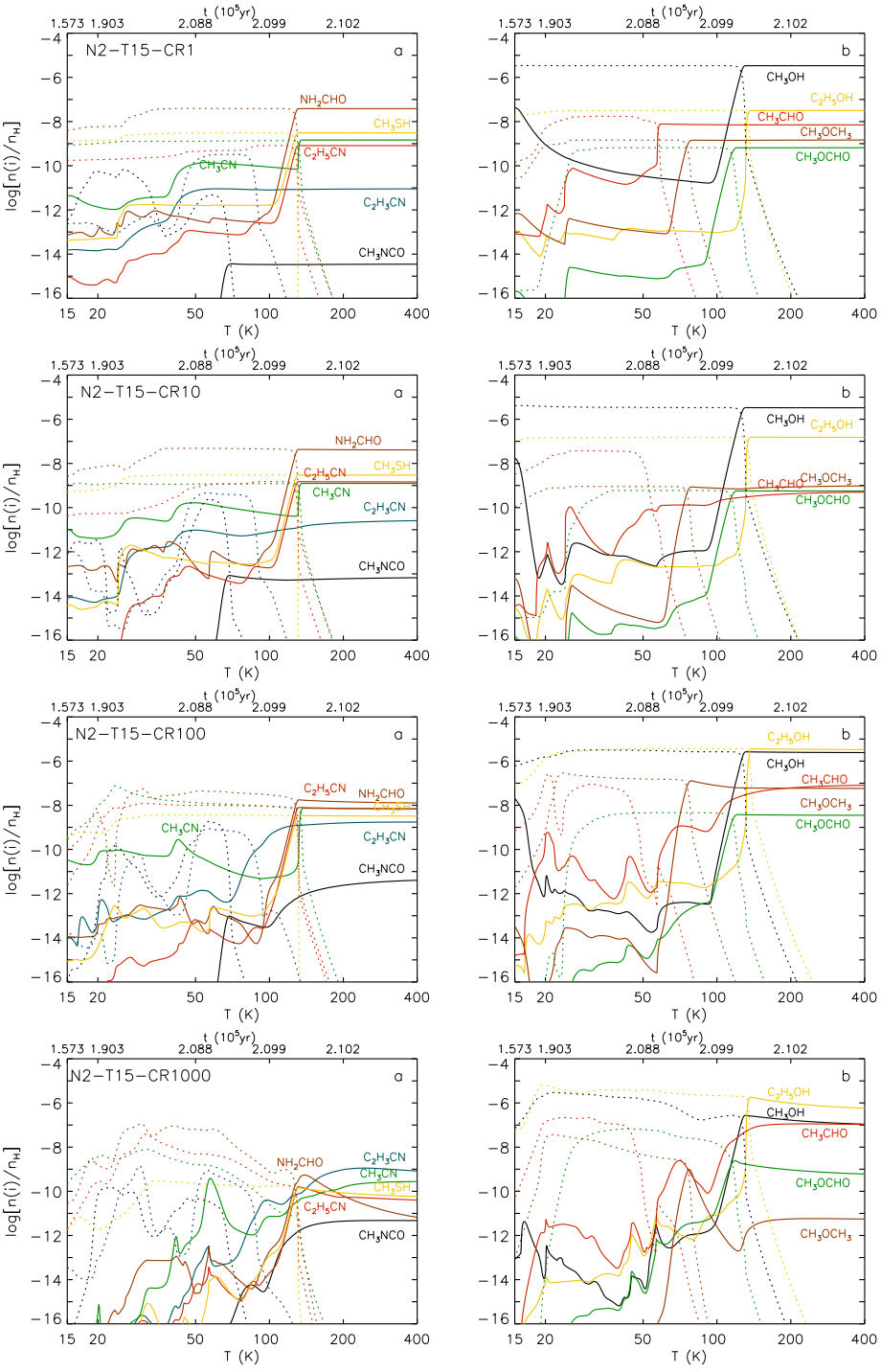

Figure 5.7: Fractional abundances of 11 COMs obtained with model N2-T15 with different values of the CRIR (as indicated in the top left corner of panel **a** of each row). Results are plotted as a function of temperature in the envelope of the sources during the free-fall collapse phase. In each panel, solid lines show the fractional abundances (with respect to total hydrogen) in the gas phase while dotted lines show the abundances of the same species on the grains (ice-surface+mantle). *Figure taken from Bonfand et al. (2019).*

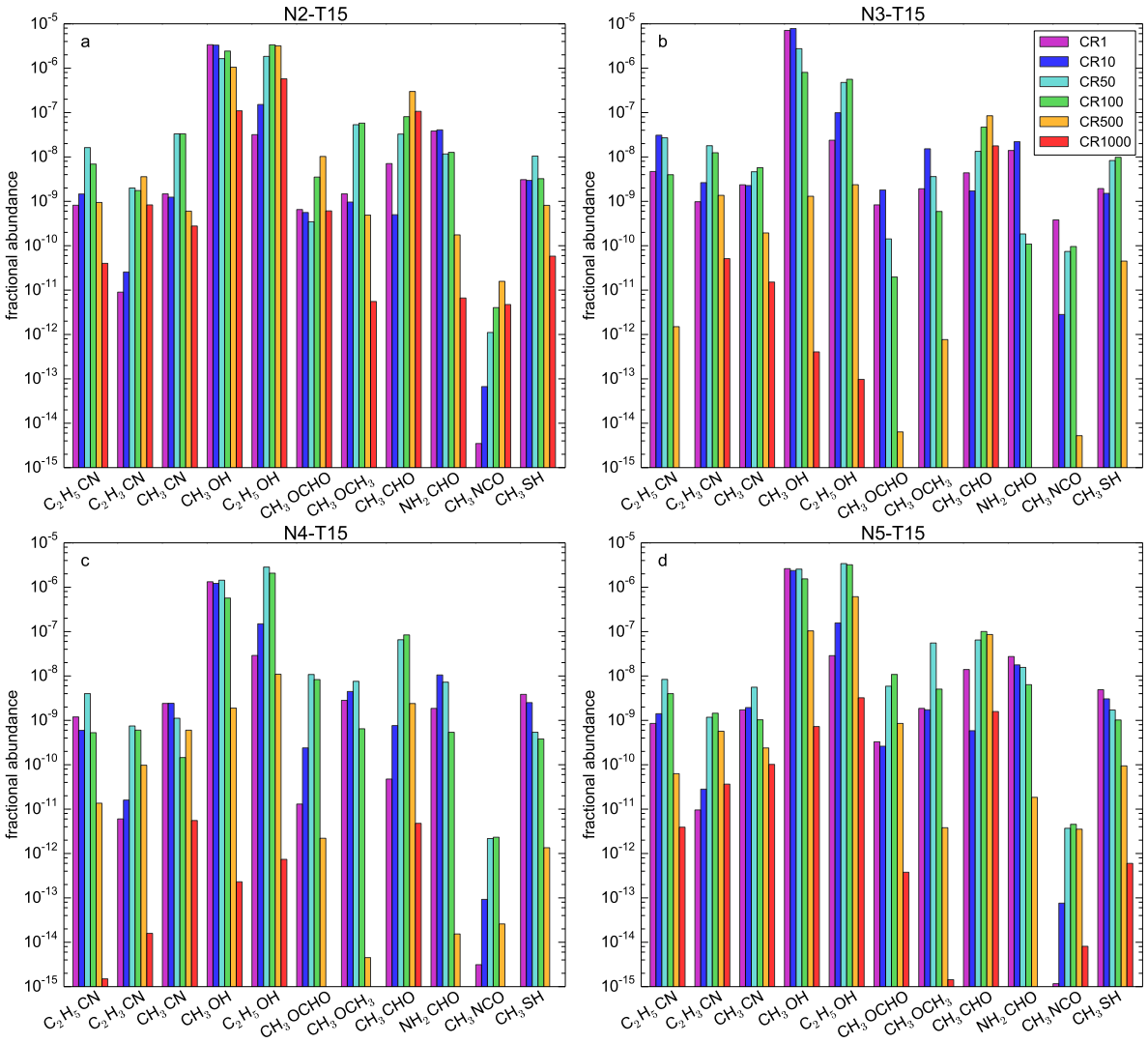

Figure 5.8: Gas-phase fractional abundances (with respect to total hydrogen) of 11 COMs calculated at the end of the simulations for models **a** N2-T15, **b** N3-T15, **c** N4-T15, and **d** N5-T15, with different values of the CRIR (see Table 5.4). Species with fractional abundances lower than 10^{-15} are not visible in the histograms. *Figure taken from Bonfand et al. (2019).*

Figure 5.8 shows the final gas-phase fractional abundances obtained for models N(2-5)-T15 for different values of the CRIR, ranging from $\zeta_0^{H_2}$ up to $1000\times\zeta_0^{H_2}$. It shows that the overall abundances of cyanides (R-CN) in the four sources rise as the CRIR increases, up to $100\times\zeta_0^{H_2}$. However, for $\zeta^{H_2} \geq 500\times\zeta_0^{H_2}$, the final gas-phase abundance of ethyl cyanide decreases significantly, leading to $[C_2H_5CN]/[C_2H_3CN] < 1$. The final fractional abundances of COMs calculated for the models N3-T15 and N4-T15 are strongly diminished in the high-CRIR models ($\zeta^{H_2} \geq 500\times\zeta_0^{H_2}$) compared to the low ionization-rate models (except for CH_3CHO in N3-T15-CR1000). The same behavior is not obvious for models N2-T15 and N5-T15. It appears that the influence of the cosmic rays on the chemistry depends on the source, suggesting that the impact of ζ^{H_2} may be exacerbated by the different physical properties of the cores.

Here we remind that our chemical model takes into account neither direct cosmic-ray bombardment of dust-grains ice mantles nor CR heating, although both processes could have an

impact on the calculated fractional abundances. For instance, laboratory experiments showed that direct cosmic-ray bombardment of ice analogs can trigger a rich chemistry that may lead to the formation of more complex species even at very low temperatures (Rothard et al. 2017). A full treatment of the effect of direct cosmic-ray collisions with dust grains on the solid-phase chemistry in chemical models can be found in Shingledecker et al. (2018) (see also Sect. 6.3). Hocuk et al. (2017) explored the impact of higher CRIRs on the dust temperatures including heating by CR-induced UV photons. They found that for an extreme ζ^{H_2} of 5×10^{-14} s^{-1} the resulting dust temperatures are higher by a factor $\leq$1.2 below $A_v = 10$ mag and up to a factor $\sim$1.8 for $A_v = 100$ mag (see their Fig. A.1). For the lower values of the CRIR used in our chemical simulations (from 1.3×10^{-17} s^{-1} up to 1.3×10^{-14} s^{-1}), dust grain heating by CR-induced UV photon should not have an important impact on our results.

Finally, for simplicity our models assume that cosmic rays are not attenuated in the envelope of the sources, although the large visual extinctions calculated for Sgr B2(N)'s sources (and in particular Sgr B2(N3), Fig. 4.14**b** and 4.15**b**) may lead to further attenuation of the cosmic-ray flux (see Sect. 6.3).

5.3.4 Influence of the minimum dust temperature

In this section we explore the influence on the chemistry and in particular on the production of COMs of varying arbitrarily the minimum dust temperature, T_{min}, that can be reached in the chemical simulations, but keeping a standard ISRF of 1 G_0. The influence of a stronger external UV field on the dust temperature and the chemistry is explored in the next section. (Sect. 5.3.5).

The dust temperature plays an important role in the chemical simulations, in particular in the early cold contraction phase, as an exponential dependence on T_d lies at the heart of most surface reaction rates (see Eqs. 5.5 and 5.6). The minimum dust temperature adopted in the simulations is thus critical as it controls the efficiency of the surface production of the main ice constituents, such as H_2O, CO, CO_2, and CH_3OH, essential to the production of COMs. The minimum dust temperature also directly impacts the conversion from atomic to molecular hydrogen on the grains.

Figure 5.9 shows the chemical composition of the ice mantles built up during the 1 Myr cold contraction phase for models N2-T10-CR1 (panel a) and N2-T20-CR1 (panel c), compared to the standard model N2-T15-CR1 (panel b). As expected significant differences can be seen in the overall chemical composition of the ice mantles compared to the standard model. The ice mantle formed in model N2-T10-CR1 is enriched in CO and depleted in CO_2 compared to the standard model. This is explained by the less efficient CO-to-CO_2 conversion when the dust temperature drops below $\sim$ 14 K. At low temperature H is converted more rapidly into H_2, thus decreasing the abundance of gas phase atomic hydrogen compared to the standard model. Surface OH mostly reacts with H_2 to form water ice rather than with CO to form CO_2. More CO is thus available to form H_2CO, and CH_3OH, enhancing their abundances in the outer ice layers compared to the standard model (N2-T15-CR1).

Model N2-T20-CR1 produces thinner ice mantles than N2-T10/15-CR1, with less than 70 ice layers formed on dust grains after 1 Myr. The mantle is enriched in carbon dioxide as most surface CO and OH react to form CO_2, decreasing the amount of H_2O, H_2CO, and CH_3OH formed on the grains. The atomic carbon accreted onto the grains mostly reacts with surface O_2 instead of reacting with atomic hydrogen to form CH, which affects the abundance of CH_4. Finally, at high dust temperature, reactions involving atomic hydrogen are less efficient

because the H coverage of the grains is reduced due to rapid desorption, cutting down the formation of complex species on grain surfaces. This can be seen also in Fig. 5.10 which compares the final gas-phase fractional abundances (with respect to total hydrogen) of the models with $T_{\rm min}$ = 10 K, 15 K, and 20 K for the four HMCs (the extreme test cases with $T_{\rm min}$ = 25 K and 28 K are discussed later in Sect. 6.3.). It shows that in most cases, a higher $T_{\rm min}$ results in lower fractional abundances. In particular, the O-bearing species CH_3OH, CH_3NCO, CH_3CHO, CH_3OCH_3, and CH_3OCHO are very sensitive to $T_{\rm min}$ with, for a given source, fractional abundances lower by more than two orders of magnitude in the 20 K models compared to the 10 K models. The fractional abundance of CH_3NCO varies by more than four orders of magnitude between the 10 K and 20 K models for N2, N3, and N5. CH_3SH is barely sensitive to changes in $T_{\rm min}$, with at most a factor 3.2 of difference between the three models for all sources. This is due to its production mechanism which relies on H_2CS which sticks to the dust grains at $T \sim 20$ K (see Sect. 5.3.2).

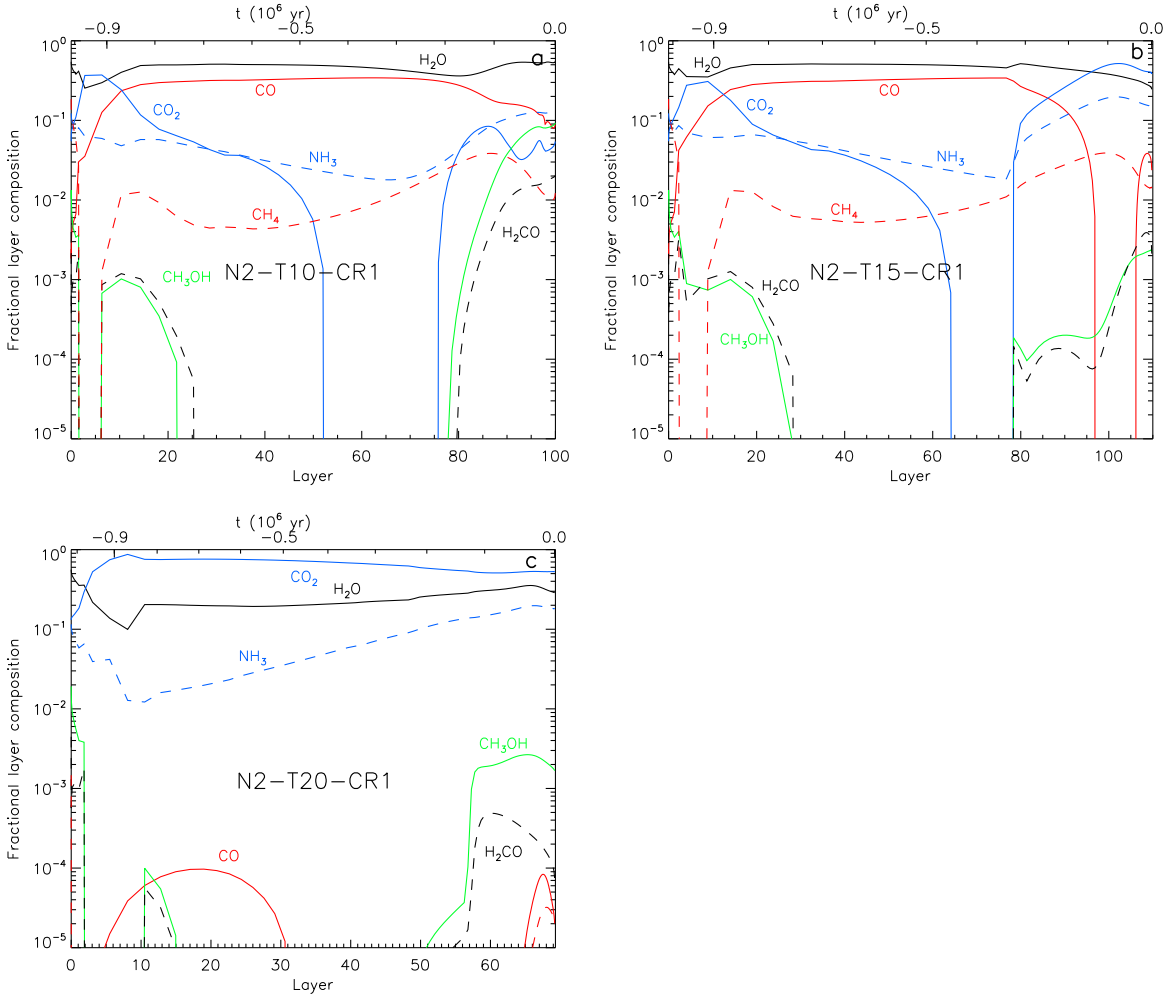

Figure 5.9: Composition of the ice mantles built up during the cold quasi-static contraction phase prior to the free-fall collapse for the model with **a** $T_{\rm min}$ = 10 K, **b** $T_{\rm min}$ = 15 K, and **c** $T_{\rm min}$ = 20 K. *Figure taken from Bonfand et al. (2019).*

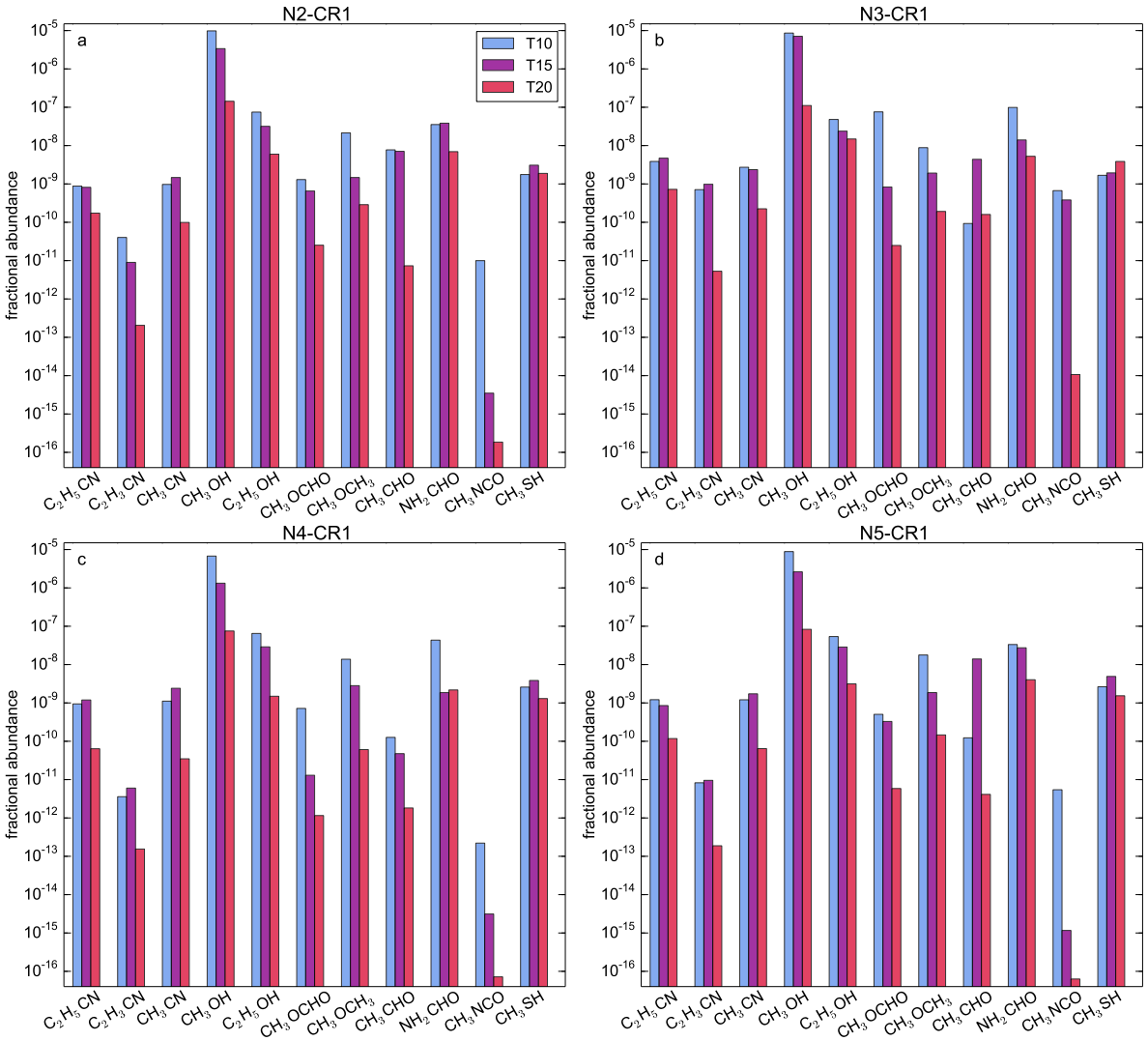

Figure 5.10: Calculated fractional abundances (with respect to total hydrogen) of 11 COMs at the end of the simulations for models **a** N2-CR1, **b** N3-CR1, **c** N4-CR1, and **d** N5-CR1, assuming a standard CRIR and different values of $T_{\rm min}$: 10 K in blue, 15 K in purple, and 20 K in red (see Table 5.4). *Figure taken from Bonfand et al. (2019).*

5.3.5 Influence of the external radiation field

A more rigorous way to characterize the dust temperature evolution during the pre-stellar phase than what we have done in Sects. 4.4.4 and 5.3.4 requires to take into account the grain heating via the external radiation field. By solving the thermal balance for equilibrium (see Eq. 2.29) and comparing their results to dust temperature measurements conducted with *Herschel*, Hocuk et al. (2017) derived a parametric expression of the visual-extinction-dependent dust temperature scalable with the interstellar radiation field strength:

$$T_{\rm d}^{\rm Hoc} = [11 + 5.7 \times \tanh(0.61 - \log(A_{\rm v}))]\ \chi_{\rm uv}^{1/5.9} \tag{5.24}$$

Figure 4.17 shows that for a standard ISRF (1 G_0) the dust temperatures computed with Eq. 4.10 given by Garrod & Pauly (2011) are higher than that computed by Hocuk et al. (2017) (Eq. 5.24), by up to a factor ∼1.3 at low visual extinctions. The disparity between

the temperatures obtained with the two expressions (Eqs. 5.24 and 4.10) arises from the different dust absorption efficiencies, Q_ν, assumed to solve the thermal balance for equilibrium equation (Eq. 2.29). For simplicity, Garrod & Pauly (2011) adopted a power law function of the frequency, $Q_\nu \propto a\nu^2$, where the grain radius a is fixed to 0.1 μm. Hocuk et al. (2017) adopted a more accurate treatment with $Q_\nu = \frac{4}{3}\kappa_\nu a \rho_{\rm gr}$, where $\rho_{\rm gr}$ is the bulk mass density of dust grain refractory material and κ_ν (per unit of mass density of dust) is obtained from semi-analytical calculations or direct laboratory measurements, giving a more realistic set of absorption efficiencies.

We note that Garrod & Pauly (2011) do not take into account the UV contribution to the ISRF spectrum, considering only the visual and IR contributions. This is an important omission in particular in the low visual extinction regime where UV photons are not efficiently absorbed. In order to explore the influence on the production of COMs of a radiation field enhanced compared to the standard neighborhood value used in our previous simulations, we scale our expression of the dust temperature (Eqs. 4.10 and 4.11) with the ISRF strength based on Eq. 5.24 as follows:

$$T_{\rm d}^{\rm uv}(A_{\rm v}) = T_{\rm d}(A_{\rm v}) \times \chi_{\rm uv}^{1/5.9} \ , \tag{5.25}$$

assuming that the whole ISRF spectrum scales in the same manner. To account for the extreme environment of the GC region (see Sect. 1.4.1) we run three additional chemical models for N2 with higher radiation field strengths, N2-UV100, N2-UV500, and N2-UV1000, with $\chi_{\rm uv}$= 100 G_0, 500 G_0, and 1000 G_0, respectively.

Figure 5.11 shows that the ISRF strength has a critical impact on the dust temperature, which is enhanced by up to a factor ∼2.4 to ∼3.5 for $\chi_{\rm uv}$ from 100 to 1000, compared to our standard model ($\chi_{\rm uv}$ = 1). In the most extreme model ($\chi_{\rm uv}$ = 1000), the dust temperature reaches up to ∼52 K at $A_{\rm v}$ = 2 mag. No arbitrary minimum threshold is fixed for the dust temperature here, such that the temperature decreases as the visual extinction increases until it reaches its minimum just before thermal heating from the central protostar takes over and dominates over external heating (see Fig. 5.11, vertical dotted lines). In models N2-UV100, N2-UV500, and N2-UV1000, the dust temperature drops as low as ∼14 K, ∼17 K, and ∼19 K, respectively (see Fig. 5.11). The gas temperature, $T_{\rm g}$, is held constant at 15 K during the whole quasi-static contraction phase.

Due to both the direct UV photo-dissociation, and -ionization of surface species that are particularly efficient at early times (when the densities are low in the pre-stellar phase) and the high dust temperature maintained by the external radiation field, ice mantles cannot form on dust grains and surface chemistry is mostly inefficient during the whole quasi-static contraction phase. Molecular species form at later times, during the free-fall collapse phase, at low temperature ($T_{\rm K}$ =15 K and $T_{\rm d} \leq$ 21 K, 19 K, and 14 K for N2-CR1-UV1000, N2-CR1-UV500, and N2-CR1-UV100, respectively, see Fig. C.9). At later times in the simulations (*i.e.* at higher densities), the impact of a stronger ISRF on the chemistry via photo-dissociation and photo-ionization is less critical as UV photons are absorbed as the visual extinction increases.

Figure 5.12a compares the fractional abundances of 11 COMs obtained with model N2-CR1 with different $\chi_{\rm uv}$ values. It shows that models with a stronger radiation field still allow the production of COMs. The strength of the radiation field adopted in the chemical simulations is critical for the O-bearing species CH_3OCHO, CH_3OCH_3, CH_3CHO, and CH_3NCO, while in comparison the fractional abundances of C_2H_5OH, CH_3OH, NH_2CHO, CH_3SH, as well as the cyanides is only slightly affected. Panel b of Fig. 5.12 shows that at higher value of the CRIR (50 times the standard value of 1.3×10^{-17} s^{-1}), the COM abundances are significantly

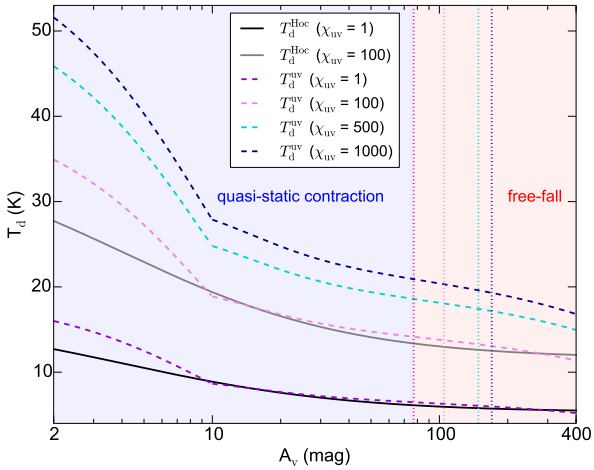

Figure 5.11: Visual-extinction-dependent dust temperature computed with the parametric expressions given in Eqs. 5.24 and 5.25, with different values of χ_{uv}. The quasi-static contraction phase and the free-fall collapse are represented with different background colors. The vertical dotted lines show the values of the visual extinction after which the dust temperature is no longer dominated by the external ISRF in the model but by the thermal heating from the central protostar.

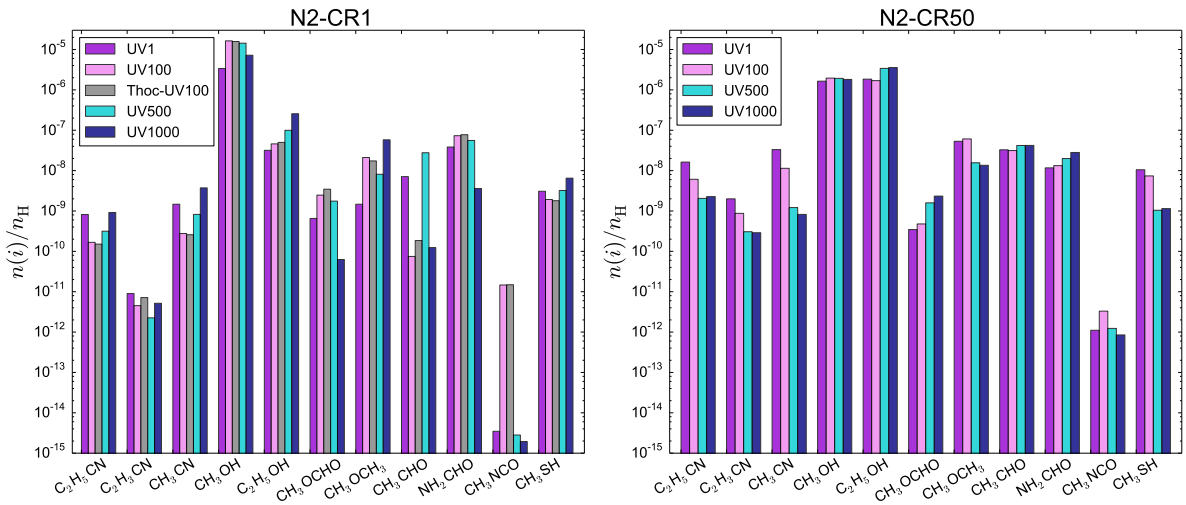

Figure 5.12: Fractional abundances (with respect to total hydrogen) obtained at the end of the simulations (*i.e.* T = 400 K) for model N2-CR1 (**a**) and N2-CR50 (**b**), with different χ_{uv} values.

less affected by the ISRF strength as the chemistry is driven by the cosmic rays. Additional chemical models (including models for the other sources, N3–N5) and further investigations of the model results will be needed to understand fully the impact of the ISRF on the formation and destruction processes of the individual COMs investigated here.

For comparison Fig. 5.12 also shows the final fractional abundances calculated by the model N2-CR1-Tdhoc-UV100, using the dust temperature expression given by Hocuk et al. (2017) (Eq. 5.24). The differences in the dust temperature profile below A_v = 10 mag between the expressions of Hocuk et al. (2017) and Garrod & Pauly (2011) does not have a strong impact on the production of COMs.

Chapter 6

Comparison with observations

Contents

In the previous chapter (Chap. 5), I used the astrochemical code MAGICKAL to model the time-dependent chemical evolution of Sgr B2(N2–N5) based on their physical evolution (Chap. 4). In this chapter I compare the abundances of selected COMs calculated by the chemical simulations to the abundances derived from the observations (Chap. 3) in order to determine the physical parameters (ζ_{H_2}, T_{min}, and χ_{UV}) that best characterize Sgr B2(N)'s hot cores.

This chapter is largely based on Bonfand et al. (2019). Other references are mentioned explicitly in the text.

6.1 Comparison of the numerical predictions with the observations

In Sect. 3.4 we derived mean rotational temperatures of 150 K from the COM emission toward Sgr B2(N2–N5). In order to compare the chemical model results to the observations, Table C.3 gives the calculated gas-phase fractional abundances obtained by all simulations at $T = 150$ K. In Fig. 6.1 we compare the calculated fractional abundances with respect to methanol to the observed values. This comparison shows that discrepancies with the model results can be large. In most cases the chemical models tend to underestimate the observed abundances. This is the case in particular for methyl formate, for which the calculated abundances from all chemical models are systematically lower than expected from the observations toward the four sources. The abundance of methyl isocyanate (with respect to methanol) is also underestimated by all models, by at least two orders of magnitude. In Sect. 5.3.2 we saw that solid-phase CH_3NCO desorbs from the grains around 70 K, however, we measured rotational temperatures > 140 K toward Sgr B2(N)'s hot cores (Sect. 3.4). This suggests that the binding energy adopted for CH_3NCO in our chemical models (see Table 5.2) is underestimated, or that some important chemical reactions involved in the production of methyl isocyanate are still missing in the chemical network (see, e.g., Quénard et al. 2018). For this reason CH_3NCO is not taken into account for the rest of our analysis.

Although no error bars are shown on the model results in Fig. 6.1, both calculated and observed abundances are uncertain in our analysis. The overall accuracy of the model results is discussed in Sect. 6.2.

6.2 Uncertainties of the chemical model results

As noted in Sect. 5.1.1, the overall accuracy of chemical model predictions resides in the knowledge of the rate coefficients and their uncertainties for the major gas-phase and grain processes. Wakelam et al. (2005) showed that the relative error on calculated abundances due to rate coefficient uncertainties may be larger than 50% for hot cores aged 10^4–10^6 yr (with $T = 100$ K, $n_{H_2} = 10^7$ cm^{-3}). Besides, additional uncertainties on the calculated abundances derive from the lack of experimental and theoretical data for grain-surface processes. As mentioned in Sect. 5.1.1 sufficient experimental or theoretical information is available only rarely and most grain-surface-related energies have to be guessed to build chemical networks. Recently, Iqbal et al. (2018) found that the abundances of both gas-phase and surface species calculated under typical dark cloud conditions are affected by large errors due to the uncertainties in the diffusion energy of surface species, in particular for the molecules predominantly formed at the grain surface like methanol.

A considerable effort is required from the laboratory experiments and theoretical computations to improve our knowledge of rate coefficients and grain-surface chemical reactions and processes, which are crucial to reproduce accurately the abundances of complex species observed in the ISM. Recently, Enrique-Romero et al. (2016) presented quantum chemical computations showing that grain-surface radical-radical addition reactions do not necessarily lead to the formation of complex species because these radicals are trapped by the water-ice molecules with an orientation that favors other two-product reactions. This might suggest that gas-phase reactions play a more important role in the formation of COMs than currently assumed in the chemical models. For instance, Skouteris et al. (2018) derived computationally rate coefficients for two gas-phase ion-molecule reactions proposed as main formation route for dimethyl ether: $CH_3OH + CH_3OH_2^+ \rightarrow (CH_3)_2OH^+ + H_2O$ followed by the reaction of $(CH_3)_2OH^+$ with ammonia to form $CH_3OCH_3 + NH_4^+$. The latter reaction, not included in our chemical network, could help in improving the agreement between the calculated and observed $[CH_3OCH_3]/[CH_3OH]$ ratios, which differ by at least one order of magnitude in our models N3–N5 (see Fig. 6.1).

We also note that in our chemical simulations, surface chemistry strongly depends on the abundance of atomic hydrogen in the gas phase. Slow H-to-H_2 conversion on the grain surfaces lead to high abundances of atomic hydrogen. If a more efficient conversion mechanism would take place, in the particular physical regime we explore here (high dust temperatures and high values of the CRIR), then fewer hydrogen atoms would be available on grain surfaces and this could significantly alter the calculated abundances. Cazaux et al. (2016) showed for instance that H_2 can also form efficiently via reaction of hydrogen atoms on polycyclic aromatic hydrocarbons (PAHs).

Finally because of the large number of parameters in the chemical code, a full analysis taking into account both observational and theoretical uncertainties (see e.g. Wakelam et al. 2006) would be too difficult and is not attempted here. In order to account for the limitations of the chemical model results presented above, a model is considered here to be in reasonable agreement with observations when it falls within one order of magnitude of the range of observed values with uncertainties (see Sect. 6.3).

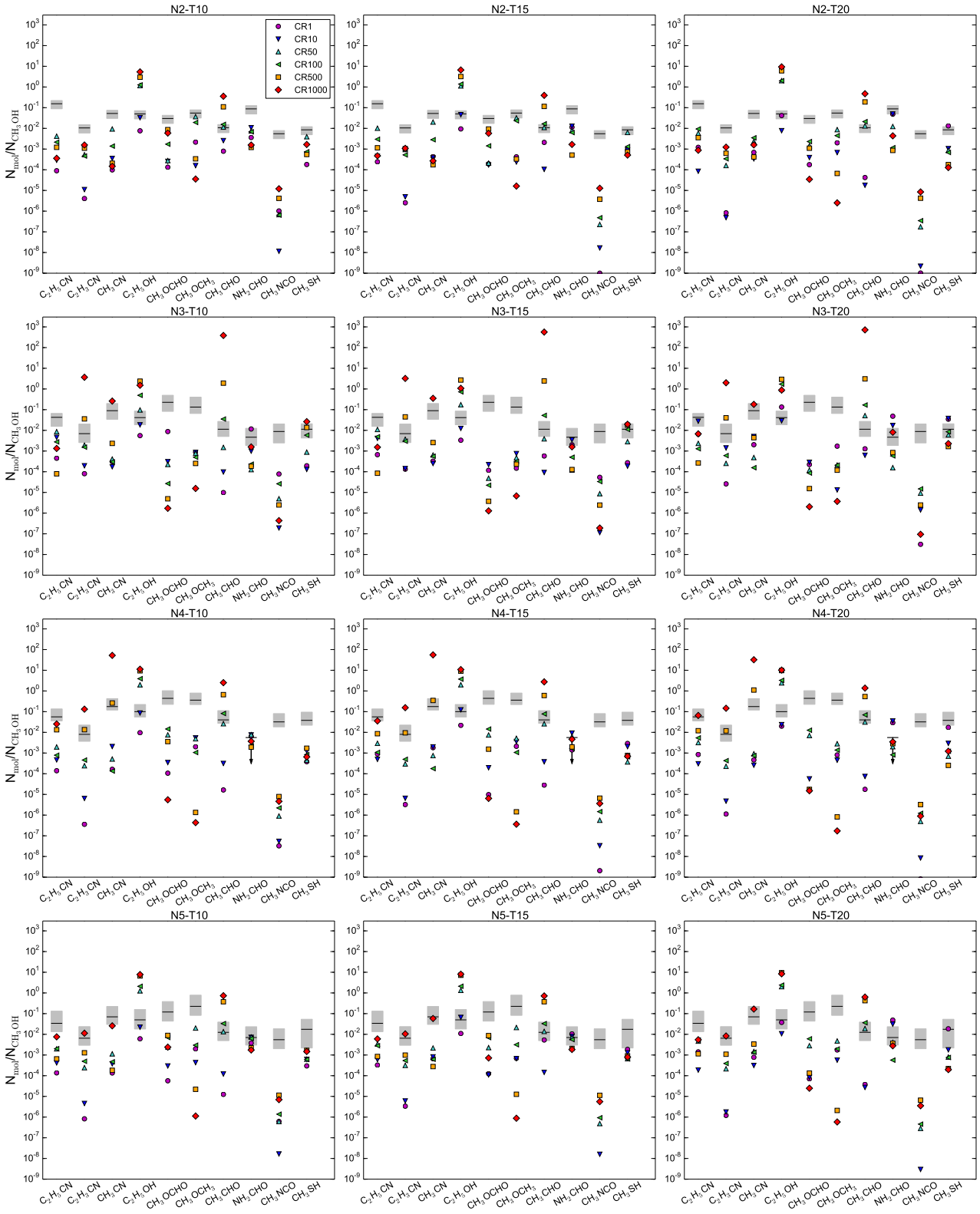

Figure 6.1: From top to bottom: chemical abundances with respect to methanol of ten COMs obtained for models N2–N5 with different values of $T_{\rm min}$. In each panel the symbols mark the calculated abundances for a given source with different values of the CRIR. In each panel the horizontal black lines show the observed abundances relative to methanol. Uncertainties on this ratio (1σ) are showed with gray boxes. Arrows indicate upper limits. *Figure taken from Bonfand et al. (2019).*

6.3 Constraining the environmental conditions in Sgr B2(N)

In order to determine which physical conditions (ζ_{H_2}, T_{min}, and χ_{UV}) best characterize Sgr B2(N2–N5), we need a quantitative method to evaluate the success of the chemical models in reproducing the observations. A mean of comparing rigorously the calculated abundances with the observed ones could be to perform a χ^2 minimization over all species. However, this method tends to skew the results in the case of large deviations from the observed values. For instance if a given species is three orders of magnitude away from the observed value in one model and six orders of magnitude in another model, the influence of this species on the resulting χ^2 will be large for both models, although in both cases the calculated value is already too far away to be credible. For this reason, we need a way to quantify to which extent variations in the calculated values are important when comparing models with large deviations from the observed values. To this aim we use the method developed by Garrod et al. (2007). For each model we compute a level of confidence, κ_i, in the agreement between calculated and observed abundances (relative to H_2, methanol, or methyl cyanide). For each calculated abundance ratio, the level of confidence is given by:

$$\kappa_i = erfc\left(\frac{|\log(R_{model,i}) - \log(R_{obs,i})|}{\sqrt{2}\sigma}\right) \tag{6.1}$$

which computes the logarithmic distance of disagreement between the calculated abundance ratio ($R_{model,i}$) and the observed one ($R_{obs,i}$). We define the standard deviation $\sigma = 1$ such that one standard deviation corresponds to one order of magnitude lower/higher than the observed abundance ratio. *erfc* is the error complementary function (*erfc* = 1-*erf*) such that κ_i ranges between 0 and 1. For instance, a calculated abundance ratio lying one order of magnitude lower/higher than the observed one has a confidence level $\kappa_i = 0.317$ (and $\kappa_i = 0.046$ for two orders of magnitude etc.). For each model we take the mean of the individual confidence levels obtained for each abundance ratio to define the overall confidence in the model with the observations.

We draw our attention first to the overall abundances of COMs with respect to H_2. Results of the confidence level calculations are given in Table D.1. Figure 6.2 shows the confidence levels for the ten investigated COMs (excluding CH_3NCO) relative to H_2, for N2–N5 taken individually and for all sources taken together. Panels a, b, and c show the confidence levels for all molecules, only the O-bearing molecules, and only the cyanides, respectively. The confidence level matrices differ from one source to the other, which may reflect the limits of our physical models assuming that all sources share the same accretion history. Given that all sources should have been exposed to the same cosmic-ray flux and probably shared a similar thermal history during the pre-stellar phase, we focus our attention on the matrices corresponding to the four sources taken together. The cyanides appear to be much more sensitive to T_{min} and CRIR than the O-bearing species and constrain the CRIR value to be about 50 times the standard one, and the minimum temperature to be below 20 K. The same result is observed for the O-bearing species but the constraints are less sharp.

In Fig. 6.2, models with $T_{min} = 20$ K still give acceptable results for the O-bearing species. Such high minimum dust temperature better represents the high temperatures measured toward the GC (T_d = 20–28 K, see Sect. 1.4.1) than the lower values usually assumed in chemical simulations (e.g. Müller et al. 2016; Belloche et al. 2017; Garrod et al. 2017). In order to derive an upper limit for the minimum dust temperature that allows the production of COMs to reproduce in an acceptable limit the abundances observed toward Sgr B2(N), we run additional

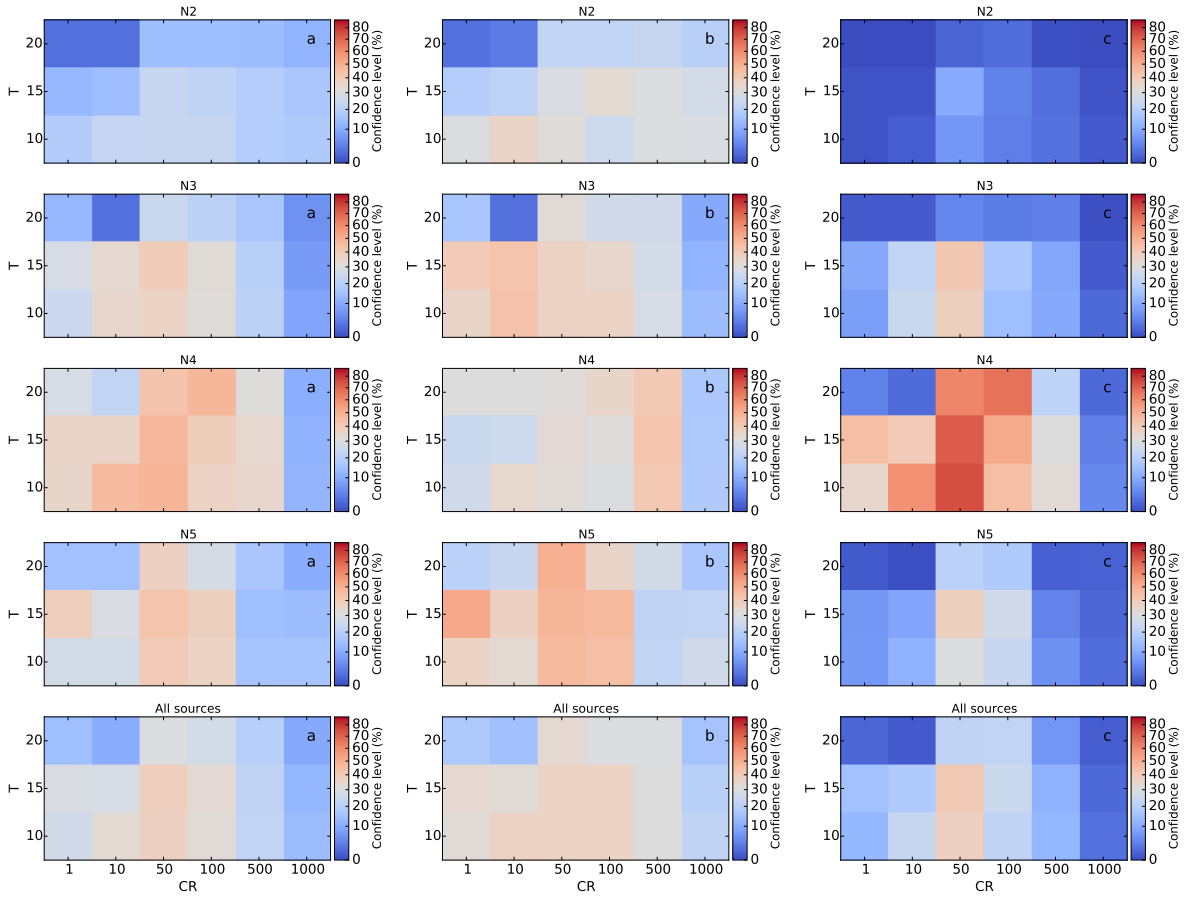

Figure 6.2: **a** Matrice of confidence levels of the models with respect to the observed abundances of ten COMs relative to H_2 (excluding CH_3NCO). The first four panels in this column show, from top to bottom, the results for N2, N3, N4, and N5, respectively. The bottom panel shows the average matrice for all four hot cores taken together. **b** Same as (a) but only for the O-bearing species CH_3OH, CH_3OCHO, CH_3OCH_3, CH_3CHO, C_2H_5OH, and NH_2CHO. **c** Same as (a) but only for the cyanides CH_3CN, C_2H_5CN, and C_2H_3CN. *Figure taken from Bonfand et al. (2019).*

simulations with $T_{\rm min} = 25$ K and 28 K for N2, with $\zeta^{\rm H_2} = 50\times\zeta_0^{\rm H_2}$ (see Fig. 6.3a). Ignoring the cyanides, we obtain confidence levels of about 10% and 5% for the models N2-T25-CR50 and N2-T28-CR50, respectively (see Table D.1). These values are much lower than the 23% obtained for N2-T20-CR50. This results from the high dust temperatures ($T_{\rm min} \geq 25$ K) preventing gas-phase atoms and simple molecular species such as CO to stick to the grains, damping the formation of ice mantles and thus the production of complex species. We expect the models of N3–N5 to behave in the same way such that the COM abundances relative to H_2 in N2–N5 certainly exclude $T_{\rm min} > 20$ K.

If we now focus on abundance ratios of COMs relative to each others to examine in more detail the influence of $T_{\rm min}$ and CRIR on the chemical composition of the sources itself, Fig. 6.4 shows the matrices of confidence levels computed for nine COMs relative to methanol (panel a), the O-bearing molecules relative to methanol (panel b), and the cyanides relative to methyl cyanide (panel c) (see also Table D.2). This refinement reveals that the O-bearing COM chemical composition relative to methanol is sensitive to the CRIR value, with the best-fit value

being 50 times the standard value, in agreement with the constraints obtained from the cyanide abundances relative to H_2 (see Fig. 6.2). A minimum temperature below 20 K seems to be favored as well. The cyanide chemical composition with respect to methyl cyanide is less sensitive to the two investigated parameters (bottom panel of Fig. 6.4c). However, a more detailed investigation reveals that the abundance ratio of C_2H_5CN to C_2H_3CN, two species that are chemically linked (see Sect. 5.3.2), is sensitive to the CRIR. Figure 6.5 shows that this ratio decreases as the CRIR increases in the four sources Sgr B2(N2–N5). The observed ratios are best reproduced by the models with $50\times\zeta_0^{H_2} \leq \zeta^{H_2} \leq 100\times\zeta_0^{H_2}$, due to the increase in the gas-phase abundance of C_2H_3CN at late times (*i.e.* high temperatures) in these models. This behavior is consistent with what we observe, in particular toward Sgr B2(N2) where the rotational temperature derived for C_2H_3CN is higher than that of C_2H_5CN. The flat gas-phase abundance profile of C_2H_3CN at $T > 40$ K in the standard models with lower CRIR (Fig. 5.4) would imply that it traces more extended regions than C_2H_5CN, which would be inconsistent with what is observed in N2.

The analysis presented above shows that chemical models with a CRIR enhanced by a factor 50 compared to the standard value best reproduce the observations for the four hot cores, N2–N5, taken together. However, here we remind that for simplicity our chemical models assume that cosmic rays are not attenuated in the envelope of the sources, although the large visual extinctions of Sgr B2(N2–N5) (see Figs. 4.15b and 4.16b) may actually lead to attenuation of the cosmic-ray flux. This might have an impact on the chemical model results as Rimmer et al. (2012) showed that a column-density-dependent CRIR improves the agreement between chemical model predictions and observations for the Horsehead nebula, compared to a standard model with a uniform CRIR (see also Willis et al. subm.). Recently Neufeld & Wolfire (2017) showed, based on H_2 and H_3^+ column densities measured toward diffuse clouds in the galactic disk, that the CRIR decreases with increasing H_2 column density with a best-fit dependence scaling as $N(H_2)^{-a}$ with $a = 0.92 \pm 0.32$ for $N(H_2) \sim 10^{20}$ – 10^{22} cm^{-2}. This implies that the cosmic-ray flux is attenuated by a factor $\sim$ 70–600 from the diffuse regions with $N(H_2) = 10^{21}$ cm^{-2} to the dense gas with $N(H_2) = 10^{23}$–10^{24} cm^{-2}. Moreover, our models do not take into account direct cosmic-ray bombardment of dust-grain ice mantles although laboratory experiments showed that it can trigger a rich chemistry that may lead to the formation of more complex species even at very low temperatures (Hudson et al. 2001; Rothard et al. 2017). Recently, Shingledecker et al. (2018) used chemical models to investigate the effect of direct cosmic-ray collisions with dust grains on the solid-phase chemistry, including the formation of suprathermal species in the ices from collision with energetic particles. For instance, for a standard CRIR (10^{-17} s^{-1}), they found that the abundance of methyl formate, which is systematically underproduced in all our models (Fig. 6.1), is significantly enhanced in the gas phase, as well as on the grains compared to the standard chemical model (that is without cosmic-ray driven reactions).

Figure 6.3 showed that our models firmly exclude minimum dust temperatures of 25 K or higher during the pre-stellar phase of N2–N5. Such high temperatures would prevent the production of COMs at the level observed in these sources. Our models show that a value of 15 K still leads to an efficient production of COMs roughly consistent with the observations, while for 20 K signs of disagreement emerge between model and observations, especially for the cyanide abundances relative to H_2 and the O-bearing COM chemical composition relative to methanol. It could be that models with T_{min} =17–18 K produce COMs in amounts that are still consistent with the abundances measured in Sgr B2(N)'s hot cores. Such temperatures are still

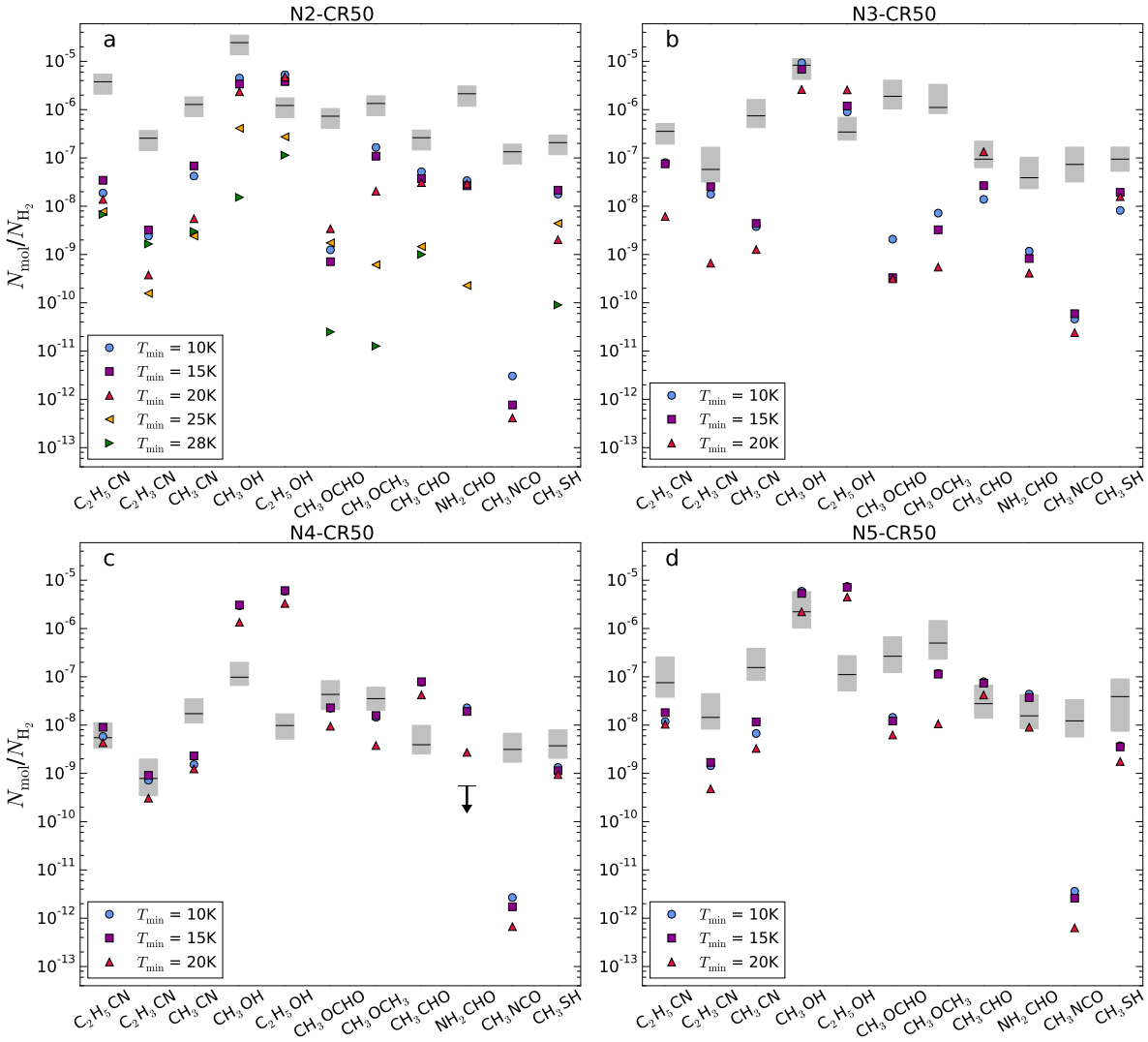

Figure 6.3: Abundances of 11 COMs with respect to H_2 for models N2-CR50 (a), N3-CR50 (b), N4-CR50 (c), and N5-CR50 (d). In each panel the different symbols indicate the abundances calculated at $T = 150$ K for different minimum dust temperatures. In each panel the horizontal black lines show the observed abundances relative to H_2. The gray boxes show the 1σ uncertainties. The arrow indicates an upper limit. *Figure taken from Bonfand et al. (2019).*

lower than expected from the measurement made toward the GC region, however, in this region the coldest dust grains may be masked by warmer outer layers and thus have been missed by *Herschel* because of its limited angular resolution. Therefore, the constraint we derived on T_{min} from the COM abundances is not inconsistent with the thermal properties of the GC region.

As mentioned earlier (see Sect. 5.3.5), a more rigorous treatment of the dust temperature behavior in the pre-stellar phase requires to compute self-consistently the dust temperature evolution accounting for dust heating from the external radiation field. Figure 6.6 shows that the chemical models with different values of the ISRF strength does not allow us to better reproduce the observed abundances ratios relative to methanol, compared to our best-fit model T15-CR50-UV1 (with $\zeta_{H_2} = 6.5\times10^{-16}$ s^{-1}, see light blue triangles in Fig. 6.6). A stronger UV field even increases the discrepancy between calculated and observed abundances for the

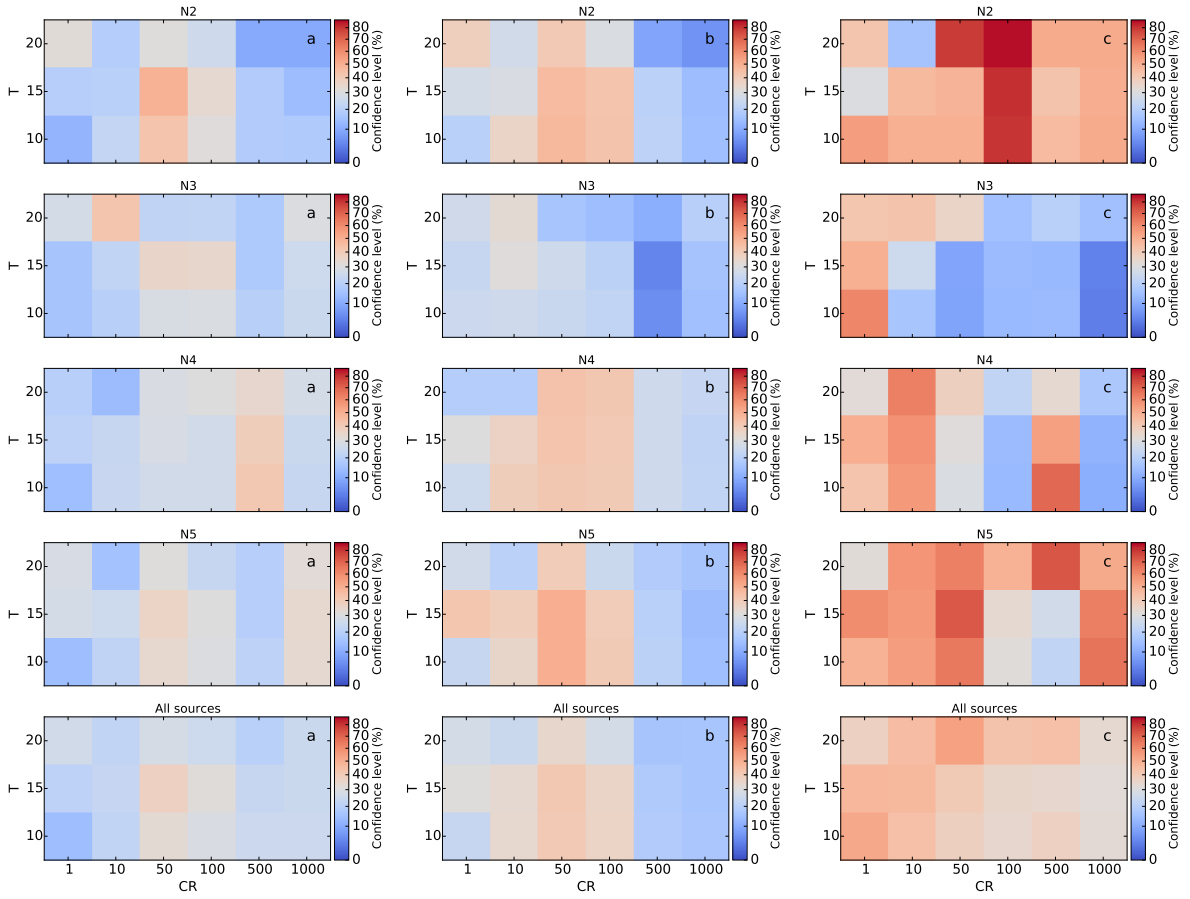

Figure 6.4: **a** Matrice of confidence levels of the models with respect to the observed abundances of nine COMs relative to CH_3OH. The first four panels in this column show, from top to bottom, the results for Sgr B2(N2), N3, N4, and N5, respectively. The bottom panel shows the average matrice for all four hot cores taken together. **b** Same as (a) but for the abundances relative to methanol of the O-bearing species CH_3OCHO, CH_3OCH_3, CH_3CHO, C_2H_5OH, and NH_2CHO only. **c** Same as (a) but for the abundances relative to methyl cyanide of the cyanides C_2H_5CN and C_2H_3CN only. *Figure taken from Bonfand et al. (2019).*

cyanides with respect to methanol, while the abundances of NH_2CHO, CH_3CHO, and C_2H_5OH relative to methanol are only slightly affected by the UV field strength. The mean confidence level of the models with the observations with respect to methanol for different χ_{UV} are given in Table D.2. It shows that the confidence levels drop significantly for models with higher χ_{UV} than the standard model T15-CR50-UV1. The opposite behavior is obtained when computing confidence levels with only the cyanides C_2H_3CN and C_2H_5CN with respect to CH_3CN (that is the agreement with observations increases with the UV field strength). Finally, all models have similar confidence levels when computed based only on the O-bearing species CH_3OCHO, CH_3OCH_3, CH_3CHO, C_2H_5OH, and NH_2CHO. This does not allow us to conclude strictly on which interstellar radiation field better characterizes Sgr B2(N).

For comparison, Fig. 6.6 also shows the fractional abundances with respect to methanol calculated by model N2-CR50-Tdhoc-UV100, which uses the dust temperature expression given by Hocuk et al. (2017) (see Eq. 5.24). As mentioned already in Sect. 5.3.5 the expression used to compute the dust temperature does not change much the results, as there is at most a

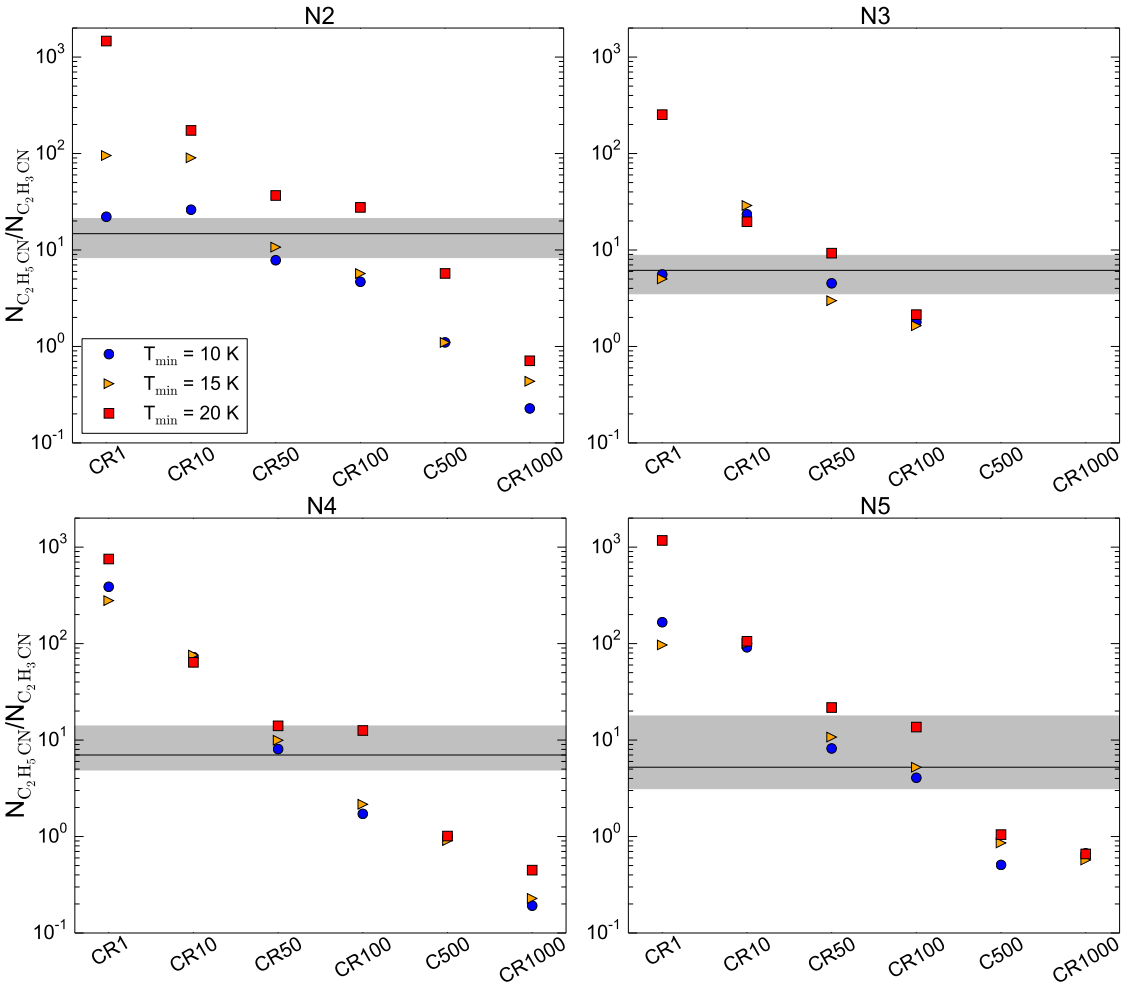

Figure 6.5: Calculated fractional abundances of ethyl cyanide with respect to vinyl cyanide as a function of the CRIR. In each panel, the different symbols indicate the abundances calculated at $T = 150$ K for different minimum dust temperatures and the horizontal black line shows the observed ratio. Uncertainties (1σ) are shown in grey. The $[C_2H_5CN]/[C_2H_3CN]$ ratios obtained for models N3-CR500 ad N3-CR1000 ($<10^{-2}$) are not displayed. *Figure taken from Bonfand et al. (2019).*

factor ∼1.6 of difference in the abundances with respect to methanol calculated by models N2-CR50-Tdhoc-UV100 and N2-CR50-UV100.

6.4 Discussion

The simplified treatment we have adopted for our physical models for N2–N5 (see Sect. 4.6), in particular assuming the same accretion history for all four investigated sources and taking an accretion rate that does not drop below $10^{-4} M_\odot$ yr^{-1} to form more massive objects, luminous enough to match the values we derived from the observational constraints (see Sects. 4.3.1 and 4.3.2) results in significant differences in the time evolution of Sgr B2(N3)'s physical parameters (n_H, A_v, and T) compared to the other three sources. Given its lower luminosity, N3 is

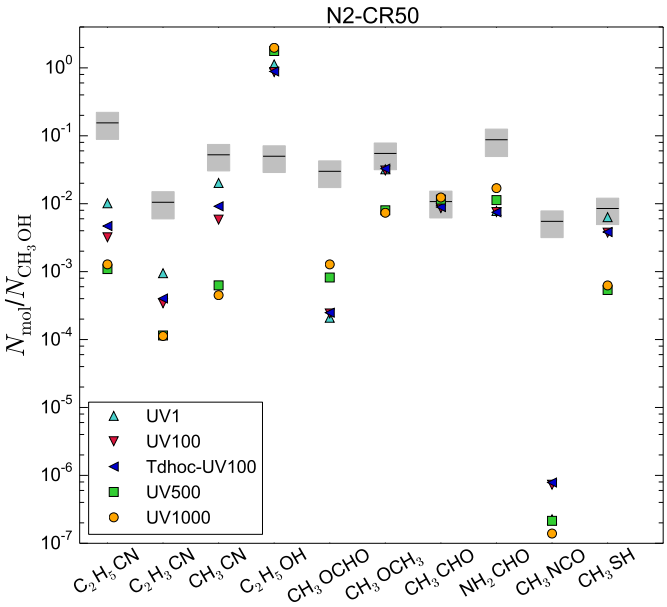

Figure 6.6: Chemical abundances with respect to methanol of ten COMs calculated at $T = 150$ K by the models N2-CR50. The different symbols indicate the abundances calculated with different χ_{UV}. Model Tdhoc-UV100 shows the results obtained using the dust temperature expression given by Hocuk et al. (2017) with $\chi_{UV} = 100$. The horizontal black lines show the observed abundances relative to methanol. The gray boxes represent the 1σ uncertainties. *Figure taken from Bonfand et al. (2019).*

apparently younger than the other sources (see Table 4.7). In the framework of our model, with a fixed duration of the pre-stellar phase, this results in a faster increase of the density and temperature at the compact radius of N3.

Figure 6.3 shows that our best models (that is with $\zeta^{H_2} = 50\times\zeta_0^{H_2}$) better reproduce the chemical abundances (with respect to H_2) of ethanol and methanol in Sgr B2(N3) compared to the other sources. However, the modeled abundances of CH_3OCHO and CH_3OCH_3 are 2–3 orders of magnitude lower than the abundances measured toward N3. This might suggest that the relations $\dot{M}(t)$, $M(t)$, and $L(t)$ we derived in Sect. 4.4.1 do not represent accurately the physical evolution of N2–N5.

We saw that the chemical composition calculated by our chemical simulations for Sgr B2(N)'s hot cores strongly depends on their history, starting from the early cold pre-stellar phase. As discussed already in Sect. 4.6, the physical profiles, and thus the chemical model results, rely on the luminosity of the protostars that we inferred from the rotational temperature measured at the radius of the COM emission (see Sect. 4.3.2). If a mechanism such as that observed toward the high-mass star-forming region G328.2551–0.5321 where methanol and other O-bearing species are thought to be released in the gas phase upon the accretion shocks (Csengeri et al. 2018, Csengeri et al. subm.), then the thermal history derived for Sgr B2(N2-N5) would then be incorrect, and this could have a significant impact on the results of our chemical modeling.

These last considerations emphasize the need for further investigations of higher angular resolution observations such that attained in the ReMoCA survey (Belloche et al. 2019) and for RMHD simulations tailored to each hot core in order to have a more realistic description of the hot cores' history and improve the reliability of the chemical model results.

Chapter 7

Conclusions

In this thesis we have investigated the on-going high-mass star-forming activity and the associated complex chemistry in the Sgr B2 molecular cloud, which stands out from other regions forming high-mass stars due to its high mass, high densities, and its exposure to the extreme GC environment. We took advantage of the high sensitivity of the 3 mm line survey EMoCA conducted with ALMA to extend our view of the distribution of active star-forming regions in Sgr B2(N). We report the discovery of multiple sources of which at least three have been qualified as HMCs, based on their association with 6.7 GHz class II methanol masers, tracers of high-mass star-forming regions. The three new HMCs, that we called N3, N4, and N5, are located at ($\alpha_{\rm J2000}$=$17^h47^m19.248^s$, $\delta_{\rm J2000}$ = -28°22′14.91″), ($\alpha_{\rm J2000}$ = $17^h47^m19.528^s$, $\delta_{\rm J2000}$ = -28°22′32.41″), and ($\alpha_{\rm J2000}$ = $17^h47^m20.047^s$, $\delta_{\rm J2000}$ = -28°22′41.34″), respectively.

We have analyzed the EMoCA survey to characterize the hot core population embedded in Sgr B2(N). The spectra observed toward N3–N5 have relatively high spectral line densities, confirming their status of HMCs. We detected toward these three sources 11–31 emission lines per GHz above the 7σ level, with typical linewidths of about 5 km s^{-1}, comparable to that of the secondary hot core N2. We performed the LTE radiative transfer modeling of the spectra observed toward the new hot cores to identify the lines and derive the chemical compositions of the sources (*i.e.* molecular column densities). Approximately 91%, 89%, and 93% of the emission lines detected above 7σ have been identified and assigned to 20–23 molecules, of which about half are complex, plus 10–20 less abundant isotopologs. We presented the first detailed comparison of the chemical composition of four HMCs embedded in Sgr B2(N) based on the column densities of 11 COMs. The analysis of the abundances relative to H_2 and methanol shows that N3 and N5 share a relatively similar chemical composition, while N2 differs significantly from the other hot cores N3–N5.

From population diagrams based on selected transitions that are well detected and not severely contaminated by lines from other species, we derived excitation temperatures ranging between ∼140 K and 190 K for N3–N5, comparable to the rotational temperatures derived for N2. We fitted 2D Gaussians to the integrated intensity maps of the transitions that have a high signal-to-noise ratio, are well reproduced by the LTE model, and are not severely contaminated by other species, in order to derive the size of the COM emission region in N3–N5. We obtained mean deconvolved diameters of 1.0″ for N4 and N5, which is slightly smaller than the size of N2 (∼ 1.″2), but larger than N3 for which we find a more compact emission region of 0.″4 in diameter.

From a combined analysis of ALMA and SMA dust continuum maps obtained at two different frequencies, we derived the dust properties that best characterize Sgr B2(N). We used these values to compute H_2 column densities toward N1-N5 assuming a dust temperature equal to the gas kinetic temperature derived from populations diagrams (150 K). For the sizes listed above we obtained H_2 column densities of 1.6×10^{24}, 0.9×10^{24}, 2.6×10^{24}, and 0.9×10^{24} cm^{-2} for N2, N3, N4, and N5, respectively. From the H_2 column densities we computed the mass of

the hot core regions N2–N5 as well as the densities within the COM emission region.

We used a radiative transfer code to estimate the current luminosities of N2–N5, based on the rotational temperatures and the average radius of the COM emission derived from the observations. We obtained luminosities of $2.6{\times}10^5$ $L_\odot$, $4.5{\times}10^4$ $L_\odot$, $3.9{\times}10^5$ $L_\odot$, $2.8{\times}10^5$ $L_\odot$ for N2, N3, N4, and N5, respectively. Based on published results of RMHD simulations of high-mass star formation and stellar structure calculations we derived the time evolution of protostellar properties and the thermal history of the sources, starting from the cold pre-stellar phase, through the HMC phase and beyond. The physical history of the sources is used as an input in the astrochemical code MAGICKAL to simulate the fully time-dependent physico-chemical evolution of N2–N5. For each hot core we investigated in detail the chemistry of 11 COMs and in particular the impact on their production of the external interstellar radiation field, the minimum dust temperature reached during the past, and the cosmic-ray flux.

We tested the reliability of our chemical models by comparing the calculated chemical abundances to the observed ones. We found that the production of the cyanides C_2H_5CN and CH_3CN as well as CH_3OH and C_2H_5OH mostly relies on the early cold grain-surface chemistry ($T_\mathrm{d} \leqslant 15$ K), while the O-bearing species CH_3CHO, CH_3OCHO, CH_3OCH_3 form predominantly during the warm-up phase of the protostellar evolution. These two groups of molecules can thus be seen as 0th and 1st–2nd generation COMs, respectively, following the classification of Herbst & van Dishoeck (2009, see also Sect. 1.3).

Assuming that all four investigated HMCs are exposed to the same environmental conditions, we used the coupled analysis of chemical models and observations to constrain the physical parameters which best characterize Sgr B2(N) and the GC center region. We obtained the best match between calculated abundances and observations for $\zeta^{\mathrm{H_2}} = 7{\times}10^{-16}$ s^{-1}, that is a CRIR enhanced by a factor 50 compared to the solar neighborhood value. This is somewhat lower than extreme values expected toward the diffuse medium in the GC region ($1 - 11{\times}10^{-14}$ s^{-1}). This difference may reflect the attenuation of cosmic rays in denser gas. We showed that COMs are produced in abundances comparable to the observed ones for $T_\mathrm{min} = 15$ K. The current chemical composition of Sgr B2(N2–N5) excludes minimum dust temperature $\geqslant$25 K. We cannot conclude firmly which value of the ISRF strength best characterizes Sgr B2(N). Further analysis are needed to fully understand the influence of the ISRF strength on the time-dependent chemical abundances computed in the chemical models, in particular during the early cold phase of the free-fall collapse.

In summary, we presented the first detailed analysis of the chemical history of four HMCs embedded in Sgr B2(N), by combining a high-angular-resolution spectral line survey and astrochemical models to compare the hot cores against each other in a systematic way. We showed that the chemical abundances calculated by our chemical models for N2–N5 strongly depend on the physical and thermal history of the sources since the earliest stages of star formation in the pre-stellar phase. We pointed out some caveats in our physical models for N2–N5. By assuming the same protostellar evolution for N2–N5, given by the relations $\dot{M}(t)$, $M(t)$ and, $L(t)$, we estimated the ages of the sources, based on their estimated current luminosities, to be $\sim$2–3$\times10^5$ yr for N2, N4, and N5, a factor $\sim$10–15 times older than N3. This is not consistent with the evolutionary sequence we proposed for Sgr B2(N)'s sources, based on their association with tracers of star formation (UCHII regions, class II methanol masers, and molecular outflows). In particular, N4 appears younger than N3, based on the detection of a molecular outflow toward N3 while N4 does not show evidence of an outflow yet. Further investigations at higher angular resolution are needed to better understand the status of the sources (see dis-

cussion in Sect. 8.1). Furthermore, based on the number of UCHII regions known in the field of view of the ALMA observations and assuming a typical lifetime of 10^5 yr for the UCHII phase, we derived statistical lifetimes of 4×10^4 yr for the class II methanol masers and 6×10^4 yr for the HMC phase in Sgr B2(N). This is a factor 3–5 shorter than the ages we estimated for N2, N4, and N5 from their current luminosities assuming they follow the same accretion history. These inconsistencies point out the fact that the accretion rate of N2–N5 might be, or might have been, higher than what we assumed to model the physical evolution of the sources. Our strong assumption about the accretion history being the same for all sources implies a much shorter evolutionary timescale for N3, which has a significant impact on its calculated chemical composition and results in a worse agreement with the observations compared to the three other HMCs. This emphasizes the need for individual RMHD simulations tailored to each HMC in order to get a more realistic description of their time-dependent physical evolution and improve the reliability of the chemical model results.

Chapter 8

Prospects

Contents

8.1 Sgr B2(N) at higher angular resolution: the ReMoCa survey

Besides the analysis presented in this thesis, mainly focused on the three new HMCs (N3–N5) detected in Sgr B2(N), another important outcome of the EMoCA survey is the first detection of several interstellar COMs. In particular, Belloche et al. (2014) reported the detection of the first interstellar branched carbon-chain molecule, *iso*-propyl cyanide (*i*-C_3H_7CN) toward N2, which was found to be almost as abundant as its straight-chain homologous, *normal*-propyl cyanide (*n*-C_3H_7CN). Following the discovery of *i*-C_3H_7CN in the EMoCA data, Garrod et al. (2017) used the chemical code MAGICKAL to perform chemical calculations with an extended chemical network including the next member of the alkyl cyanide series, n-butyl cyanide (*n*-C_4H_9CN) and its three branched isomers (*s*−, *i*−, and *t*−C_4H_9CN). The chemical models predicted that *s*−C_4H_9CN will dominate over the other forms, with a peak abundance comparable to that of *n*-C_3H_7CN, which makes of *s*−C_4H_9CN a good candidate for detection toward Sgr B2(N).

Motivated by the first detection of interstellar *i*-C_3H_7CN and the search for C_4H_9CN, a new imaging spectral line survey covering the same frequency range as the EMoCA data has been recently conducted with ALMA toward Sgr B2(N) (Cycle 4, PI: A. Belloche). This new line survey, called ReMoCa (for Re-exploring molecular complexity with ALMA, Belloche et al. subm.), represents an improvement in sensitivity to compact emission by a factor ∼3 (rms ∼1.2 mJy) compared to the EMoCA data (∼3.0 mJy).

Besides the quest for new detections, the ReMoCa data will be used to deepen the analysis of the sources embedded in Sgr B2(N). The improvement in sensitivity will allow us to investigate fainter emission lines than those detected with the EMoCA data, to search for already known molecular species that have not been identified yet toward the fainter HMCs N3–N5. This analysis will tell us whether the chemical differences observed between N3–N5 and the secondary HMC N2 (in terms of number of identified species, see Sect. 3.5) is significant or simply limited by the sensitivity of the EMoCA data. The high angular resolution attained in the ReMoCA survey, enhanced by a factor ∼3 (∼0.54″) compared to the EMoCA data (∼1.6″), will allow us to resolve small structures in Sgr B2(N) that could not be separated with the angular resolution of the EMoCA survey (see, e.g., the case of N2 discussed in Sects. 3.1.2 and 4.5). The ReMoCa data will help us to characterize better the physical and chemical structure of the HMCs already investigated, in particular N3–N5 for which only a few transitions showed resolved emission in the EMoCA data (see Sect. 3.3), as well as other possible hot cores/corinos detected in

Sgr B2(N) (see Sect. 3.1.2). The new ALMA dataset will be useful to investigate further the evolutionary stage of these sources, for instance, to look for molecular outflows (see, e.g., the case of N4 discussed in Sects. 4.1.2 and 4.5), and to determine whether a chemical differentiation between N- and O-bearing species occurs in Sgr B2(N)'s hot cores. Finally, thanks to the high angular resolution of the ReMoCa survey, we will also be able to characterize better the spatial structure and the chemical composition of the main HMC N1, for which some species detected in the EMoCA data have already revealed a more complex structure than the compact emission concentrated toward the HMC peak position observed for most species (see Fig. 8.1c). In Figs 8.1a and b, the transitions of methanol and methyl formate clearly show double-peaked emission, offset North and South from the peak position of N1 (see also Xue et al. 2019). The investigation toward a new position called N1-South, harboring lines narrower than the peak position N1 in the EMoCa dataset, has already unveiled the first detection of interstellar urea (Belloche et al. subm.).

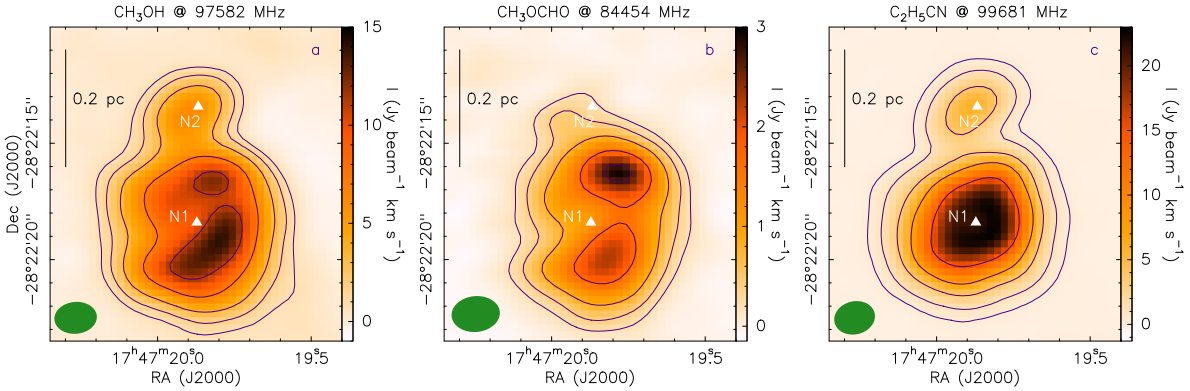

Figure 8.1: Integrated intensity maps of transitions of **a** methanol, **b** methyl formate, and **c** ethyl cyanide, toward N1 ($v_{\rm LSR}$ = 64 km s^{-1}) in the EMoCA data. The frequency of the transitions is indicated on top of each panel. In all panels, the white triangles mark the peak positions of the HMCs N1 and N2 (see Table 3.1). The green filled ellipse shows the mean synthesized beam of the EMoCA data (see Table 2.2). The contour levels are (3, 6, 12, 25, 40, 106)×3σ, with σ = 93 mJy beam^{-1} km s^{-1} in panel **a** and σ = 22 mJy beam^{-1} km s^{-1} in panel **b**. In panel **c** the contour levels are (3, 10, 30, 60, 120)×3σ, with σ = 40 mJy beam^{-1} km s^{-1}.

8.2 Characterizing the hot environment of genuine high-mass protostars

The analysis of the EMoCA spectral line survey coupled with the use of the astrochemical code MAGICKAL has allowed us to probe the influence of physical properties and environmental conditions on the chemical composition of the HMCs embedded in Sgr B2(N) (Chaps. 5 and 6). Applied to a larger number of sources, this method of analysis will help us to understand better the high-mass star-formation process and the complex organic associated chemistry.

We plan to extend the analysis conducted toward Sgr B2(N), using its HMCs as references, to perform further statistical studies of the physical and chemical properties of high-mass star-forming cores. Due to its location in the CMZ, Sgr B2(N) is exposed to the extreme conditions characterizing the GC region (higher dust temperatures, stronger ISRF, higher cosmic-ray flux,

see Sects. 1.4.1 and 6.3), that differ from other typical high-mass star-forming sites. Therefore we plan to investigate a larger sample of sources evolving in different environments (*i.e.* at different galactic locations). As mentioned previously in Sect. 1.2.1, the number of young high-mass stellar objects is still limited, but we have seen that 6.7 GHz Class II methanol masers, exclusively associated with young high-mass (proto)stars, are excellent probes of the early HMC phase. Therefore, our idea is to target 6.7 GHz Class II methanol masers to reveal their associated HMCs. To this aim we use the Global view on star formation survey (GLOSTAR, PI: K. Menten) which scans the entire galactic plane observable with the Karl G. Jansky Very Large Array (JVLA). GLOSTAR is an unbiased survey that searches for compact HII regions and Class II methanol masers with the aim to study the star formation process across the Galaxy at different evolutionary stages of star formation. Using both the B and D configurations of the JVLA instrument, GLOSTAR is the most sensitive Class II methanol maser survey to date, nearly one order of magnitude better than the Methanol-Multibeam survey (Green et al. 2008). A total number of 116 methanol masers were detected in the GLOSTAR pilot field, that spans a range of $l = 28° - 36°$ and $b = \pm 1°$, with 48 masers that are new detections (Murugeshan 2015). The distances to the 116 masers were derived using the kinematic distance estimation method based on the rotation curve of the galaxy. For sources with orbits interior to the solar orbit, a given radial velocity can correspond to two distances, near and far. This ambiguity could be resolved for 54 sources by Murugeshan (2015) by checking for HI self-absorption in previous surveys. For the other 62 sources, we used the online Bayesian distance calculator to evaluate the probabilities p_n and p_f of the near and far distances (see, e.g., Fig. 8.2). The ambiguity is considered to be resolved for $\frac{p_\mathrm{n}}{p_\mathrm{f}} > 5$ (near) or $\frac{p_\mathrm{n}}{p_\mathrm{f}} < 0.2$ (far), which yields 43 additional sources with resolved distance ambiguity. Among the (54+43) 97 sources with known distance, we selected all Class II methanol masers closer than 4 kpc. In this way we built up a distance-limited sample of 15 methanol masers of which 7 are new detections. The selected maser sources are listed in Table 8.1 and represented with red crosses in Fig. 8.3.

Some of the Class II methanol masers selected in our sample are known to be associated with HMCs of which some have already been investigated in detail (see Table 8.1). G35.03+0.35 is a well known high-mass star-forming region (see, *e.g.,* Paron et al. 2012) which is associated with several masers, including a methanol maser at 6.7 GHz (Cyganowski et al. 2009). The maser sources G30.59-0.04, G31.08+0.46, G32.70-0.06, and G32.75-0.06 are associated with ATLASGAL sources which are thought to host young stellar objects, based on the excitation temperatures measured from the observed $NH_3(3, 3)$ lines (Wienen et al. 2012). Finally in Sect. 3.6 we have seen that Allen et al. (2017) used ALMA data to derive the chemical composition of the HMCs associated with the maser sources G35.20-0.74 and G35.03+0.35 (see Fig. 3.12). These associations with HMCs confirm the potential of our sample of Class II methanol masers to search for early-type high-mass protostars and investigate the chemical complexity of their hot environment. Although some sources in our selected sample are already known and have been investigated before, this project will provide an homogeneous analysis of the chemical composition of the whole sample.

For this project we proposed to use the IRAM-30m single dish telescope to target the selected sample of Class II methanol masers at 1.3 mm (Project ID: 146-18, PI: M. Bonfand). This proposal was accepted and observations are going on. Each source is observed with a single tuning at 216 GHz (LSB) to detect multiple emission lines from several COMs, predicted to be observable in the selected frequency range based on the LTE-synthetic spectra built for Sgr B2(N3–N5) (see Sect. 3.2.1) adjusted to the distance of the maser sources. The sample

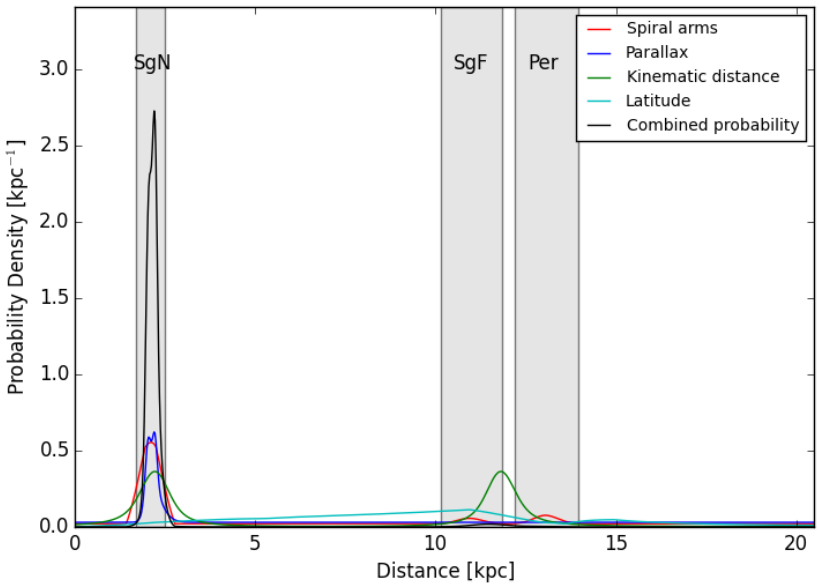

Figure 8.2: Probability density of the distance of G32.75-0.06 from the Sun calculated using the online Bayesian distance calculator. Here the near distance is adopted with a probability ratio $\frac{p_n}{p_f} >> 5$.

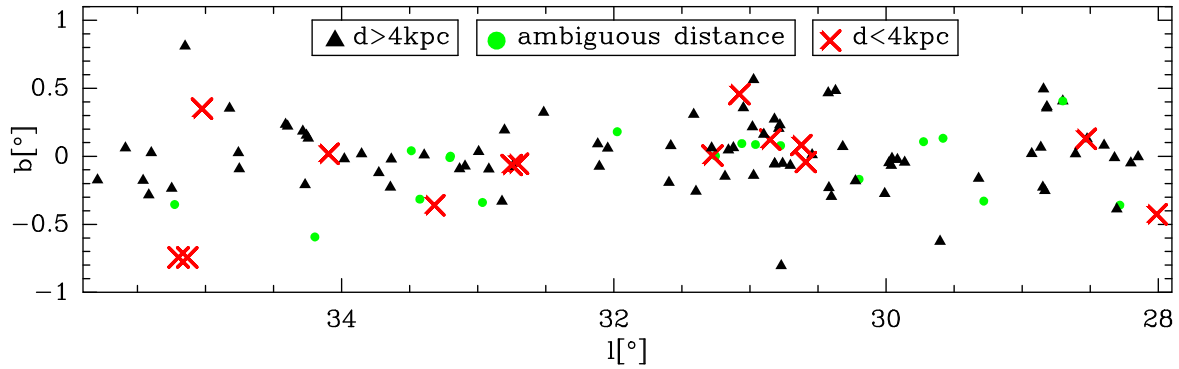

Figure 8.3: Location of the 6.7 GHz Class II methanol masers in the GLOSTAR pilot field. The red crosses show the distance-limited sample of masers selected for this new project (see also Table 8.1).

of molecules that we probe includes O-, N-, and S-bearing COMs in order to provide a good census of the chemical composition of the sources. In particular the proposed spectral setup is chosen to include key transitions of methanol and formaldehyde (and their ^{13}C isotopologs) that have been shown to be excellent tracers of physical conditions in star-forming regions (Leurini et al. 2004, 2007). Because CH_3OH and H_2CO have known collisional rates, their detected transitions will be used to derive kinetic temperatures and densities with a non-LTE radiative transfer approach, using the Large Velocity Gradient (LVG) approximation. The broad frequency bandwidth offered by the IRAM-30m telescope (16 GHz) is an asset to identify as many transitions of COMs as possible over a broad range of upper-state energies and derive reliable rotational temperatures and column densities. As HMCs can have linewidths as narrow

Table 8.1: Distance-limited sample of Class II methanol masers selected from the pilot field of the GLOSTAR survey for a detailed study with the IRAM-30m telescope.

Source[a]	RA[b] (J2000)	Dec[b] (J2000)	d[c] (kpc)	new detection[d]	known hot core[e]
G28.01-0.43	18:43:58.054	-04:34:24.02	$1.76^{+0.44}_{-0.47}$	–	–
G28.53+0.13	18:42:56.578	-03:51:21.74	$2.39^{+0.39}_{-0.42}$	–	–
G30.59-0.04	18:47:18.938	-02:06:16.84	$3.23^{+0.36}_{-0.37}$	–	maybe[1]
G30.62+0.08	18:46:55.811	-02:01:06.06	$3.07^{+0.36}_{-0.38}$	yes	–
G30.85+0.12	18:47:12.325	-01:47:46.68	$2.43^{+0.39}_{-0.41}$	yes	–
G31.08+0.46	18:46:25.496	-01:26:33.63	$2.28^{+0.40}_{-0.42}$	yes	maybe[1]
G31.28+0.01	18:48:23.944	-01:28:18.45	$2.93^{+0.37}_{-0.38}$	yes	–
G32.70-0.06	18:51:13.336	-00:13:42.42	$3.11^{+0.37}_{-0.38}$	yes	maybe[1]
G32.75-0.06	18:51:20.069	-00:11:29.34	$2.80^{+0.38}_{-0.39}$	yes	maybe[1]
G33.32-0.36	18:53:25.359	00:10:43.80	$2.47^{+0.39}_{-0.41}$	yes	–
G34.10+0.02	18:53:29.968	01:02:38.35	$3.95^{+0.39}_{-0.38}$	–	–
G35.03+0.35	18:54:00.717	02:01:19.22	$3.33^{+0.39}_{-0.39}$	–	yes[2, 3]
G35.13-0.74	18:58:06.212	01:37:07.52	$2.59^{+0.40}_{-0.41}$	–	–
G35.20-0.74N(A)	18:58:13.018	01:40:37.33	$2.44^{+0.40}_{-0.41}$	–	yes[3]
G35.20-0.74N(B1)	18:58:13.118	01:40:35.59	$2.44^{+0.40}_{-0.41}$	–	yes[3]

Notes. [(a)] Selected maser source detected in the pilot field of the GLOSTAR survey with a resolved distance < 4 kpc. [(b)] Source position in J2000 Equatorial coordinates. [(c)] Distance in kpc (Murugeshan 2015). [(d)] Yes means that the existence of a 6.7 GHz Class II methanol maser in this source was not known before the GLOSTAR survey (Murugeshan 2015). [(e)] Association with known hot molecular cores. [(1)] Wienen et al. (2012), [(2)] Cyganowski et al. (2009); Paron et al. (2012), [(3)] Allen et al. (2017).

as ~ 2 km s^{-1} (Allen et al. 2017; McGuire et al. 2017), the high spectral resolution achievable with the IRAM-30m telescope while covering the full bandwidth (200 kHz, 0.3 km s^{-1} at 216 GHz) is ideal to resolve the lines and secure the line identification, in particular in the case of overlap between transitions of different molecules.

Finally, we will use astrochemical models to interpret the observational results and model the physico-chemical evolution of the targeted sources. Our sizable sample of sources will allow us to explore the impact of their galactic location (*i.e.* environment, with different ISRF and CRIR values), stellar properties (mass, luminosity) and evolutionary stage on their chemical composition and on the production of COMs. However, the angular resolution of the IRAM-30m telescope (11.4″ at 216 GHz) is not sufficient to resolve the spatial structure of the sources. For instance, one of the selected sources, G35.20-0.74, is resolved as a binary in the JVLA B configuration map (see also Allen et al. 2017). Besides, other sources not associated with a maser may be present close to the proposed targets. See, e.g, N2 in Sgr B2(N) (Bonfand et al. 2017; Sánchez-Monge et al. 2017) and the multiple sources in G35.03+0.35 and G35.20-0.74 (Allen et al. 2017). Therefore observations at higher angular resolution for instance with ALMA will be needed to address the source multiplicity and better resolve the compact COM emission. Based on the outcome of the IRAM-30m observations, the project will be submitted for ALMA observations in its next cycles.

Appendix A

Appendix to Chapter 3

Contents

A.1 LTE best-fit parameters

Appendix to Sect. 3.2.1.

A.2 Unidentified lines

Appendix to Sect. 3.2.2.

A.3 Emission size and spatial distribution of the detected molecules

Appendix to Sect. 3.3.

A.4 Spectra

Appendix to Sect. 3.2.1.

Table A.1: Parameters of our best-fit LTE model for Sgr B2(N2–N5).

Species	N_l [a]	$N_{\rm mol}$ [b] ($\rm cm^{-2}$)	$C_{\rm vib}$ [c]	$T_{\rm rot}$ [d] (K)	D [e] ($''$)	$v_{\rm off}$ [f] ($\rm km\ s^{-1}$)	Δv [g] ($\rm km\ s^{-1}$)
		N3					
C_2H_5CN, $v=0$	55	3.2×10^{17}	1.54	170	0.4	-0.3	5.5
C_2H_5CN, $v_{20}=1$	17	4.6×10^{17}	1.54	170	0.4	-0.3	5.5
C_2H_5CN, $v_{13+21}=1$	53	6.1×10^{17}	1.54	170	0.4	-0.3	5.5
$^{13}CH_3CH_2CN$, $v=0$	18	8.0×10^{15}	1.54	170	0.4	-0.3	5.5
$CH_3{}^{13}CH_2CN$, $v=0$	13	1.2×10^{16}	1.54	170	0.4	-0.3	5.5
$C_2H_5{}^{13}CN$, $v=0$	17	1.2×10^{16}	1.54	170	0.4	-0.3	5.5
C_2H_3CN, $v=0$	40	5.2×10^{16}	1.00	150	0.4	0.0	7.0
C_2H_3CN, $v_{11}=1$	8	7.0×10^{16}	1.00	150	0.4	0.0	7.0
CH_3CN, $v=0$ [*]	8	_	1.06	_	0.4	0.5	6.0
CH_3CN, $v_8=1$	17	8.5×10^{17}	1.06	145	0.4	0.0	5.0
CH_3CN, $v_8=2$	3	2.7×10^{18}	1.06	145	0.4	0.0	5.0
$^{13}CH_3CN$, $v=0$	8	3.2×10^{16}	1.06	145	0.4	0.0	5.0
$CH_3{}^{13}CN$, $v=0$	6	3.2×10^{16}	1.06	145	0.4	0.0	5.0
$CH_3C^{15}N$, $v=0$	2	3.0×10^{15}	1.06	145	0.4	0.0	5.0
CH_3CCH, $v=0$	6	1.5×10^{17}	1.00	145	0.4	0.0	3.6
CH_3OH, $v=0$	31	7.5×10^{18}	1.00	170	0.4	0.0	5.0
CH_3OH, $v=1$	14	7.5×10^{18}	1.00	170	0.4	0.0	5.0
CH_3OH, $v=2$	3	2.0×10^{19}	1.00	170	0.4	0.0	5.0
$^{13}CH_3OH$, $v=0$	19	6.5×10^{17}	1.00	145	0.4	0.5	4.5
$CH_3{}^{18}OH$, $v=0$	1	1.5×10^{17}	1.00	170	0.4	0.0	5.0
C_2H_5OH, $v=0$	71	3.1×10^{17}	1.24	145	0.4	1.0	4.0
CH_3OCHO, $v=0$	76	1.7×10^{18}	1.19	145	0.4	0.6	4.1
CH_3OCHO, $v=1$	59	1.5×10^{18}	1.19	145	0.4	0.8	4.1
CH_3CHO, $v=0$	15	8.5×10^{16}	1.00	145	0.4	0.0	4.7
CH_3COCH_3, $v=0$	73	2.7×10^{17}	1.00	145	0.4	0.5	4.5
CH_3COCH_3, $v_{12}=1$	18	2.0×10^{17}	1.00	145	0.4	0.5	4.5
CH_3OCH_3, $v=0$	43	1.0×10^{18}	1.00	145	0.4	0.0	5.0
CH_3OCH_3, $v_{11}=1$	3	1.0×10^{18}	1.00	145	0.4	0.5	5.0
CH_3NCO, $v=0$	65	6.6×10^{16}	1.00	145	0.4	0.5	4.0
$HNCO$, $v=0$	7	1.8×10^{17}	1.005	145	0.4	0.6	7.7
H_2CCO, $v=0$	6	7.5×10^{16}		145	0.4	0.0	4.5
H_2CO, $v=0$	1	1.1×10^{18}		200	0.4	0.0	5.0
$H_2{}^{13}CO$, $v=0$	1	4.5×10^{16}		145	0.4	0.0	4.0
CH_3SH, $v=0$	7	8.5×10^{16}	1.00	145	0.4	0.0	4.0
H_2CS, $v=0$	4	8.0×10^{16}		145	0.4	0.0	4.5
HC_3N, $v=0$	3	1.1×10^{16}		200	0.4	0.0	4.0
HC_3N, $v_6=1$	2	2.3×10^{16}		200	0.4	0.0	4.0
HC_3N, $v_7=1$	6	2.0×10^{16}		200	0.4	0.0	4.0
HC_3N, $v_7=2$	3	2.0×10^{16}		200	0.4	0.0	4.0
$HC^{13}CCN$, $v=0$	3	1.5×10^{15}		200	0.4	0.0	4.0
$HC^{13}CCN$, $v_7=1$	2	1.8×10^{15}		200	0.4	0.0	4.0
$HCC^{13}CN$, $v=0$	3	1.8×10^{15}		200	0.4	0.0	4.0
$HC^{15}N$, $v=0$	1	7.6×10^{15}		145	0.4	0.0	4.8
CH_2NH, $v=0$	3	1.5×10^{17}		145	0.4	0.0	6.5

continued on next page

Table A.1: Continued.

Species	N_l [a]	$N_{\rm mol}$ [b] ($\rm cm^{-2}$)	$C_{\rm vib}$ [c]	$T_{\rm rot}$ [d] (K)	D [e] ($''$)	$v_{\rm off}$ [f] ($\rm km\ s^{-1}$)	Δv [g] ($\rm km\ s^{-1}$)
			N3				
NH_2CHO, $v=0$	10	3.5×10^{16}	1.09	145	0.4	0.5	5.6
NH_2CHO, $v_{12}=1$	11	3.3×10^{17}	1.09	145	0.4	0.5	5.6
$NH_2{}^{13}CHO$, $v=0$	3	7.6×10^{15}	1.09	145	0.4	0.5	5.6
OCS, $v=0$	3	1.0×10^{18}		145	0.4	-0.4	4.0
OCS, $v_2=1$	3	2.4×10^{18}		145	0.4	-0.4	4.0
$O^{13}CS$, $v=0$	3	6.5×10^{16}		145	0.4	0.0	4.0
$OC^{33}S$, $v=0$	2	7.5×10^{16}		145	0.4	0.5	4.0
$OC^{34}S$, $v=0$	1	2.0×10^{16}		145	0.4	-0.4	4.0
NH_2D, $v=0$	1	2.6×10^{16}		145	0.4	0.0	5.0
SO_2, $v=0$	1	6.8×10^{16}		145	0.4	-1.3	5.0
SO, $v=0$	3	9.0×10^{16}		145	0.4	0.4	5.0
^{13}CO, $v=0$	1	$>4.0\times10^{18}$		145	0.4	0.0	5.0
^{13}CS, $v=0$	1	1.5×10^{18}		145	0.4	0.0	4.0
$C^{34}S$, $v=0$	1	1.2×10^{16}		145	0.4	0.0	4.0
$^{13}C^{34}S$, $v=0$	1	2.2×10^{15}		145	0.4	0.0	4.0
			N4				
C_2H_5CN, $v=0$	25	1.4×10^{16}	1.35	145	1.0	-0.5	5.5
C_2H_5CN, $v_{13+21}=1$	41	5.4×10^{16}	1.35	145	1.0	-0.5	5.5
$^{13}CH_3CH_2CN$, $v=0$	2	1.5×10^{15}	1.35	145	1.0	0.0	5.0
$CH_3{}^{13}CH_2CN$, $v=0$	1	2.0×10^{15}		145	1.0	0.0	5.0
C_2H_3CN, $v=0$	8	2.0×10^{15}	1.00	145	1.0	-0.6	4.5
CH_3CN, $v=0^*$	4	_	1.06	_	1.0	0.0	5.3
CH_3CN, $v_8=1$	13	3.2×10^{16}	1.06	145	1.0	0.5	4.0
$^{13}CH_3CN$, $v=0$	6	2.1×10^{15}	1.06	145	1.0	0.0	5.3
$CH_3{}^{13}CN$, $v=0$	7	2.1×10^{15}	1.06	145	1.0	0.0	5.3
CH_3OH, $v=0$	23	2.5×10^{17}	1.00	190	1.0	-0.6	5.0
CH_3OH, $v=1$	8	4.5×10^{17}	1.00	190	1.0	-0.6	5.0
$^{13}CH_3OH$, $v=0$	4	5.5×10^{16}	1.00	145	1.0	-0.6	5.0
C_2H_5OH, $v=0$	14	2.5×10^{16}	1.24	150	1.0	-0.3	3.5
CH_2NH, $v=0$	2	1.5×10^{16}		145	1.0	-0.2	5.5
CH_3CCH, $v=0$	6	4.0×10^{16}		145	1.0	-0.8	4.5
CH_3COCH_3, $v=0$	4	2.0×10^{16}	1.00	145	1.0	-0.7	4.5
CH_3OCH_3, $v=0$	23	9.0×10^{16}	1.00	145	1.0	0.0	5.0
CH_3OCHO, $v=0$	57	1.1×10^{17}	1.23	145	1.0	0.0	4.5
CH_3OCHO, $v=1$	4	1.1×10^{17}	1.23	145	1.0	0.0	4.5
CH_3CHO, $v=0$	12	1.0×10^{16}	1.00	145	1.0	-0.5	4.0
CH_3SH, $v=0$	1	9.5×10^{15}	1.00	145	1.0	0.0	4.0
CH_3NCO, $v=0$	16	5.8×10^{15}	1.00	150	1.0	0.0	4.0
HNCO, $v=0$	3	2.5×10^{15}	1.006	150	1.0	-0.9	4.1
H_2CCO, $v=0$	5	8.5×10^{15}		145	1.0	-0.4	4.9
H_2CO, $v=0$	1	5.5×10^{16}		145	1.0	0.0	6.0
H_2CS, $v=0$	3	$<1.0\times10^{16}$		145	1.0	0.0	5.0

continued on next page

Table A.1: Continued.

Species	N_l [a]	$N_{\rm mol}$ [b] ($\rm cm^{-2}$)	$C_{\rm vib}$ [c]	$T_{\rm rot}$ [d] (K)	D [e] ($''$)	$v_{\rm off}$ [f] ($\rm km\ s^{-1}$)	Δv [g] ($\rm km\ s^{-1}$)
			N4				
HC_3N, $v=0$ [**]	3	–		–	1.0	-0.5	5.0
HC_3N, $v_7=1$	2	1.6×10^{15}		145	1.0	-0.5	5.0
$HC^{13}CCN$, $v=0$	3	2.0×10^{14}		145	1.0	-0.5	5.0
$HCC^{13}CN$, $v=0$	3	2.0×10^{14}		145	1.0	-0.5	5.0
OCS, $v=0$	3	4.7×10^{16}		145	1.0	-0.5	7.0
$O^{13}CS$, $v=0$	3	7.0×10^{15}		145	1.0	0.0	5.0
$OC^{33}S$, $v=0$	1	2.5×10^{15}		145	1.0	0.0	5.0
$OC^{34}S$, $v=0$	2	7.0×10^{15}		145	1.0	0.0	5.0
SO, $v=0$	2	6.0×10^{15}		145	1.0	-1.0	4.7
			N5				
C_2H_5CN, $v=0$	41	6.8×10^{16}	1.35	145	1.0	-0.5	5.5
C_2H_5CN, $v_{13+21}=1$	55	2.4×10^{16}	1.35	145	1.0	-0.5	5.5
$^{13}CH_3CH_2CN$, $v=0$	9	6.8×10^{15}	1.35	145	1.0	-0.2	4.5
$CH_3{}^{13}CH_2CN$, $v=0$	15	6.8×10^{15}	1.35	145	1.0	-0.2	4.5
$C_2H_5{}^{13}CN$, $v=0$	11	6.8×10^{15}	1.35	145	1.0	-0.2	4.5
C_2H_3CN, $v=0$	27	1.3×10^{16}	1.00	145	1.0	-0.6	6.0
CH_3CN, $v=0$ [*]	9	–	1.00	–	1.0	-0.5	5.0
CH_3CN, $v_8=1$	16	1.3×10^{17}	1.00	145	1.0	-0.5	5.0
$^{13}CH_3CN$, $v=0$	7	6.5×10^{15}	1.06	145	1.0	-0.6	4.6
$CH_3{}^{13}CN$, $v=0$	7	6.5×10^{15}	1.06	145	1.0	-0.6	4.6
CH_3OH, $v=0$	29	1.5×10^{18}	1.00	190	1.0	-0.7	4.5
CH_3OH, $v=1$	9	2.2×10^{18}	1.00	190	1.0	-0.7	4.5
CH_3OH, $v=2$	2	3.5×10^{18}	1.00	190	1.0	-0.7	4.5
$^{13}CH_3OH$, $v=0$	13	2.5×10^{17}	1.00	145	1.0	-0.7	3.6
C_2H_5OH, $v=0$	37	1.0×10^{17}	1.24	145	1.0	-0.8	3.5
CH_3CCH, $v=0$	6	1.1×10^{17}		145	1.0	-0.5	4.5
CH_3COCH_3, $v=0$	4	5.0×10^{16}	1.00	145	1.0	-0.9	3.7
CH_3OCH_3, $v=0$	47	2.5×10^{17}	1.00	145	1.0	0.0	4.5
CH_3OCHO, $v=0$	63	2.4×10^{17}	1.19	145	1.0	-0.5	3.5
CH_3OCHO, $v=1$		2.4×10^{17}	1.19	145	1.0	-0.5	3.5
CH_3CHO, $v=0$	9	2.5×10^{16}	1.00	145	1.0	0.0	4.5
CH_3NCO, $v=0$	4	1.1×10^{16}	1.00	145	1.0	-0.5	3.5
HNCO, $v=0$	5	3.0×10^{16}	1.005	145	1.0	-0.8	6.8
H_2CCO, $v=0$	6	2.3×10^{16}		145	1.0	-0.5	4.8
H_2CO, $v=0$	1	3.3×10^{17}		145	1.0	-0.3	5.5
$H_2{}^{13}CO$, $v=0$	1	2.5×10^{16}		145	1.0	-0.3	5.5
H_2CS, $v=0$	4	$>2.3\times10^{16}$		145	1.0	-1.5	4.6
HC_3N, $v=0$ [**]	3	–		–	1.0	0.0	7.5
HC_3N, $v_7=1$	5	1.8×10^{16}		145	1.0	0.0	7.5
$H^{13}CCCN$, $v=0$		1.1×10^{15}		145	1.0	0.0	7.0
$HC^{13}CCN$, $v=0$		1.1×10^{15}		145	1.0	0.0	7.0
$HCC^{13}CN$, $v=0$		1.1×10^{15}		145	1.0	0.0	7.0

continued on next page

Table A.1: Continued.

Species	N_l [a]	$N_{\rm mol}$ [b] ($\rm cm^{-2}$)	$C_{\rm vib}$ [c]	$T_{\rm rot}$ [d] (K)	D [e] ($''$)	$v_{\rm off}$ [f] ($\rm km\ s^{-1}$)	Δv [g] ($\rm km\ s^{-1}$)
N5							
CH_3SH, $v=0$	2	3.5×10^{16}		145	1.0	-0.5	5.0
CH_2NH, $v=0$	3	8.5×10^{16}		145	1.0	-1.0	6.1
NH_2CHO, $v=0$	10	1.3×10^{16}	1.09	145	1.0	-0.5	6.0
NH_2CHO, $v_{12}=1$	2	7.6×10^{16}	1.09	145	1.0	-0.5	6.0
OCS, $v=0$	3	2.5×10^{17}		145	1.0	-0.4	5.0
$O^{13}CS$, $v=0$	3	2.7×10^{16}		145	1.0	-0.5	4.5
$OC^{33}S$, $v=0$	1	8.0×10^{15}		145	1.0	-0.2	4.5
$OC^{34}S$, $v=0$	2	3.5×10^{16}		145	1.0	-0.5	4.0
NH_2D, $v=0$	2	9.5×10^{15}		145	1.0	-0.6	6.2
SO_2, $v=0$	1	3.2×10^{16}		145	1.0	-1.0	5.0
SO, $v=0$	4	3.7×10^{16}		145	1.0	0.0	5.5
^{13}CO, $v=0$	1	$>1.5\times10^{18}$		145	1.0	0.0	4.0
N2 [***]							
C_2H_5CN, $v=0$	154	6.2×10^{18}	1.38	150	1.2	-0.8	5.0
C_2H_3CN, $v=0$	44	4.2×10^{17}	1.00	200	1.1	-0.6	6.0
$^{13}CH_3CN$, $v=0$	8	9.9×10^{16}	1.10	170	1.4	-0.5	5.4
$CH_3{}^{13}CN$, $v=0$	7	9.9×10^{16}	1.10	170	1.4	-0.5	5.4
CH_3OH, $v_t=0$	41	4.0×10^{19}	1.00	160	1.4	-0.5	5.4
C_2H_5OH, $v=0$	168	2.0×10^{18}	1.24	150	1.5	-0.4	4.7
CH_3OCHO, $v=0$	90	1.2×10^{18}	1.23	150	1.5	-0.4	4.7
CH_3OCH_3, $v=0$	66	2.2×10^{18}	1.00	130	1.6	-0.5	5.0
CH_3CHO, $v=0$	19	4.3×10^{17}	1.00	150	1.2	0.0	5.6
NH_2CHO, $v=0$	30	3.5×10^{18}	1.17	200	0.8	0.2	5.5
CH_3NCO, $v=0$	60	2.2×10^{17}	1.00	150	0.9	-0.6	5.0
CH_3SH, $v=0$	12	3.4×10^{17}	1.00	180	1.4	-0.5	5.4

Notes. [a] Number of lines detected above 3σ (see also Table 2.2). One line may mean a group of transitions of the same molecule blended together. [b] Total column density of the molecule (see Sect. 3.2.1). [c] Correction factor applied to the column density to account for the contribution of vibrationally or torsionally excited states not included in the partition function (Eq. 2.51). The correction factors that have not been calculated in this thesis are left blank. [d] Rotational temperature (Sect. 3.4). [e] Source diameter (FWHM, Sect 3.3) . [f] Velocity offset with respect to the assumed systemic velocity of the source: 74 $\rm km\ s^{-1}$ for N2 and N3, 64 $\rm km\ s^{-1}$ for N4, and 60 $\rm km\ s^{-1}$ for N5 (Sect. 4.1.1). [g] Linewidth (Sect. 3.2.1). [*] Transitions are optically thick and cannot be used to derive the total column density. [**] Transitions are contaminated by absorption and cannot be used to derive the total column density. [***] N2's best-fit parameters are also shown for selected COMs for comparison. They are taken from Belloche et al. (2016), Belloche et al. (2017), and Müller et al. (2016) for all species, except for CH_3CHO, CH_3OCH_3 (Belloche, priv. comm.).

Table A.2: List of remaining unidentified lines toward Sgr B2(N3–N5) compared to N2.

Freq.	N3		N4		N5		N2*	
(MHz)	$T_{\rm peak}$[a]	rms[b]	$T_{\rm peak}$[a]	rms[b]	$T_{\rm peak}$[a]	rms[b]	$T_{\rm peak}$[a]	rms[b]
87868	_		1.26	0.15	_		_	
87899	_		1.75	0.15	_		_	
87927	_		2.51	0.15	_		_	
88239	_		2.38	0.15	_		_	
89585	_		1.56	0.15	_		_	
94815	1.87	0.12	_		_		_	
95728	2.32	0.11	1.19	0.15	3.67	0.23	_	
95915	_		6.01	0.14	_		_	
96058	1.82	0.11	_		_		17.4	0.10
96396	5.19	0.11	_		_		_	
96494	7.59	0.11	_		_		_	
96501	3.81	0.11	_		_		_	
96514	4.38	0.11	_		_		_	
97172	2.81	0.16	_		_		_	
97618	1.68	0.16	_		_		17.4	0.16
97985	_		1.17	0.13	11.4	0.38	_	
100035	2.29	0.15			_		_	
101092	2.02	0.14	_		4.16	0.35	_	
101293	2.34	0.14	_		_		_	
101469	3.15	0.14	_		5.24	0.35	_	
101659	1.78	0.13	_		_		21.8	0.14
101737	4.45	0.13	_		_		_	
102123	5.60	0.13	1.38	0.15	7.39	0.34	_	
107481	2.25	0.17	_		_		_	
108210	3.13	0.17	1.22	0.15	_		_	
108227	3.17	0.17	1.47	0.15	_		_	
109010	1.40	0.13	_		_		_	
109719	2.64	0.13	_		_		26.3	0.12
109782	4.62	0.13	2.25	0.16	7.60	0.37	_	
109784	3.06	0.13	_		_		_	
109881	3.66	0.13	_		_		_	
109959	2.02	0.13	_		_		_	
110144	2.97	0.13	_		_		_	
111944	1.94	0.16	_		_		_	
112359	1.95	0.16	_		_		7.3	0.17
112490	1.66	0.16	_		_		_	
112522	2.51	0.16	_		_		_	
113631	2.22	0.21	_		_		21.2	0.24
114271	2.45	0.21	_		_		_	

Notes. [a] Peak brightness temperature (in K) measured in the continuum-subtracted spectra observed toward the HMCs and after correction for the primary beam attenuation. [b] rms noise level (1σ, in K) corrected for the primary beam attenuation. Only the U-lines above 7σ for which more than $\sim$70% of the line intensity is not reproduced by our LTE best-fit synthetic spectra are listed for Sgr B2(N3–N5). For comparison, the peak brightness temperature of the corresponding U-lines in the spectra observed toward N2 are also indicated. [*] Belloche et al. (priv. comm.).

Table A.3: Results of elliptical 2D-Gaussian fits to the integrated intensity maps of the transitions with resolved emission.

Source	Molecule	Transition	Freq. (MHz)	E_{up} (K)	I_{peak} [a] (Jy beam^{-1} km s^{-1})	rms[a]	S/N [b]	Beam[c] ($'' \times ''$)	PA[c] (°)	maj.[d] ($''$)	min.[d] ($''$)	PA[d] (°)	$\Delta\alpha$[e] ($''$)	$\Delta\beta$[e] ($''$)	θ_{maj}[f] ($''$)	θ_{min}[f] ($''$)	PA[f] (°)	D_l[g] ($''$)
N3	OCS	7-6	85139.103	16.3	1.26(2)	0.050	25.2	2.08×1.54	-84.6	2.09(3)	1.57(3)	+83.9(23)	-8.24(2)	0.96(1)	0.34	0.20	+13.7	0.26
		8-7	97301.208	21.0	1.49(4)	0.051	29.2	1.83×1.37	-84.5	1.96(3)	1.42(5)	+81.2(29)	-8.29(2)	0.96(2)	0.74	0.32	+64.8	0.48
	C_2H_5CN	$10_{0,11}$-$10_{0,10}$	96919.762	28.1	0.98(2)	0.037	26.5	1.83×1.37	-84.5	1.88(3)	1.40(4)	+84.5(27)	-8.27(2)	0.99(1)	0.44	0.26	+89.3	0.34
		$11_{2,8}$-$11_{3,7}$	98701.101	38.4	0.96(2)	0.038	25.3	1.79×1.34	-84.7	1.88(2)	1.46(3)	+87.6(6)	-8.30(1)	1.02(1)	0.64	0.52	-51.4	0.58
N4	OCS	7-6	85139.103	16.3	0.62(1)	0.050	12.4	2.08×1.54	-84.6	2.38(4)	1.86(5)	-97.8(34)	-4.72(2)	-16.68(2)	1.24	0.95	-60.2	1.08
		8-7	97301.208	21.0	0.64(1)	0.055	11.6	1.83×1.37	-84.5	2.01(5)	1.75(4)	-50.5(18)	-4.73(2)	-16.43(2)	1.34	0.23	-22.0	0.55
	CH_3OH	13_2-12_3	100638.872	233.6	0.22(1)	0.024	9.2	1.72×1.40	-75.5	2.13(3)	1.63(2)	-59.5(4)	-4.48(1)	-16.53(1)	1.48	0.26	-45.4	0.62
	CH_3OCH_3	$4_{1,4}$-$3_{0,3}$ [*]	99324.362	10.2	0.32(1)	0.020	16.0	1.77×1.42	-76.2	2.09(4)	1.57(6)	-86.6(31)	-4.45(2)	-16.58(2)	1.20	0.51	-70.5	0.78
		$7_{0,7}$-$6_{1,6}$ [*]	111782.600	25.2	0.43(1)	0.053	8.1	1.58×1.31	-72.1	2.57(3)	1.78(4)	+80.6(16)	-4.51(2)	-16.46(1)	2.03	1.19	+83.0	1.56
	H_2CCO	$5_{1,5}$-$4_{1,4}$	100094.514	27.5	0.17(1)	0.017	10.0	1.77×1.42	-76.2	2.21(4)	1.74(9)	-83.4(44)	-4.81(2)	-16.58(2)	1.42	0.88	-65.4	1.12
		$5_{1,4}$-$4_{1,3}$	101981.429	27.7	0.17(1)	0.018	9.4	1.72×1.40	-75.5	2.59(4)	1.80(6)	-85.5(27)	-4.64(3)	-16.60(2)	1.97	1.06	-79.1	1.44
	CH_3CN	6_3-5_3	110364.354	82.8	0.36(1)	0.030	12.0	1.61×1.18	-81.7	2.58(1)	1.32(1)	+60.9(6)	-4.70(2)	-16.58(1)	2.07	0.39	+55.3	0.90
		6_2-5_2	110374.989	47.1	0.41(1)	0.031	13.2	1.61×1.18	-81.7	2.06(5)	1.28(11)	+62.1(38)	-4.55(4)	-16.60(3)	1.37	0.20	+49.9	0.52
	CH_3CCH	6_3-5_3	102530.348	82.3	0.18(1)	0.022	8.2	1.57×1.42	+48.6	3.39(1)	1.63(4)	+38.7(2)	-4.59(1)	-16.57(1)	3.07	0.43	+38.9	1.15
		6_2-5_2	102540.145	46.1	0.19(1)	0.021	9.0	1.57×1.42	+48.6	2.63(6)	1.77(3)	+50.3(24)	-4.78(2)	-16.81(2)	2.21	0.81	+49.4	1.34
	CH_3OCHO	$8_{3,5}$-$7_{3,4}$	100308.179	27.4	0.14(1)	0.017	8.2	1.77×1.42	-76.2	2.40(3)	1.70(6)	-80.7(31)	-4.32(3)	-16.57(2)	1.70	0.79	-70.3	1.16
N5	C_2H_5CN	$10_{0,11}$-$10_{0,10}$	96919.762	28.1	0.85(1)	0.032	26.9	1.83×1.37	-84.5	1.85(2)	1.56(2)	-87.4(30)	2.39(1)	-25.43(1)	0.78	0.10	-19.3	0.28
		$11_{2,10}$-$11_{2,9}$	98177.574	32.8	0.86(1)	0.035	24.6	1.79×1.34	-84.7	1.85(2)	1.51(2)	+87.1(1)	2.38(1)	-25.47(1)	0.7	0.46	-15.2	0.57
		$11_{2,8}$-$11_{3,7}$	98701.101	38.4	0.85(1)	0.036	23.6	1.79×1.34	-84.7	1.87(2)	1.55(2)	+87.7(29)	2.41(1)	-25.45(1)	0.78	0.53	-15.5	0.64
		$11_{2,9}$-$10_{2,8}$	99681.461	33.0	0.95(1)	0.038	25.0	1.79×1.34	-84.7	1.84(2)	1.57(2)	+86.3(1)	2.39(1)	-25.43(1)	0.81	0.43	-8.6	0.59
	CH_3OCH_3	$15_{2,13}$-$15_{2,14}$ [*]	88706.231	116.9	0.90(1)	0.062	14.5	1.91×1.65	+86.3	2.27(3)	1.78(4)	+58.2(28)	2.19(2)	-25.60(1)	1.39	0.18	+44.4	0.50
	CH_3CN	5_3-4_3	91971.130	77.5	1.29(1)	0.067	19.3	2.88×1.45	+83.5	3.79(1)	2.09(1)	+76.0(1)	2.38(3)	-25.52(1)	2.73	0.90	+57.3	1.57
		6_3-5_3	110364.354	82.8	1.81(3)	0.047	38.5	1.61×1.18	-81.7	1.84(2)	1.35(2)	+84.4(15)	2.37(1)	-25.37(1)	0.89	0.66	-86.4	0.76
		6_2-5_2	110374.989	47.1	1.65(2)	0.051	32.4	1.61×1.18	-81.7	2.19(2)	1.45(3)	+80.6(17)	2.33(1)	-25.37(1)	1.48	0.83	+79.7	1.11
	OCS	8-7	91301.208	21.0	1.94(2)	0.026	74.6	1.82×1.33	-81.8	2.25(2)	1.75(2)	+84.5(16)	2.41(1)	-25.37(1)	1.32	1.13	-86.4	1.22
		9-8	109463.063	26.3	1.98(2)	0.020	99.0	1.61×1.18	-81.7	1.96(1)	1.61(2)	+81.6(17)	2.41(1)	-25.39(1)	1.12	1.10	+79.1	1.11
	CH_3OH	6_2-7_1	85568.131	74.7	0.75(1)	0.028	26.8	2.08×1.54	-84.6	2.38(2)	1.87(2)	-85.2(15)	2.29(1)	-25.41(1)	1.27	0.92	-53.7	1.08
		8_0-7_1	95169.391	83.5	1.00(2)	0.049	20.4	1.86×1.36	-82.1	2.26(2)	1.45(5)	-84.8(16)	2.28(2)	-25.31(1)	1.35	0.33	-72.6	0.66
		$2_{1,0}$-$1_{1,0}$	96755.501	28.0	0.48(2)	0.026	18.5	1.86×1.36	-82.1	3.34(5)	1.78(17)	-89.6(20)	2.20(5)	-25.43(3)	2.78	1.12	-87.6	1.77
	CH_3OCHO	$7_{2,6}$-$6_{2,5}$(E) [**]	84449.169	19.0	0.14(1)	0.014	10.0	2.08×1.54	-84.6	3.42(5)	2.03(8)	+82.6(15)	2.00(2)	-25.47(1)	2.71	1.33	+81.9	1.9
		$7_{2,6}$-$6_{2,5}$(A)	84454.754	19.0	0.14(1)	0.012	11.7	2.08×1.54	-84.6	2.85(3)	2.02(3)	+88.8(14)	2.14(2)	-25.33(1)	1.95	1.30	-87.3	1.59
		$7_{3,5}$-$6_{3,4}$(A)	86265.796	22.5	0.14(1)	0.010	14.0	2.04×1.51	-83.3	2.41(1)	1.75(1)	-70.7(1)	2.39(1)	-25.35(1)	1.52	0.38	-49.2	0.76
		$7_{3,5}$-$6_{3,4}$(E)	86268.739	22.5	0.15(1)	0.010	15.0	1.86×1.36	-82.1	2.85(1)	1.69(1)	-74.4(1)	2.53(1)	-25.33(1)	2.08	0.45	-65.0	0.97
		$7_{1,6}$-$6_{1,5}$(A)	88851.607	17.9	0.21(1)	0.019	11.1	1.91×1.65	+96.3	2.37(6)	1.79(6)	+78.6(42)	2.05(3)	-25.56(2)	1.44	0.62	-70.7	0.94
		$7_{2,5}$-$6_{2,4}$(E)	90145.723	19.7	0.18(1)	0.013	13.8	1.77×1.58	+51.5	2.11(5)	1.83(5)	-89.3(107)	2.14(3)	-25.37(1)	1.30	0.74	+73.5	0.98
		$7_{2,5}$-$6_{2,4}$(A)	90156.473	19.7	0.16(1)	0.012	13.3	1.77×1.58	+51.5	2.65(10)	2.00(13)	+87.7(62)	2.13(4)	-25.42(1)	2.05	1.10	+81.4	1.50
		$8_{5,3}$-$7_{5,2}$(E)	98424.207	37.9	0.14(1)	0.012	11.7	1.79×1.34	-84.7	1.95(4)	1.51(5)	-86.6(30)	2.38(2)	-25.49(2)	0.88	0.56	-52.7	0.70
		$8_{1,7}$-$7_{1,6}$(E)	100482.241	22.8	0.25(1)	0.016	15.6	1.77×1.42	-76.2	2.10(2)	1.56(3)	+83.4(23)	2.50(2)	-25.27(1)	1.15	0.60	-88.2	0.83

Notes. Numbers in parentheses are uncertainties given by the fitting routine GAUSS-2D in units of the last digit.
[a] Peak flux density and rms noise level measured in the integrated intensity map. [b] Signal-to-noise ratio. [c] Size of the synthesized beam (HPBW) and position angle (East from North). [d] Size (FWHM) and position angle of the fitted Gaussian. [e] Equatorial offset with respect to the phase center (see Sect. 2.3). [f] Deconvolved major and minor diameters of the emission (FWHM) and position angle. [g] Average deconvolved size of the emitting region. [*] The line is a group of transitions from the same molecule blended together. [**] The A and E labels mark the two substates of the ground torsional level of methyl formate.

Table A.4: Spatial distribution of the species detected toward Sgr B2(N3–N5).

Species	N3		N4*		N5	
	$\Delta\alpha$	$\Delta\delta$	$\Delta\alpha$	$\Delta\delta$	$\Delta\alpha$	$\Delta\delta$
	(arcsec)		(arcsec)		(arcsec)	
C_2H_5CN, $v=0$	-8.04(0.05)	1.03(0.04)	-4.50(0.04)	-16.47(0.04)	2.32(0.12)	-25.44(0.05)
C_2H_3CN, $v=0$	-8.05(0.08)	0.90(0.07)	-4.47(0.06)	-16.52(0.04)	2.30(0.02)	-25.52(0.02)
CH_3CN, $v=0$	-8.34(0.03)	1.04(0.02)	-4.70(0.04)	-16.65(0.15)	2.38(0.06)	-25.46(0.07)
CH_3OH, $v=0$	-8.09(0.20)	1.00(0.05)	-4.51(0.14)	-16.57(0.12)	2.32(0.01)	-25.56(0.05)
C_2H_5OH, $v=0$	-8.22(0.10)	1.00(0.09)	-4.40(0.12)	-16.52(0.13)	2.41(0.18)	-25.21(0.15)
CH_3OCHO, $v=0$	-8.27(0.10)	0.91(0.08)	-4.51(0.14)	-16.53(0.08)	2.42(0.10)	-25.45(0.11)
CH_3OCH_3, $v=0$	-8.15(0.09)	1.06(0.05)	-4.46(0.13)	-16.63(0.06)	2.45(0.04)	-25.40(0.03)
CH_3COCH_3, $v=0$	-8.20(0.09)	0.98(0.10)	-4.19(0.06)	-16.57(0.11)	2.41(0.12)	-25.25(0.04)
CH_3CHO, $v=0$	-8.24(0.07)	1.10(0.06)	-4.60(0.10)	-16.46(0.13)	2.18(0.12)	-25.46(0.25)
H_2CO, $v=0$	-8.22(0.01)	1.04(0.08)	-4.49(0.10)	-16.51(0.03)	2.43(0.01)	-25.37(0.06)
H_2CCO, $v=0$	-8.23(0.05)	0.99(0.12)	-4.54(0.09)	-16.57(0.03)	2.17(0.20)	-25.26(0.12)
NH_2CHO, $v=0$	-8.11(0.09)	0.98(0.06)	_	_	2.40(0.16)	-25.41(0.16)
CH_3NCO, $v=0$	-8.24(0.10)	1.02(0.08)	-4.15(0.11)	-16.74(0.14)	2.54(0.14)	-25.42(0.11)
HNCO, $v=0$	-8.24(0.03)	1.07(0.06)	-4.61(0.11)	-16.33(0.06)	2.18(0.56)	-25.39(0.13)
HC_3N, $v=0$**	-8.69(0.05)	0.66(0.03)	_	_	_	_
HC_3N, $v_7=1$	-8.27(0.18)	1.09(0.07)	-4.53(0.04)	-16.42(0.03)	2.38(0.10)	-25.32(0.02)
CH_2NH, $v=0$	-8.24(0.17)	1.05(0.07)	-4.89(0.51)	-16.71(0.28)	2.42(0.05)	-25.39(0.08)
CH_3CCH, $v=0$	-8.67(0.03)	0.68(0.03)	-4.68(0.10)	-16.61(0.10)	2.10(0.10)	-25.44(0.10)
CH_3SH, $v=0$	-8.10(0.05)	1.26(0.14)	-4.41(0.27)	-16.99(0.15)	2.41(0.15)	-24.91(0.13)
H_2CS, $v=0$	-8.34(0.08)	0.79(0.12)	-4.70(0.18)	-16.54(0.23)	2.29(0.64)	-25.05(0.16)
OCS, $v=0$	-8.29(0.03)	1.01(0.05)	-4.62(0.08)	-16.51(0.04)	2.40(0.01)	-25.40(0.05)
SO_2, $v=0$	-8.19(0.26)	0.84(0.24)	_	_	2.44(0.02)	-25.49(0.01)
SO, $v=0$	-8.50(0.20)	0.72(0.11)	-4.58(0.56)	-16.10(0.06)	2.53(0.13)	-25.43(0.16)
NH_2D, $v=0$	-8.06(0.02)	1.03(0.07)	_	_	2.42(0.05)	-25.35(0.12)

Notes. Emission peak positions derived from 2D-Gaussian fits to the integrated intensity maps that are well detected and not severely contaminated by emission from other species (see Sect. 3.3). Positions are given in equatorial offsets with respect to the phase center (see Sect. 2.3). (*) NH_2CHO, SO_2, and NH_2D are not detected toward N4 (see Table 3.3) . (**) The transitions of HC_3N, $v=0$ observed toward N4 and N5 are contaminated by absorption and cannot be used to derive the emission peak position.

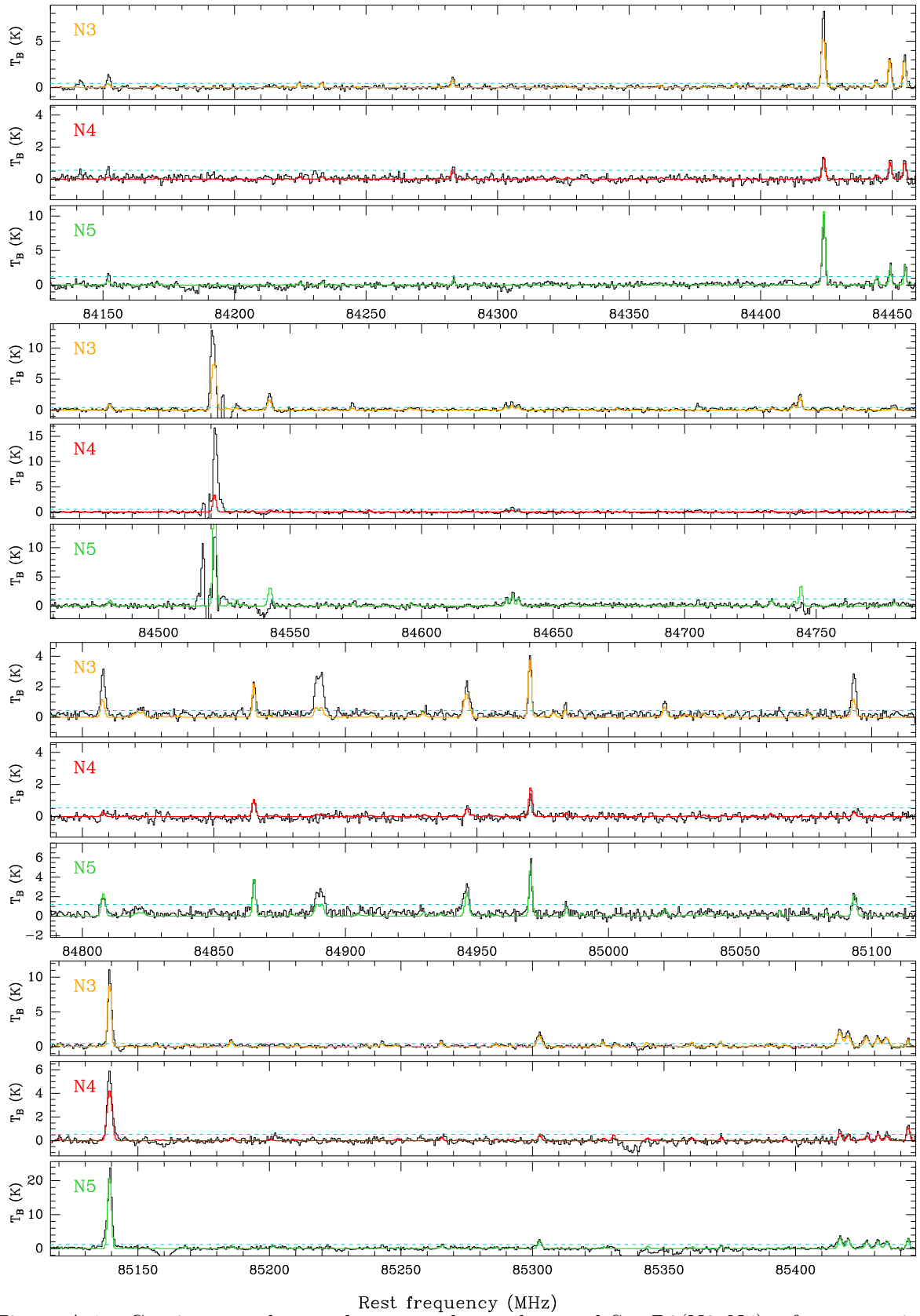

Figure A.1: Continuum-subtracted spectra observed toward Sgr B2(N3–N5), after correction for the primary beam attenuation. The frequency axis corresponds to the systemic velocities of the HMCs (see Sect. 4.1.1). The best-fit LTE synthetic spectra obtained for N3, N4, and N5 are overlaid in yellow, red, and green, respectively (see Sect. 3.2). The horizontal dotted line shows the 3σ noise level (see Table 2.2).

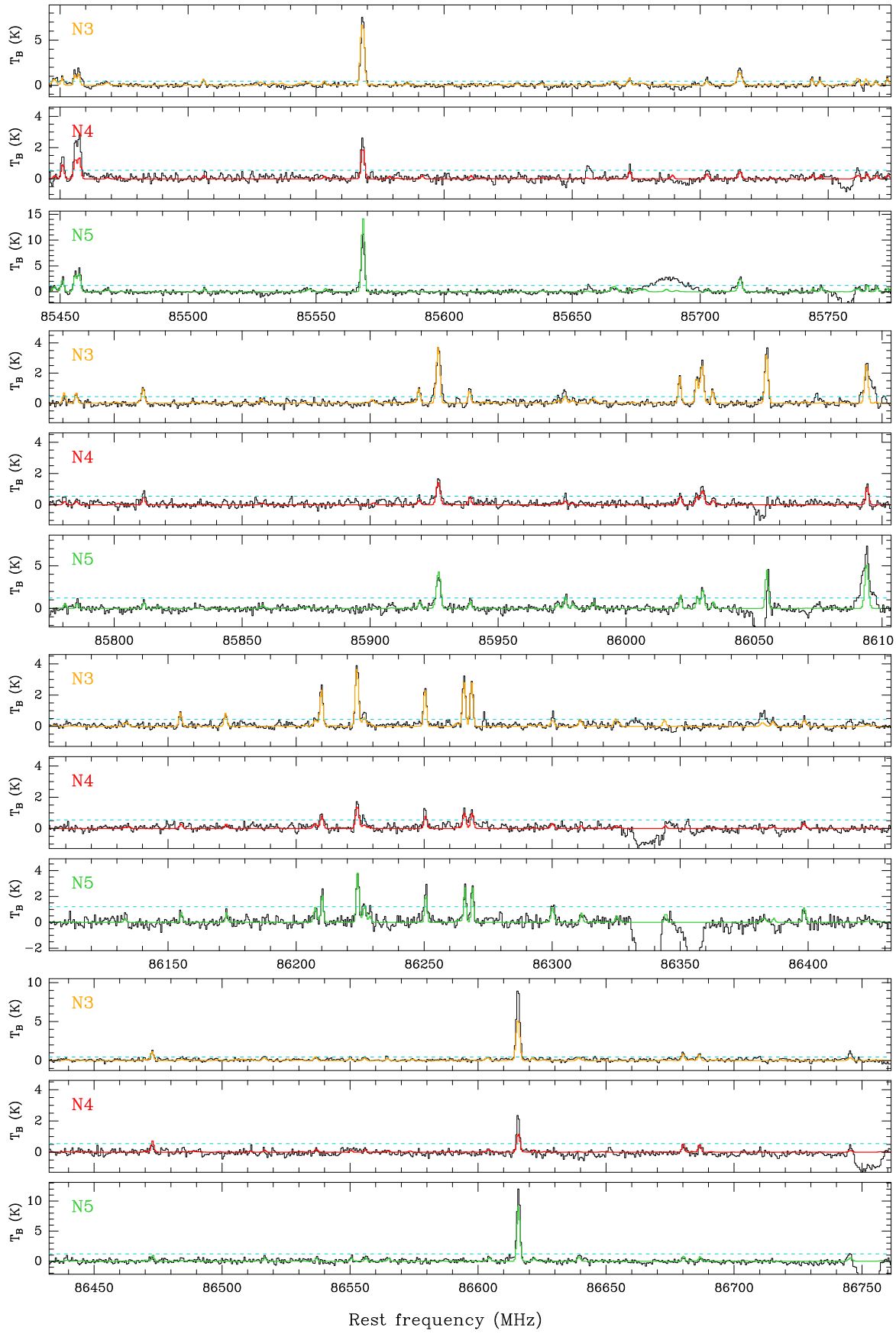

Figure A.1: continued.

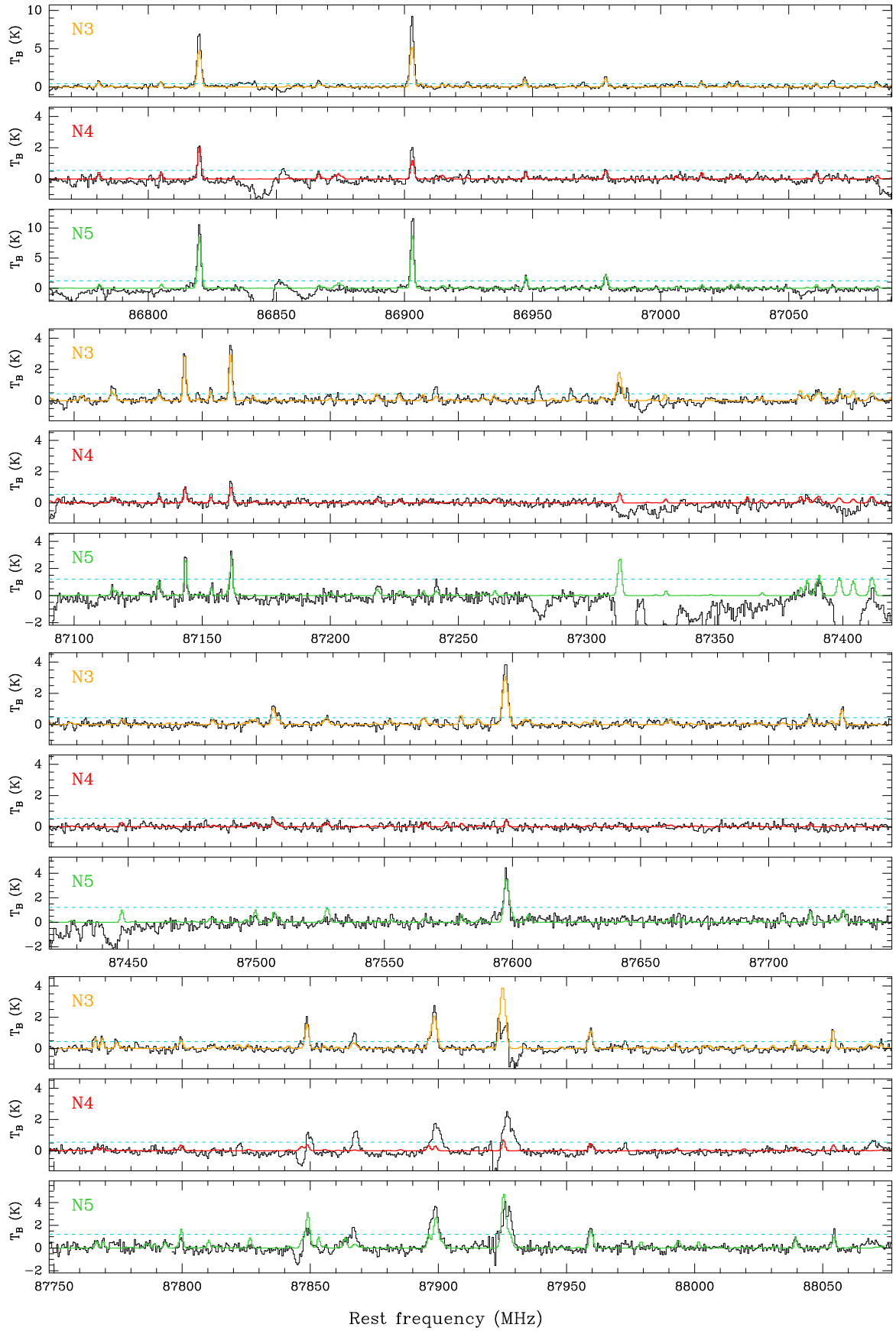

Figure A.1: continued.

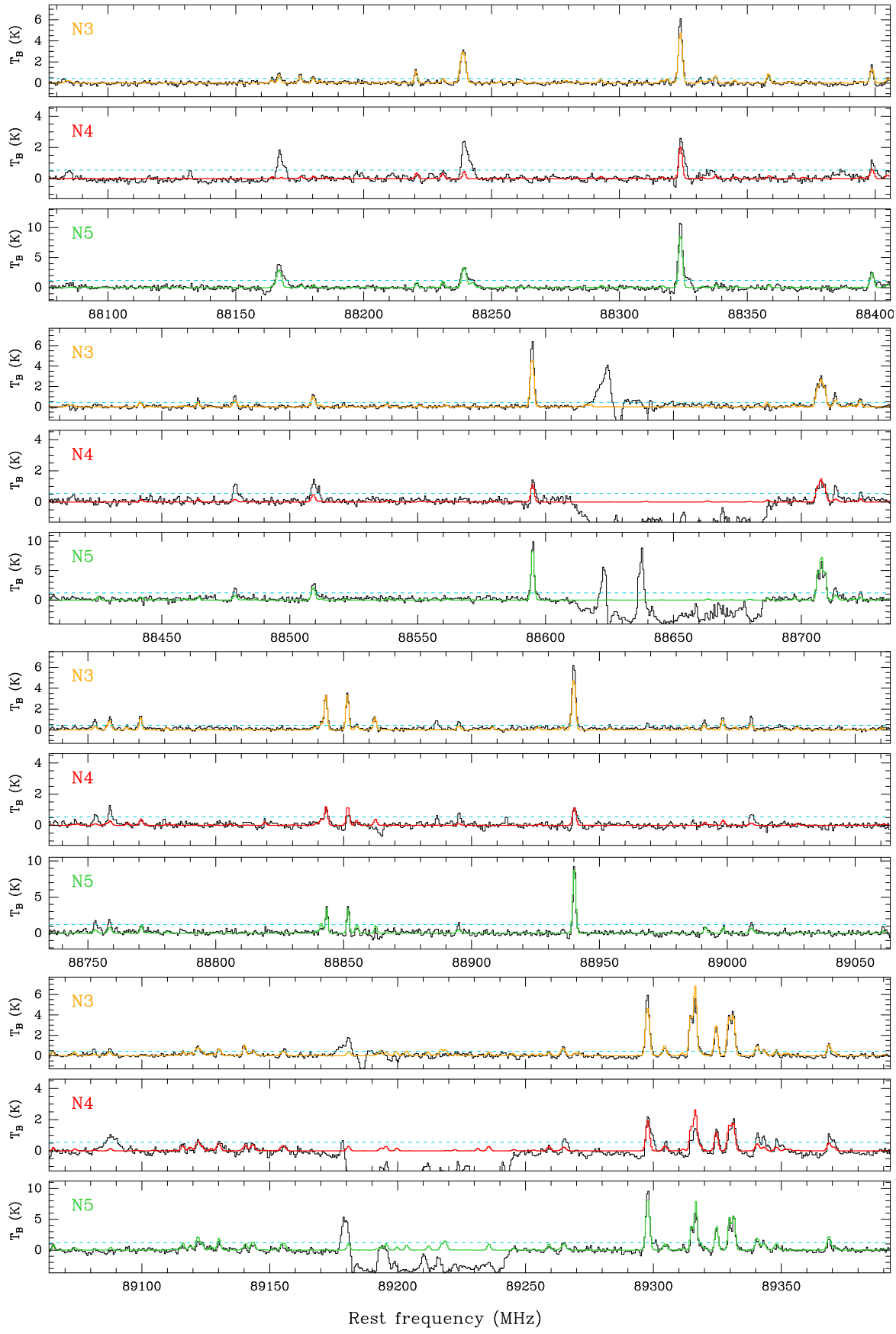

Figure A.1: continued.

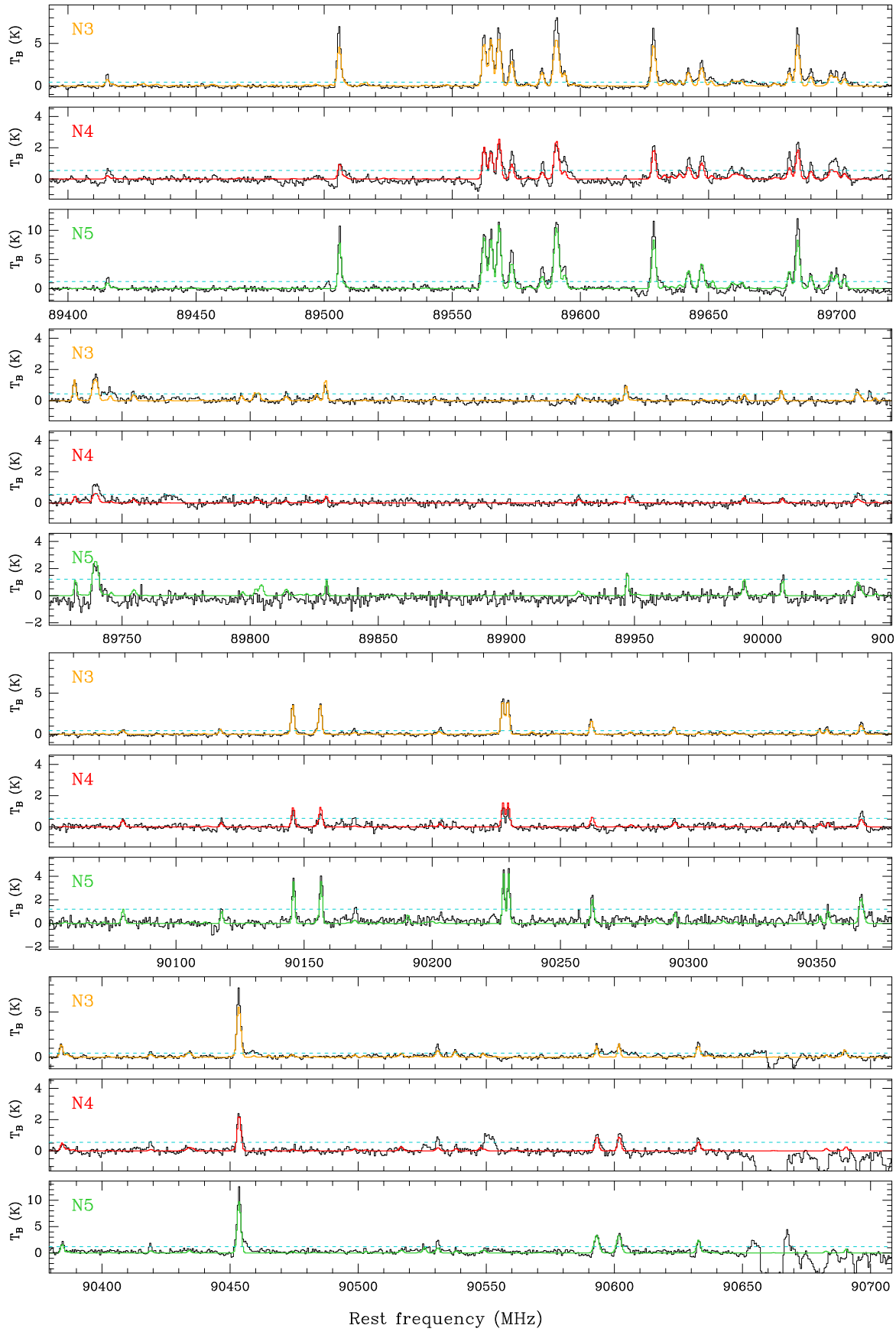

Figure A.1: continued.

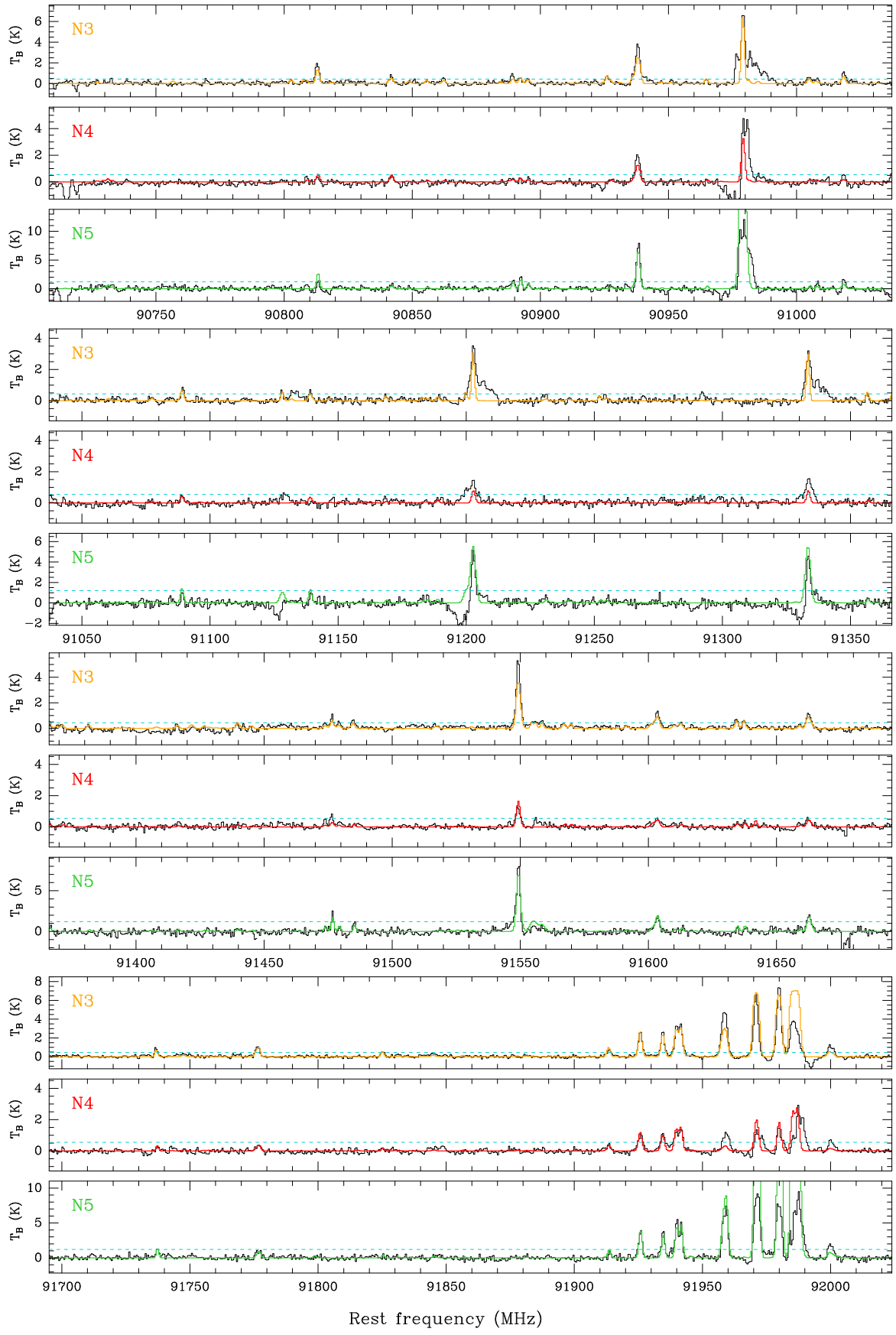

Figure A.1: continued.

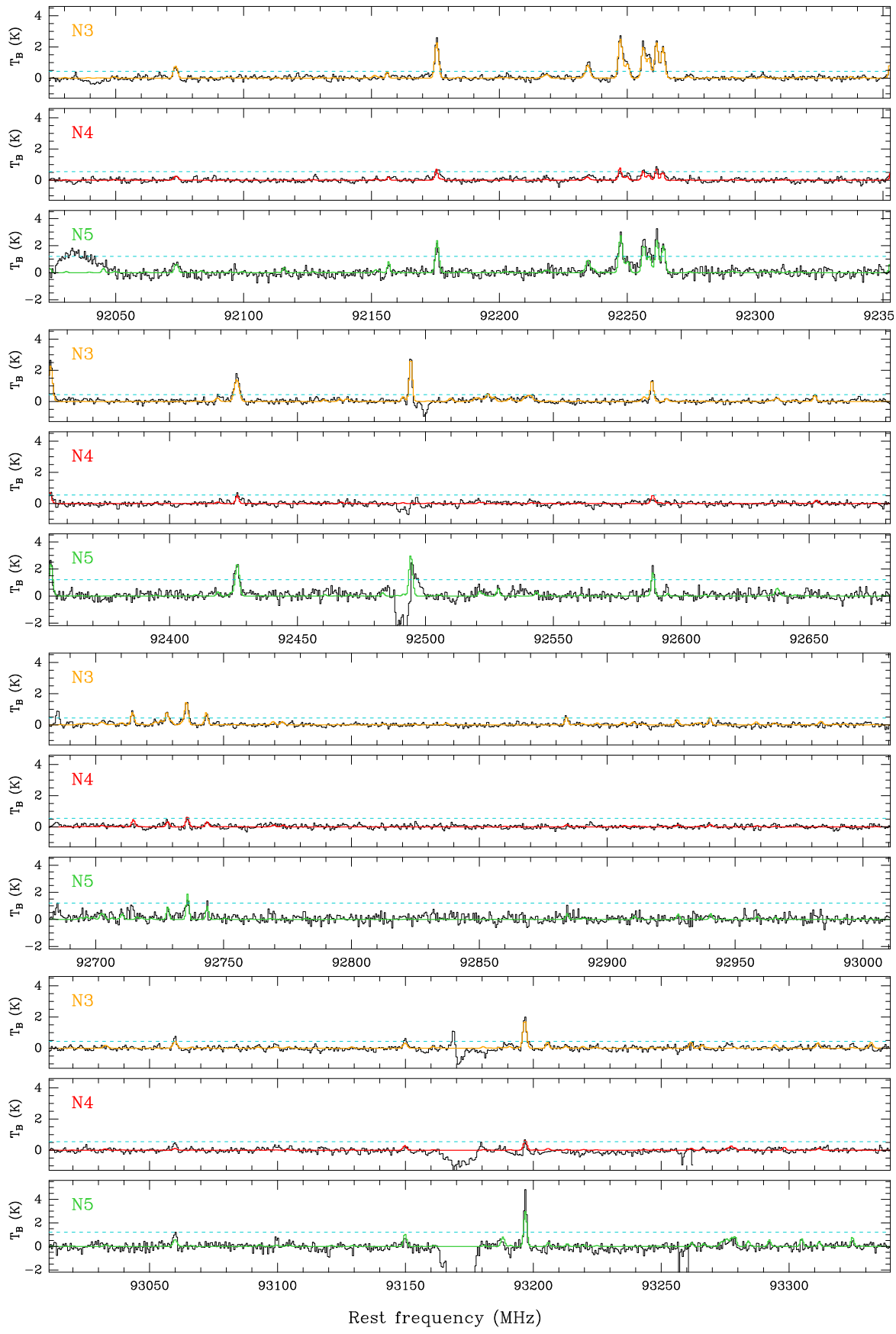

Figure A.1: continued.

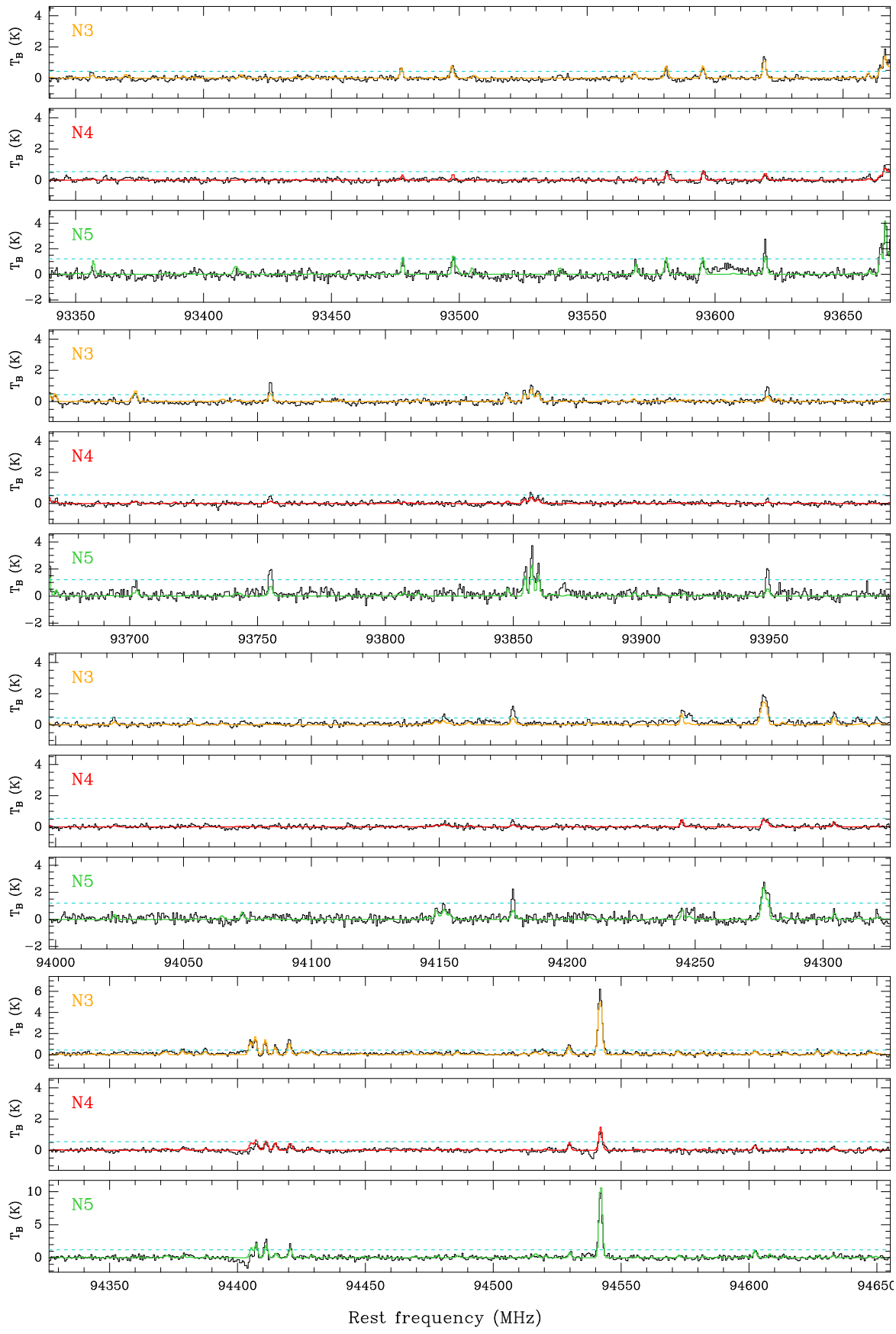

Figure A.1: continued.

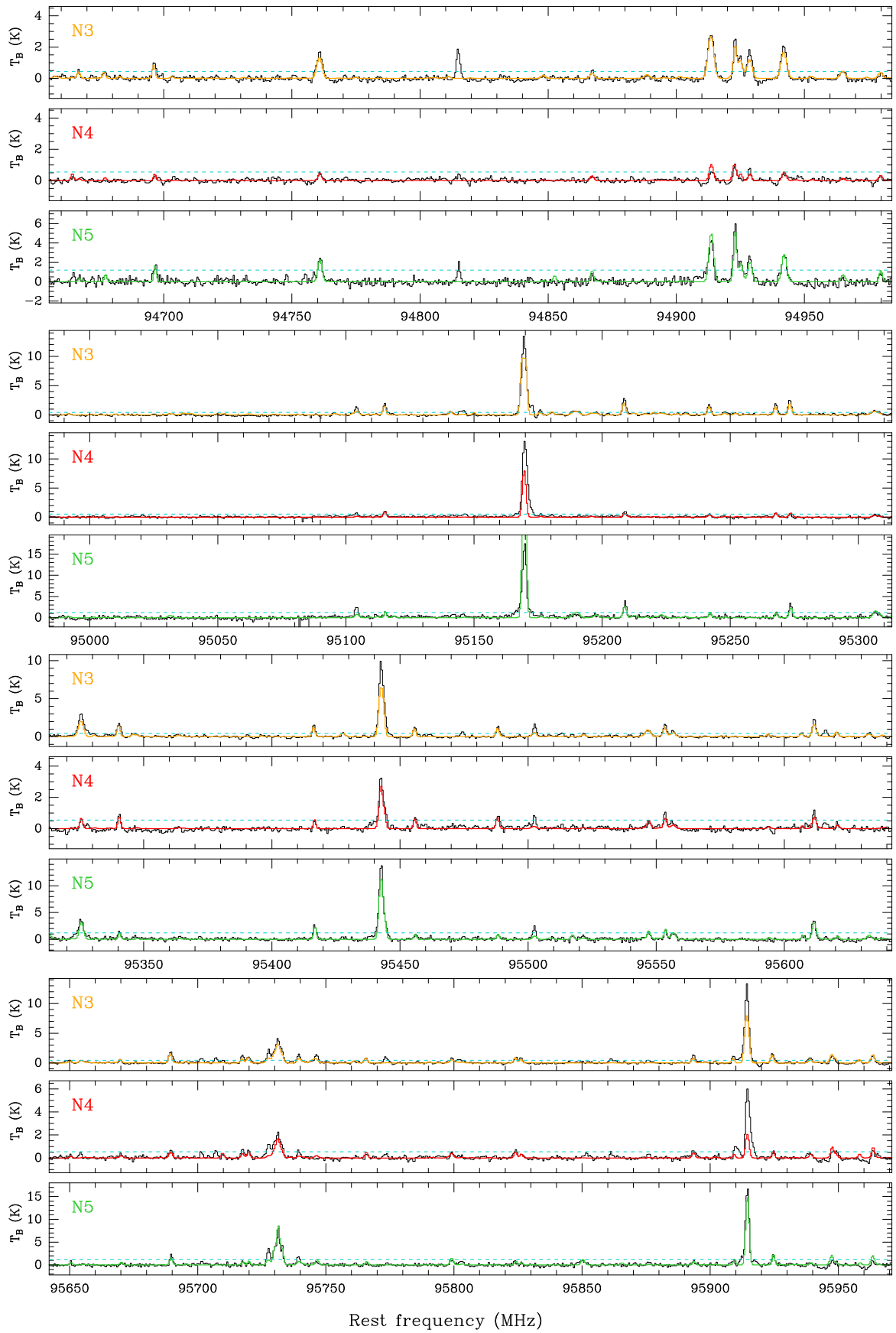

Figure A.1: continued.

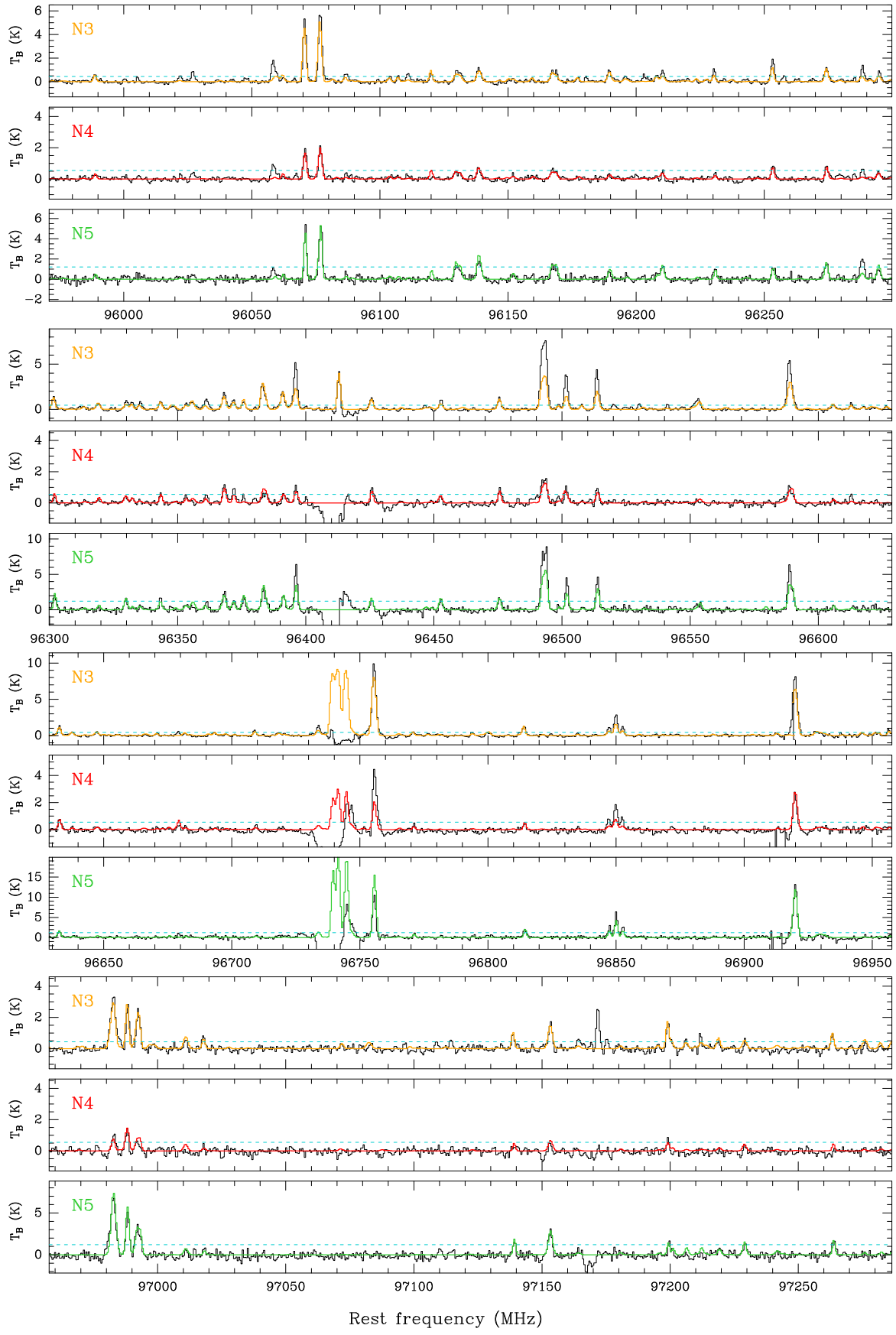

Figure A.1: continued.

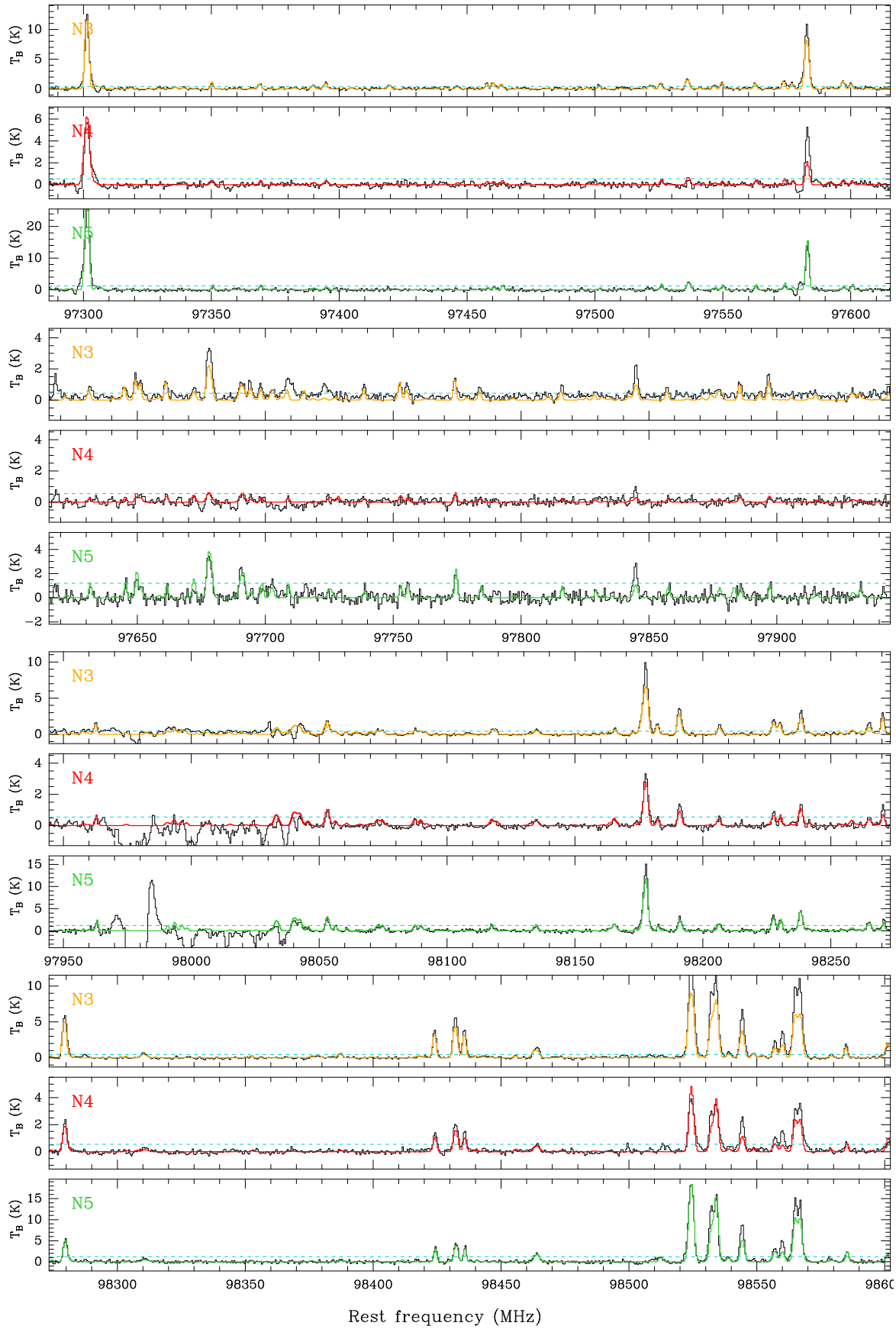

Figure A.1: continued.

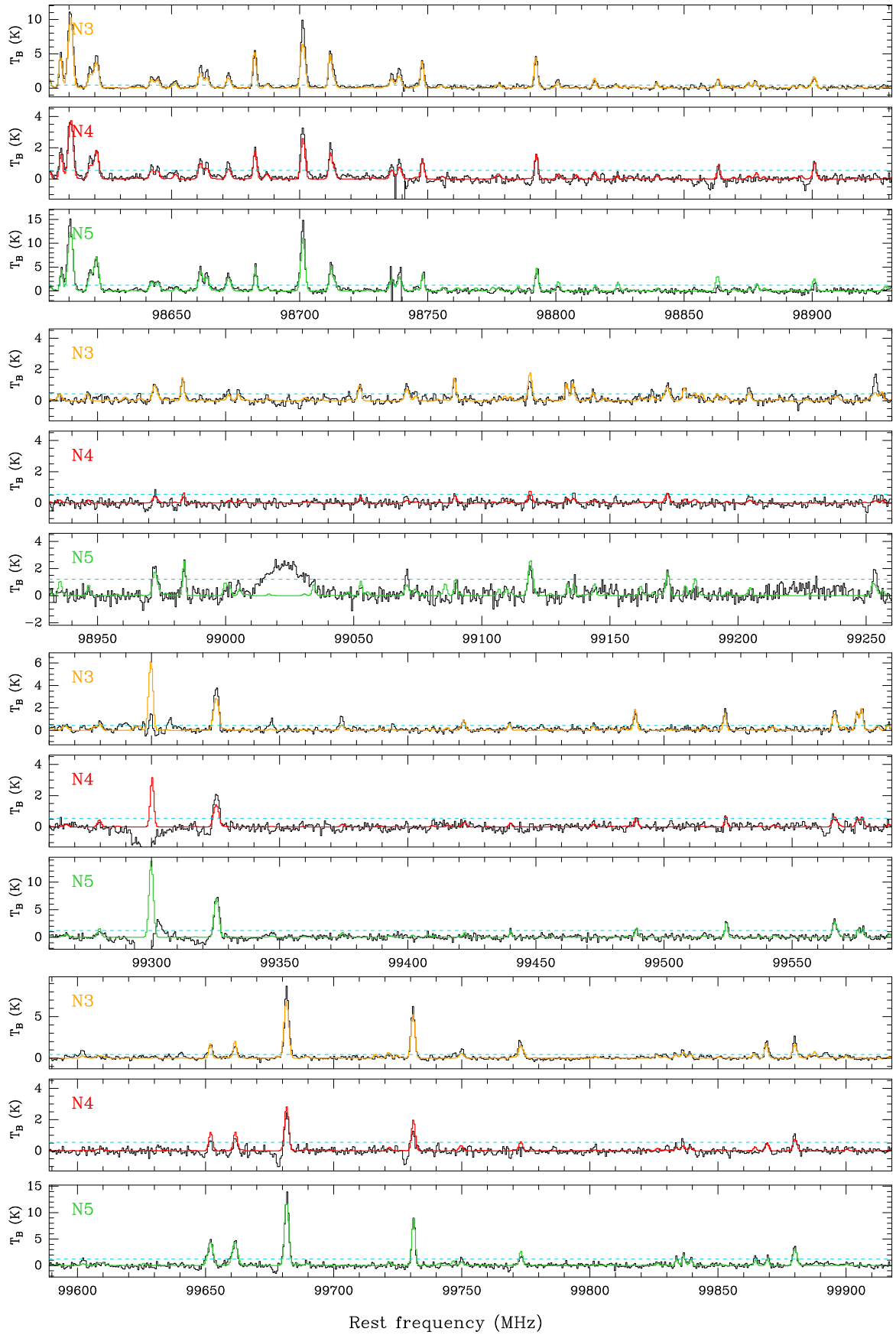

Figure A.1: continued.

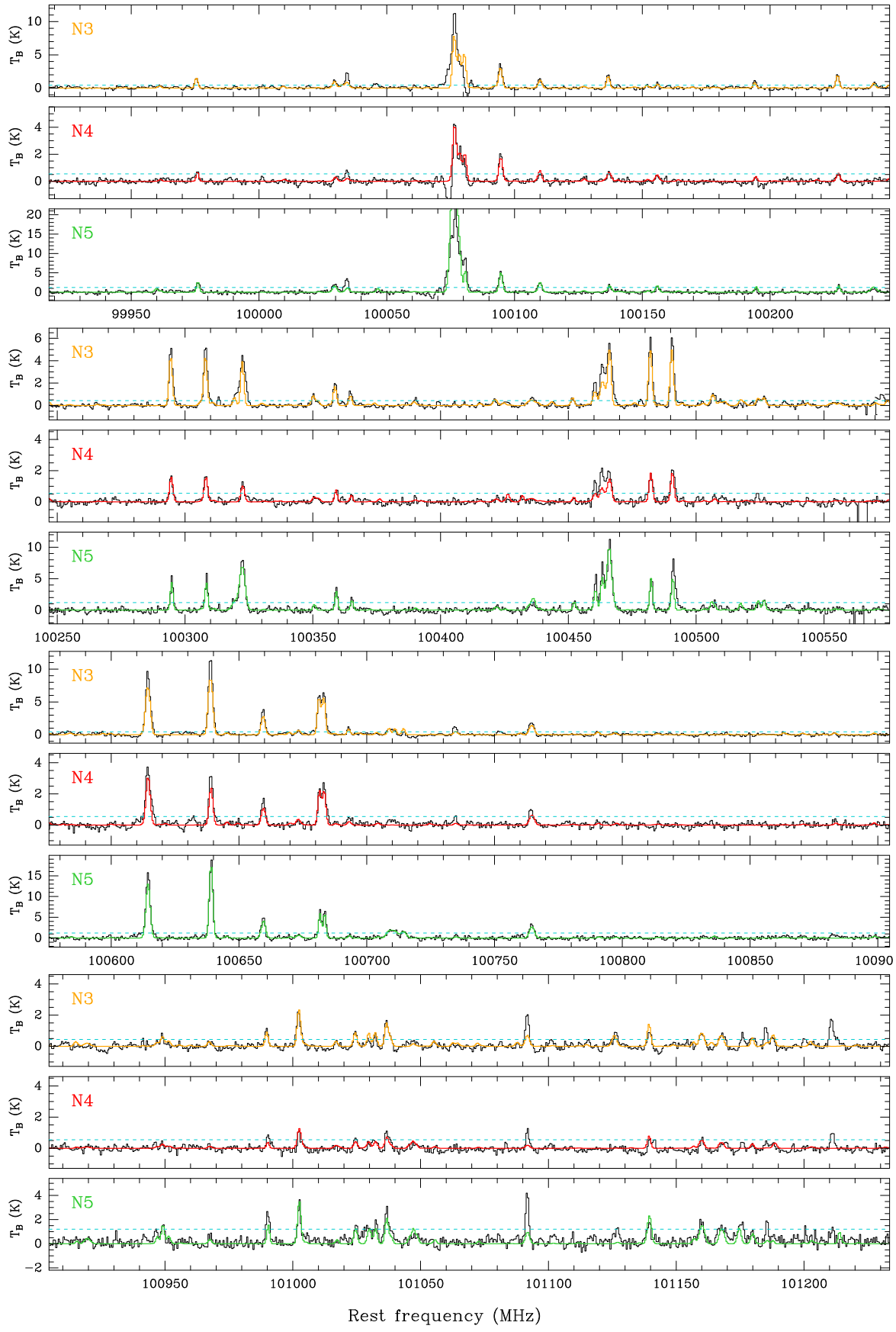

Figure A.1: continued.

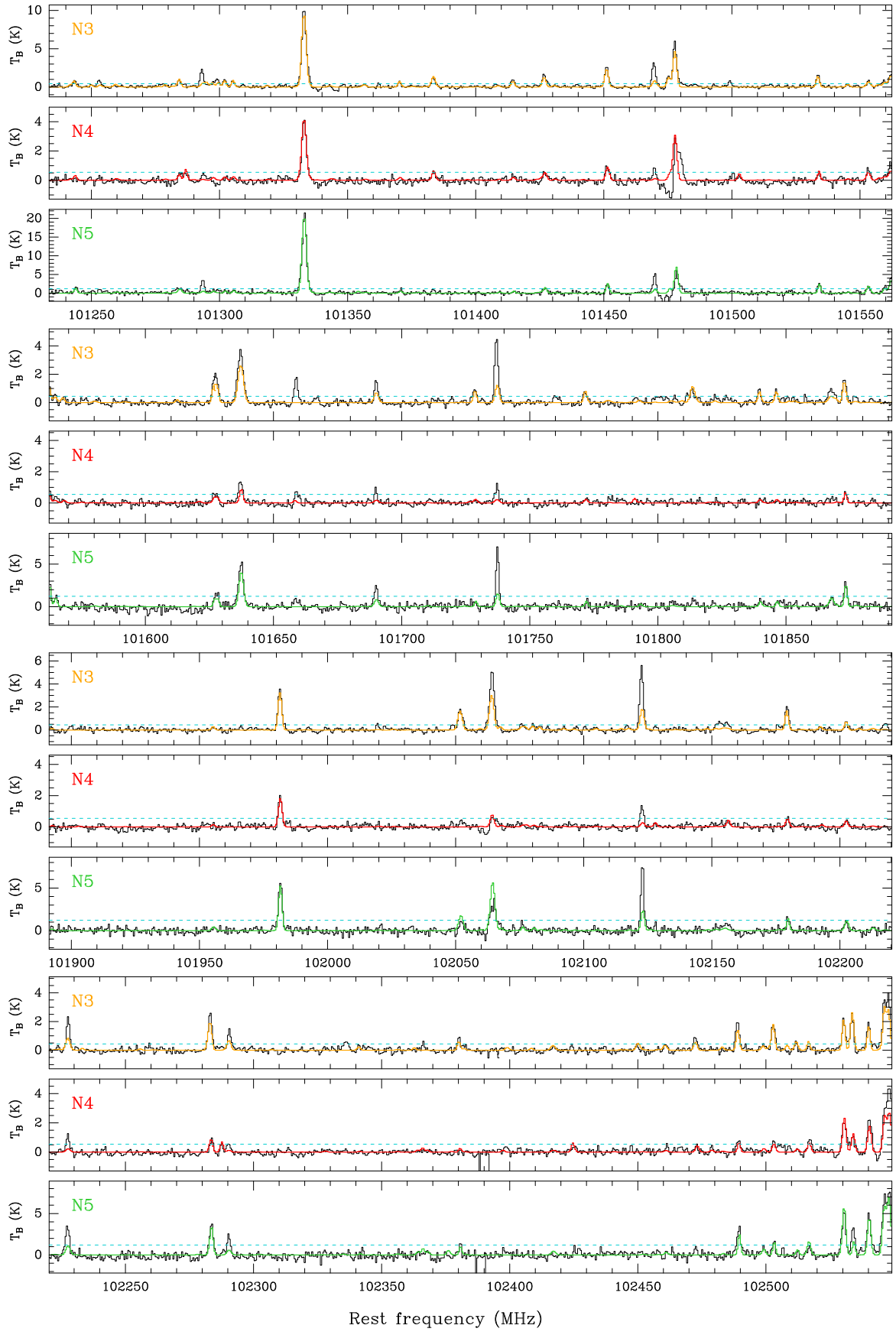

Figure A.1: continued.

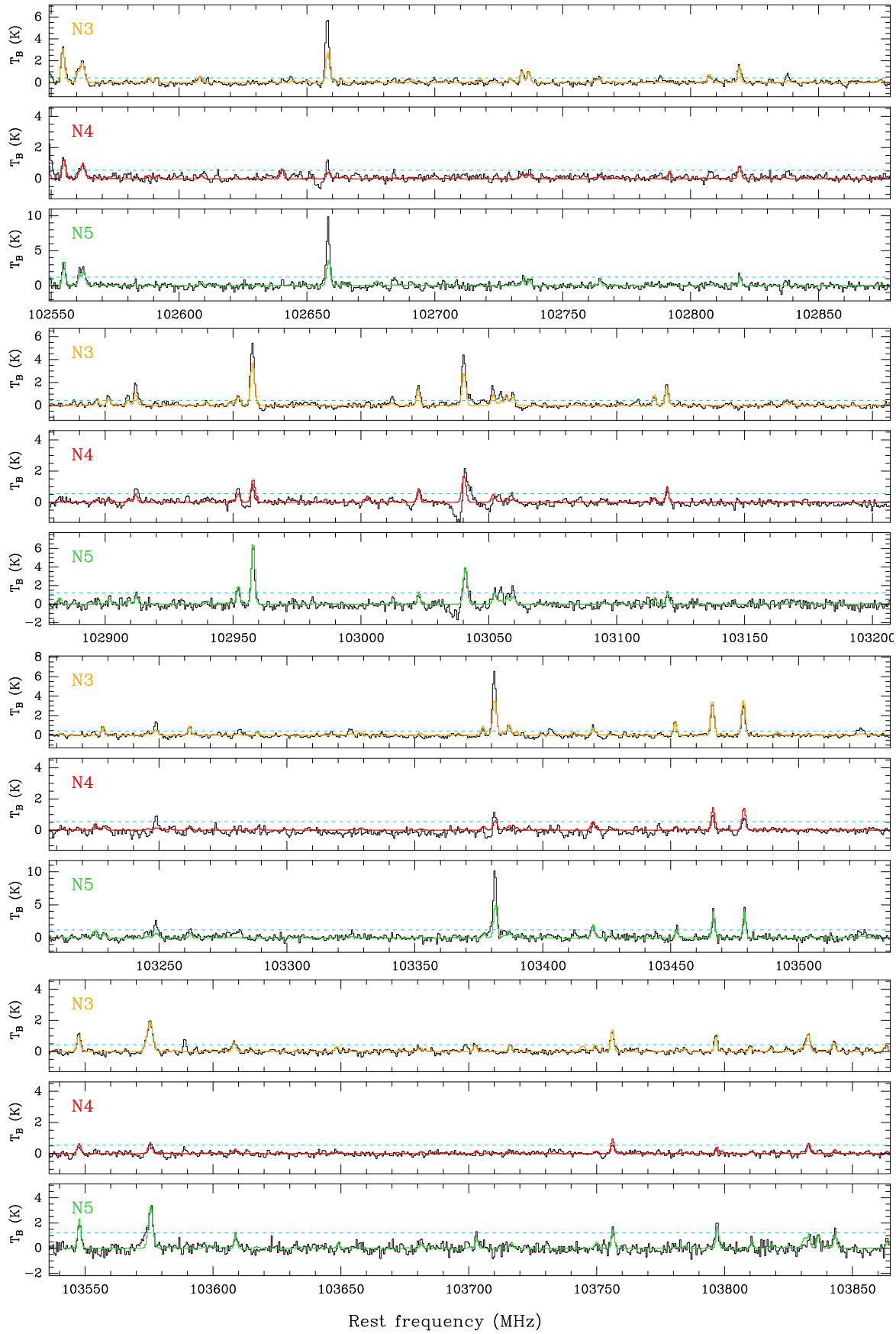

Figure A.1: continued.

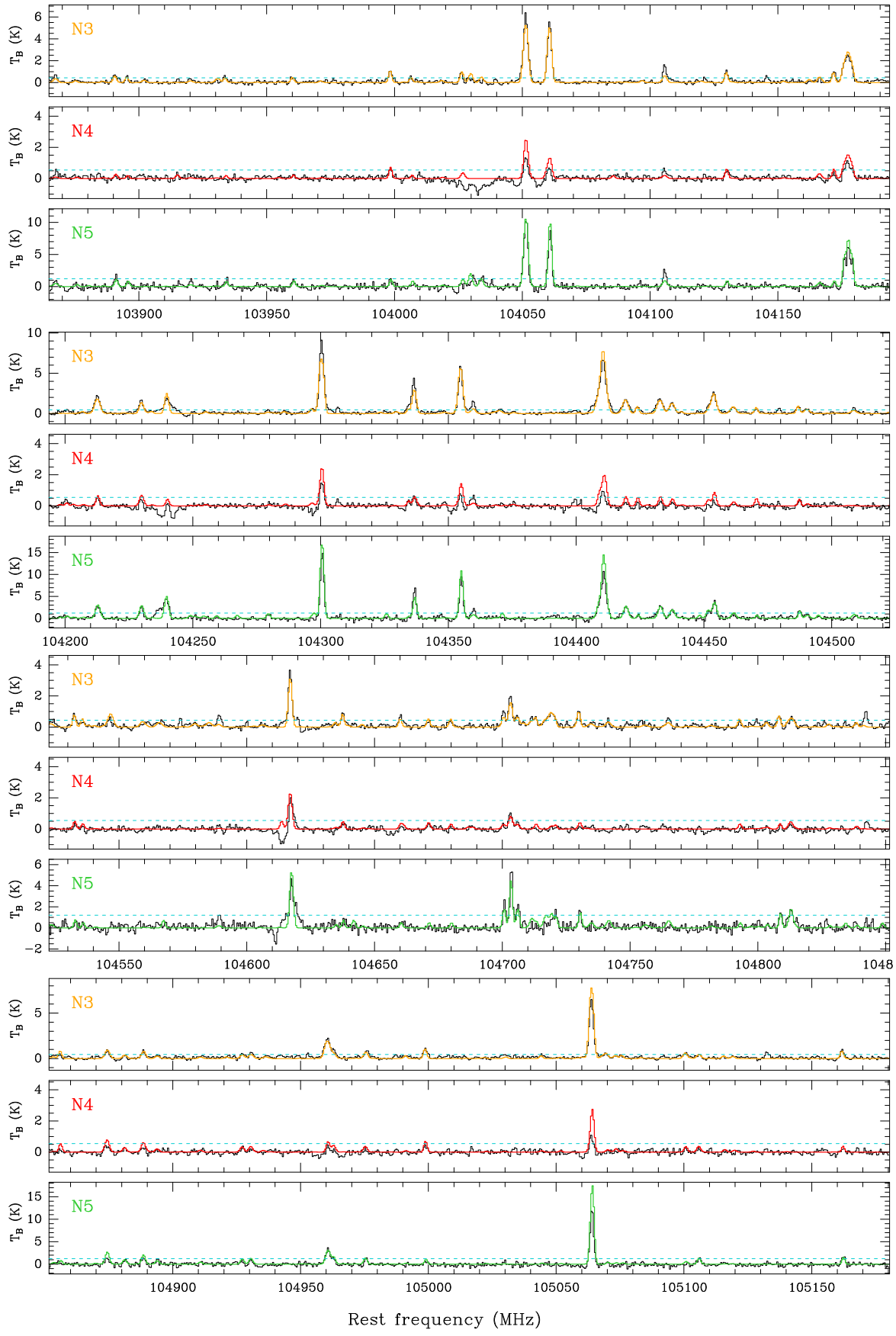

Figure A.1: continued.

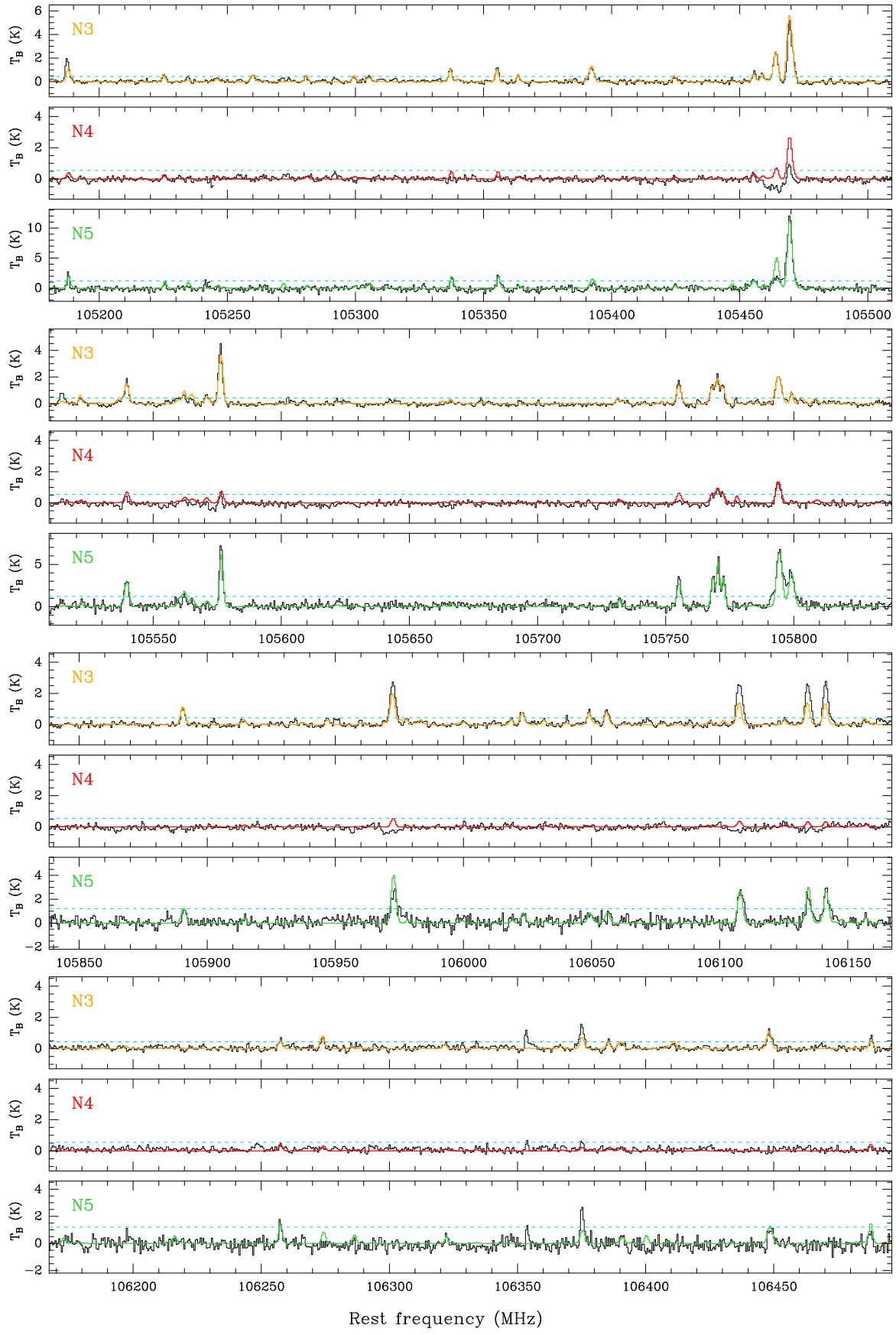

Figure A.1: continued.

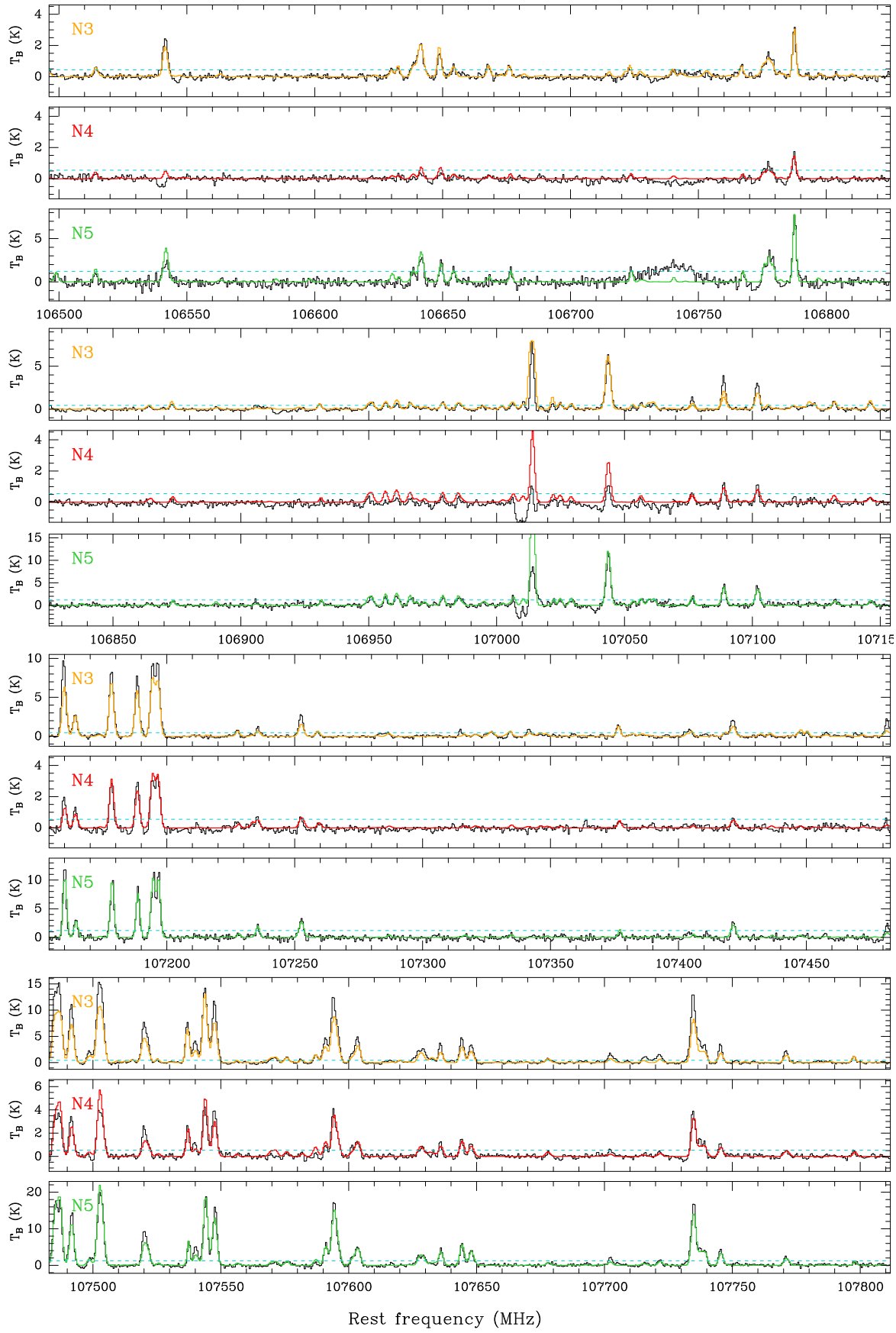

Figure A.1: continued.

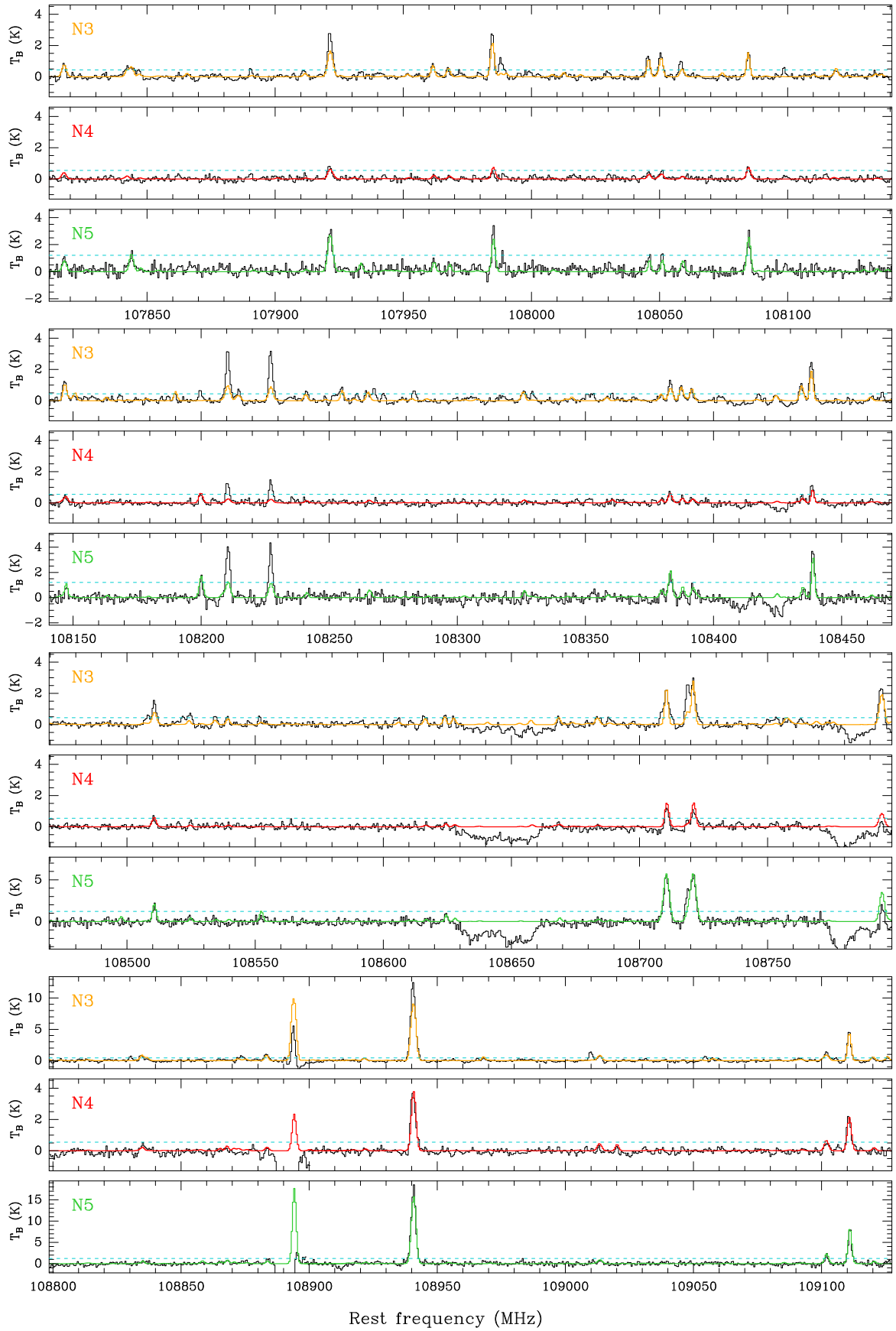

Figure A.1: continued.

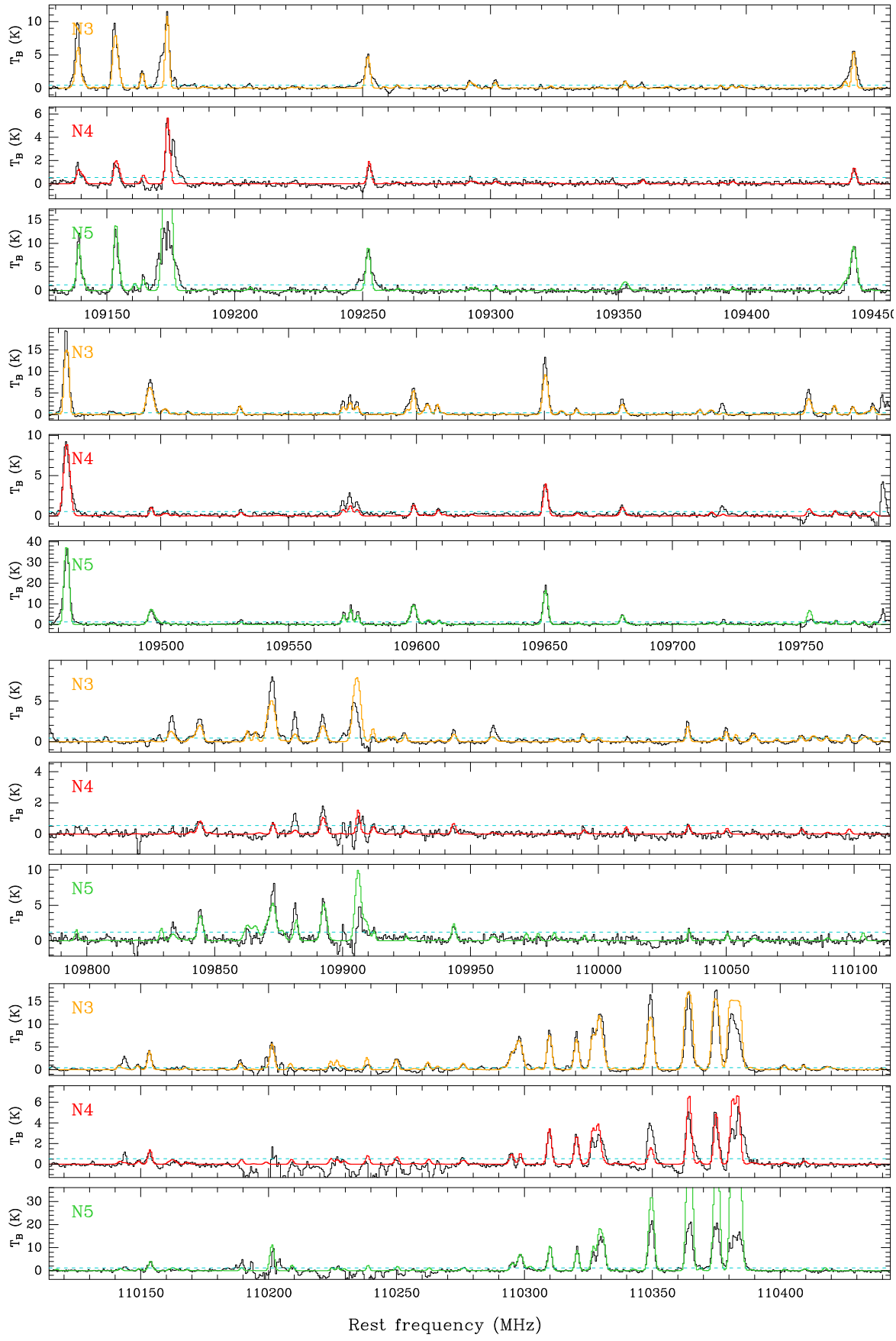

Figure A.1: continued.

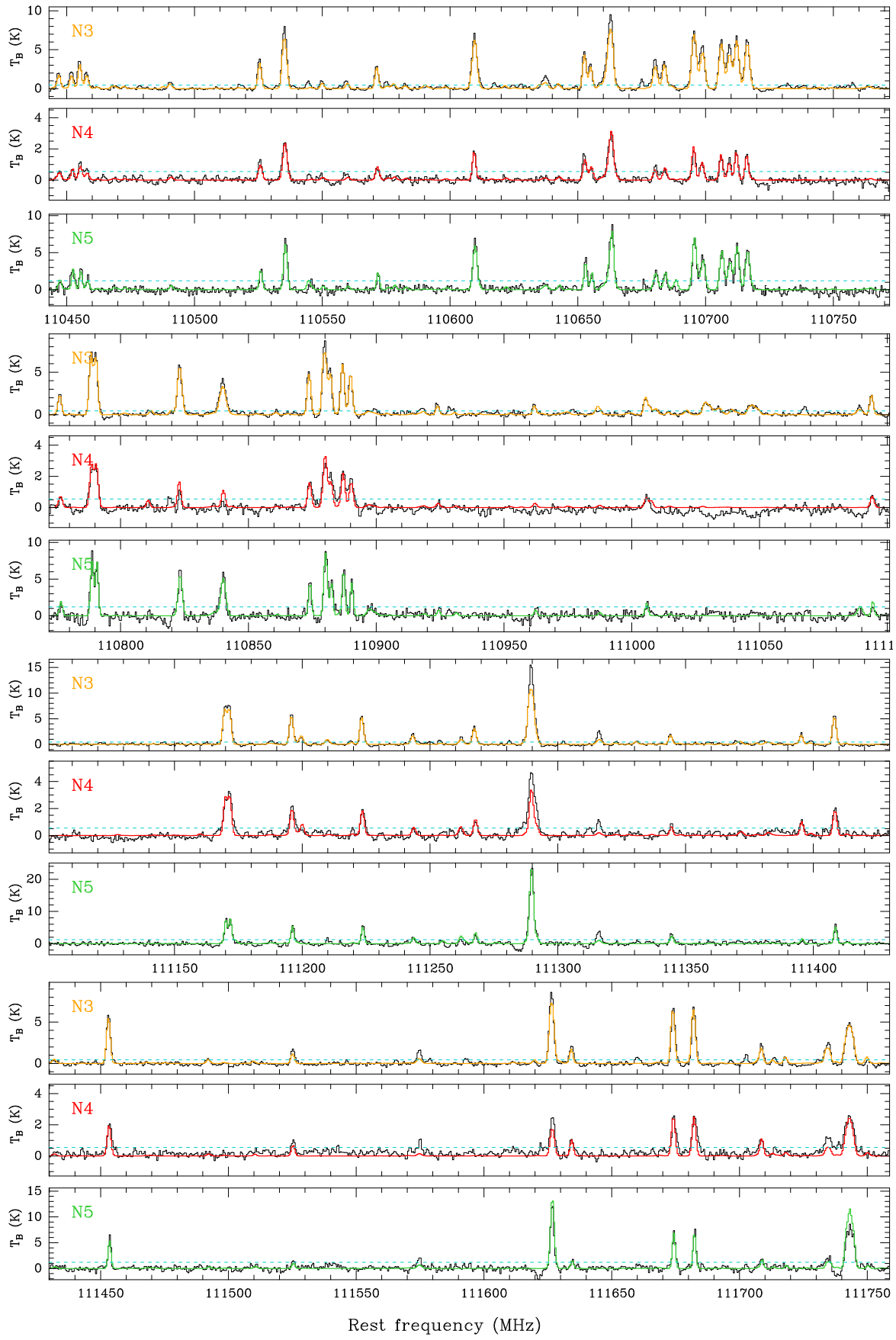

Figure A.1: continued.

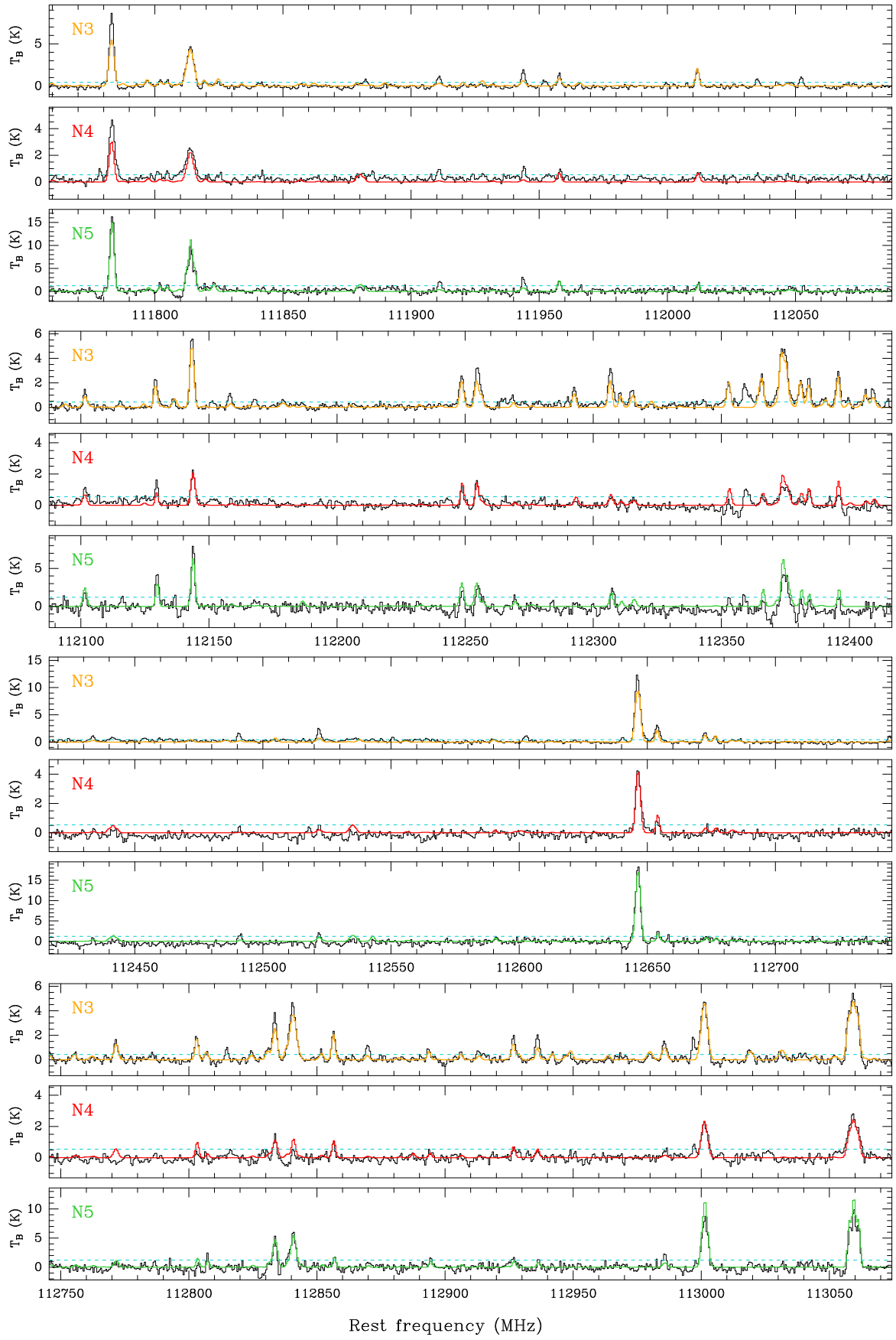

Figure A.1: continued.

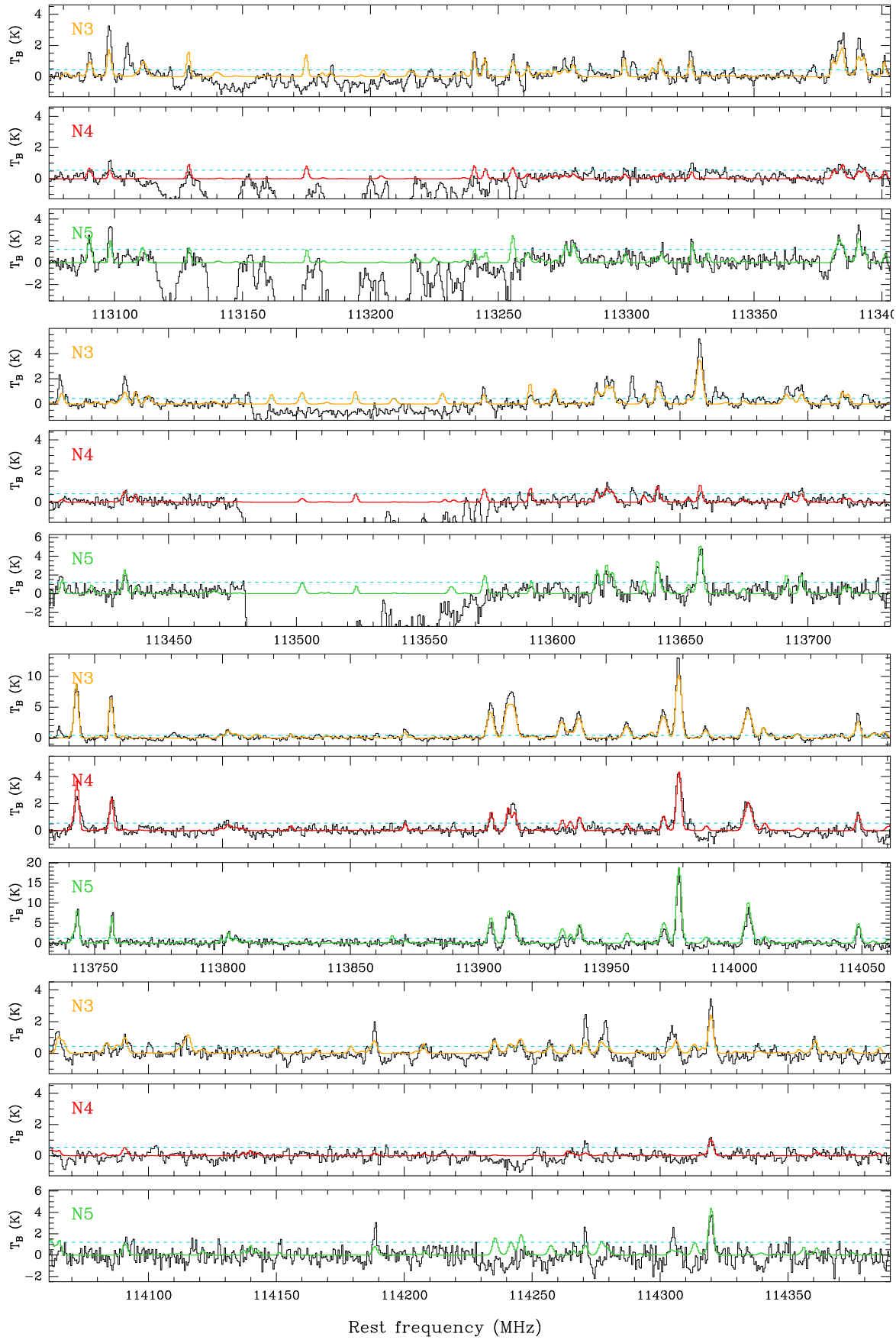

Figure A.1: continued.

Appendix B

Appendix to Chapter 4

Contents

B.1 H_2 column densities

Appendix to Sect. 4.2.4.

B.2 ALMA continuum data

Appendix to Sect. 4.2.

Table B.1: Peak flux densities and H_2 column densities toward Sgr B2(N)'s hot cores.

					N1				N2				N3	N4		N5	
Setup	SPW	Freq. (GHz)	HPBW ($'' \times ''$)	$\mathrm{rms_{ALMA}}$ [a] (mJy beam^{-1})	F_ν^{ALMA} (Jy beam^{-1})	F_ν^{SMA} (Jy beam^{-1})	$N_{\mathrm{H_2}}^{\mathrm{ALMA}}$ [b] (10^{25}cm^{-2})	$N_{\mathrm{H_2}}^{\mathrm{SMA}}$ [c] (10^{25}cm^{-2})	F_ν^{ALMA} [b] (Jy beam^{-1})	F_ν^{SMA} [c] (Jy beam^{-1})	$N_{\mathrm{H_2}}^{\mathrm{ALMA}}$ [b] (10^{24}cm^{-2})	$N_{\mathrm{H_2}}^{\mathrm{SMA}}$ [c] (10^{24}cm^{-2})	$N_{\mathrm{H_2}}^{\mathrm{ALMA}}$ [b] (10^{23} cm^{-2})	F_ν^{ALMA} (mJy beam^{-1})	$N_{\mathrm{H_2}}^{\mathrm{ALMA}}$ [b] (10^{23} cm^{-2})	F_ν^{ALMA} (mJy beam^{-1})	$N_{\mathrm{H_2}}^{\mathrm{ALMA}}$ [b] (10^{23} cm^{-2})
S1	0	85.0	2.1×1.5	5.3	0.569(3)	24.15(11)	0.90(1)	0.52(1)	0.051(8)	6.51(2)	0.72(11)	1.04(1)	<3.9	_	<3.88	0.073(1)	10.46(2)
S1	1	86.5	2.0×1.5	4.3	0.594(3)	23.69(2)	0.93(1)	0.53(1)	0.058(8)	6.42(2)	0.82(11)	1.07(1)	<3.1	21.82(60)	3.04(9)	0.070(1)	9.84(4)
S2	0	88.0	1.9×1.7	9.6	0.688(4)	24.35(3)	1.00(1)	0.54(1)	0.070(8)	6.60(2)	0.91(11)	1.07(1)	<6.4	_	<6.45	0.063(1)	8.28(8)
S2	1	90.5	1.8×1.6	8.3	0.789(3)	23.08(1)	1.22(1)	0.60(1)	0.078(9)	6.34(1)	1.04(12)	1.17(1)	<5.8	_	<5.79	0.055(1)	7.27(4)
S3	0	92.0	2.9×1.5	7.4	0.878(5)	25.67(2)	0.82(1)	0.39(1)	0.073(7)	6.69(1)	0.61(6)	0.81(1)	<3.3	_	<3.25	0.059(1)	5.03(10)
S3	1	94.5	2.8×1.5	7.5	0.942(7)	25.65(4)	0.82(1)	0.39(1)	0.060(7)	6.69(1)	0.47(6)	0.82(1)	<3.1	_	<3.07	0.054(1)	4.22(10)
S4	0	96.0	1.9×1.4	2.7	0.810(7)	21.57(3)	1.15(1)	0.63(1)	0.103(16)	5.97(3)	1.25(20)	1.22(1)	<1.7	35.90(12)	4.32(2)	0.053(1)	6.50(2)
S1	2	97.0	1.8×1.4	4.4	0.776(5)	21.39(4)	1.06(1)	0.63(1)	0.098(9)	5.97(2)	1.16(11)	1.24(1)	<2.7	33.06(50)	3.88(7)	0.067(11)	8.02(14)
S4	1	97.5	1.8×1.3	2.6	0.883(7)	20.93(2)	1.17(1)	0.65(1)	0.114(9)	5.87(1)	1.39(11)	1.26(1)	<1.6	33.77(50)	4.04(7)	0.058(1)	7.02(6)
S1	3	98.5	1.8×1.3	4.3	0.809(6)	20.91(2)	1.11(1)	0.66(1)	0.104(10)	5.87(4)	1.23(11)	1.27(1)	<2.6	28.88(76)	3.37(10)	0.070(1)	8.35(2)
S5	0	99.0	1.8×1.4	4.8	1.028(9)	21.58(14)	1.37(2)	0.64(1)	0.138(9)	6.02(2)	1.53(10)	1.25(1)	<2.8	31.10(76)	3.40(10)	0.046(1)	5.09(2)
S2	2	100.0	1.6×1.4	5.0	1.022(7)	20.78(2)	1.47(1)	0.70(1)	0.137(10)	5.88(6)	1.61(12)	1.34(2)	<3.0	33.53(64)	3.87(8)	0.062(1)	7.27(8)
S5	1	101.5	1.7×1.4	3.7	1.047(10)	21.11(2)	1.35(2)	0.66(1)	0.152(9)	5.93(2)	1.63(10)	1.28(1)	<2.1	34.03(64)	3.58(8)	0.062(1)	6.59(2)
S2	3	102.5	1.6×1.4	5.3	1.051(11)	20.41(31)	1.44(2)	0.72(2)	0.144(10)	5.80(2)	1.62(11)	1.37(1)	<3.1	36.90(103)	4.06(13)	0.056(1)	6.23(2)
S3	2	104.0	2.5×1.3	5.0	1.149(10)	23.40(6)	0.93(1)	0.46(1)	0.169(9)	6.26(2)	1.20(7)	0.95(1)	<1.8	29.66(104)	2.06(8)	0.075(1)	5.29(6)
S3	3	106.5	2.5×1.3	5.0	1.220(11)	22.85(1)	0.97(1)	0.48(1)	0.159(9)	6.16(2)	1.10(7)	0.99(1)	<1.8	38.82(105)	2.63(8)	0.076(1)	5.23(13)
S4	2	108.0	1.7×1.2	3.0	1.300(10)	18.80(9)	1.32(2)	0.76(1)	0.163(10)	5.42(1)	1.74(11)	1.43(1)	<1.7	41.37(66)	4.29(8)	0.048(1)	5.07(8)
S4	3	109.5	1.6×1.2	2.5	1.012(10)	18.25(4)	1.31(2)	0.79(1)	0.173(9)	5.30(1)	1.85(11)	1.48(1)	<1.4	42.23(13)	4.40(2)	0.051(1)	5.44(2)
S5	2	111.0	1.6×1.3	8.2	1.192(11)	19.44(3)	1.37(2)	0.75(1)	0.198(10)	5.58(2)	1.86(10)	1.42(1)	<4.0	44.44(54)	4.06(6)	0.074(1)	6.87(2)
S5	3	113.5	1.6×1.2	7.6	1.161(14)	18.51(16)	1.34(2)	0.79(1)	0.211(10)	5.39(1)	1.99(10)	1.48(1)	<3.8	_	<3.76	0.075(1)	6.99(1)

Notes. Uncertainties in parentheses are given in units of the last digit. They take into account the error on F_ν given by the Gaussian fitting procedure and the uncertainty on the free-free correction factor. Results obtained from maps belonging to the frequency range covered by setup 3 are highlighted in gray. The upper limits correspond to 5σ. [(a)] Noise level measured in the ALMA continuum map with GO NOISE. [(b)] Peak flux density derived from the 2D-Gaussian fit to the continuum map, corrected for the primary beam attenuation and for the free-free contamination. [(c)] Peak flux density measured on the SMA map obtained at 343 GHz and smoothed to the resolution of the ALMA map.

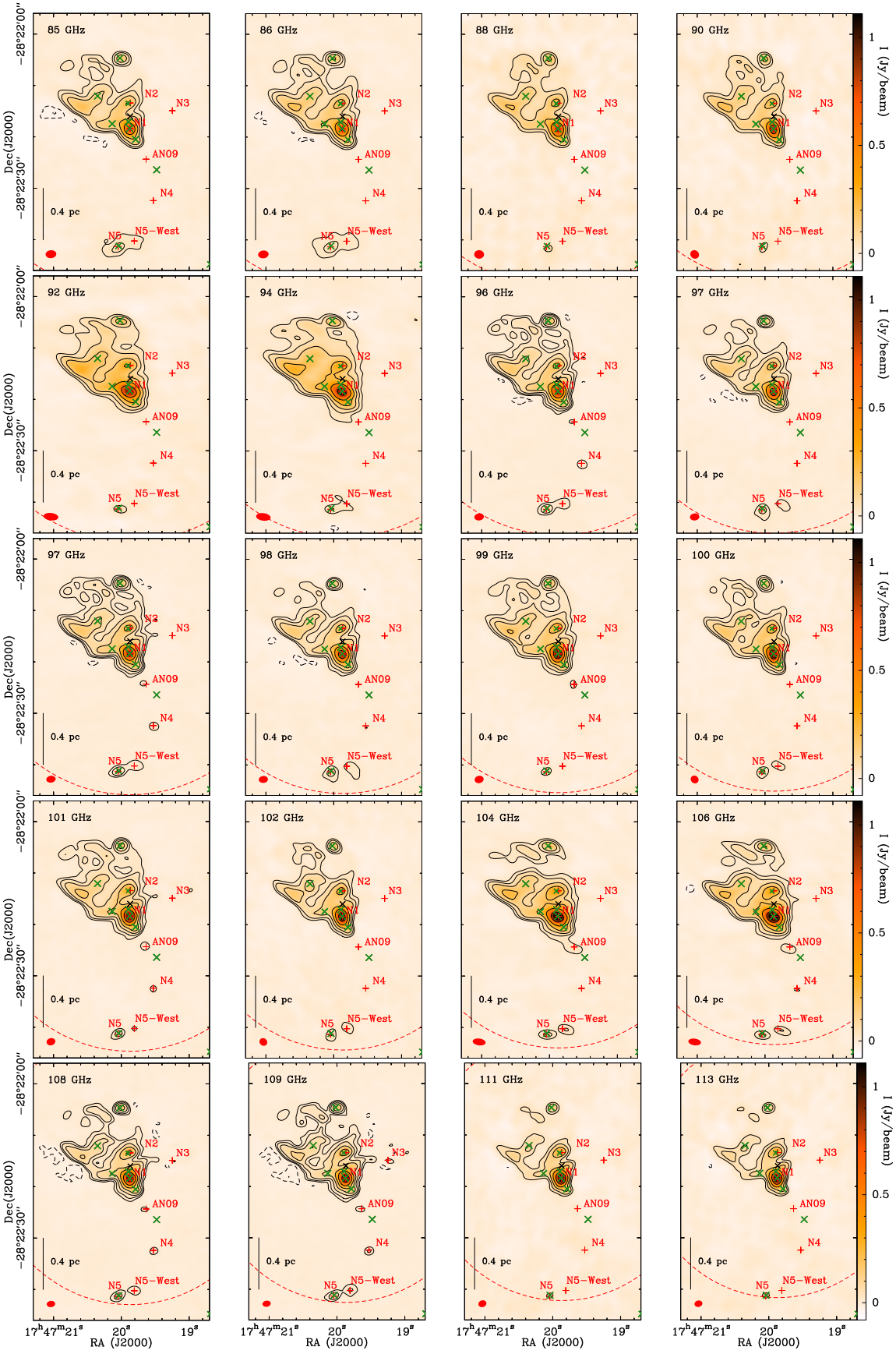

Figure B.1: Continuum maps of Sgr B2(N) obtained with ALMA at different frequencies (one for each spectral window of the survey). In each panel, contour levels (positive in solid line and negative in dashed line) start at 5σ (σ ~3.0 mJy/beam) and double in value up to 320σ. The red filled ellipse shows the synthesized beam (Table 2.2). The red crosses mark the peaks of spectral line density (Fig. 3.1a). The green crosses represent (UC)HII regions. The dashed red circle represents the size (HPBW) of the primary beam of the 12 m antennas. The maps are not corrected for the primary beam attenuation.

Appendix C

Appendix to Chapter 5

Contents

C.1 Activation energies for surface chemical reactions

Appendix to Sect. 5.3.

C.2 Results of the chemical models

C.2.1 Additional tables

Appendix to Sects. 5.3 and 6.1.

C.2.2 Influence of the CRIR on the chemistry during the free-fall collapse

Appendix to Sect. 5.3.3.

C.2.3 Influence of the minimum dust temperature on the chemistry during the free-fall collapse

Appendix to Sect. 5.3.4.

C.2.4 Influence of the radiation field strength on the chemistry during the free-fall collapse

Appendix to Sect. 5.3.5.

Table C.1: Activation energies of selected surface chemical reactions involved in the production/destruction of COMs.

Reaction	E_A [a] (K)	Width[b] (Å)
$H + H \rightarrow H_2$	0	_
$OH + H_2 \rightarrow H_2O + H$	2100	1.0
$OH + CH_4 \rightarrow H_2O + CH_3$	1780	1.0
$OH + CO \rightarrow CO_2 + H$	80	1.0
$H + CO \rightarrow HCO$	2320	1.35
$H + HCO \rightarrow H_2CO$	0	_
$H + H_2CO \rightarrow CH_3O$	2320	1.35
$H + CH_3O \rightarrow CH_3OH$	0	_
$C + CH_3 \rightarrow C_2H_3$	0	_
$H + C_2H_3 \rightarrow C_2H_4$	0	_
$H + C_2H_4 \rightarrow C_2H_5$	605	1.0
$O + C_2H_5 \rightarrow C_2H_5O$	0	_
$H + C_2H_5O \rightarrow C_2H_5OH$	0	_
$H + OCN \rightarrow HNCO$	0	_
$H + HNCO \rightarrow NH_2CO$	1390	1.0
$H + NH_2CO \rightarrow NH_2CHO$	0	_
$C + CN \rightarrow C_2N$	0	_
$H + C_2N \rightarrow HCCN$	0	_
$H + H_2CN \rightarrow CH_2NH$	0	_
$H + CH_2CN \rightarrow CH_3CN$	0	_
$HCO + CH_3O \rightarrow HCOOCH_3$	0	_
$H + H_2CS \rightarrow CH_2SH$	1000	1.0
$H + H_2CS \rightarrow CH_3S$	1000	1.0
$H + CH_3S \rightarrow CH_3SH$	0	_
$H + CH_2SH \rightarrow CH_3SH$	0	_
$H + C_2H_2CN \rightarrow C_2H_3CN$	0	_
$H + HC_3N \rightarrow C_2H_2CN$	1710	1.0
$H + C_2H_2CN \rightarrow C_2H_3CN$	0	_
$H + C_2H_3CN \rightarrow C_2H_4CN$	1320	1.0
$H + C_2H_4CN \rightarrow C_2H_5CN$	0	_
$CH_3 + OCN \rightarrow CH_3NCO$	0	_
$H + CH3NCO \rightarrow CH_3NHCO$	605	1.0
$H + CH3NHCO \rightarrow CH_3NHCHO$	0	_
$CH_3 + CH_3O \rightarrow CH_3OCH_3$	0	_
$CH_2 + HCO \rightarrow CH_2CHO$	0	_
$H + CH2CHO \rightarrow CH_3CHO$	0	_
$CH_3 + HCO \rightarrow CH_3CHO$	0	_
$CH_3 + CH_3CHO \rightarrow CH_4 + CH_3CO$	1720	1.0
$NH_2 + CH_3CHO \rightarrow NH_3 + CH_3CO$	1250	1.0

Notes. [a] Activation energy (in K). [b] Width of the rectangular barrier for quantum tunneling (in Å). For references see Garrod (2013), Belloche et al. (2017), and references therein.

Table C.2: Final gas-phas fractional abundances calculated by the chemical models.

Model	C_2H_5CN	C_2H_3CN	CH_3CN	CH_3OH	C_2H_5OH	CH_3OCHO	CH_3OCH_3	CH_3CHO	NH_2CHO	CH_3NCO	CH_3SH
N2-T10-1	8.78(-10)	4.02(-11)	9.72(-10)	9.81(-6)	7.48(-8)	1.30(-9)	2.14(-8)	7.74(-9)	3.54(-8)	9.99(-12)	1.76(-9)
N2-T10-10	2.02(-9)	9.25(-11)	2.52(-9)	7.07(-6)	2.33(-7)	1.81(-9)	1.94(-9)	1.84(-8)	7.39(-8)	1.32(-13)	4.04(-9)
N2-T10-50	8.87(-9)	1.45(-9)	2.03(-8)	2.18(-6)	2.55(-6)	6.09(-10)	8.11(-8)	4.70(-8)	1.48(-8)	3.13(-12)	8.66(-9)
N2-T10-100	6.50(-9)	2.04(-9)	4.44(-9)	3.17(-6)	3.98(-6)	5.53(-9)	6.27(-8)	9.95(-8)	1.79(-8)	6.49(-12)	2.38(-9)
N2-T10-500	1.13(-9)	4.25(-9)	8.14(-10)	1.18(-6)	3.33(-6)	1.07(-8)	5.76(-10)	3.21(-7)	4.51(-10)	1.88(-11)	6.89(-10)
N2-T10-1000	5.57(-11)	1.71(-9)	3.67(-10)	1.73(-7)	7.74(-7)	1.04(-9)	1.51(-11)	1.54(-7)	1.25(-11)	7.20(-12)	3.08(-10)
N2-T15-1	8.16(-10)	9.00(-12)	1.47(-9)	3.38(-6)	3.18(-8)	6.53(-10)	1.47(-9)	7.09(-9)	3.84(-8)	3.49(-15)	3.08(-9)
N2-T15-10	1.46(-9)	2.56(-11)	1.24(-9)	3.30(-6)	1.52(-7)	5.60(-10)	9.62(-10)	4.99(-10)	4.08(-8)	6.69(-14)	2.96(-9)
N2-T15-50	1.63(-8)	2.00(-9)	3.31(-8)	1.64(-6)	1.85(-6)	3.47(-10)	5.33(-8)	3.28(-8)	1.17(-8)	1.11(-12)	1.05(-8)
N2-T15-100	6.91(-9)	1.75(-9)	6.89(-9)	2.43(-6)	3.36(-6)	3.52(-9)	5.78(-8)	8.09(-8)	1.27(-8)	4.03(-12)	3.24(-9)
N2-T15-500	9.44(-10)	3.59(-9)	6.01(-10)	1.05(-6)	3.19(-6)	1.03(-8)	4.90(-10)	2.99(-7)	1.76(-10)	1.58(-11)	8.13(-10)
N2-T15-1000	4.01(-11)	8.31(-10)	2.78(-10)	1.10(-7)	5.76(-7)	6.09(-10)	5.53(-12)	1.07(-7)	6.64(-12)	4.73(-12)	5.81(-11)
N2-T20-1	1.73(-10)	2.05(-13)	9.90(-11)	1.43(-7)	5.97(-9)	2.52(-11)	2.88(-10)	7.33(-12)	6.95(-9)	1.85(-16)	1.89(-9)
N2-T20-10	2.63(-11)	2.73(-13)	1.05(-10)	3.13(-7)	2.42(-9)	1.22(-10)	2.14(-10)	8.20(-12)	1.50(-8)	2.26(-15)	3.29(-10)
N2-T20-50	6.60(-9)	3.01(-10)	2.69(-9)	1.15(-6)	2.37(-6)	1.68(-9)	1.01(-8)	2.80(-8)	1.31(-8)	7.69(-13)	9.95(-10)
N2-T20-100	8.19(-9)	6.25(-10)	3.21(-9)	9.18(-7)	1.83(-6)	2.14(-9)	4.17(-9)	3.97(-8)	8.95(-10)	1.31(-12)	6.35(-10)
N2-T20-500	2.75(-10)	6.24(-10)	3.53(-10)	9.90(-8)	5.38(-7)	1.08(-10)	8.58(-12)	4.79(-8)	1.82(-11)	1.80(-12)	1.80(-11)
N2-T20-1000	1.58(-11)	1.78(-10)	1.21(-10)	1.73(-8)	1.09(-7)	4.89(-13)	1.60(-13)	1.85(-8)	1.19(-12)	4.93(-13)	2.09(-12)
N3-T10-CR1	3.86(-9)	7.10(-10)	2.72(-9)	8.61(-6)	4.81(-8)	7.58(-8)	8.83(-9)	9.29(-11)	9.88(-8)	6.69(-10)	1.68(-09
N3-T10-CR10	3.43(-8)	3.63(-9)	1.87(-9)	7.83(-6)	1.49(-7)	2.50(-9)	1.83(-8)	8.95(-10)	6.18(-9)	4.59(-12)	1.06(-9)
N3-T10-CR50	2.65(-8)	1.38(-8)	4.36(-9)	3.56(-6)	3.48(-7)	8.65(-10)	7.86(-9)	6.22(-9)	2.29(-10)	5.77(-11)	3.42(-9)
N3-T10-CR100	3.27(-9)	1.07(-8)	4.87(-9)	1.19(-6)	5.73(-7)	3.55(-11)	1.43(-9)	5.04(-8)	6.91(-11)	1.14(-10)	7.83(-9)
N3-T10-CR500	2.45(-12)	2.07(-9)	2.65(-10)	2.66(-9)	4.43(-9)	1.79(-14)	1.62(-12)	8.20(-8)	1.14(-17)	1.19(-14)	6.91(-11)
N3-T10-CR1000	1.36(-17)	1.48(-10)	2.57(-11)	5.89(-13)	1.63(-13)	1.49(-18)	5.28(-20)	2.87(-8)	6.93(-19)	7.87(-24)	2.32(-16)
N3-T15-CR1	4.70(-9)	9.80(-10)	2.36(-9)	7.10(-6)	2.38(-8)	8.32(-10)	1.92(-9)	4.38(-9)	1.40(-8)	3.82(-10)	1.94(-9)
N3-T15-CR10	3.09(-8)	2.64(-9)	2.27(-9)	7.81(-6)	9.91(-8)	1.80(-9)	1.53(-8)	1.71(-9)	2.21(-8)	2.82(-12)	1.51(-9)
N3-T15-CR50	2.70(-8)	1.79(-8)	4.64(-9)	2.75(-6)	4.77(-7)	1.42(-10)	3.62(-9)	1.34(-8)	1.84(-10)	7.42(-11)	8.31(-9)
N3-T15-CR100	3.98(-9)	1.25(-8)	5.72(-9)	8.05(-7)	5.62(-7)	1.97(-11)	5.92(-10)	4.71(-8)	1.09(-10)	9.60(-11)	9.83(-9)
N3-T15-CR500	1.50(-12)	1.37(-9)	1.94(-10)	1.30(-9)	2.37(-9)	6.38(-15)	7.67(-13)	8.48(-8)	1.67(-18)	5.25(-15)	4.51(-11)
N3-T15-CR1000	6.61(-19)	5.12(-11)	1.51(-11)	4.06(-13)	9.75(-14)	1.18(-18)	1.38(-20)	1.76(-8)	1.49(-19)	1.13(-25)	1.05(-16)
N3-T20-CR1	7.22(-10)	5.29(-12)	2.25(-10)	1.11(-7)	1.49(-8)	2.48(-11)	1.92(-10)	1.60(-10)	5.26(-9)	1.07(-14)	3.85(-9)
N3-T20-CR10	5.36(-10)	5.20(-11)	1.07(-10)	2.07(-8)	5.98(-10)	6.00(-12)	3.76(-13)	2.44(-11)	2.77(-10)	1.06(-13)	7.92(-10)
N3-T20-CR50	2.12(-9)	9.24(-10)	7.56(-10)	1.06(-6)	1.02(-6)	1.34(-10)	5.01(-10)	1.17(-7)	9.04(-11)	3.82(-11)	6.73(-9)
N3-T20-CR100	5.16(-10)	1.44(-9)	5.79(-10)	5.26(-7)	8.47(-7)	4.90(-11)	2.47(-10)	2.05(-7)	7.71(-11)	3.03(-11)	4.89(-9)
N3-T20-CR500	4.14(-14)	1.96(-10)	9.81(-11)	1.21(-10)	2.16(-10)	2.14(-15)	4.57(-14)	3.30(-8)	5.26(-18)	4.03(-16)	4.48(-13)
N3-T20-CR1000	4.02(-21)	1.52(-11)	2.45(-11)	6.07(-13)	4.21(-14)	1.90(-18)	4.20(-20)	9.80(-9)	1.73(-21)	4.43(-27)	6.70(-19)

continued on next page

Table C.2: Continued.

Model	C_2H_5CN	C_2H_3CN	CH_3CN	CH_3OH	C_2H_5OH	CH_3OCHO	CH_3OCH_3	CH_3CHO	NH_2CHO	CH_3NCO	CH_3SH
N4-T10-CR1	9.43(-10)	3.59(-12)	1.11(-9)	6.76(-6)	6.49(-8)	7.19(-10)	1.38(-8)	1.26(-10)	4.34(-8)	2.21(-13)	2.59(-9)
N4-T10-CR10	1.20(-9)	3.58(-11)	5.42(-9)	2.63(-6)	2.26(-7)	9.17(-10)	1.44(-8)	1.32(-9)	1.84(-8)	2.84(-13)	3.31(-9)
N4-T10-CR50	2.54(-9)	6.05(-10)	7.44(-10)	1.39(-6)	2.73(-6)	1.06(-8)	6.97(-9)	6.41(-8)	8.42(-9)	3.20(-12)	6.30(-10)
N4-T10-CR100	3.36(-10)	5.23(-10)	1.10(-10)	5.05(-7)	1.92(-6)	7.37(-9)	5.70(-10)	7.85(-8)	6.14(-10)	2.99(-12)	4.31(-10)
N4-T10-CR500	1.55(-11)	1.10(-10)	4.84(-10)	1.86(-9)	1.09(-8)	4.95(-12)	4.23(-15)	2.60(-9)	1.19(-14)	2.91(-14)	2.77(-12)
N4-T10-CR1000	2.56(-15)	2.26(-14)	6.59(-12)	2.91(-13)	9.71(-13)	1.12(-18)	1.25(-19)	5.53(-12)	4.97(-22)	1.18(-18)	3.09(-16)
N4-T15-CR1	1.19(-9)	6.01(-12)	2.41(-9)	1.33(-6)	2.90(-8)	1.30(-11)	2.82(-9)	4.76(-11)	1.86(-9)	3.12(-15)	3.85(-9)
N4-T15-CR10	5.95(-10)	1.60(-11)	2.42(-9)	1.22(-6)	1.50(-7)	2.39(-10)	4.47(-9)	7.63(-10)	1.05(-8)	9.25(-14)	2.51(-9)
N4-T15-CR50	4.00(-9)	7.47(-10)	1.12(-9)	1.44(-6)	2.84(-6)	1.08(-8)	7.58(-9)	6.56(-8)	7.26(-9)	2.17(-12)	5.39(-10)
N4-T15-CR100	5.28(-10)	6.02(-10)	1.45(-10)	5.70(-7)	2.07(-6)	8.30(-9)	6.46(-10)	8.42(-8)	5.39(-10)	2.33(-12)	3.81(-10)
N4-T15-CR500	1.36(-11)	9.76(-11)	6.01(-10)	1.89(-9)	1.10(-8)	2.20(-12)	4.51(-15)	2.40(-9)	1.54(-14)	2.59(-14)	1.35(-12)
N4-T15-CR1000	1.50(-15)	1.59(-14)	5.53(-12)	2.30(-13)	7.38(-13)	9.82(-19)	8.18(-20)	4.78(-12)	4.65(-22)	7.55(-19)	2.51(-16)
N4-T20-CR1	6.38(-11)	1.55(-13)	3.49(-11)	7.52(-8)	1.49(-9)	1.16(-12)	6.07(-11)	1.82(-12)	2.18(-9)	7.18(-17)	1.30(-9)
N4-T20-CR10	2.34(-11)	6.10(-13)	2.04(-11)	7.87(-8)	1.86(-9)	4.45(-12)	3.58(-11)	9.40(-12)	2.62(-9)	1.64(-15)	2.32(-10)
N4-T20-CR50	1.89(-9)	2.83(-10)	5.96(-10)	6.31(-7)	1.53(-6)	4.48(-9)	1.81(-9)	3.50(-8)	1.02(-9)	8.80(-13)	4.48(-10)
N4-T20-CR100	2.48(-9)	5.90(-10)	5.07(-10)	5.20(-7)	1.65(-6)	6.68(-9)	7.56(-10)	7.03(-8)	2.72(-10)	1.86(-12)	6.45(-10)
N4-T20-CR500	4.89(-12)	3.40(-11)	4.76(-10)	5.29(-10)	3.14(-9)	6.72(-15)	5.97(-16)	5.44(-10)	5.45(-15)	3.67(-15)	1.67(-13)
N4-T20-CR1000	4.15(-16)	6.84(-15)	2.31(-12)	1.58(-13)	5.61(-13)	1.25(-18)	3.01(-20)	1.32(-12)	3.65(-22)	1.80(-19)	2.36(-16)
N5-T10-CR1	1.22(-9)	8.26(-12)	1.21(-9)	8.85(-6)	5.38(-8)	5.05(-10)	1.78(-8)	1.23(-10)	3.34(-8)	5.44(-12)	2.64(-9)
N5-T10-CR10	2.20(-9)	4.76(-11)	2.01(-9)	5.33(-6)	1.18(-7)	1.58(-9)	2.96(-9)	8.35(-10)	3.62(-8)	1.52(-13)	3.31(-9)
N5-T10-CR50	5.42(-9)	1.00(-9)	3.23(-9)	2.82(-6)	3.54(-6)	6.97(-9)	5.75(-8)	6.91(-8)	1.81(-8)	4.82(-12)	1.80(-9)
N5-T10-CR100	3.07(-9)	1.46(-9)	8.45(-10)	1.66(-6)	3.43(-6)	1.19(-8)	5.22(-9)	1.09(-7)	7.49(-9)	6.99(-12)	1.04(-9)
N5-T10-CR500	6.26(-11)	8.44(-10)	2.51(-10)	1.25(-7)	6.95(-7)	1.07(-9)	6.36(-12)	1.03(-7)	2.48(-11)	4.31(-12)	2.13(-10)
N5-T10-CR1000	5.03(-12)	4.89(-11)	1.18(-10)	1.01(-9)	4.44(-9)	1.81(-12)	2.69(-15)	2.39(-9)	2.79(-16)	1.42(-14)	1.45(-12)
N5-T15-CR1	8.53(-10)	9.57(-12)	1.73(-9)	2.62(-6)	2.87(-8)	3.29(-10)	1.86(-9)	1.40(-8)	2.74(-8)	1.17(-15)	4.90(-9)
N5-T15-CR10	1.41(-9)	2.82(-11)	1.94(-9)	2.38(-6)	1.57(-7)	2.61(-10)	1.73(-9)	5.84(-10)	1.78(-8)	7.61(-14)	3.05(-9)
N5-T15-CR50	8.37(-9)	1.18(-9)	5.58(-9)	2.56(-6)	3.41(-6)	5.88(-9)	5.53(-8)	6.47(-8)	1.56(-8)	3.70(-12)	1.71(-9)
N5-T15-CR100	4.00(-9)	1.45(-9)	1.03(-9)	1.54(-6)	3.20(-6)	1.08(-8)	5.06(-9)	1.01(-7)	6.37(-9)	4.55(-12)	1.02(-9)
N5-T15-CR500	6.29(-11)	5.69(-10)	2.39(-10)	1.04(-7)	6.12(-7)	8.52(-10)	3.81(-12)	8.60(-8)	1.85(-11)	3.53(-12)	9.43(-11)
N5-T15-CR1000	3.92(-12)	3.66(-11)	1.02(-10)	7.26(-10)	3.23(-9)	3.78(-13)	1.44(-15)	1.58(-9)	1.93(-16)	8.11(-15)	5.99(-13)
N5-T20-CR1	1.18(-10)	1.88(-13)	6.43(-11)	8.31(-8)	3.14(-9)	5.86(-12)	1.46(-10)	4.12(-12)	4.03(-9)	6.30(-17)	1.54(-9)
N5-T20-CR10	3.29(-11)	5.47(-13)	5.60(-11)	1.78(-7)	1.90(-9)	1.48(-11)	1.01(-10)	7.78(-12)	5.29(-9)	1.52(-15)	3.18(-10)
N5-T20-CR50	4.82(-9)	3.96(-10)	1.58(-9)	1.07(-6)	2.13(-6)	3.03(-9)	5.15(-9)	3.71(-8)	3.80(-9)	1.01(-12)	8.54(-10)
N5-T20-CR100	3.26(-9)	5.71(-10)	9.45(-10)	6.67(-7)	1.57(-6)	4.10(-9)	1.35(-9)	4.90(-8)	2.76(-10)	1.08(-12)	5.16(-10)
N5-T20-CR500	2.01(-11)	1.57(-10)	1.36(-10)	1.88(-8)	1.31(-7)	2.12(-12)	1.37(-13)	1.64(-8)	3.45(-12)	3.66(-13)	3.87(-12)
N5-T20-CR1000	1.99(-12)	1.87(-11)	7.24(-11)	4.31(-10)	1.95(-9)	7.55(-15)	5.14(-16)	7.73(-10)	2.02(-16)	3.50(-15)	1.27(-13)

Notes. Gas-phase fractional abundances (with respect to total hydrogen) reached at the end of the simulations (that is when the temperature reaches 400 K in the envelope of the sources). $X(Y)$ means $X\times10^{Y}$.

Table C.3: Gas-phase fractional abundances calculated at $T = 150$ K.

Model	C_2H_5CN	C_2H_3CN	CH_3CN	CH_3OH	C_2H_5OH	CH_3OCHO	CH_3OCH_3	CH_3CHO	NH_2CHO	CH_3NCO	CH_3SH
N2-T10-CR1	8.80(-10)	3.98(-11)	9.67(-10)	9.82(-6)	7.49(-8)	1.30(-9)	2.13(-8)	7.74(-9)	3.56(-8)	1.00(-11)	1.76(-9)
N2-T10-CR10	2.06(-9)	7.90(-11)	2.53(-9)	7.16(-6)	2.35(-7)	1.83(-9)	1.14(-9)	1.83(-8)	7.73(-8)	8.24(-14)	4.07(-9)
N2-T10-CR50	9.41(-9)	1.20(-9)	2.10(-8)	2.25(-6)	2.64(-6)	6.25(-10)	8.29(-8)	2.59(-8)	1.69(-8)	1.53(-12)	8.89(-9)
N2-T10-CR100	7.27(-9)	1.55(-9)	4.68(-9)	3.37(-6)	4.26(-6)	5.81(-9)	6.52(-8)	5.26(-8)	2.31(-8)	2.17(-12)	2.50(-9)
N2-T10-CR500	1.98(-9)	1.80(-9)	3.37(-10)	1.63(-6)	4.86(-6)	1.42(-8)	5.50(-10)	1.80(-7)	1.96(-9)	6.77(-12)	8.94(-10)
N2-T10-CR1000	1.30(-10)	5.72(-10)	5.34(-11)	3.64(-7)	1.96(-6)	2.16(-9)	1.30(-11)	1.30(-7)	5.71(-10)	4.39(-12)	6.06(-10)
N2-T15-CR1	8.17(-10)	8.57(-12)	1.46(-9)	3.38(-6)	3.19(-8)	6.53(-10)	1.43(-9)	7.09(-9)	3.85(-8)	3.38(-15)	3.08(-9)
N2-T15-CR10	1.48(-9)	1.64(-11)	1.25(-9)	3.34(-6)	1.54(-7)	5.67(-10)	7.88(-10)	3.49(-10)	4.26(-8)	5.56(-14)	2.98(-9)
N2-T15-CR50	1.72(-8)	1.61(-9)	3.42(-8)	1.70(-6)	1.91(-6)	3.55(-10)	5.44(-8)	1.86(-8)	1.33(-8)	3.83(-13)	1.07(-8)
N2-T15-CR100	7.68(-9)	1.35(-9)	7.30(-9)	2.58(-6)	3.55(-6)	3.68(-9)	6.01(-8)	4.27(-8)	1.62(-8)	1.24(-12)	3.39(-9)
N2-T15-CR500	1.67(-9)	1.52(-9)	2.52(-10)	1.45(-6)	4.63(-6)	1.35(-8)	4.78(-10)	1.67(-7)	7.42(-10)	5.44(-12)	1.06(-9)
N2-T15-CR1000	1.09(-10)	2.50(-10)	6.20(-11)	2.31(-7)	1.53(-6)	1.33(-9)	3.75(-12)	9.09(-8)	3.86(-10)	2.95(-12)	1.18(-10)
N2-T20-CR1	1.74(-10)	1.19(-13)	9.91(-11)	1.43(-7)	5.98(-9)	2.53(-11)	2.88(-10)	6.03(-12)	6.97(-9)	1.46(-16)	1.89(-9)
N2-T20-CR10	2.68(-11)	1.54(-13)	1.06(-10)	3.16(-7)	2.44(-9)	1.23(-10)	2.14(-10)	5.63(-12)	1.56(-8)	6.89(-16)	3.31(-10)
N2-T20-CR50	6.92(-9)	1.88(-10)	2.76(-9)	1.18(-6)	2.38(-6)	1.71(-9)	1.02(-8)	1.54(-8)	1.45(-8)	2.06(-13)	1.02(-9)
N2-T20-CR100	9.08(-9)	3.28(-10)	3.40(-9)	9.71(-7)	1.95(-6)	2.24(-9)	4.33(-9)	2.05(-8)	1.13(-9)	3.35(-13)	6.63(-10)
N2-T20-CR500	5.12(-10)	8.96(-11)	5.97(-11)	1.44(-7)	8.69(-7)	1.58(-10)	9.54(-12)	2.72(-8)	1.24(-10)	6.06(-13)	2.55(-11)
N2-T20-CR1000	3.27(-11)	4.60(-11)	5.94(-11)	3.73(-8)	3.50(-7)	1.29(-12)	9.37(-14)	1.76(-8)	1.62(-10)	3.16(-13)	4.76(-12)
N3-T10-CR1	3.90(-9)	7.00(-10)	2.68(-9)	8.68(-6)	4.83(-8)	7.61(-8)	7.69(-9)	8.52(-11)	1.01(-7)	6.74(-10)	1.68(-9)
N3-T10-CR10	3.97(-8)	1.69(-9)	1.51(-9)	8.70(-6)	1.61(-7)	2.67(-9)	7.47(-9)	8.48(-10)	8.62(-9)	1.66(-12)	1.13(-9)
N3-T10-CR50	3.99(-8)	8.84(-9)	1.89(-9)	4.63(-6)	4.48(-7)	1.04(-9)	3.60(-9)	6.93(-9)	5.86(-10)	2.30(-11)	4.10(-9)
N3-T10-CR100	5.20(-9)	2.90(-9)	5.67(-10)	1.88(-6)	9.28(-7)	5.03(-11)	9.43(-10)	6.62(-8)	4.37(-10)	4.91(-11)	1.10(-8)
N3-T10-CR500	5.59(-12)	2.52(-9)	1.65(-10)	7.04(-8)	1.68(-7)	3.47(-13)	1.77(-11)	1.35(-7)	1.29(-11)	1.75(-13)	9.67(-10)
N3-T10-CR1000	1.05(-13)	2.89(-10)	2.05(-11)	7.86(-11)	1.19(-10)	1.34(-16)	1.22(-15)	3.03(-8)	1.24(-13)	3.41(-17)	2.07(-12)
N3-T15-CR1	4.79(-9)	9.56(-10)	2.33(-9)	7.16(-6)	2.39(-8)	8.35(-10)	1.06(-9)	4.14(-9)	1.43(-8)	3.85(-10)	1.95(-9)
N3-T15-CR10	3.52(-8)	1.22(-9)	2.14(-9)	8.57(-6)	1.06(-7)	1.90(-9)	6.45(-9)	7.91(-10)	2.99(-8)	9.81(-13)	1.60(-9)
N3-T15-CR50	3.77(-8)	1.27(-8)	2.20(-9)	3.42(-6)	5.95(-7)	1.66(-10)	1.63(-9)	1.33(-8)	4.13(-10)	2.97(-11)	9.68(-9)
N3-T15-CR100	6.03(-9)	3.67(-9)	6.88(-10)	1.23(-6)	8.90(-7)	2.73(-11)	3.86(-10)	6.48(-8)	6.17(-10)	4.11(-11)	1.35(-8)
N3-T15-CR500	4.40(-12)	2.33(-9)	1.34(-10)	5.19(-8)	1.40(-7)	1.94(-13)	1.20(-11)	1.27(-7)	6.63(-12)	1.27(-13)	9.25(-10)
N3-T15-CR1000	5.61(-14)	1.19(-10)	1.30(-11)	3.66(-11)	3.95(-11)	4.71(-17)	2.48(-16)	2.06(-8)	5.85(-14)	6.98(-18)	7.19(-13)
N3-T20-CR1	7.30(-10)	2.89(-12)	2.26(-10)	1.12(-7)	1.49(-8)	2.50(-11)	1.92(-10)	1.43(-10)	5.39(-9)	3.48(-15)	3.87(-9)
N3-T20-CR10	6.19(-10)	3.15(-11)	1.12(-10)	2.22(-8)	6.45(-10)	6.38(-12)	2.93(-13)	1.39(-11)	3.82(-10)	3.15(-14)	8.39(-10)
N3-T20-CR50	3.06(-9)	3.30(-10)	6.34(-10)	1.31(-6)	1.29(-6)	1.57(-10)	2.74(-10)	6.72(-8)	2.05(-10)	1.20(-11)	7.90(-9)
N3-T20-CR100	1.04(-9)	4.85(-10)	1.26(-10)	8.04(-7)	1.38(-6)	6.97(-11)	1.67(-10)	1.35(-7)	4.69(-10)	1.20(-11)	6.88(-9)
N3-T20-CR500	5.04(-12)	7.66(-10)	8.39(-11)	1.90(-8)	5.56(-8)	2.91(-13)	2.26(-12)	5.85(-8)	1.60(-11)	4.67(-14)	3.12(-11)
N3-T20-CR1000	1.29(-13)	3.80(-11)	3.43(-12)	1.90(-11)	1.68(-11)	3.86(-17)	7.01(-17)	1.37(-8)	1.54(-13)	1.80(-18)	4.36(-14)

continued on next page

Table C.3: Continued.

Model	C_2H_5CN	C_2H_3CN	CH_3CN	CH_3OH	C_2H_5OH	CH_3OCHO	CH_3OCH_3	CH_3CHO	NH_2CHO	CH_3NCO	CH_3SH
N4-T10-CR1	9.46(-10)	2.44(-12)	1.11(-9)	6.78(-6)	6.50(-8)	7.20(-10)	1.36(-8)	1.11(-10)	4.38(-8)	2.21(-13)	2.59(-9)
N4-T10-CR10	1.25(-9)	1.72(-11)	5.53(-9)	2.68(-6)	2.31(-7)	9.33(-10)	1.45(-8)	8.44(-10)	2.02(-8)	1.45(-13)	3.37(-9)
N4-T10-CR50	2.90(-9)	3.60(-10)	7.61(-10)	1.49(-6)	2.95(-6)	1.12(-8)	7.26(-9)	3.88(-8)	1.14(-8)	1.34(-12)	6.65(-10)
N4-T10-CR100	4.61(-10)	2.69(-10)	7.95(-11)	5.88(-7)	2.30(-6)	8.53(-9)	6.24(-10)	4.79(-8)	1.32(-9)	1.30(-12)	4.93(-10)
N4-T10-CR500	6.74(-11)	6.80(-11)	1.32(-9)	5.05(-9)	4.76(-8)	1.81(-11)	6.80(-15)	3.35(-9)	9.70(-12)	3.97(-14)	8.61(-12)
N4-T10-CR1000	1.33(-13)	6.91(-13)	2.74(-10)	5.24(-12)	5.89(-11)	2.89(-17)	2.27(-18)	1.32(-11)	1.93(-14)	2.42(-17)	3.41(-15)
N4-T15-CR1	1.20(-9)	4.30(-12)	2.41(-9)	1.33(-6)	2.91(-8)	1.30(-11)	2.81(-9)	3.76(-11)	1.88(-9)	2.74(-15)	3.86(-9)
N4-T15-CR10	6.17(-10)	8.11(-12)	2.47(-9)	1.25(-6)	1.53(-7)	2.43(-10)	4.50(-9)	4.71(-10)	1.15(-8)	4.14(-14)	2.55(-9)
N4-T15-CR50	4.52(-9)	4.54(-10)	1.15(-9)	1.53(-6)	3.05(-6)	1.14(-8)	7.88(-9)	3.95(-8)	9.56(-9)	8.65(-13)	5.67(-10)
N4-T15-CR100	7.02(-10)	3.25(-10)	1.16(-10)	6.54(-7)	2.44(-6)	9.43(-9)	6.99(-10)	5.07(-8)	1.06(-9)	9.62(-13)	4.30(-10)
N4-T15-CR500	4.32(-11)	4.76(-11)	1.75(-9)	5.02(-9)	4.57(-8)	7.73(-12)	7.25(-15)	3.03(-9)	9.92(-12)	3.30(-14)	3.85(-12)
N4-T15-CR1000	1.38(-13)	6.04(-13)	2.15(-10)	3.88(-12)	4.19(-11)	2.49(-17)	1.41(-18)	1.07(-11)	1.79(-14)	1.41(-17)	2.70(-15)
N4-T20-CR1	6.40(-11)	8.50(-14)	3.49(-11)	7.53(-8)	1.50(-9)	1.16(-12)	6.08(-11)	1.33(-12)	2.20(-9)	6.10(-17)	1.30(-9)
N4-T20-CR10	2.42(-11)	3.79(-13)	2.06(-11)	8.00(-8)	1.89(-9)	4.52(-12)	3.61(-11)	5.92(-12)	2.83(-9)	6.75(-16)	2.35(-10)
N4-T20-CR50	2.15(-9)	1.53(-10)	6.19(-10)	6.74(-7)	1.65(-6)	4.73(-9)	1.89(-9)	2.11(-8)	1.36(-9)	3.35(-13)	4.73(-10)
N4-T20-CR100	3.16(-9)	2.52(-10)	4.42(-10)	5.87(-7)	1.91(-6)	7.43(-9)	8.16(-10)	4.10(-8)	4.79(-10)	7.17(-13)	7.15(-10)
N4-T20-CR500	1.66(-11)	1.64(-11)	1.54(-9)	1.38(-9)	1.35(-8)	2.42(-14)	1.13(-15)	7.41(-10)	3.93(-12)	4.47(-15)	3.51(-13)
N4-T20-CR1000	1.79(-13)	3.98(-13)	8.82(-11)	2.73(-12)	2.79(-11)	4.11(-17)	4.70(-19)	3.76(-12)	9.46(-15)	2.44(-18)	3.34(-15)
N5-T10-CR1	1.22(-9)	7.31(-12)	1.20(-9)	8.87(-6)	5.39(-8)	5.04(-10)	1.76(-8)	1.11(-10)	3.35(-8)	5.45(-12)	2.64(-9)
N5-T10-CR10	2.26(-9)	2.47(-11)	2.04(-9)	5.42(-6)	1.20(-7)	1.60(-9)	2.34(-9)	6.56(-10)	3.87(-8)	8.97(-14)	3.35(-9)
N5-T10-CR50	5.89(-9)	7.19(-10)	3.36(-9)	2.95(-6)	3.72(-6)	7.22(-9)	5.92(-8)	3.96(-8)	2.19(-8)	1.81(-12)	1.86(-9)
N5-T10-CR100	3.70(-9)	9.09(-10)	8.58(-10)	1.83(-6)	3.82(-6)	1.28(-8)	5.47(-9)	6.04(-8)	1.14(-8)	2.52(-12)	1.12(-9)
N5-T10-CR500	1.38(-10)	2.72(-10)	3.87(-11)	2.12(-7)	1.41(-6)	1.88(-9)	4.68(-12)	7.97(-8)	4.74(-10)	2.42(-12)	3.56(-10)
N5-T10-CR1000	4.49(-11)	6.71(-11)	1.53(-10)	5.94(-9)	4.60(-8)	1.43(-11)	6.67(-15)	4.36(-9)	1.04(-11)	4.14(-14)	8.79(-12)
N5-T15-CR1	8.55(-10)	8.83(-12)	1.73(-9)	2.63(-6)	2.87(-8)	3.29(-10)	1.83(-9)	1.40(-8)	2.76(-8)	8.52(-16)	4.91(-9)
N5-T15-CR10	1.45(-9)	1.45(-11)	1.97(-9)	2.41(-6)	1.59(-7)	2.64(-10)	1.62(-9)	3.51(-10)	1.89(-8)	3.85(-14)	3.09(-9)
N5-T15-CR50	9.05(-9)	8.43(-10)	5.82(-9)	2.67(-6)	3.57(-6)	6.08(-9)	5.69(-8)	3.69(-8)	1.86(-8)	1.30(-12)	1.77(-9)
N5-T15-CR100	4.74(-9)	9.08(-10)	1.05(-9)	1.69(-6)	3.55(-6)	1.17(-8)	5.30(-9)	5.54(-8)	9.43(-9)	1.57(-12)	1.10(-9)
N5-T15-CR500	1.48(-10)	1.73(-10)	4.84(-11)	1.75(-7)	1.25(-6)	1.51(-9)	2.21(-12)	6.57(-8)	3.65(-10)	1.97(-12)	1.59(-10)
N5-T15-CR1000	2.54(-11)	4.44(-11)	2.46(-10)	4.23(-9)	3.41(-8)	3.04(-12)	3.72(-15)	3.04(-9)	7.85(-12)	2.37(-14)	3.36(-12)
N5-T20-CR1	1.18(-10)	1.00(-13)	6.44(-11)	8.32(-8)	3.14(-9)	5.86(-12)	1.46(-10)	3.16(-12)	4.05(-9)	4.89(-17)	1.54(-9)
N5-T20-CR10	3.37(-11)	3.19(-13)	5.65(-11)	1.80(-7)	1.93(-9)	1.49(-11)	1.02(-10)	4.90(-12)	5.58(-9)	5.33(-16)	3.22(-10)
N5-T20-CR50	5.20(-9)	2.39(-10)	1.64(-9)	1.11(-6)	2.23(-6)	3.13(-9)	5.29(-9)	2.10(-8)	4.51(-9)	3.16(-13)	8.82(-10)
N5-T20-CR100	3.89(-9)	2.86(-10)	9.94(-10)	7.32(-7)	1.75(-6)	4.43(-9)	1.43(-9)	2.66(-8)	4.15(-10)	3.34(-13)	5.56(-10)
N5-T20-CR500	3.59(-11)	3.43(-11)	1.06(-10)	3.14(-8)	2.98(-7)	4.20(-12)	6.57(-14)	1.33(-8)	1.15(-10)	2.05(-13)	6.90(-12)
N5-T20-CR1000	1.32(-11)	2.01(-11)	4.02(-10)	2.42(-9)	2.03(-8)	5.99(-14)	1.40(-15)	1.53(-9)	6.73(-12)	8.53(-15)	4.77(-13)

Notes. Gas-phase fractional abundances (with respect to total hydrogen) obtained when the temperature reaches 150 K in the envelopes of the sources (gas and dust temperatures are assumed to be well coupled). $X(Y)$ means $X\times10^{Y}$.

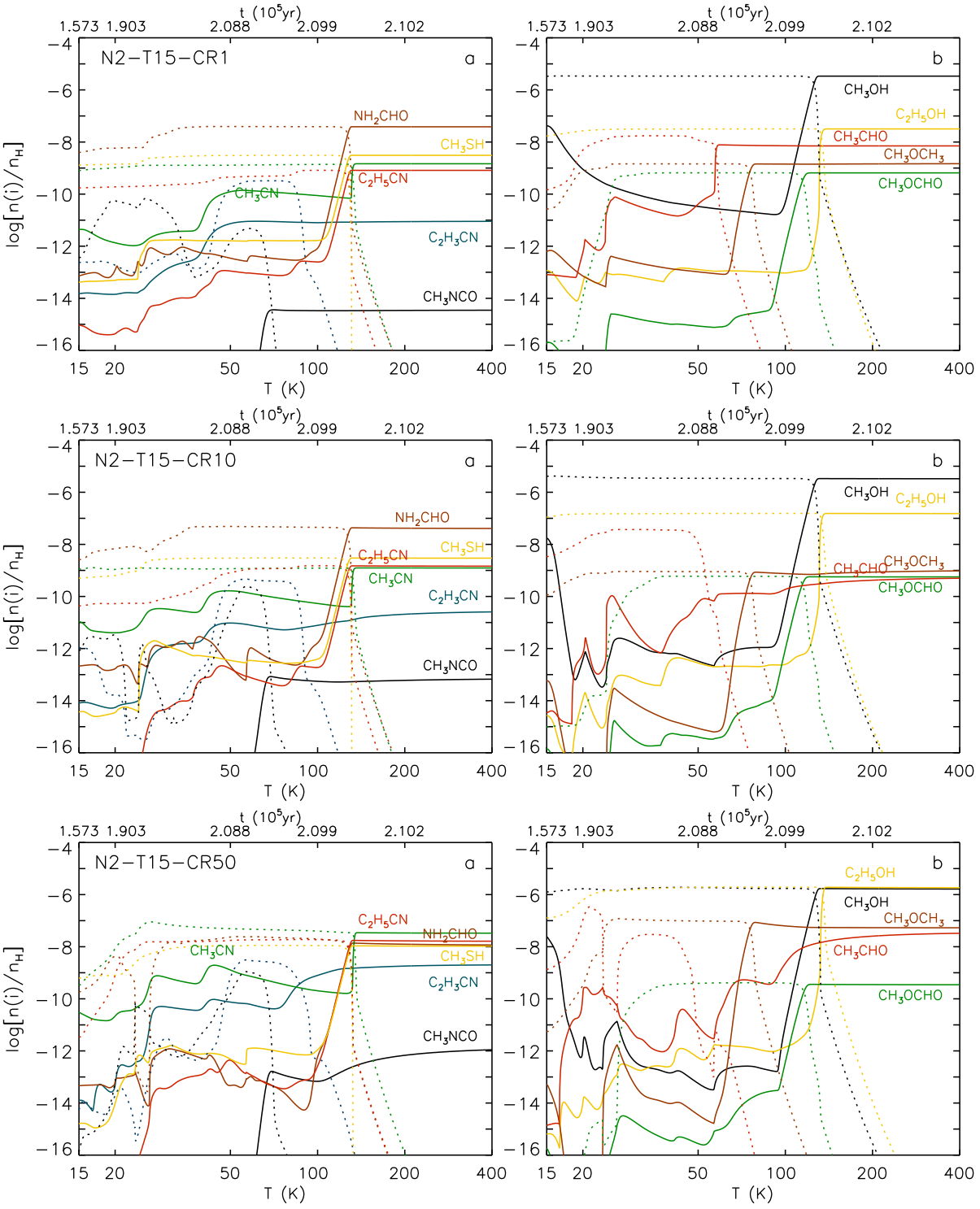

Figure C.1: Fractional abundances of 11 COMs calculated by the chemical model, plotted as a function of the temperature in the envelope of the sources during the free-fall collapse phase (gas and dust temperatures are assumed to be well coupled). In each panel a timescale is also shown on top. The solid lines show the fractional abundances (with respect to total hydrogen) in the gas phase while the dotted lines show the abundances of the same species on the grains (ice surface+mantle). Each row shows the results of models N2-T15 with different CRIR values, as indicated on the top left corner of panel **a**.

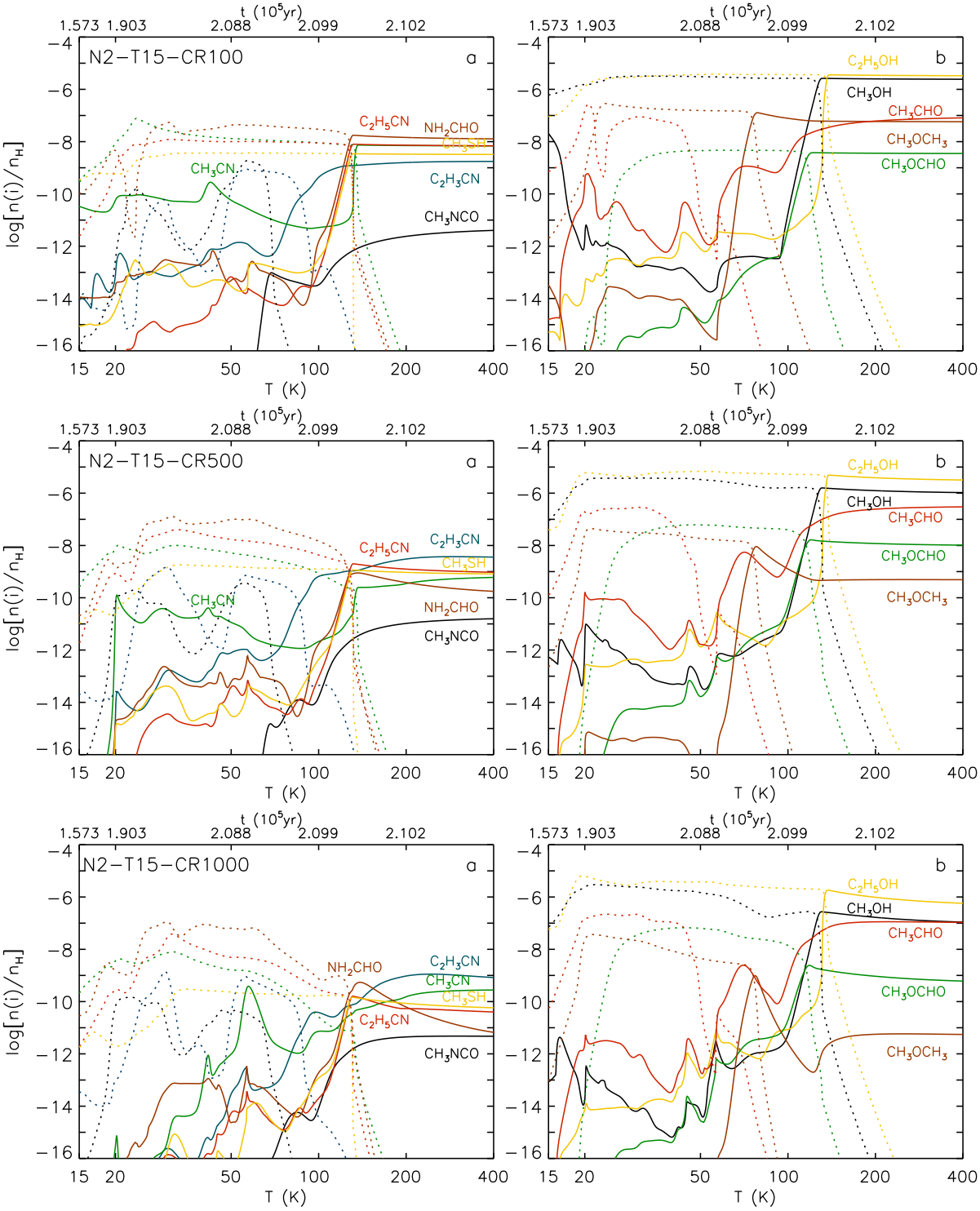

Figure C.1: Continued.

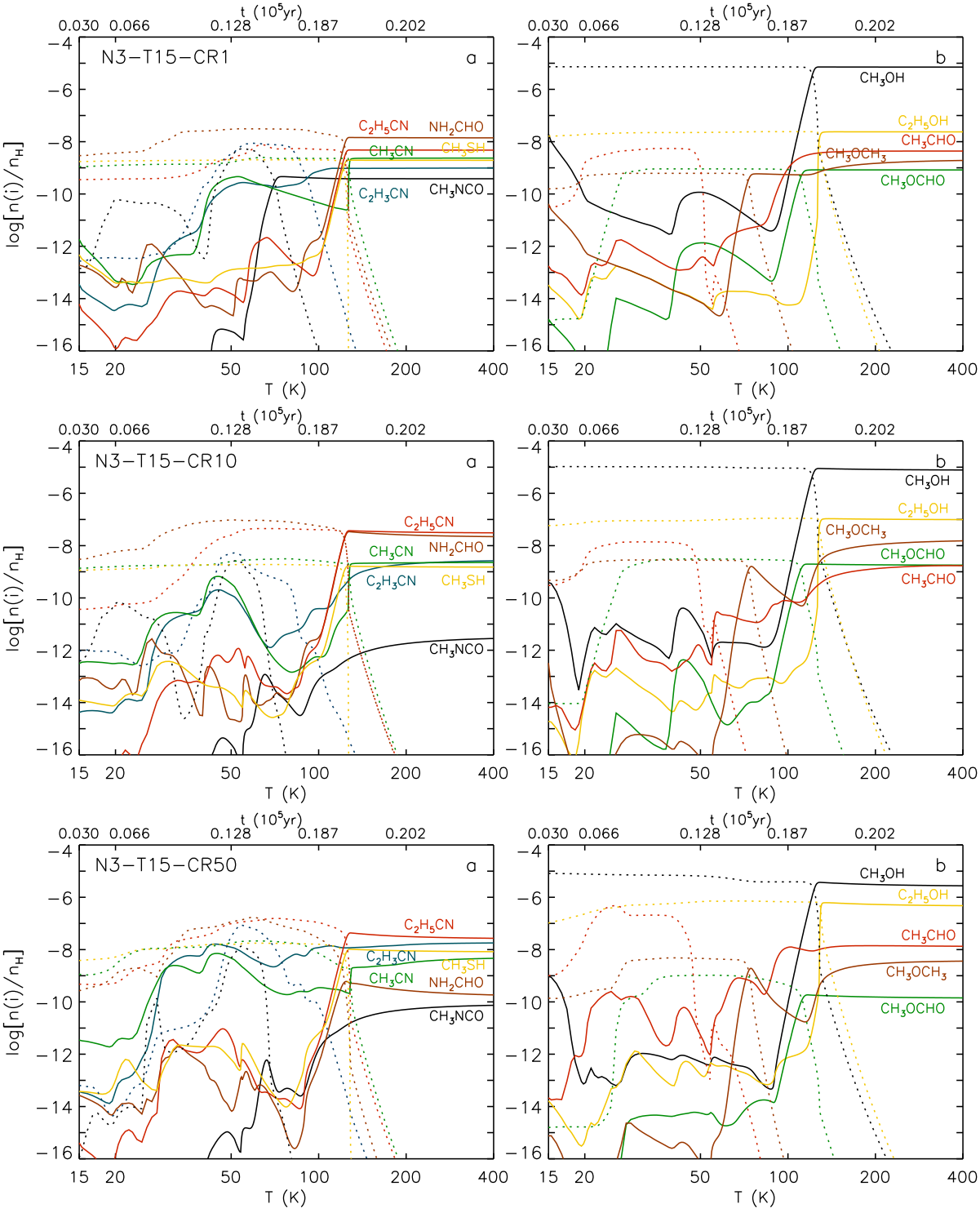

Figure C.2: Same as C.1 but for models N3-T15.

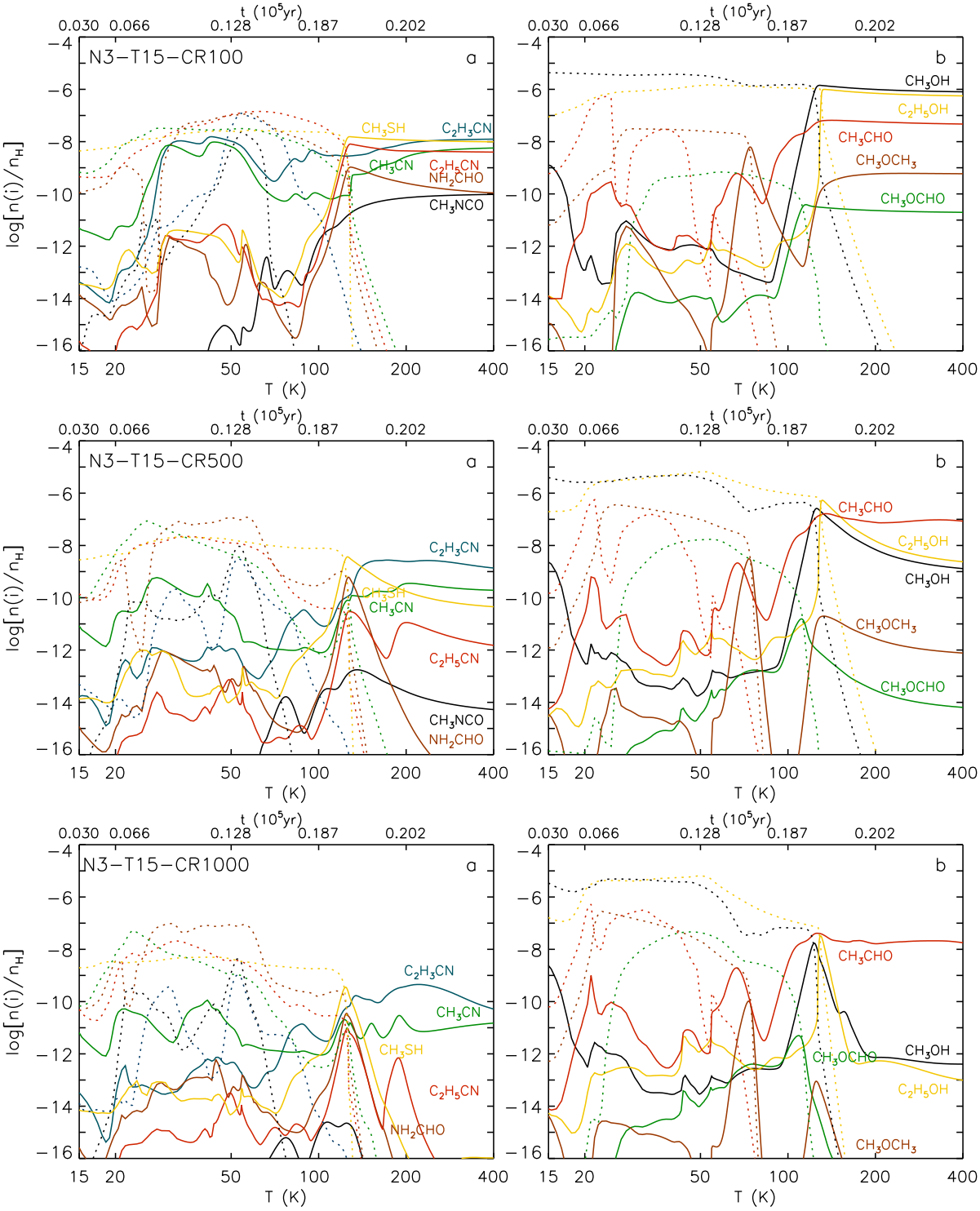

Figure C.2: Continued.

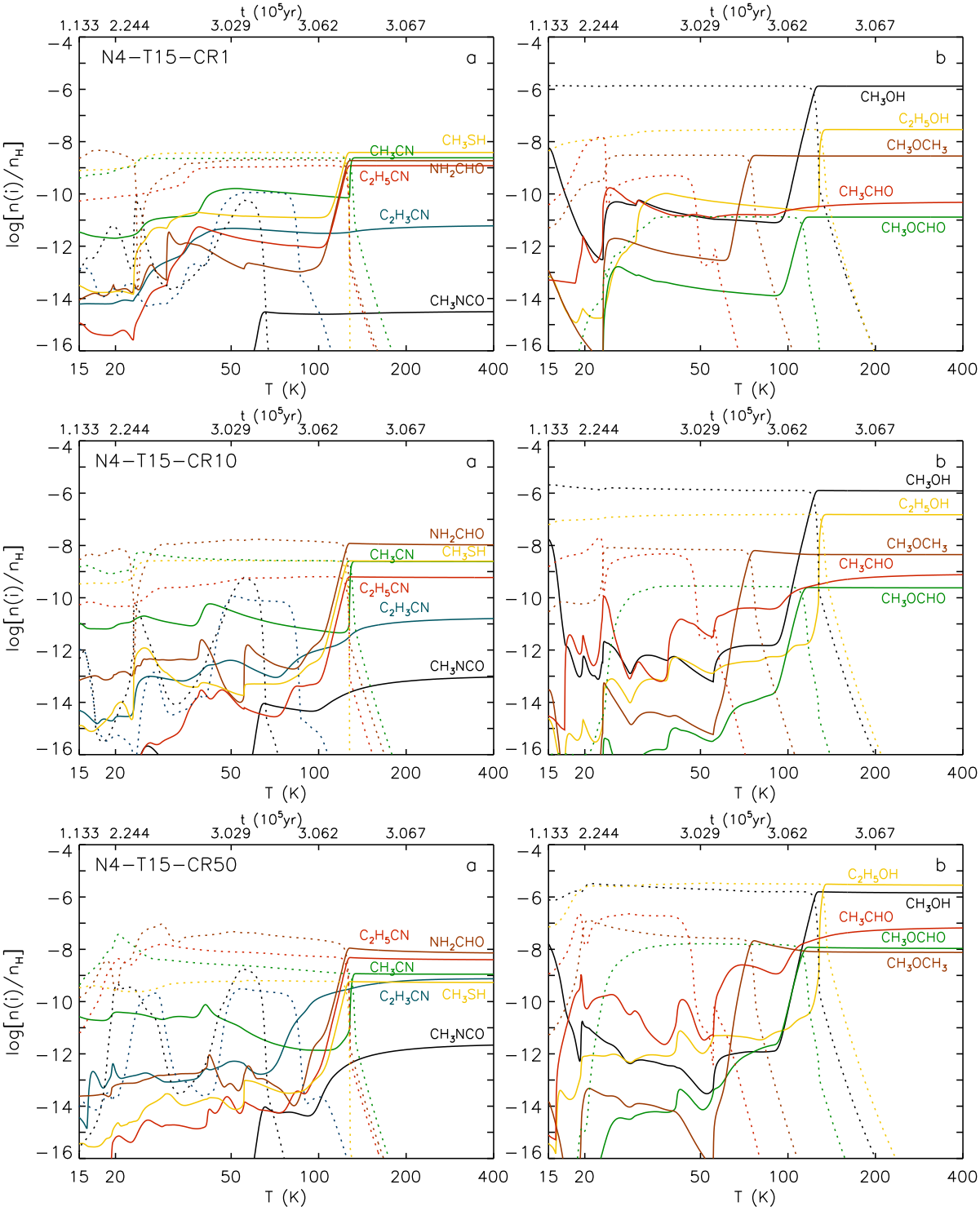

Figure C.3: Same as C.1 but for models N4-T15.

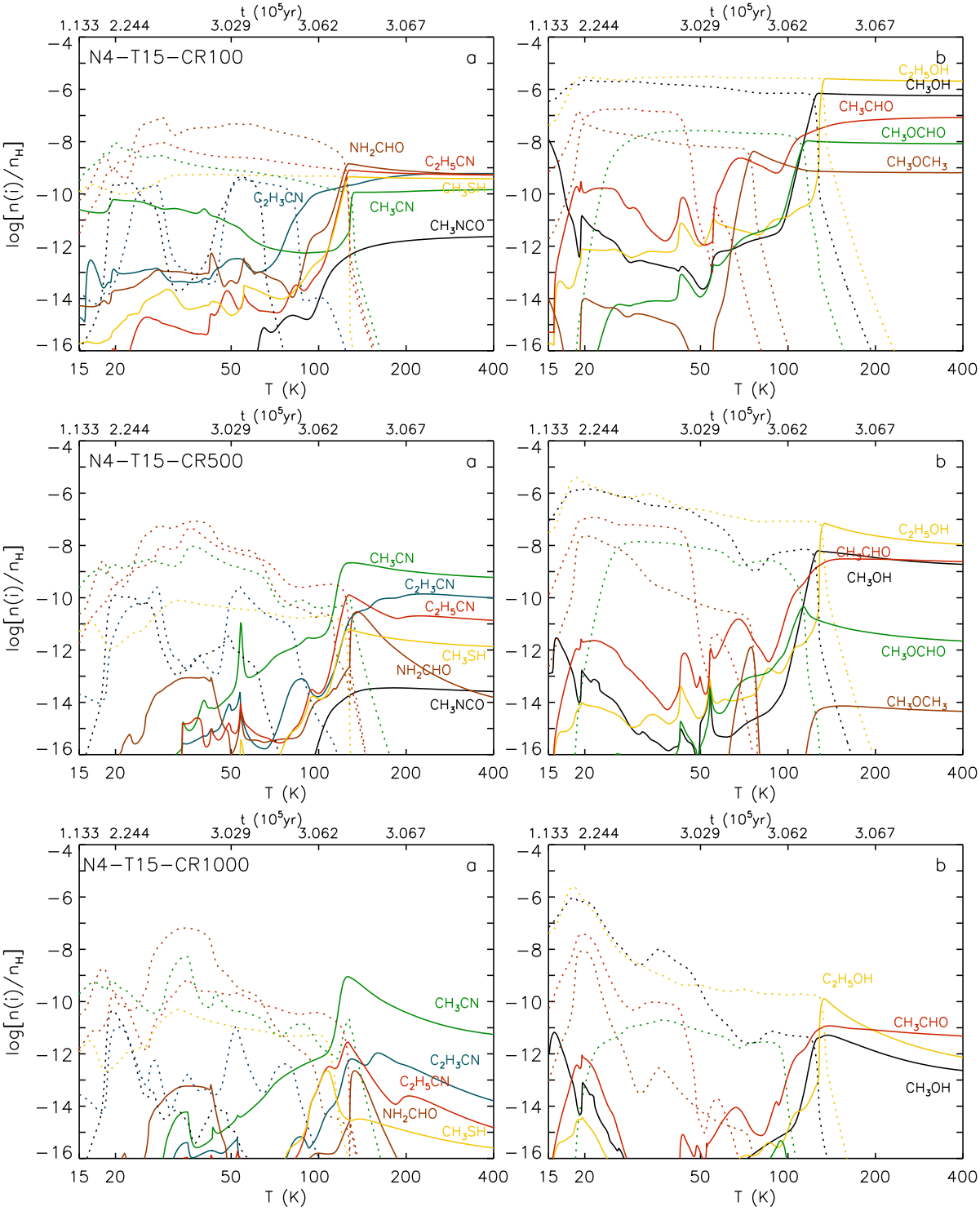

Figure C.3: Continued.

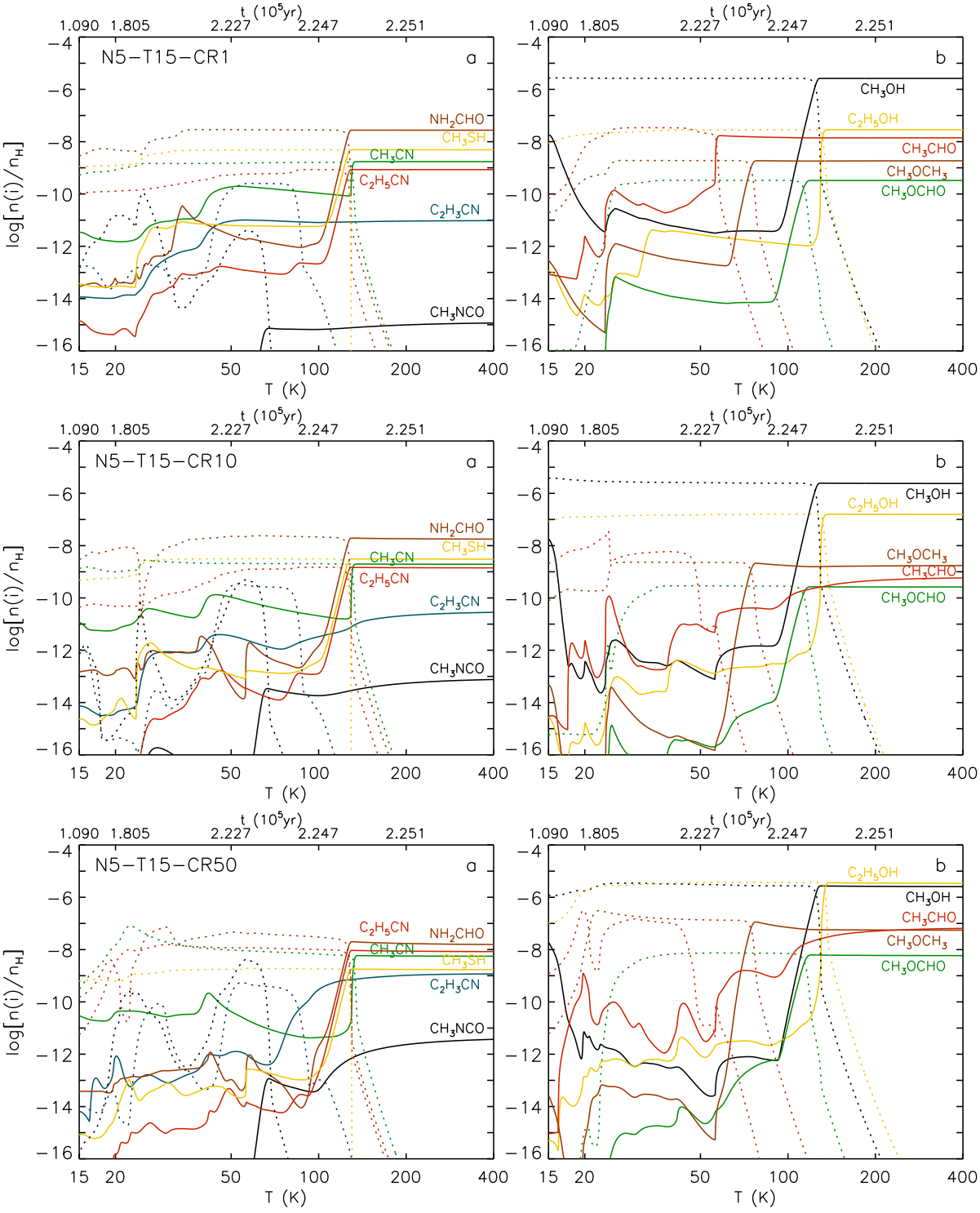

Figure C.4: Same as C.1 but for models N5-T15.

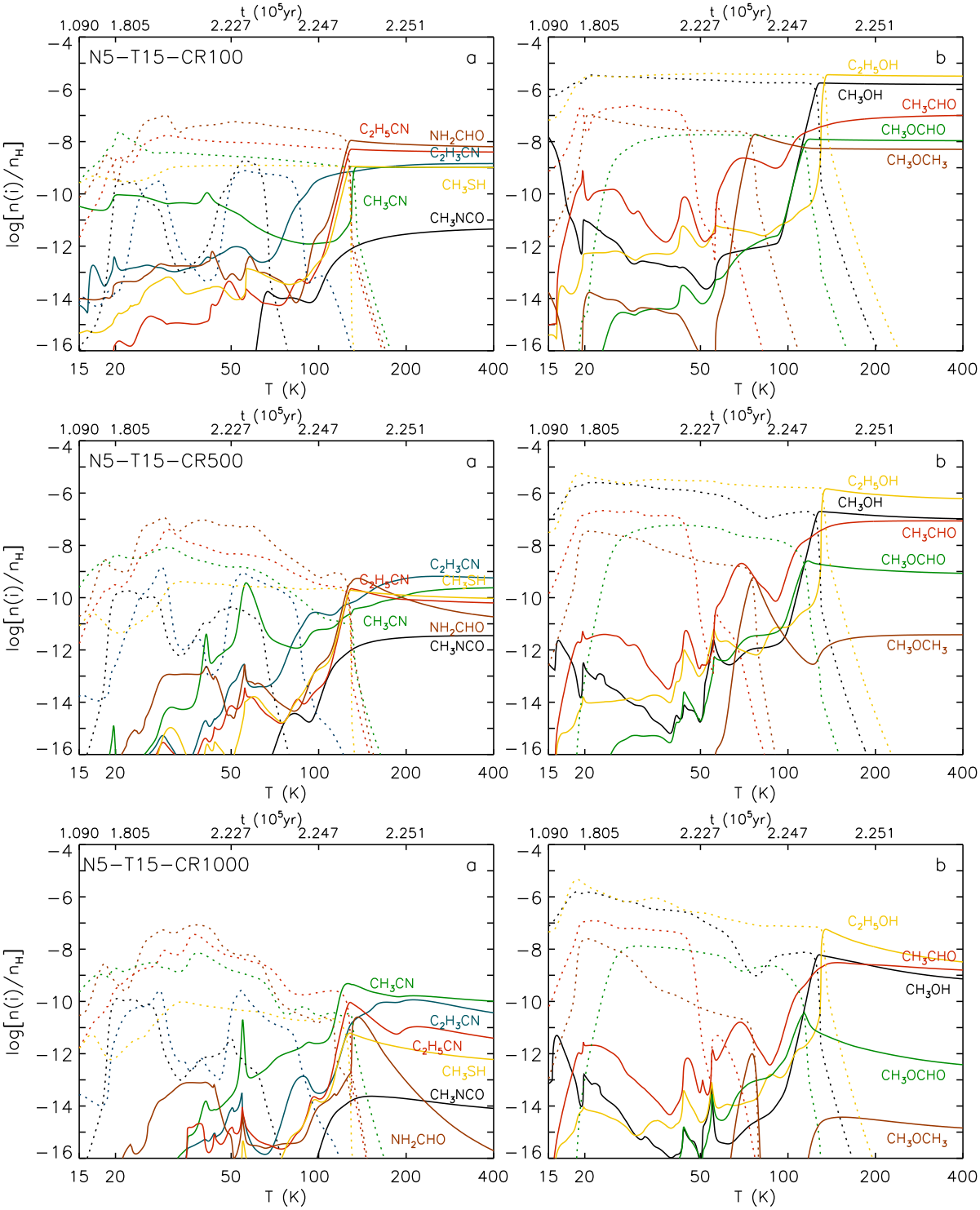

Figure C.4: Continued.

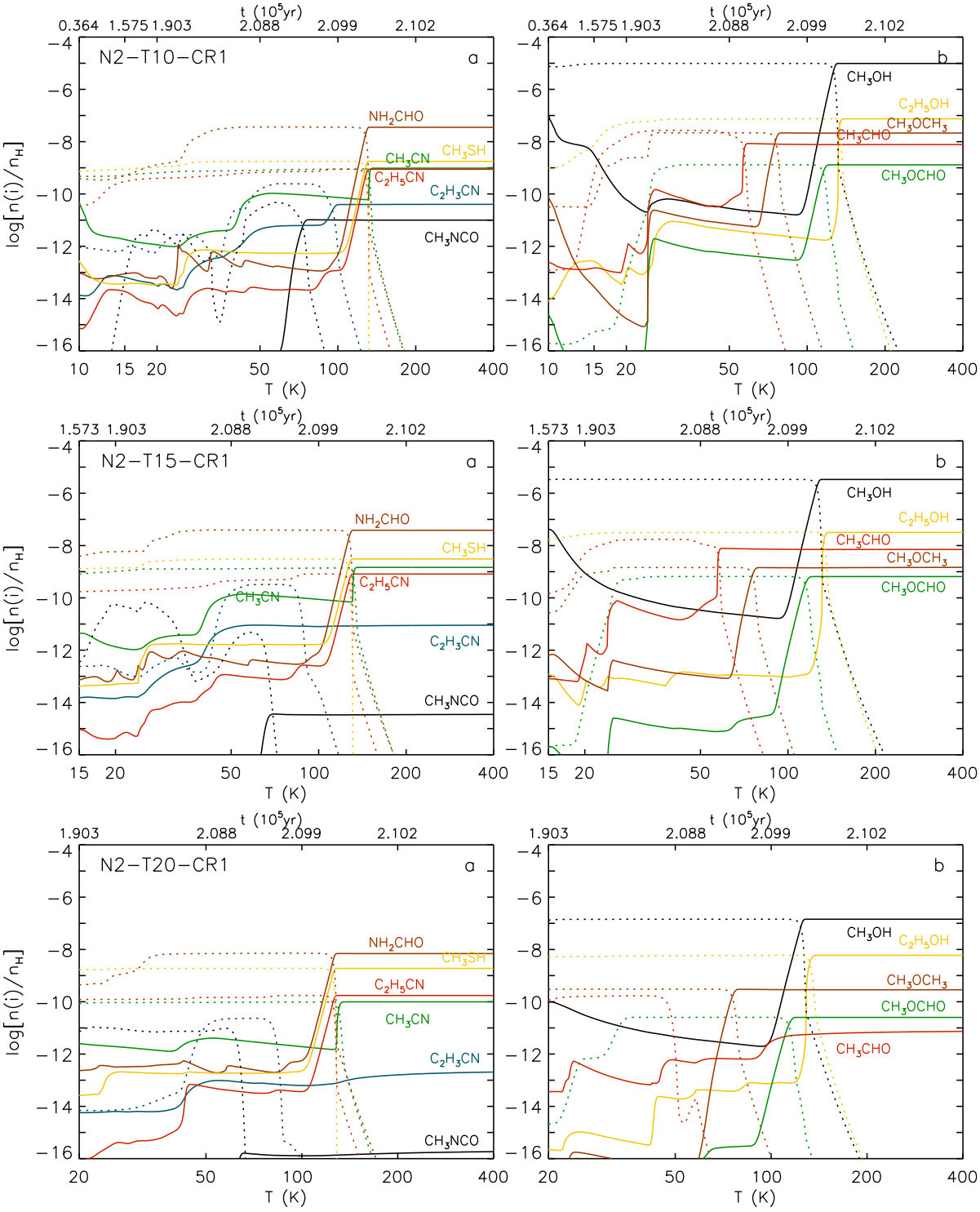

Figure C.5: Same as Fig. C.1 but for models N2-CR1 with different minimum dust temperatures $T_{\rm min}$.

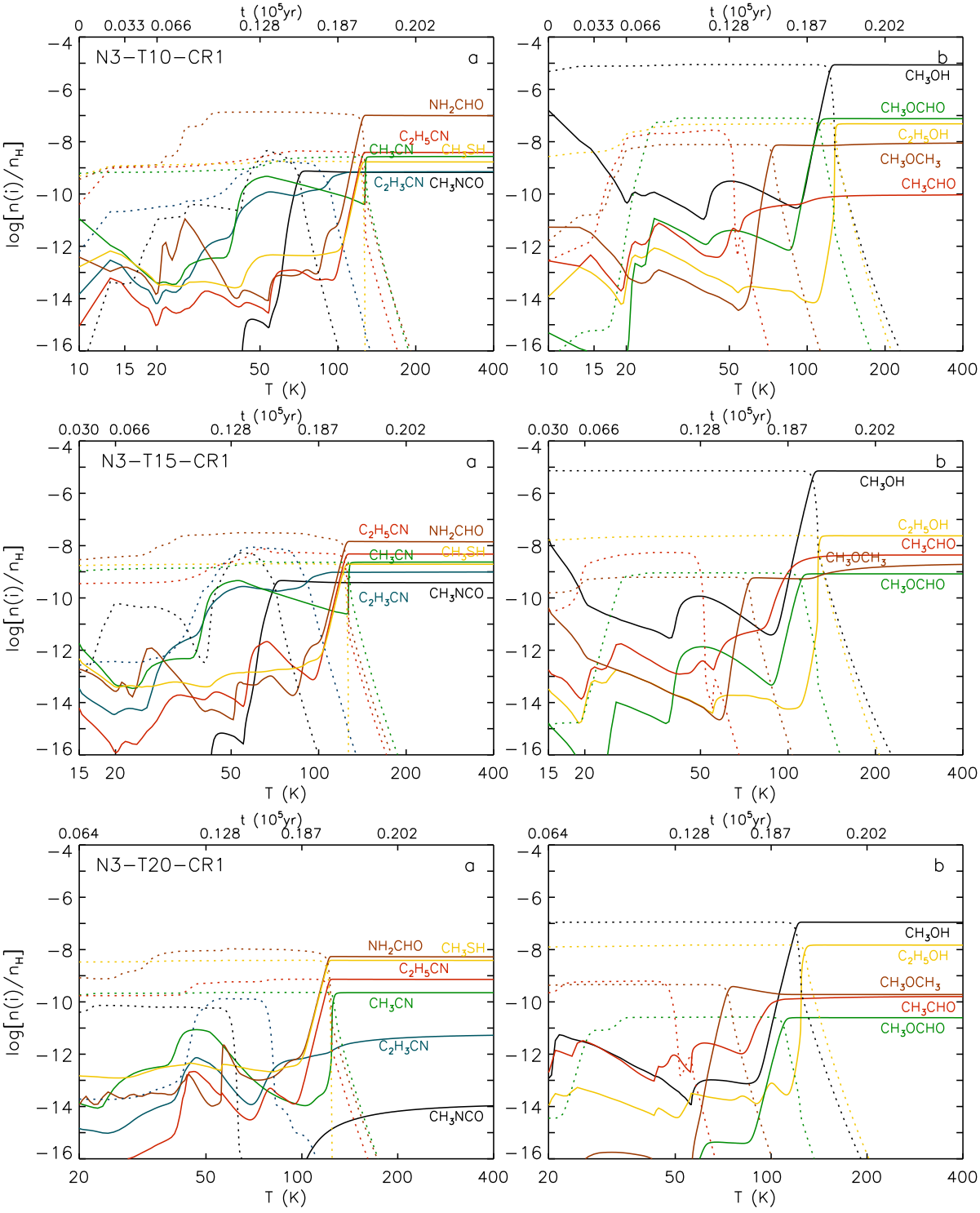

Figure C.6: Same as Fig. C.5 but for N3-CR1.

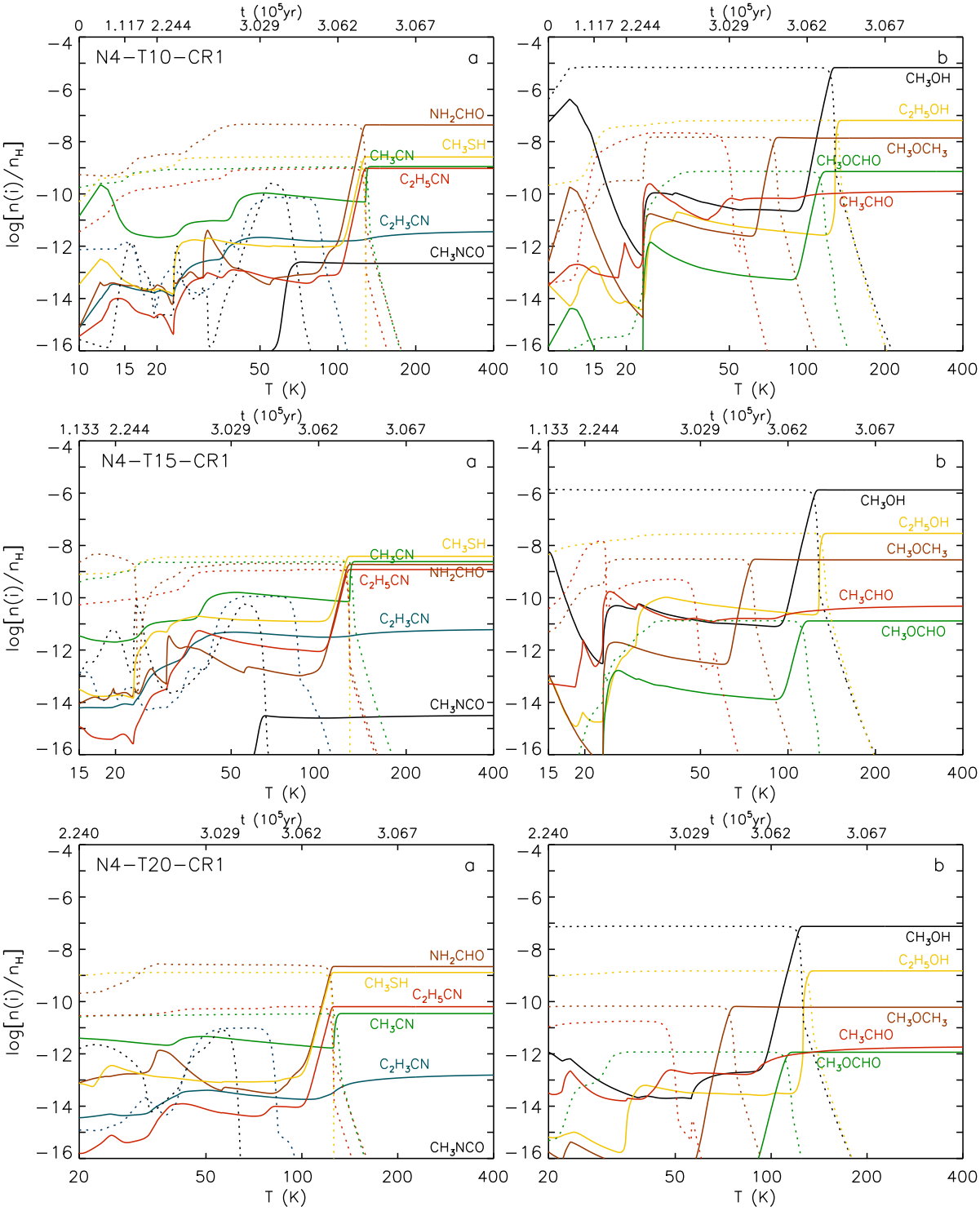

Figure C.7: Same as Fig. C.5 but for N4-CR1.

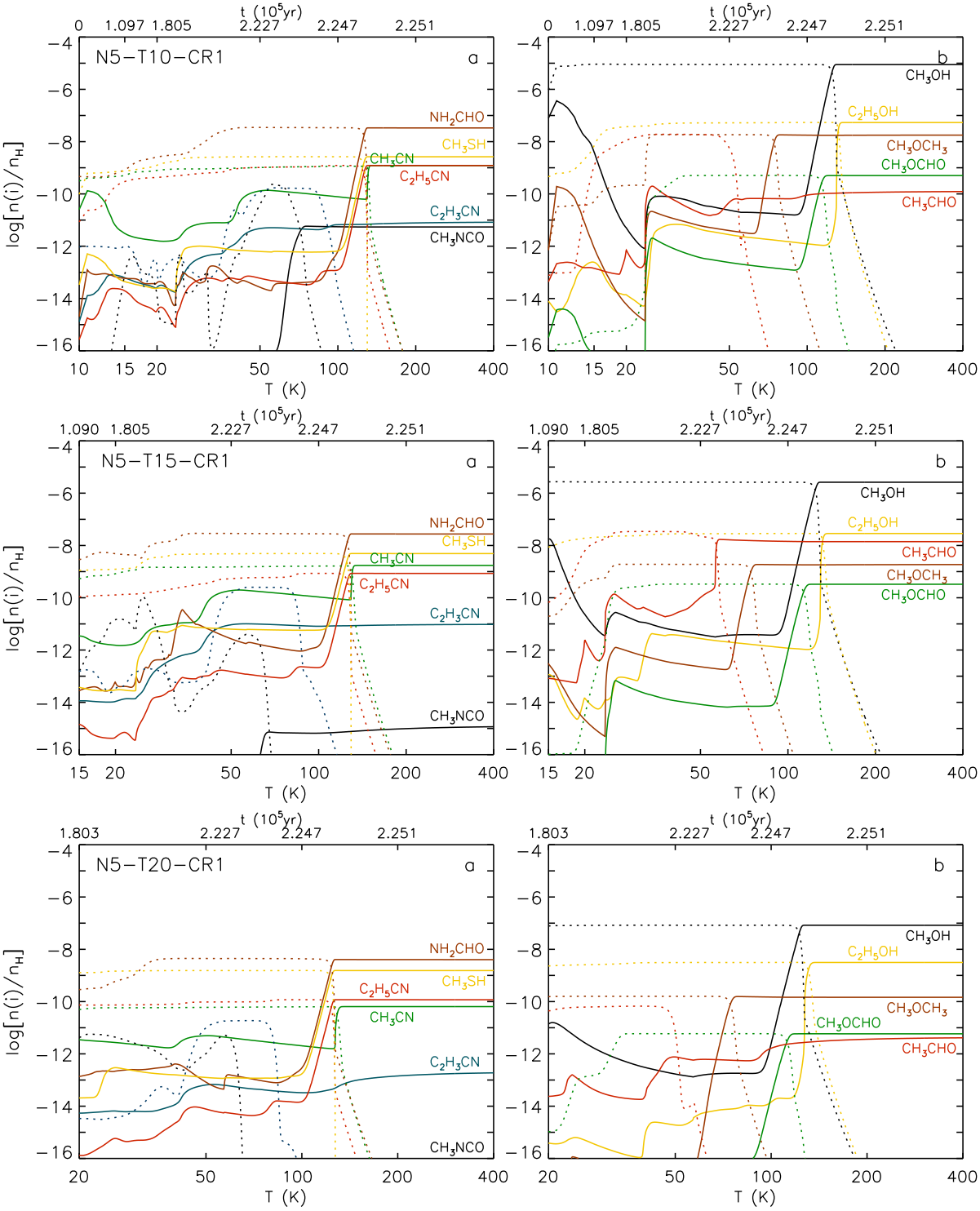

Figure C.8: Same as Fig. C.5 but for N5-CR1.

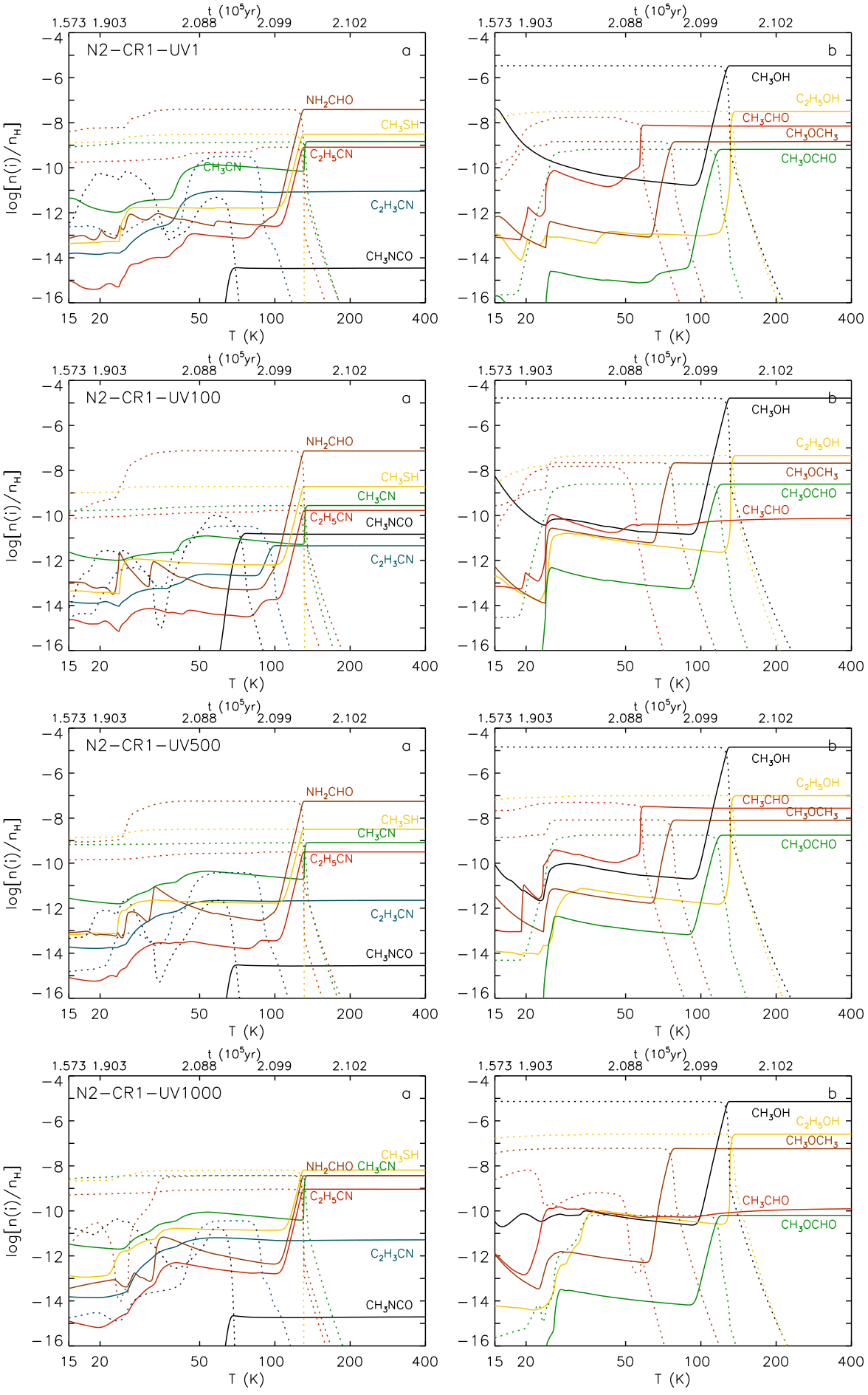

Figure C.9: Same as Fig. C.1 but for models N2-CR1 with different values of the ISRF strength χ_{uv} .

Appendix D

Appendix to Chapter 6

Contents

D.1 Confidence levels of the models with the observations

Appendix to Sect. 6.3.

Table D.1: Mean confidence level (%) of the chemical models with respect to H_2.

Model	10 COMs[a]					O-bearing species[b]					Cyanides[c]				
	N2	N3	N4*	N5	All	N2	N3	N4*	N5	All	N2	N3	N4	N5	All
T10–CR1	18.8	25.3	35.2	27.8	26.8	29.9	35.8	26.4	36.4	32.1	0.2	7.9	34.8	7.0	12.5
T10–CR10	23.5	34.6	46.1	27.9	33.0	36.2	43.4	34.3	33.3	36.8	0.7	25.0	58.5	11.6	23.9
T10–CR50	24.0	36.4	48.2	39.9	37.1	31.8	36.8	32.0	46.3	36.7	6.7	38.2	74.8	30.3	37.5
T10–CR100	23.6	31.6	37.0	36.4	32.1	35.8	36.4	29.7	44.9	36.7	3.5	14.9	45.0	24.4	21.9
T10–CR500	19.1	21.0	34.5	16.2	22.7	30.1	28.6	41.1	22.8	30.7	2.3	9.7	32.3	5.7	12.5
T10–CR1000	18.1	9.0	12.3	16.3	13.9	29.4	14.2	18.1	26.3	22.0	0.6	1.5	4.7	1.8	2.1
T15–CR1	12.8	28.5	36.1	38.6	29.0	19.1	40.0	25.1	51.8	34.0	0.3	9.4	45.0	6.7	15.4
T15–CR10	14.4	33.9	36.3	29.3	28.5	21.7	42.9	25.7	37.2	31.9	0.3	22.5	39.9	9.1	18.0
T15–CR50	23.7	39.5	47.3	42.9	38.4	29.1	36.8	32.7	47.5	36.5	10.1	41.6	72.0	38.2	40.5
T15–CR100	22.3	32.0	39.4	38.0	32.9	33.0	35.0	31.1	46.6	36.4	3.9	17.3	51.7	26.6	24.9
T15–CR500	19.1	20.2	34.3	14.9	22.1	30.1	27.6	41.8	22.2	30.4	1.9	9.2	30.6	4.1	11.4
T15–CR1000	16.7	7.4	11.8	14.0	12.5	27.7	12.0	17.7	22.7	20.0	0.2	0.6	3.8	1.4	1.5
T20–CR1	2.1	12.9	28.4	15.4	14.7	2.1	16.6	30.7	20.8	17.6	0.01	0.6	4.0	0.5	1.3
T20–CR10	2.1	2.2	22.6	15.4	10.6	3.3	2.1	30.7	24.4	15.1	0.01	0.6	1.7	0.1	0.6
T20–CR50	14.5	25.	43.0	37.8	30.1	22.8	32.1	31.6	49.6	34.0	1.3	4.5	61.7	20.7	22.1
T20–CR100	14.5	21.0	47.8	28.0	27.8	22.8	26.6	35.2	35.6	30.0	1.8	3.4	66.5	18.1	22.4
T20–CR500	14.3	16.9	31.0	16.7	19.7	23.8	26.2	40.9	27.3	29.6	0.1	3.8	21.6	0.9	6.6
T20–CR1000	12.1	5.9	10.8	10.4	9.8	20.1	9.8	17.2	16.8	16.0	0.02	0.1	1.6	1.1	0.7
T25–CR50	6.7					10.4					0.5				
T28–CR50	3.3					5.3					1.4				

Notes. [(a)] Mean confidence level calculated for ten COMs (excluding CH_3NCO) with respect to H_2 for each chemical model compared to the observations toward N2, N3, N4, and N5 taken individually and all four sources taken together. [(b)] Mean confidence level calculated for the O-bearing species CH_3OH, CH_3OCHO, CH_3OCH_3, CH_3CHO, C_2H_5OH, and NH_2CHO, with respect to H_2. [(c)] Mean confidence level calculated for the cyanides CH_3CN, C_2H_5CN, and C_2H_3CN relative to H_2. Results are given in percentages. [(*)] Because formamide is not detected toward N4 and we estimated only an upper limit to its molecular column density, a level of confidence of unity is attributed if the calculated ratio $[NH_2CHO]/[H_2]$ is lower than the upper limit, otherwise it is treated normally.

Table D.2: Mean confidence level (%) of the chemical models with respect to methanol and methyl cyanide.

Model	10 COMs[a]					O-bearing species[b]					Cyanides[c]				
	N2	N3	N4*	N5	All	N2	N3	N4*	N5	All	N2	N3	N4	N5	All
T10–CR1	12.4	16.2	14.9	14.4	14.5	20.3	25.3	25.7	23.9	23.8	55.1	61.3	42.9	49.3	52.1
T10–CR10	23.1	20.1	24.3	22.2	22.4	36.0	26.0	39.0	35.5	34.1	49.8	16.4	56.3	54.8	44.3
T10–CR50	42.7	28.8	26.9	34.4	33.2	46.7	24.7	41.6	50.0	40.8	50.0	8.8	29.5	64.7	38.2
T10–CR100	31.2	29.4	26.6	29.8	29.2	43.3	22.2	40.4	40.4	36.6	80.3	13.4	13.4	31.7	34.7
T10–CR500	18.7	20.0	41.1	21.5	25.3	21.4	5.4	26.2	21.0	18.5	46.0	13.6	69.2	22.3	37.8
T10–CR1000	18.2	25.0	24.0	33.5	25.2	14.7	15.1	22.3	14.8	16.7	50.9	3.6	10.7	66.4	32.9
T15–CR1	19.6	16.3	21.3	27.9	21.3	27.7	23.8	30.7	41.9	31.0	29.7	49.7	50.3	60.1	47.5
T15–CR10	20.4	22.8	23.8	25.8	23.2	29.2	31.3	37.0	38.7	34.0	46.5	25.5	58.5	56.4	46.7
T15–CR50	49.1	35.8	28.5	36.7	37.5	46.2	26.0	42.9	50.2	41.3	48.5	9.1	31.2	73.0	40.4
T15–CR100	33.9	34.9	27.0	30.4	31.5	43.0	21.2	40.8	39.6	36.1	81.3	13.6	13.7	33.4	35.5
T15–CR500	18.7	17.8	39.1	19.6	23.8	20.8	4.3	26.1	20.5	17.9	43.2	13.2	54.6	26.9	34.5
T15–CR1000	14.3	25.7	24.9	34.4	24.9	14.2	16.0	22.2	13.9	16.6	50.7	4.0	11.7	63.7	32.5
T20–CR1	31.9	27.6	19.7	28.3	26.9	38.6	26.5	19.3	27.0	27.8	42.4	42.0	32.5	32.0	37.2
T20–CR10	19.3	42.4	14.0	15.6	22.8	26.8	33.2	19.3	20.8	25.0	15.9	43.3	63.2	57.6	45.0
T20–CR50	30.8	22.1	29.2	30.9	28.2	40.9	16.5	43.7	39.5	35.2	79.2	36.2	38.0	63.0	54.1
T20–CR100	26.1	22.7	30.5	23.9	25.8	29.6	14.4	41.6	24.9	27.6	85.9	15.3	22.4	49.4	43.3
T20–CR500	10.0	17.8	34.8	19.5	20.5	9.0	10.8	26.1	18.6	16.1	51.2	20.3	33.6	73.2	44.6
T20–CR1000	9.9	29.8	27.6	32.3	24.9	6.4	19.9	23.4	16.1	16.4	51.1	15.0	17.2	51.5	33.7
T15–CR50–UV100	39.5					45.3					53.0				
T15–CR50–UV500	26.2					39.8					89.3				
T15–CR50–UV1000	27.5					41.8					95.5				

Notes. [(a)] Mean confidence level calculated for nine COMs (excluding CH_3NCO) with respect to methanol for each chemical model compared to the observations toward N2, N3, N4, and N5 taken individually and all four sources taken together. [(b)] Mean confidence level calculated for the abundance ratios of the O-bearing species CH_3OCHO, CH_3OCH_3, CH_3CHO, C_2H_5OH, and NH_2CHO, with respect to CH_3OH for each model. [(c)] Mean confidence level calculated for the abundance of the cyanides C_2H_5CN and C_2H_3CN relative to CH_3CN. Results are given in percentages. [(*)] Because formamide is not detected toward N4 and we estimated only an upper limit to its molecular column density, a level of confidence of unity is attributed if the calculated ratio $[NH_2CHO]/[CH_3OH]$ is lower than the upper limit, otherwise it is treated normally.

Bibliography

Allen, V., van der Tak, F. F. S., Sánchez-Monge, Á., Cesaroni, R., & Beltrán, M. T. 2017, A&A, 603, A133 (Cited on pages 20, 58, 59, 135 and 137.)

Allen, V., van der Tak, F. F. S., & Walsh, C. 2018, A&A, 616, A67 (Cited on page 59.)

Altwegg, K., Balsiger, H., Bar-Nun, A., et al. 2016, Science Advances, 2, e1600285 (Cited on page 14.)

Altwegg, K., Balsiger, H., Berthelier, J. J., et al. 2017, MNRAS, 469, S130 (Cited on page 14.)

André, P., Di Francesco, J., Ward-Thompson, D., et al. 2014, Protostars and Planets VI, 27 (Cited on page 10.)

Ao, Y., Henkel, C., Menten, K. M., et al. 2013, A&A, 550, A135 (Cited on page 16.)

Arce, H. G., Santiago-García, J., Jørgensen, J. K., Tafalla, M., & Bachiller, R. 2008, ApJ, 681, L21 (Cited on page 13.)

Arzoumanian, D., André, P., Didelon, P., et al. 2011, A&A, 529, L6 (Cited on page 10.)

Bacmann, A., Taquet, V., Faure, A., Kahane, C., & Ceccarelli, C. 2012, A&A, 541, L12 (Cited on page 13.)

Barnes, A. T., Longmore, S. N., Battersby, C., et al. 2017, MNRAS, 469, 2263 (Cited on page 16.)

Battersby, C., Bally, J., Ginsburg, A., et al. 2011, A&A, 535, A128 (Cited on page 17.)

Belloche, A., Garrod, R. T., Müller, H. S. P., & Menten, K. M. 2014, Science, 345, 1584 (Cited on pages 20, 72 and 133.)

Belloche, A., Garrod, R. T., Müller, H. S. P., et al. 2009, A&A, 499, 215 (Cited on page 20.)

Belloche, A., Garrod, R. T., Müller, H. S. P., et al. 2019, arXiv e-prints, arXiv:1906.04614 (Cited on pages 19, 44, 88 and 128.)

Belloche, A., Menten, K. M., Comito, C., et al. 2008, A&A, 482, 179 (Cited on pages 14, 18, 19 and 20.)

Belloche, A., Meshcheryakov, A. A., Garrod, R. T., et al. 2017, A&A, 601, A49 (Cited on pages 19, 20, 39, 45, 48, 86, 92, 122, 143 and 176.)

Belloche, A., Müller, H. S. P., Garrod, R. T., & Menten, K. M. 2016, A&A, 587, A91 (Cited on pages 18, 19, 36, 37, 38, 39, 44, 45, 46, 48, 54, 56 and 143.)

Belloche, A., Müller, H. S. P., Menten, K. M., Schilke, P., & Comito, C. 2013, A&A, 559, A47 (Cited on pages 17, 18, 19, 20, 48 and 88.)

Benson, J. M. & Johnston, K. J. 1984, ApJ, 277, 181 (Cited on page 18.)

Bergin, E. A., Phillips, T. G., Comito, C., et al. 2010, A&A, 521, L20 (Cited on page 59.)

Bergner, J. B., Guzmán, V. G., Öberg, K. I., Loomis, R. A., & Pegues, J. 2018, ApJ, 857, 69 (Cited on page 14.)

Beuther, H., Zhang, Q., Bergin, E. A., & Sridharan, T. K. 2009, AJ, 137, 406 (Cited on pages 20 and 58.)

Black, J. H. 1994, 58, 355 (Cited on page 4.)

Blake, G. A., Sutton, E. C., Masson, C. R., & Phillips, T. G. 1986, ApJS, 60, 357 (Cited on page 59.)

Blake, G. A., Sutton, E. C., Masson, C. R., & Phillips, T. G. 1987, ApJ, 315, 621 (Cited on pages 20 and 59.)

Bockelée-Morvan, D., Biver, N., Colom, P., et al. 2004, Icarus, 167, 113 (Cited on page 14.)

Bockelée-Morvan, D., Lis, D. C., Wink, J. E., et al. 2000, A&A, 353, 1101 (Cited on page 14.)

Bohlin, R. C., Savage, B. D., & Drake, J. F. 1978, ApJ, 224, 132 (Cited on page 82.)

Bonfand, M., Belloche, A., Garrod, R. T., et al. 2019, Astronomy and Astrophysics, 628, A27 (Cited on pages 41, 57, 61, 71, 77, 78, 79, 82, 83, 84, 85, 86, 87, 91, 102, 103, 105, 109, 111, 112, 113, 115, 116, 119, 121, 123, 125, 126, 127 and 128.)

Bonfand, M., Belloche, A., Menten, K. M., Garrod, R. T., & Müller, H. S. P. 2017, A&A, 604, A60 (Cited on pages 18, 19, 41, 42, 43, 49, 50, 51, 52, 53, 54, 55, 61, 63, 65, 66, 69, 71, 72, 73, 89, 91 and 137.)

Bonnell, I. A. & Bate, M. R. 2006, MNRAS, 370, 488 (Cited on page 10.)

Bonnell, I. A., Bate, M. R., Clarke, C. J., & Pringle, J. E. 2001, MNRAS, 323, 785 (Cited on page 10.)

Botta, O. & Bada, J. L. 2002, Surveys in Geophysics, 23, 411 (Cited on page 14.)

Bottinelli, S., Ceccarelli, C., Lefloch, B., et al. 2004, ApJ, 615, 354 (Cited on page 13.)

Bujarrabal, V., Gomez-Gonzalez, J., Bachiller, R., & Martin-Pintado, J. 1988, A&A, 204, 242 (Cited on page 13.)

Carlstrom, J. E. & Vogel, S. N. 1989, ApJ, 337, 408 (Cited on page 18.)

Caswell, J. L. 1996, MNRAS, 283, 606 (Cited on pages 18, 42 and 44.)

Cazaux, S., Minissale, M., Dulieu, F., & Hocuk, S. 2016, A&A, 585, A55 (Cited on page 120.)

Cernicharo, J. 2000, 456, 81 (Cited on page 13.)

Cernicharo, J., Kisiel, Z., Tercero, B., et al. 2016, A&A, 587, L4 (Cited on page 59.)

Clark, P. C., Glover, S. C. O., Ragan, S. E., Shetty, R., & Klessen, R. S. 2013, ApJ, 768, L34 (Cited on page 15.)

Codella, C., Lorenzani, A., Gallego, A. T., Cesaroni, R., & Moscadelli, L. 2004, A&A, 417, 615 (Cited on pages 12 and 86.)

Compiègne, M., Verstraete, L., Jones, A., et al. 2011, A&A, 525, A103 (Cited on page 31.)

Corby, J. F., Jones, P. A., Cunningham, M. R., et al. 2015, MNRAS, 452, 3969 (Cited on pages 13 and 18.)

Crockett, N. R., Bergin, E. A., Neill, J. L., et al. 2014, ApJ, 787, 112 (Cited on page 59.)

Csengeri, T., Bontemps, S., Wyrowski, F., et al. 2018, A&A, 617, A89 (Cited on pages 51, 60, 90 and 128.)

Csengeri, T., Bontemps, S., Wyrowski, F., et al. 2017, A&A, 601, A60 (Cited on page 77.)

Csengeri, T., Urquhart, J. S., Schuller, F., et al. 2014, A&A, 565, A75 (Cited on page 77.)

Csengeri, T., Weiss, A., Wyrowski, F., et al. 2016, A&A, 585, A104 (Cited on page 18.)

Cuadrado, S., Goicoechea, J. R., Cernicharo, J., et al. 2017, A&A, 603, A124 (Cited on page 13.)

Cyganowski, C. J., Brogan, C. L., Hunter, T. R., & Churchwell, E. 2009, ApJ, 702, 1615 (Cited on pages 135 and 137.)

Dalgarno, A. 2006, Proceedings of the National Academy of Science, 103, 12269 (Cited on page 5.)

De Pree, C. G., Goss, W. M., & Gaume, R. A. 1998, ApJ, 500, 847 (Cited on page 18.)

De Pree, C. G., Peters, T., Mac Low, M. M., et al. 2015, ApJ, 815, 123 (Cited on pages 18, 42, 44, 68 and 88.)

Draine, B. T. 1978, ApJS, 36, 595 (Cited on pages 4 and 93.)

Draine, B. T. 2011 (Cited on pages 1, 5, 6, 27 and 29.)

Drury, L. 1983, Space Sci. Rev., 36, 57 (Cited on page 4.)

Duley, W. W. & Williams, D. A. 1984 (Cited on page 92.)

Dullemond, C. P., Juhasz, A., Pohl, A., et al. 2012, ASCL (Cited on page 76.)

Dunham, J. T. 1937, PASP, 49, 26 (Cited on page 13.)

Elitzur, M., Hollenbach, D. J., & McKee, C. F. 1989, ApJ, 346, 983 (Cited on pages 12 and 64.)

Endres, C. P., Schlemmer, S., Schilke, P., Stutzki, J., & Müller, H. S. P. 2016, Journal of Molecular Spectroscopy, 327, 95 (Cited on page 39.)

Enrique-Romero, J., Rimola, A., Ceccarelli, C., & Balucani, N. 2016, MNRAS, 459, L6 (Cited on page 120.)

Favre, C., Pagani, L., Goldsmith, P. F., et al. 2017, A&A, 604, L2 (Cited on page 59.)

Federrath, C., Rathborne, J. M., Longmore, S. N., et al. 2016, ApJ, 832, 143 (Cited on page 16.)

Feng, S., Beuther, H., Henning, T., et al. 2015, A&A, 581, A71 (Cited on pages 20, 58 and 59.)

Ferrière, K., Gillard, W., & Jean, P. 2007, A&A, 467, 611 (Cited on page 15.)

Fleck, A. J. & Canfield, E. H. 1983, JCP, 54, 508 (Cited on page 77.)

Garrod, R. T. 2008, A&A, 491, 239 (Cited on pages 14 and 98.)

Garrod, R. T. 2013, ApJ, 765, 60 (Cited on pages 81, 91, 92, 95, 98, 99 and 176.)

Garrod, R. T., Belloche, A., Müller, H. S. P., & Menten, K. M. 2017, A&A, 601, A48 (Cited on pages 20, 92, 122 and 133.)

Garrod, R. T. & Herbst, E. 2006, A&A, 457, 927 (Cited on page 15.)

Garrod, R. T. & Pauly, T. 2011, ApJ, 735, 15 (Cited on pages 83, 102, 116, 117 and 118.)

Garrod, R. T., Vasyunin, A. I., Semenov, D. A., Wiebe, D. S., & Henning, T. 2009, ApJ, 700, L43 (Cited on page 98.)

Garrod, R. T., Wakelam, V., & Herbst, E. 2007, A&A, 467, 1103 (Cited on pages 14, 95, 96 and 122.)

Gaume, R. A. & Claussen, M. J. 1990, ApJ, 351, 538 (Cited on page 18.)

Gaume, R. A., Claussen, M. J., de Pree, C. G., Goss, W. M., & Mehringer, D. M. 1995, ApJ, 449, 663 (Cited on pages 18, 42, 44, 67, 68 and 88.)

Giannetti, A., Brand, J., Sánchez-Monge, Á., et al. 2013, A&A, 556, A16 (Cited on page 16.)

Gibb, E. L., Whittet, D. C. B., Schutte, W. A., et al. 2000, ApJ, 536, 347 (Cited on page 104.)

Ginsburg, A. 2017, ArXiv e-prints (Cited on page 43.)

Ginsburg, A., Bally, J., Barnes, A., et al. 2018, ApJ, 853, 171 (Cited on pages 16, 17, 18 and 19.)

Ginsburg, A., Henkel, C., Ao, Y., et al. 2016, A&A, 586, A50 (Cited on page 16.)

Glassgold, A. E. & Langer, W. D. 1974, ApJ, 193, 73 (Cited on page 5.)

Goldsmith, P. F. & Langer, W. D. 1978, ApJ, 222, 881 (Cited on page 4.)

Goldsmith, P. F. & Langer, W. D. 1999, ApJ, 517, 209 (Cited on pages 27 and 35.)

Gómez, L., Rodriguez, L. F., Loinard, L., et al. 2005, ApJ, 635, 1166 (Cited on page 59.)

Gordon, M. A., Berkermann, U., Mezger, P. G., et al. 1993, A&A, 280, 208 (Cited on page 18.)

Graedel, T. E., Langer, W. D., & Frerking, M. A. 1982, ApJS, 48, 321 (Cited on page 98.)

Green, J. A., Caswell, J. L., Fuller, G. A., et al. 2008, MNRAS, 385, 948 (Cited on page 135.)

Guzmán, A. E., Sanhueza, P., Contreras, Y., et al. 2015, ApJ, 815, 130 (Cited on page 16.)

Guzmán, V. V., Pety, J., Gratier, P., et al. 2014, Faraday Discussions, 168, 103 (Cited on page 13.)

Hachisuka, K., Brunthaler, A., Menten, K. M., et al. 2006, ApJ, 645, 337 (Cited on page 88.)

Halfen, D. T., Ilyushin, V. V., & Ziurys, L. M. 2015, ApJ, 812, L5 (Cited on page 18.)

Harada, N., Herbst, E., & Wakelam, V. 2010, ApJ, 721, 1570 (Cited on page 100.)

Hasegawa, T. I., Herbst, E., & Leung, C. M. 1992, ApJS, 82, 167 (Cited on pages 92 and 95.)

Hayakawa, S., Nishimura, S., & Takayanagi, T. 1961, PASJ, 13, 184 (Cited on page 5.)

Helmich, F. P. & van Dishoeck, E. F. 1997, A&A, 124, 205 (Cited on page 20.)

Herbst, E. & van Dishoeck, E. F. 2009, ARA&A, 47, 427 (Cited on pages 1, 13, 14, 15, 96 and 130.)

Higuchi, A. E., Hasegawa, T., Saigo, K., Sanhueza, P., & Chibueze, J. O. 2015, ApJ, 815, 106 (Cited on pages 62 and 64.)

Hildebrand, R. H. 1983, QJRAS, 24, 267 (Cited on pages 31 and 32.)

Ho, P. T. P., Moran, J. M., & Lo, K. Y. 2004, ApJ, 616, L1 (Cited on page 26.)

Hocuk, S., Szűcs, L., Caselli, P., et al. 2017, A&A, 604, A58 (Cited on pages 30, 114, 116, 117, 118, 126 and 128.)

Hollenbach, D., Elitzur, M., & McKee, C. F. 2013, ApJ, 773, 70 (Cited on page 64.)

Hollis, J. M., Jewell, P. R., Lovas, F. J., & Remijan, A. 2004, ApJ, 613, L45 (Cited on page 13.)

Hollis, J. M., Lovas, F. J., & Jewell, P. R. 2000, ApJ, 540, L107 (Cited on page 19.)

Hollis, J. M., Lovas, F. J., Remijan, A. J., et al. 2006, ApJ, 643, L25 (Cited on page 19.)

Hosokawa, T. & Omukai, K. 2009, ApJ, 691, 823 (Cited on pages 81, 82 and 89.)

Hudson, R. L., Moore, M. H., & Gerakines, P. A. 2001, ApJ, 550, 1140 (Cited on page 124.)

Hüttemeister, S., Wilson, T. L., Henkel, C., & Mauersberger, R. 1993, A&A, 276, 445 (Cited on pages 18 and 19.)

Hüttemeister, S., Wilson, T. L., Mauersberger, R., et al. 1995, A&A, 294, 667 (Cited on page 18.)

Indriolo, N., Neufeld, D. A., Gerin, M., et al. 2015, ApJ, 800, 40 (Cited on page 15.)

Iqbal, W., Wakelam, V., & Gratier, P. 2018, A&A, 620, A109 (Cited on page 120.)

Ivlev, A. V., Padovani, M., Galli, D., & Caselli, P. 2015, ApJ, 812, 135 (Cited on page 5.)

Jeffreson, S. M. R. & Kruijssen, J. M. D. 2018, MNRAS, 476, 3688 (Cited on page 10.)

Jeffreson, S. M. R., Kruijssen, J. M. D., Krumholz, M. R., & Longmore, S. N. 2018, MNRAS, 478, 3380 (Cited on pages 11 and 78.)

Juvela, M., Demyk, K., Doi, Y., et al. 2015, A&A, 584, A94 (Cited on page 31.)

Kauffmann, J., Bertoldi, F., Bourke, T. L., Evans, I. N. J., & Lee, C. W. 2008, A&A, 487, 993 (Cited on page 31.)

Kauffmann, J., Pillai, T., & Zhang, Q. 2013, ApJ, 765, L35 (Cited on page 16.)

Kauffmann, J., Pillai, T., Zhang, Q., et al. 2017a, A&A, 603, A89 (Cited on page 16.)

Kauffmann, J., Pillai, T., Zhang, Q., et al. 2017b, A&A, 603, A90 (Cited on pages 16 and 17.)

Klein, U. 2006, University of Bonn (Cited on page 21.)

Kounkel, M., Hartmann, L., Loinard, L., et al. 2017, ApJ, 834, 142 (Cited on page 57.)

Krügel, E. 2007, 377 (Cited on page 92.)

Krügel, E. 2008, An introduction to the physics of interstellar dust, 377–380 (Cited on pages 1 and 30.)

Kruijssen, J. M. D., Dale, J. E., & Longmore, S. N. 2015, MNRAS, 447, 1059 (Cited on pages 16, 17 and 209.)

Kruijssen, J. M. D., Longmore, S. N., Elmegreen, B. G., et al. 2014, MNRAS, 440, 3370 (Cited on page 16.)

Krumholz, M. 2017 (Cited on pages 16 and 27.)

Krumholz, M. R., Klein, R. I., McKee, C. F., Offner, S. S. R., & Cunningham, A. J. 2009, Science, 323, 754 (Cited on page 9.)

Krumholz, M. R. & Kruijssen, J. M. D. 2015, MNRAS, 453, 739 (Cited on page 16.)

Kuan, Y.-J. & Snyder, L. E. 1996, ApJ, 470, 981 (Cited on page 66.)

Kutner, M. L. & Ulich, B. L. 1981, ApJ, 250, 341 (Cited on page 22.)

Lada, C. J., Forbrich, J., Lombardi, M., & Alves, J. F. 2012, ApJ, 745, 190 (Cited on page 16.)

Lada, C. J., Lombardi, M., & Alves, J. F. 2010, ApJ, 724, 687 (Cited on page 16.)

Le Petit, F., Ruaud, M., Bron, E., et al. 2016, A&A, 585, A105 (Cited on page 15.)

Lee, E. J., Murray, N., & Rahman, M. 2012, ApJ, 752, 146 (Cited on page 16.)

Lee, H.-H., Herbst, E., Pineau des Forets, G., Roueff, E., & Le Bourlot, J. 1996, A&A, 311, 690 (Cited on page 99.)

Leger, A., Jura, M., & Omont, A. 1985, A&A, 144, 147 (Cited on page 5.)

Lequeux, J. 2005 (Cited on pages 1 and 27.)

Leurini, S., Codella, C., López-Sepulcre, A., et al. 2014, A&A, 570, A49 (Cited on page 12.)

Leurini, S., Schilke, P., Menten, K. M., et al. 2004, A&A, 422, 573 (Cited on page 136.)

Leurini, S., Schilke, P., Wyrowski, F., & Menten, K. M. 2007, A&A, 466, 215 (Cited on page 136.)

Lis, D. C., Carlstrom, J. E., & Keene, J. 1991, ApJ, 380, 429 (Cited on page 18.)

Lis, D. C. & Goldsmith, P. F. 1990, ApJ, 356, 195 (Cited on page 17.)

Lis, D. C., Serabyn, E., Zylka, R., & Li, Y. 2001, ApJ, 550, 761 (Cited on page 15.)

Liszt, H., Gerin, M., Beasley, A., & Pety, J. 2018, ApJ, 856, 151 (Cited on page 13.)

Liu, S.-Y., Girart, J. M., Remijan, A., & Snyder, L. E. 2002, ApJ, 576, 255 (Cited on page 59.)

Longmore, S. N., Bally, J., Testi, L., et al. 2013, MNRAS, 429, 987 (Cited on pages 15 and 16.)

Longmore, S. N., Rathborne, J., Bastian, N., et al. 2012, ApJ, 746, 117 (Cited on page 16.)

Louvet, F., Dougados, C., Cabrit, S., et al. 2018, A&A, 618, A120 (Cited on page 9.)

Lu, X., Zhang, Q., Kauffmann, J., et al. 2019, ApJ, 872, 171 (Cited on pages 16 and 17.)

Luhman, K. L., Robberto, M., Tan, J. C., et al. 2017, ApJ, 838, L3 (Cited on page 59.)

Mangum, J. G. & Shirley, Y. L. 2015, PASP, 127, 266 (Cited on pages 27 and 33.)

Maret, S., Hily-Blant, P., Pety, J., Bardeau, S., & Reynier, E. 2011, A&A, 526, A47 (Cited on page 39.)

Martin-Pintado, J., de Vicente, P., Wilson, T. L., & Johnston, K. J. 1990, A&A, 236, 193 (Cited on page 18.)

Mathis, J. S., Mezger, P. G., & Panagia, N. 1983, A&A, 128, 212 (Cited on page 4.)

Mattern, M., Kauffmann, J., Csengeri, T., et al. 2018, A&A, 619, A166 (Cited on page 10.)

Maury, A. J., Belloche, A., André, P., et al. 2014, A&A, 563, L2 (Cited on page 13.)

McGrath, E. J., Goss, W. M., & De Pree, C. G. 2004, ApJS, 155, 577 (Cited on page 65.)

McGuire, B. A. 2018, ApJS, 239, 17 (Cited on page 13.)

McGuire, B. A., Shingledecker, C. N., Willis, E. R., et al. 2017, ApJ, 851, L46 (Cited on page 137.)

McKee, C. F. & Tan, J. C. 2003, ApJ, 585, 850 (Cited on page 9.)

Mehringer, D. M., Palmer, P., Goss, W. M., & Yusef-Zadeh, F. 1993, ApJ, 412, 684 (Cited on page 18.)

Mehringer, D. M., Snyder, L. E., Miao, Y., & Lovas, F. J. 1997, ApJ, 480, L71 (Cited on page 18.)

Menten, K. M. 1991, ApJ, 380, L75 (Cited on page 12.)

Menten, K. M. 2004, in The Dense Interstellar Medium in Galaxies, ed. S. Pfalzner, C. Kramer, C. Staubmeier, & A. Heithausen, Vol. 91, 69 (Cited on page 19.)

Menten, K. M., Reid, M. J., Forbrich, J., & Brunthaler, A. 2007, A&A, 474, 515 (Cited on page 10.)

Menten, K. M., Reid, M. J., Pratap, P., Moran, J. M., & Wilson, T. L. 1992, ApJ, 401, L39 (Cited on page 88.)

Millar, T. J. & Williams, D. A. 1993 (Cited on page 92.)

Minier, V., Ellingsen, S. P., Norris, R. P., & Booth, R. S. 2003, A&A, 403, 1095 (Cited on page 12.)

Morgan, J. W. & Anders, E. 1980, Proceedings of the National Academy of Science, 77, 6973 (Cited on page 7.)

Morris, M. & Serabyn, E. 1996, ARA&A, 34, 645 (Cited on page 15.)

Motte, F., Bontemps, S., & Louvet, F. 2018, ARA&A, 56, 41 (Cited on pages 1, 9, 10 and 11.)

Müller, H. S. P., Belloche, A., Xu, L.-H., et al. 2016, A&A, 587, A92 (Cited on pages 20, 39, 45, 56, 92, 122 and 143.)

Murray, N. & Chang, P. 2012, ApJ, 746, 75 (Cited on page 10.)

Murugeshan, C. 2015, Master thesis, Univ. of Bonn (Cited on pages 135 and 137.)

Neill, J. L., Bergin, E. A., Lis, D. C., et al. 2014, ApJ, 789, 8 (Cited on page 18.)

Neufeld, D. A. & Wolfire, M. G. 2017, ApJ, 845, 163 (Cited on pages 5 and 124.)

Öberg, K. I., Bottinelli, S., Jørgensen, J. K., & van Dishoeck, E. F. 2010, ApJ, 716, 825 (Cited on page 13.)

Öberg, K. I., Guzmán, V. V., Furuya, K., et al. 2015, Nature, 520, 198 (Cited on page 14.)

Oka, T., Geballe, T. R., Goto, M., Usuda, T., & McCall, B. J. 2005, ApJ, 632, 882 (Cited on page 15.)

Orozco-Aguilera, M. T., Zapata, L. A., Hirota, T., Qin, S.-L., & Masqué, J. M. 2017, ApJ, 847, 66 (Cited on page 59.)

Ossenkopf, V. & Henning, T. 1994, A&A, 291, 943 (Cited on pages 71 and 76.)

Ott, J., Weiß, A., Staveley-Smith, L., Henkel, C., & Meier, D. S. 2014, ApJ, 785, 55 (Cited on page 16.)

Padovani, M. & Galli, D. 2013, 34, 61 (Cited on page 5.)

Padovani, M., Galli, D., & Glassgold, A. E. 2009, A&A, 501, 619 (Cited on page 5.)

Padovani, M., Marcowith, A., Hennebelle, P., & Ferrière, K. 2016, A&A, 590, A8 (Cited on page 4.)

Pagani, L., Bergin, E., Goldsmith, P. F., et al. 2019, arXiv e-prints (Cited on page 59.)

Palau, A., Walsh, C., Sánchez-Monge, Á., et al. 2017, MNRAS, 467, 2723 (Cited on page 13.)

Parker, E. N. 1958, Physical Review, 110, 1445 (Cited on page 5.)

Paron, S., Ortega, M. E., Petriella, A., et al. 2012, MNRAS, 419, 2206 (Cited on pages 135 and 137.)

Peretto, N., Fuller, G. A., Plume, R., et al. 2010, A&A, 518, L98 (Cited on page 4.)

Peters, T., Banerjee, R., Klessen, R. S., & Mac Low, M.-M. 2011, ApJ, 729, 72 (Cited on pages 79, 82 and 89.)

Peters, T., Mac Low, M.-M., Banerjee, R., Klessen, R. S., & Dullemond, C. P. 2010, ApJ, 719, 831 (Cited on pages 13 and 88.)

Planck Collaboration, Abergel, A., Ade, P. A. R., et al. 2014a, A&A, 571, A11 (Cited on pages 3 and 31.)

Planck Collaboration, Abergel, A., Ade, P. A. R., et al. 2014b, A&A, 566, A55 (Cited on page 4.)

Prasad, S. S. & Tarafdar, S. P. 1983, ApJ, 267, 603 (Cited on page 5.)

Pratap, P., Megeath, S. T., & Bergin, E. A. 1999, ApJ, 517, 799 (Cited on page 57.)

Qin, S.-L., Schilke, P., Rolffs, R., et al. 2011, A&A, 530, L9 (Cited on pages 18, 19, 40, 65, 66 and 73.)

Qin, S.-L., Schilke, P., Wu, J., et al. 2015, ApJ, 803, 39 (Cited on page 20.)

Quénard, D., Jiménez-Serra, I., Viti, S., Holdship, J., & Coutens, A. 2018, MNRAS, 474, 2796 (Cited on page 119.)

Rathborne, J. M., Longmore, S. N., Jackson, J. M., et al. 2014, ApJ, 795, L25 (Cited on page 16.)

Reach, W. T., Heiles, C., & Bernard, J.-P. 2015, ApJ, 811, 118 (Cited on page 31.)

Reid, M. J., Menten, K. M., Brunthaler, A., et al. 2014, ApJ, 783, 130 (Cited on page 17.)

Remijan, A. J. 2015, IAU General Assembly, 22, 2257092 (Cited on pages 25 and 26.)

Requena-Torres, M. A., Martín-Pintado, J., Rodríguez-Franco, A., et al. 2006, A&A, 455, 971 (Cited on page 13.)

Rimmer, P. B., Herbst, E., Morata, O., & Roueff, E. 2012, A&A, 537, A7 (Cited on pages 5 and 124.)

Rodriguez, L. F., Dzib, S. A., Loinard, L., et al. 2017, ApJ, 834, 140 (Cited on page 59.)

Rodriguez, L. F., Poveda, A., Lizano, S., & Allen, C. 2005, ApJ, 627, L65 (Cited on page 59.)

Rothard, H., Domaracka, A., Boduch, P., et al. 2017, Journal of Physics B Atomic Molecular Physics, 50, 062001 (Cited on pages 114 and 124.)

Sakai, N. & Yamamoto, S. 2011, 280, 43 (Cited on page 13.)

Sánchez-Monge, Á., Schilke, P., Schmiedeke, A., et al. 2017, A&A, 604, A6 (Cited on pages 18, 19, 42, 43, 44, 72, 74, 75, 88 and 137.)

Schilke, P., Benford, D. J., Hunter, T. R., Lis, D. C., & Phillips, T. G. 2001, ApJS, 132, 281 (Cited on page 59.)

Schilke, P., Walmsley, C. M., Pineau des Forets, G., & Flower, D. R. 1997, A&A, 321, 293 (Cited on page 12.)

Schmiedeke, A., Schilke, P., Möller, T., et al. 2016, A&A, 588, A143 (Cited on pages 17, 18 and 19.)

Schnee, S., Enoch, M., Noriega-Crespo, A., et al. 2010, ApJ, 708, 127 (Cited on page 31.)

Shi, H., Zhao, J.-H., & Han, J. L. 2010, ApJ, 710, 843 (Cited on page 43.)

Shingledecker, C. N., Tennis, J., Le Gal, R., & Herbst, E. 2018, ApJ, 861, 20 (Cited on pages 114 and 124.)

Shu, F. H. 1977, ApJ, 214, 488 (Cited on pages 76 and 77.)

Shu, F. H., Adams, F. C., & Lizano, S. 1987, ARA&A, 25, 23 (Cited on page 8.)

Skouteris, D., Balucani, N., Ceccarelli, C., et al. 2018, MNRAS (Cited on page 120.)

Snow, T. P. & Bierbaum, V. M. 2008, Annual Review of Analytical Chemistry, 1, 229 (Cited on pages 5 and 7.)

Snow, T. P. & McCall, B. J. 2006, ARA&A, 44, 367 (Cited on pages 6, 7 and 81.)

Sobolev, A. M., Cragg, D. M., & Godfrey, P. D. 1997, A&A, 324, 211 (Cited on page 12.)

Spitzer, J. L. & Tomasko, M. G. 1968, ApJ, 152, 971 (Cited on page 5.)

Sutton, E. C., Blake, G. A., Genzel, R., Masson, C. R., & Phillips, T. G. 1986, ApJ, 311, 921 (Cited on page 59.)

Sutton, E. C., Peng, R., Danchi, W. C., et al. 1995, ApJS, 97, 455 (Cited on page 20.)

Suzuki, H., Ohishi, M., Kaifu, N., Ishikawa, S.-I., & Kasuga, T. 1986, PASJ, 38, 911 (Cited on page 13.)

Swings, P. & Rosenfeld, L. 1937, ApJ, 86, 483 (Cited on page 13.)

Tercero, B., Cernicharo, J., Pardo, J. R., & Goicoechea, J. R. 2010, A&A, 517, A96 (Cited on page 59.)

Tercero, B., Cuadrado, S., López, A., et al. 2018, A&A, 620, L6 (Cited on pages 20, 58 and 59.)

Tercero, B., Vincent, L., Cernicharo, J., Viti, S., & Marcelino, N. 2011, A&A, 528, A26 (Cited on page 59.)

Thiel, V., Belloche, A., Menten, K. M., Garrod, R. T., & Müller, H. S. P. 2017, A&A, 605, L6 (Cited on page 13.)

Tigé, J., Motte, F., Russeil, D., et al. 2017, A&A, 602, A77 (Cited on pages 11 and 16.)

Umebayashi, T. & Nakano, T. 1981, PASJ, 33, 617 (Cited on page 5.)

van der Tak, F. F. S., Belloche, A., Schilke, P., et al. 2006, A&A, 454, L99 (Cited on page 15.)

van der Walt, J. 2005, MNRAS, 360, 153 (Cited on pages 12, 86 and 88.)

van Dishoeck, E. F. & Blake, G. A. 1998, ARA&A, 36, 317 (Cited on page 12.)

Vastel, C., Ceccarelli, C., Lefloch, B., & Bachiller, R. 2014, ApJ, 795, L2 (Cited on page 13.)

Vasyunin, A. I., Semenov, D. A., Wiebe, D. S., & Henning, T. 2009, ApJ, 691, 1459 (Cited on page 98.)

Wakelam, V. & Herbst, E. 2008, ApJ, 680, 371 (Cited on page 98.)

Wakelam, V., Herbst, E., & Selsis, F. 2006, A&A, 451, 551 (Cited on page 120.)

Wakelam, V., Selsis, F., Herbst, E., & Caselli, P. 2005, A&A, 444, 883 (Cited on page 120.)

Walsh, C., Loomis, R. A., Öberg, K. I., et al. 2016, ApJ, 823, L10 (Cited on page 14.)

Whittet, D. C. B., Gerakines, P. A., Tielens, A. G. G. M., et al. 1998, ApJ, 498, L159 (Cited on page 104.)

Wienen, M., Wyrowski, F., Schuller, F., et al. 2012, A&A, 544, A146 (Cited on pages 135 and 137.)

Wilcock, L. A., Ward-Thompson, D., Kirk, J. M., et al. 2012, MNRAS, 422, 1071 (Cited on pages 10, 11, 77 and 78.)

Willis, E. R. & Garrod, R. T. 2017, ApJ, 840, 61 (Cited on page 95.)

Wilson, T. L., Rohlfs, K., & Hüttemeister, S. 2009 (Cited on pages 21, 25 and 26.)

Wolfire, M. G. & Cassinelli, J. P. 1987, ApJ, 319, 850 (Cited on pages 8 and 9.)

Wood, D. O. S. & Churchwell, E. 1989, ApJS, 69, 831 (Cited on page 13.)

Wright, M. C. H. & Plambeck, R. L. 2017, ApJ, 843, 83 (Cited on page 59.)

Wright, M. C. H., Plambeck, R. L., & Wilner, D. J. 1996, ApJ, 469, 216 (Cited on page 59.)

Wu, Y. W., Sato, M., Reid, M. J., et al. 2014, A&A, 566, A17 (Cited on page 57.)

Wyrowski, F., Schilke, P., Walmsley, C. M., & Menten, K. M. 1999, ApJ, 514, L43 (Cited on page 88.)

Xu, Y., Li, J. J., Hachisuka, K., et al. 2008, A&A, 485, 729 (Cited on page 12.)

Xue, C., Remijan, A. J., Burkhardt, A. M., & Herbst, E. 2019, ApJ, 871, 112 (Cited on page 134.)

Yorke, H. W. & Sonnhalter, C. 2002, ApJ, 569, 846 (Cited on page 9.)

Yusef-Zadeh, F., Muno, M., Wardle, M., & Lis, D. C. 2007, ApJ, 656, 847 (Cited on page 15.)

Zhang, B., Zheng, X. W., Reid, M. J., et al. 2009, ApJ, 693, 419 (Cited on page 57.)

Zinnecker, H. & Yorke, H. W. 2007, ARA&A, 45, 481 (Cited on pages 1 and 9.)

Zucconi, A., Walmsley, C. M., & Galli, D. 2001, A&A, 376, 650 (Cited on pages 4 and 83.)

List of Figures

List of Tables